Università di Pisa

Corso di laurea magistrale in Ingegneria Energetica

Hybrid CFD-BEM Modelling of a Diffuser-Augmented Vertical Axis Wind Turbine and Comparison with an Existing Solution for Sustainable Buildings

Tesi di laurea magistrale in Ingegneria Energetica

Relatori:

Ing. Stefania Zanforlin

Prof. Daniele Testi

Candidato:

Stefano Letizia

Anno accademico 2014/2015

Acknowledgement

First of all, I would like to express my gratitude to my advisors Ing. Stefania Zanforlin and Prof. Daniele Testi that through their careful supervision made this work possible. I wish this result could, at least partially, repay them for the great material and intellectual effort spent during these months to help me in my research.

A special thanks to Ing. Lorenzo Ferrari for his determinant support in the validation phase.

I also would like to express my gratitude to Prof. Guido Buresti, whose precious suggestions really helped me to overcome one of the most troublesome question arisen during my study.

Concerning my family, my girlfriend and all the friends of mine, I can hardly express my thankfulness for the love and support they gave me during these hard years. If there will be much more than equations inside me at the end of this transforming path it's just because of them.

To conclude, thanks to everyone that had remembered me, day by day, through their humility or their pride, through their passion for knowledge or their greed for power, how much there still to learn out there. Could the fecund ignorance and not the blinding self-pride be the engine of my life.

Index

Symbols and abbreviations

ρ	Fluid density
μ	Fluid dynamic vicosity
V_0 *or* U	Wind undisturbed velocity
A	Rotor swept area
T	Torque
P	Power
AoA	Angle of attack
ω	Rotor speed
R	Rotor radius
D	Rotor diameter
$TSR = \frac{\omega R}{U}$	Tip-speed ratio
c	Blade chord
AR	Blade aspect ratio
Re	Reynolds number
M	Mach number
k	Reduced frequency
C_l o Cl	Lift coefficient
C_d o Cd	Drag coefficient
$Cp = \frac{T}{\frac{1}{2}\rho U^3 A}$	Power coefficient
$Ct = \frac{T}{\frac{1}{2}\rho U^2 A\, R}$	Torque coefficient (for a single blade when not specified)
$HAWT$	Horizontal-axis wind turbine
$VAWT$	Vertical-axis wind turbine
$DAWT$	Diffuser-augmented wind turbine
BL	Boundary layer

Introduction

The general concern about the negative impacts of power generation on climate changes is growing, because of the increasing number of researches confirming that the global temperature is rising. Human activities are in part responsible for this global warming, through the emission of greenhouse gases. In fact, atmospheric concentrations of GHGs are at levels that are unprecedented in at least 800,000 years and the total anthropogenic radiative forcing over 1750-2011 is calculated to be a warming effect of 2.3 (1.1 to 3.3) W/m^2 [1]. A promising way for reducing GHG emissions from energy generators is through using Renewable Energy Sources (RES) such as solar, wind, and geothermal in generating electricity [2]. However, some technical, economical and regulatory issues are still hindering wider deployment of RES in power systems [2, 3]. The main troublesome questions are the uncontrollability of the source and the necessity for an instantaneous satisfaction of energy demand. A feasible solution could rely on the possibilities offered by distributed hybrid power systems (HPS). Supplying the load by means of multiple renewable energy generation systems can offer the advantages of exploiting more complementary sources (e.g. sun and wind) [4]. Moreover, the distributed generation approach promotes the self-consumption and permits a tailor-made system. On the other side, the sizing and optimization of autonomous renewable hybrid energy systems is more complex than that of single systems [5]. The HPS solution becomes even more attractive for stand-alone buildings, since a minimal generation system is anyway required.
The most common and universally available renewable energy source for householder-size systems are the sun and the wind. However, unlike the solar energy exploitation systems (i.e. PV panels and solar collectors), that have reached a level of maturity, small wind turbines[1] are not still very attractive for householders investors [6, 7]. The main reasons are [8, 9, 10, 11]:

- relatively high costs
- noise concerns
- visual integration
- limited efficiency of small and near ground installations

The conditions in which a small turbine operates, in fact, greatly differs from the favorable wind regime characterizing the multi-MW installation. The wind near ground is affected by the presence of buildings, trees and other obstacles increasing its turbulence and multi-directionality [10, 12, 13, 14], without forgetting the wind gradient due to the no-slip condition at the ground.

Concerning the appropriate choice of the type of turbine suitable for small buildings careful considerations are needed. It is well known that the most efficient and cost-effective machines for the exploitation of wind energy are the multi-MW Horizontal Axis Wind Turbine (HAWT), with a maximum Cp of 0.5 [15]. Unfortunately, the performance of fluid machines are greatly affect by the scale factor so that these efficiency level cannot be even approached by small turbines (the chord-based Reynolds number is low). As several wind tunnel experiments confirmed, the typical Cp for micro-HAWT is around 0.2-0.3 [16-20].

[1]A turbine having less tan 20kW of rated power is conventionally called micro or householder-size.

The operative Cp in turbulent and weak winds is expected to further reduce. Moreover, the HAWTs need for a yaw control and are known for being noisy, having a high tip speed [21]. These issues brought many researchers to investigate another concept of wind turbine: the vertical axis type (VAWT).

The VAWT can be divided in two categories:

- drag-driven, in which the torque is the results of an asymmetric pressure distribution on a rotating surface. The most common design is the Savonius (fig. 0.1-**a**).
- lift-driven, where aerodynamic blades experience a lift force that, as result of the interaction between relative and absolute speed, generates always a positive contribution to the torque. The most diffused lift-driven VAWT are the Darrieus model both in straight blades (or H-type) and curved blades (or Trposkein) configurations (fig. 0.1-**b**, **c**)

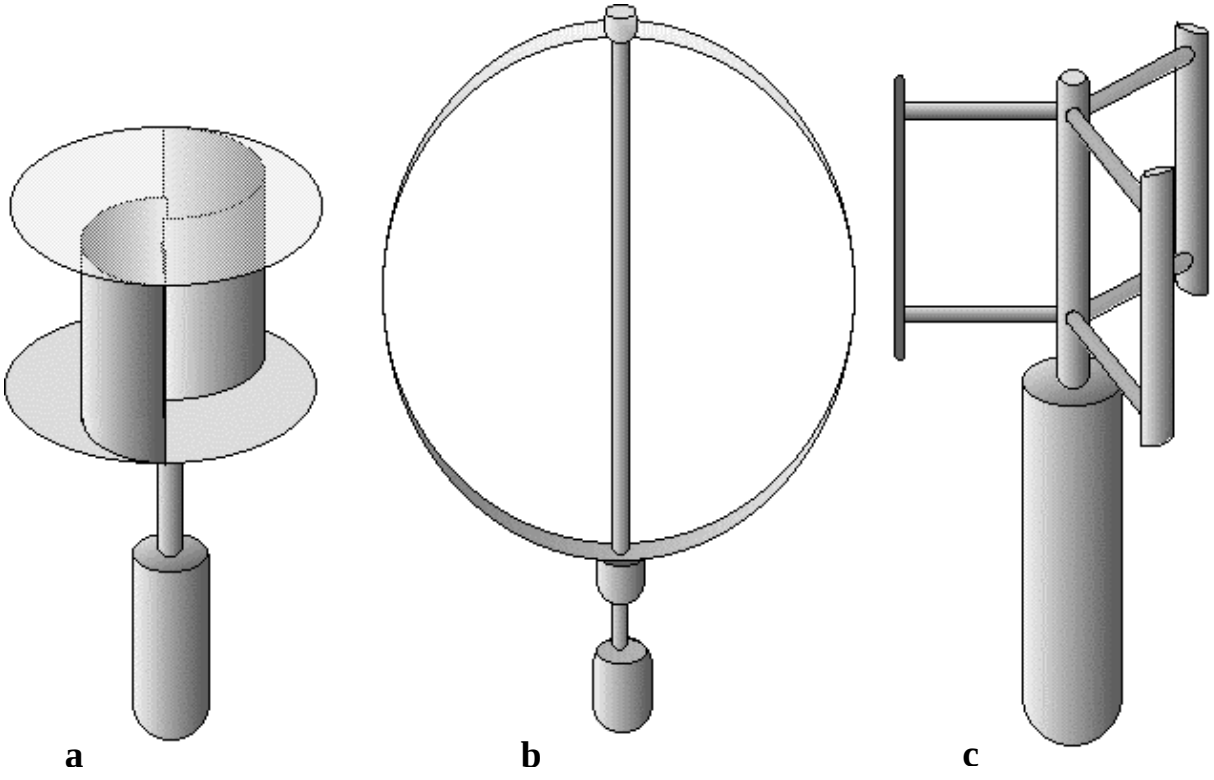

Figure 0.1 - VAWT: **a**-Savonius, **b**-Troposkein, **c**-H-Darriueus

The Darrieus model has much better performances than the Savonius, and this is the reason why it is the object of the present study.

A great effort have been spent in the past century to investigate the performance of Vertical Axis Wind Turbine [22] and some large-scale utilities were built. During the 1980s, prototype H-type turbines based on the work of Musgrove [23, 24] were developed in the UK. The reported optimal Cp is about 0.4 [22]. In 1988, 4MW Darrius type VAWT called Eole [25] was developed in a collaborative work with industry. The only significant

commercial exploitation of a VAWT was by FloWind Inc, but the company went bankrupt in 1997 because its design were not competitive with modern HAWTs.

As already mentioned, a new interest in VAWT comes from the investigation of the unfair operating conditions that wind turbines experience when they are introduced in urban areas. With respect to the HAWT, the vertical axes models have the following main advantages [9, 14, 21]:

- no need for yaw control
- lower noise emission (lower rotor speed)
- generator installed at the ground

Another not negligible effect that a Darrieus rotor could exploit is the skewed flow, a regime that a turbine placed on roof top would experience. It has been demonstrated by Bussel et al. [26, 27] that performance improvement are achievable by this turbines when the incoming flow has a non-null z-velocity.

However, negative aspects of Darrieus turbine in respect to HAWT are its more problematic self-starting behavior [21] and the higher torque ripple.

As regards the choice between a H-Darrieus and a Troposkein, the main difference between them, from an aerodynamic point of view, is that in the H-type, the blade operates (ideally) at the same speed along the entire span, whereas in the Troposkein the relative velocity and thus the torque output change along the blade. In contrast, the Troposkein does not need for struts that can represent a significant parasitic loss [28].

In the last 5 years, thanks to the increased computational speed of new processors and the spread of commercial CFD solvers, an undefined number of scientific articles to investigate the H-Darrieus rotor were produced (it would be even redundant to cite some of them). Beyond the above-mentioned advantages, the great interest of the researchers into this technology comes also from the possibility of studying their aerodynamics by means of a straightforward 2D approach.

For the sake of honesty, since a 3D modelling in the previous work would have been unaffordable, the H-Rotor represented almost a forced choice and will be adopted throughout this study.

The following table shows the main feature of the HAWT and H-Darrieus for micro-generation.

	HAWT	**H-Darrieus**
Yaw control	Necessary	Unnecessary
Noise level	High	Low
Generator position	Hub	Ground
Self-starting	Yes	No
Struts	No	Yes
Performance in skewed flow	Low	High
Torque ripple	Null	High
Blade profile	Complicated	Simple

Table 0.1 - HAWT-VAWT comparison

A very recent branch of research concerns the study a new kind of device for the augmentation of the power output of a VAWT, namely a diffuser. A diffuser ideally consists of a flow accelerating apparatus used to increase the mass flow and consequently the power output if a wind turbine. The original concept applied on conventional HAWTs and can be traced back to the 1920s, when A. Betz studied the economic viability of DAWTs compared to bare HAWTs [29]. Through the years, several eminent experimental and theoretical studies have been made on the DAWT technology development [30, 31, 32, 33] and clear power augmentation possibilities have been proofed. A commercial prototype called Vortec have been installed in New Zeeland (fig. 0.2).
An empty diffuser essentially works as a Venturi, as it increases the flow velocity in his throat, but when it works coupled with a turbine, complex phenomena take place, such as turbulent wake mixing [34], wake sub-atmosferic pressure [35], wake rotation suppression [36].

Figure 0.2 - Vortec DAWT in New Zeland

Recently, the same concept has been applied to a Darrieus turbine.
In particular, Ponta et al. in [37] tested the performance of Darrieus hydro-turbine operating in a convergent-divergent channel measuring an interesting power increase and regularization, and a higher rotor speed.
Malipeddi et al. [38] carried on a CFD optimization of a diffuser for H-Darrieus, obtained a Cp increment of 60%, a torque ripple reduction, and focused on the confined flow effects.
Geurts et al. [39] investigated on the aerodynamics of a diffuser-augmented Darrieus by means of a potential flow solver to obtain a maximum 80% increment of Cp.

Khan et al. [40] made a review of hydro-turbine recent researches and states that diffuser is more suitable for VAWT than for DAWT for structural considerations. The author makes also a classification of the proposed diffuser geometries (fig. 0.3)
Maitre et al. [41] and Van Beveren [42] hypothesized a stall prevention by virtue of the adverse pressure gradient smoothing operated by the turbine trust that is an important fringe benefit.

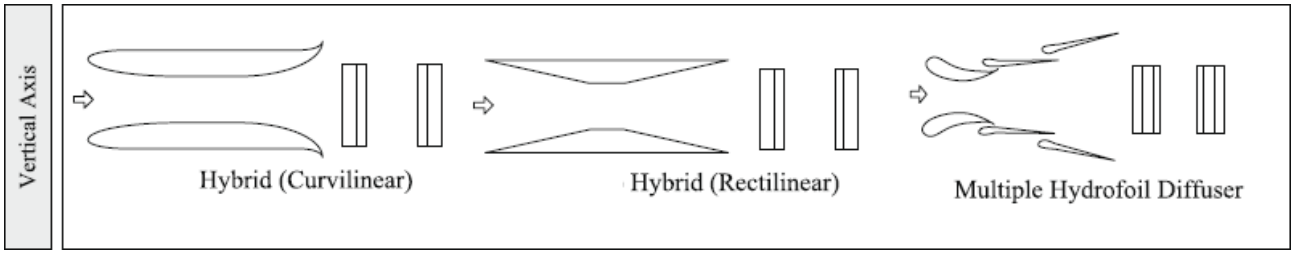

Figure 0.3 - Diffusers geometries for VAHT [40]

All this advantages claimed by the above-cited authors makes the diffuser an attractive power augmentation device for VAWT, especially for the upgrading of householder-size machines that, as stated before, have a very low operative efficiency.
To conclude, the study of the performance a diffuser-augmented vertical axis wind micro-turbine will be the object of the present work. For the sake of clearness, a brief outlook resuming the essential phases of the present study is here presented.

0.1 Present work summary

The study originates from considerations about the result of an optimization analysis of a sustainable building supplied by a hybrid power system. The optimization is the first part of the PRA Project 2015 [44] . This study brought out the problematic integration of a commercial model of VAWT with the more effective PV panels.

In the rest of this introductory chapter, the PRA project is described.

In the first part of the work, the existing models for the modelling of VAWT are described.

In the second part, the accuracy of a CFD URANS approach in the prediction of the torque generated by a Darrieus turbine is checked against experimental data and a time-effective set of parameter for the continuation of the study is validated.

In the third part, the existing aerodynamic models for the prediction of DAWTs' performances are briefly discussed.

In the fourth part, a new, faster and tailor-made model is formulated and the discrepancies with a full URANS CFD are highlighted.

The fifth part consists in an analysis of the influence of the main geometric parameters on the performance of the new configuration. At the end of this part, the most suitable design is selected.

In the sixth part, appropriate corrections to the power curve obtained with the simplified 2D model are adopted in order to evaluate the performance of the new device in a 3D open field.

In the last part, the new DAWT is compared with the original one and integrated with the whole building to verify his energy performance.

Since this study concentrates on the aerodynamics and the modelling of DAWTs, economical concerns and structural issues are beyond the scopes of the present work.

0.2 PRA project

The PRA project [44] is an interdepartmental activity financed by the University of Pisa whose main aim is the promotion of the cooperation between teachers and researchers from different departments for the production of scientific material concerning advanced research topics. In particular, the present work departs from the 2015 edition of the PRA project titled "Metodi e tecniche per l'integrazione di sistema per l'energia elettrica e termica" (Methods and techniques for electric and heating energy systems integrations) and it is worthwhile to briefly present the most important issues concerning the modelling approach and the early results of this larger-scale study. The case study of the PRA project is a farmhouse for agri-tourist use in Enna, Sicily. It does not refer to any particular real building, but realistic parameter for site's and users' characterization have been chosen. The following table summarizes the main feature of the farmhouse.

Site	Enna (EN)
Environment characteristics	Open countryside
Building size	200 m^2, 2 floors (basement + ground floor)
Wall	60cm ashlar
Roof	Isolated (recent renovation)

Table 0.2 - Characteristics of the case study from PRA project

Thermal energy demand	
DHW	10 MWh/y
Space heating	20 MWh/y
Cooling	8 MWh/y
Electric energy demand	
Cooking, lighting, other appliance	6 MWh/y

Table 0.3 - Energy demand of the case study from PRA project

The conceptual scheme of the system layout is shown in the flow chart below.

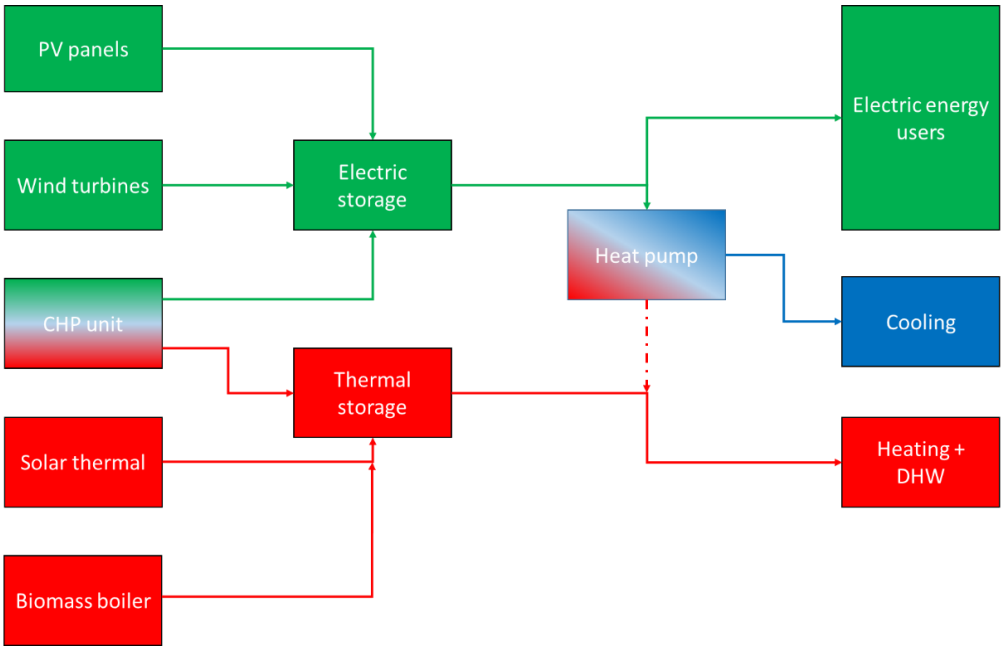

Flow Chart 0.1 - System layout of the case study from PRA project

The dash-dotted line indicates that above a certain switch temperature, the heating and DWT demand is supplied entirely by the thermal storage and the heat pump is shut down.

The adopted technologies are reported in the table below.

PV panel	Policrystalline silicium
Solar thermal panel	Flat collector
Wind turbine	Windspire 1.2 kW H-Darrieus turbine
CHP unit	Diesel fueled
Heat pump	Air-to-water, reversible, modulating
Thermal storage	Vertical insulated
Electric storage	Litium-iron-phosphate batteries
Radiant floor	320 m^2

Table 0.4 - Technologies of the case study from PRA project

Nine parameter have been chosen (seven discrete and two Boolean) to perform an optimization study:

- the number of PV panels
- the number of wind turbines
- the number of solar thermal collectors
- the electric storage capacity
- the thermal storage capacity
- the switch temperature to thermal storage direct heating mode
- the limit of the power flow from/to the electric storage
- the possibility of heat recovery from CHP
- the presence/absence of a biomass boiler

Two algorithm have been implemented:

- a simulator, reproducing the building dynamics and resolving the transient energies balances with a time step discretization of 1h; the main output were the net present value (NPV) with respect to a configuration without renewable energy sources (no-RES) and the CO2 savings in respect to the no-RES configuration (ΔCO2) along a period of 20 years.
- an optimizer, performing a two-objective optimization by means of a genetic algorithm

The combined algorithms gave as output a Pareto Front of optimal configurations in the NPV-ΔCO2 plane. The result is reported in the following graph.

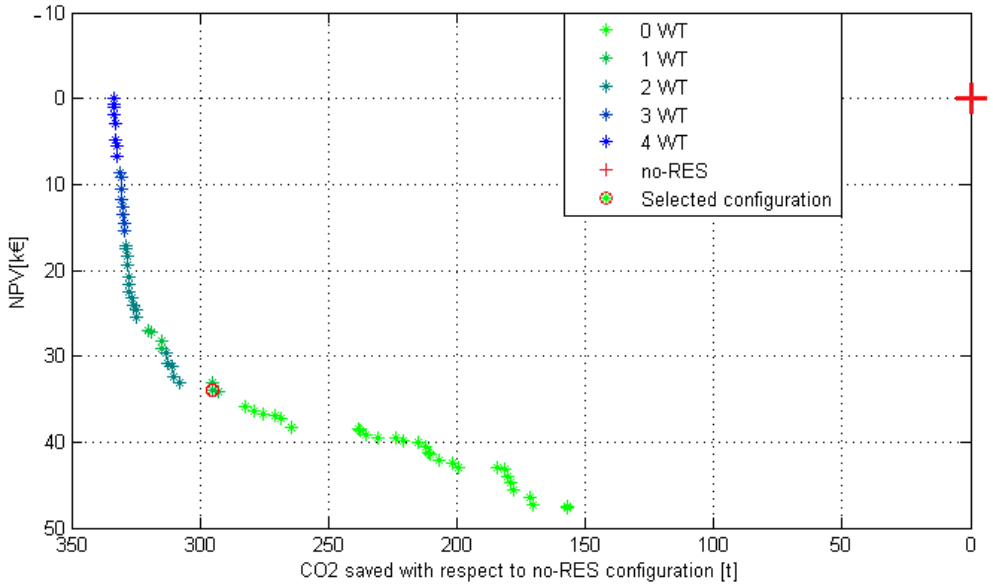

Graph 0.1 - Pareto front at the end of the optimization

The basis for comparison of both NPV and ΔCO2 is a configuration without renewable energy sources (no-RES) that therefore represents the origin of the axis (N.B. the axis have a reversed orientation).

The Pareto front is coherent with the expectancies, as the "greener" solution tend to approach a null NPV, meaning that high investment cost match the fuel saving, whereas it is possible to achieve high NPV with a more cost-effective renewable sources mix.

The more competitive solutions, in particular, do not consider the adoption of wind turbine that becomes interesting only when low carbon emissions are required. Moreover, in many cases, the installation of wind turbines becomes feasible just when the upper limit to the number of PV panels (imposed according to hypothetical dimensional constraints) is reached.

To sum up, this study showed how the small wind turbines are still inadequate to supply a small stand alone system when they are compared with more mature solutions such as PV panels, as previous studies highlighted [44, 45].

From this, the decision on investigating the possibility of increasing the wind resource exploitation by adopting an upgraded version of the conventional wind turbine: the diffuser augmented vertical axis wind turbine (DAWT). At the end of the work, the new turbine design equipped with a diffuser will be integrated into the configuration indicated in graph 0.1 to evaluate its energetic performance. The selected configuration is the highest NPV solution containing a wind turbine and is therefore the more feasible, according to these results. A cost analysis of the new model have not been performed, as already stated, so the present work does not give any answer about the economical convenience a DAWT with respect to the bare one.

Introduction references

[1] International Panel on Climate Change, *Climate Change 2014: Synthesis Report*, www.ipcc.ch (2014)

[2] Saif A, Gad Elrab K, Zeineldin HH, Kennedy S. *Multi-objective Capacity Planning of a PV-wind diesel-battery Hybrid Power System*, IEEE International Energy Conference and Exhibition (EnergyCon), (2010), 217-222

[3] Paskal J, Bizcel P, Klos M. Hybrid power systems - *An effective way of utilizing primary energy sources*, *Renewable Energy*, Volume 34, Issue 11, (2009), 2414-2421

[4] Markvart T. *Sizing of hybrid photovoltaic-wind energy systems*, Solar Energy Vol. 51. No. 4. (1996), 277-281

[5] Celik AN. *Techno-economic analysis of autonomous PV-wind hybrid energy systems using different sizing methods*, Energy Conversion and Management 44 (2003) 1951-1968

[6] Bahaj AS, Myers L, James PAB. *Urban energy generation: Influence of micro-wind turbine output on electricity consumption in buildings*, Energy and Buildings 39 (2007) 154-165.

[7] Grieser B, Sunak Y, Madlener R. *Economics of small wind turbines in urban settings: An empirical investigation for Germany*, Renewable Energy 78 (2015) 334-350.

[8] Singh RK, Ahmed MR. *Blade design and performance testing of a small wind turbine rotor for low wind speed applications*. Renew Energy 2013;50:812-9.

[9] Riegler H. *HAWT versus VAWT: small VAWTs find a clear niche*. Refocus (2003);4(4):44-6

[10] Mertens S. *Wind energy in urban areas - Concentrator effects for wind turbine close to buildings*; Refocus, Volume 3, Issue 2, March-April 2002, Pages 22-24

[11] A Tummala , Velamati RK, Sinha DK, Indraja V, Krishna VH, *Review on small scale wind turbines*, Renewable and Sustainable Energy Reviews 56 (2016)1351-1371

[12] Grauthoff M. *Utilization of wind energy in urban areas. Chance or utopian dream?* Energy and Buildings 1990 /91;15-16:517-23.

[13] Ledo L, Kosasih PB ,Cooper P. *Roof mounting site analysis for micro-wind turbines*. Renewable Energy (2011); 36:1379-91.

[14] Toja-Silva F, Colmenar-Santos A, Castro-Gil A. *Urban wind energy exploitation systems: Behaviour under multi directional flow conditions, Opportunities and challenges*, Renewable and Sustainable Energy Reviews 24 (2013) 364-378.

[15] Burton T, Jenkis N, Sharpe D, Bossanyi E. *Wind Energy Handbook, Second Edition*, 2011 John Wiley & Sons, Ltd. Published 2011 by John Wiley & Sons, Ltd. ISBN: 978-0-470-69975-1

[16] Freere P, Sacher M, Derricott J, Hanson B . *A low cost wind turbine and blade performance*. Wind Eng 2010; 34(3):289-302.

[17] Refan M, Hangan H. *Aerodynamic performance of as mall horizontal axis wind turbine*, Sol Energy Eng (2012); 134 (2) 021013-021013.

[18] Singh RK, Ahmed MR. *Blade design and performance testing of a small wind turbine rotor for low wind speed applications*. Renew Energy (2013);50:812-9.

[19] Duquette MM, Visser KD. *Numerical implications of solidity and blade number on rotor performance of horizontal-axis wind turbines.* J Sol Energy Eng (2003), 125(4):425-32.

[20] Chen T Y, Liou LR. *Blockage corrections in wind tunnel tests of small horizontal-axis wind turbine,* Exp Therm Fluid Sc (2011);35(3):565-9

[21] Eriksson S, Bernhoff H, Leijon M. *Evaluation of different turbine concepts for wind power*, Renewable & Sustainable, Energy Reviews 12 (2008) 1419-34.

[22] Jamieson P, *Innovation in Wind Turbine Design*, First Edition (2011)

[23] Powles SJR, Anderson MB Tan CC, *Two years of operation of the 25m VAWT at Carmathen Bay*, Proceedings EWEC (1989)

[24] Mays D, Morgan CA, Anderson MB, Powles SJR, *Experience with the VAWT 850 demonstration project*, Proceeding EWEC (1990)

[25] Dery J, *Eole, aerogereateur a axe vertical de 4MW a Capchat, Quebec, Canada*, 9th Biennal Congress of the Internation Solar Energy Society (1985)

[26] Mertens S, van Kuik G, van Bussel G. *Performance of an H-Darrieus in the skewed flow on a roof*, J Solar Energy Eng 125 (2003) 433-40.

[27] Simão Ferreira CJ, van Bussel G, van Kuik G, *An analytical method to predict the variation in performance of an H-Darrieus in skewed flow and its experimental validation*. In*:* Proceedings of the european wind energy conference 2006; February 27-March 2, Athens (Greece); 2006.

[28] Li Y, Sanderc MC. *Three-dimensional effects and arm effects on modeling a vertical axis tidal current turbine*, Renewable Energy 35 (2010) 2325-2334
[29] Hjort H, Sorsen H, *A Multi-Element Diffuser Augmented Wind Turbine*, Energies 7 (2014) , 3256-3281
[30] Foreman KM, Gilbert B, Oman RA, *Diffuser augmentation of wind turbines*, Solar Energy 20 (1977), 305-311.
[31] Igra O. *Research and development for shrouded wind turbines*. Energy Conc. & mgmt. 21,(1981),13-48.
[32] Van Bussel GJW, *An assessment of the performance of diffuser augmented wind turbines (DAWTs)*, Proceedings of the ASME Joint Engineering Fluyd Conference, (1999)
[33] Hansen MOL, Sørensen NN, Flay RGJ, *Effect of Placing a Diffuser around a Wind Turbine*, Wind Energy (2000)
[34] Werle M, Presz W. *Shrouds and ejector augmentors for subsonic propulsion and power systems*. J. Propuls Power, 25 (2009), 228-236.
[35] Ohya Y, Karasudani, Sakurai T, Abe A, Inoue K,M. *Development of a shrouded wind turbine with flanged diffuser*. J. Wind Eng. and Ind. Aero. 96(2008): 524-539
[36] Kosasih B, Tondelli A, *Experimental study of shrouded micro-wind turbine*, Procedia Engineering 49(2012):92 - 98
[37] Ponta F, Dutt GS, *An improved vertical-axis water-current turbine incorporating a channelling device*, Renewable Energy 20, (2000) 223-241.
[38] Malipeddi AR, Chatterjee D. *Influence of duct geometry on the performance of Darrieus hydroturbine*, Renewable Energy 43 (2012) 292-300
[39] Geurts B, Simão Ferreira CJ, Van Zuijlen A, H. *Van Bussel Aerodynamic Analysis of a Vertical Axis Wind Turbine in a Diffuser*, 3rd EWEA Conference - Torque 2010: The Science of making Torque from Wind, Heraklion, Crete, Greece, (2010)28-30
[40] Khan MJ, Bhuyan, Iqbal M, Quaicoe JE, *Hydrokinetic energy conversion systems and assessment of horizontal and vertical axis turbines for river and tidal applications: A technology status review*, Applied Energy 86 (2009) 1823-1835
[41] Maître T, Mentxaka Roa A, Pellone C, Achard JL, *Numerical 2D hydrodynamic optimization of channeling devices for cross-flow water turbines*, U.P.B. Sci. Bull., Series D, Vol. 72, Iss. 1, (2010)
[42] Van Beveren C, Design of an urban wind turbine with diffuser, Master Thesis, Delft University (2008)
[43] Aloini D, Dulmin R, Mininno V, Raugi M, Testi D, Tucci M. *Investment Evaluation under Multiple Uncertainty: Optimal Sizing and Configuration of an Integrated Energy Production System by Renewable Sourcse,* Proceedings of the Nineteenth International Working Seminar on Production Economics 2016, Innsbruck, Austria 12 pp.
[44] Bahaj A.S, Myers L, James P.A.B. *Urban energy generation: Influence of micro-wind turbine output on electricity consumption in buildings,* Energy and Buildings 39 (2007) 154-165.
[45] Grieser B, Sunak Y, Madlener R. *Economics of small wind turbines in urban settings: An empirical investigation for Germany*, Renewable Energy 78 (2015) 334-350.

Part I - Modeling the aerodynamics of a VAWT

In this part, the main features concerning the aerodynamics of a lift-driven VAWT and a brief summary of the most important models are provided.

1.1 Working principle of a H-Darrieus turbine

The operation of a lift-driven VAWT greatly differs from the one of a HAWT. Even if the driving force is always lift, in a Darrieus turbine, unlike in a conventional HAWT, the blades, also in ideal conditions, experience time-varying angle of attack (AoA). This makes the modelling of the aerodynamic load on the blade quite challenging. The following picture describes the operation in ideal conditions of a H-Darrieus according to a 2D approach.

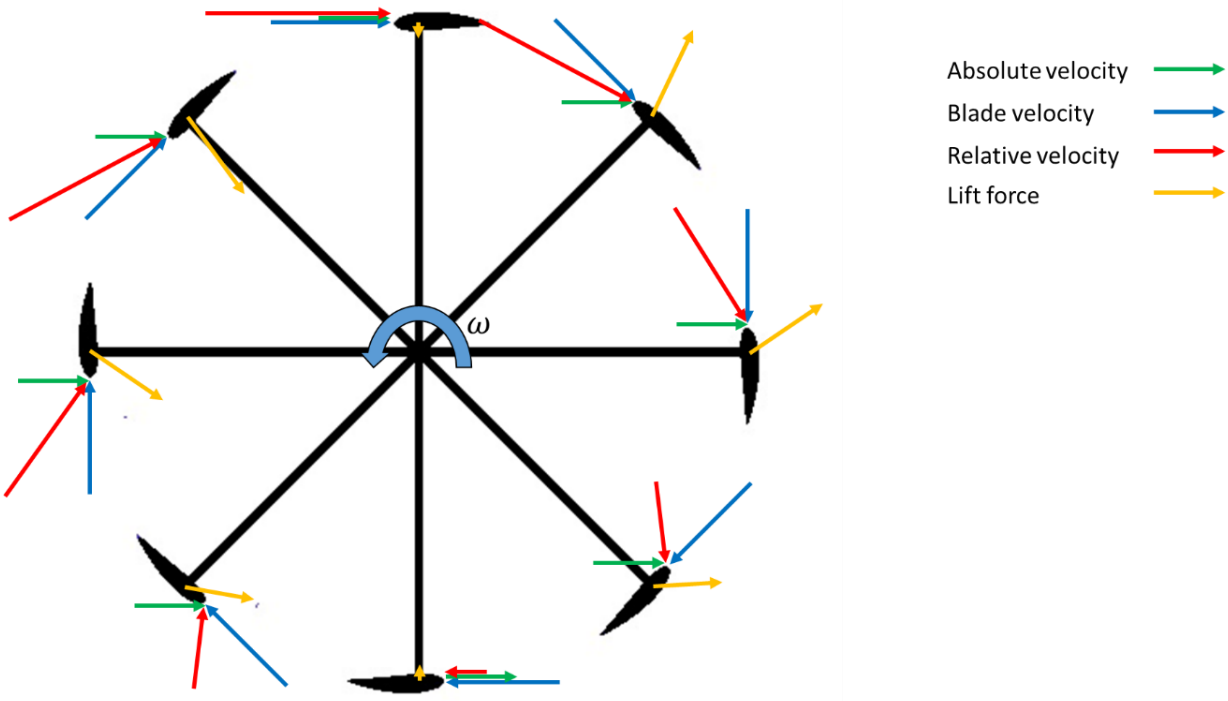

Figure 1.1 - VAWT working principle scheme

The velocity experienced by the blade is the vector sum of the absolute flow velocity and the blade velocity. Supposing a constant absolute velocity across the rotor, it is easy to see how the resulting relative velocity approach the blade with an AoA and generates a lift force having a positive component in the direction of rotation throughout the revolution. However, during normal operations, a certain number of unideal effect contribute to make his modelling very challenging. It follows a description of these phenomena.

1.1.1 - Drag force

A real wing operating in a viscous fluid experience a drag force. This also happens for the blades of a VAWT. The drag becomes in particular determinant when the stall occurs and

cause a catastrophic decay of the performances. An accurate model must include drag to have reasonable accuracy.

1.1.2 - Velocity variations

The assumption of constant induced velocity along the blades' path is very far from being satisfied in a real VAWT. In fact, the absolute velocity experienced in the downwind path ($180 < \theta < 360$ in fig. 1.1) is lowered by the power extraction in the upwind passage ($0 < \theta < 180$ in fig. 1.1). This creates an uneven torque profile during a revolution (fig. 1.2). This is the so-called torque ripple, which has a negative effect on the fatigue load of the drive train and on the power quality [1].

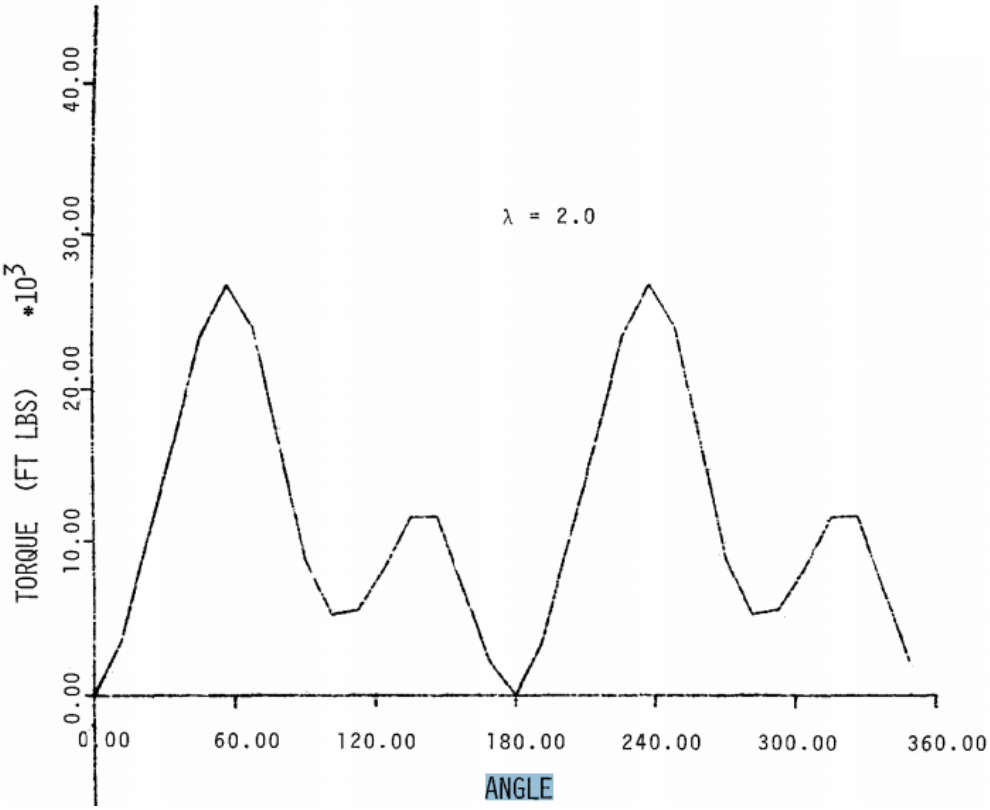

Figure 1.2 - Experimental torque curve over a revolution for a 2-bladed Troposkein at TSR = 2 [2]

1.1.3 - Y-velocity

The simplest VAWT models adopts a one-dimensional approach, whereas in real condition the velocity vector is seldom aligned with the undisturbed flow. The y-velocity assumes both positive and negative value for two reasons:

- the aerodynamic forces exerted by the blades have a not negligible y-component
- the stream tends to expand as the flow slows down

This effect become crucial when the turbine is not isolated, i.e. a diffuser or another turbine influence the near flow field [3].

1.1.4 - Dynamic stall

A turbine's blade operates with a variable AoA and for conventional rotation speed this fluctuations have a frequency that is enough high to cause an evident departure the lift and drag characteristics differ from the quasi-static ones. This issue will be the object of an in depth analysis in par 4.4.

1.1.5 - Virtual cambering

The blades describe a circular path during a revolution. It is therefore only an approximation the velocity composition show in fig. 1.1. Because of this circular trajectory, the blades manifest in a ‘‘virtual” blade cambering, giving blade performance characteristics analogous to those of a cambered blade in rectilinear motion (the virtual camber line has the maximum direct toward the center of rotation)[4].

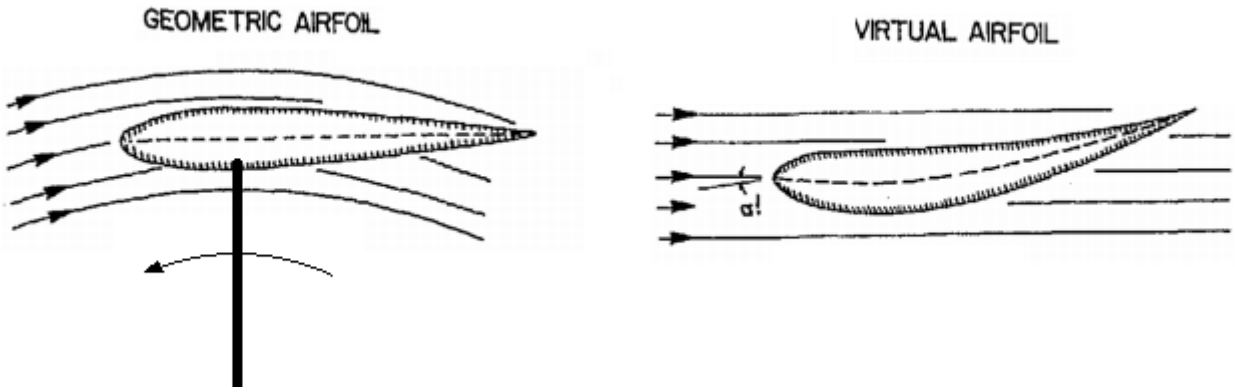

Figure 1.3 - Virtual camber equivalence according to Migliore [4]

In particular, this effect augments the torque in the upwind half (the cambering acts positively) while it diminishes in downwind (the cambering works conversely), therefore enhancing the torque ripple. By adopting a cambered airfoil this effect almost vanishes and the blade can be actually treated as a symmetrical airfoil [5].

1.1.6 - 3D effects

A real turbine is made of blades of finite span and therefore the tip vortex can cause remarkable lift reduction and induced drag generation. Another effect that becomes evident in a 3D approach is the appearance of the z-velocity that greatly complicates the modelling [7, 8]. The so-called skewed flow is expected to happen also for an ideally horizontal undisturbed velocity, since the fluid tends to overstep the turbine.

1.1.7 - Struts drag

As already mentioned an H-Darrieus needs for struts to link the blades to the rotating shaft. These struts experience a torque due to their drag that must be subtracted to the ideal one. Fortunately, when these struts have aerodynamic profile, their modelling is very easy [9].

To conclude, it must be said that the most critical issue in simulating a VAWT is related to the fact that the aerodynamic forces experienced by the blade, for the action-reaction principle, are experienced by the flow that, according to the momentum equation, change his velocity. This creates a very strong coupling between the flow field and the aerodynamic action on the blades that makes the analytical description of the problem very troublesome.

All the above-mentioned effects make the modelling of this type of machines very challenging and many attempt have been made in this sense. It follows a summary of the most important models for the estimation of the power of VAWT.

1.2 Single streamtube model

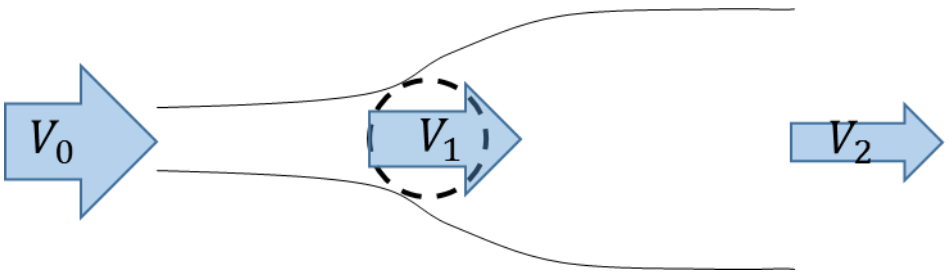

Figure 1.4 - Single streamtube model

It is the simplest model for Darrieus rotor since it is based on a lumped parameter momentum balance. The first inventor of this approach is considered Templin [10]. To evaluate the force experienced by the blades, the following kinematic scheme is adopted.

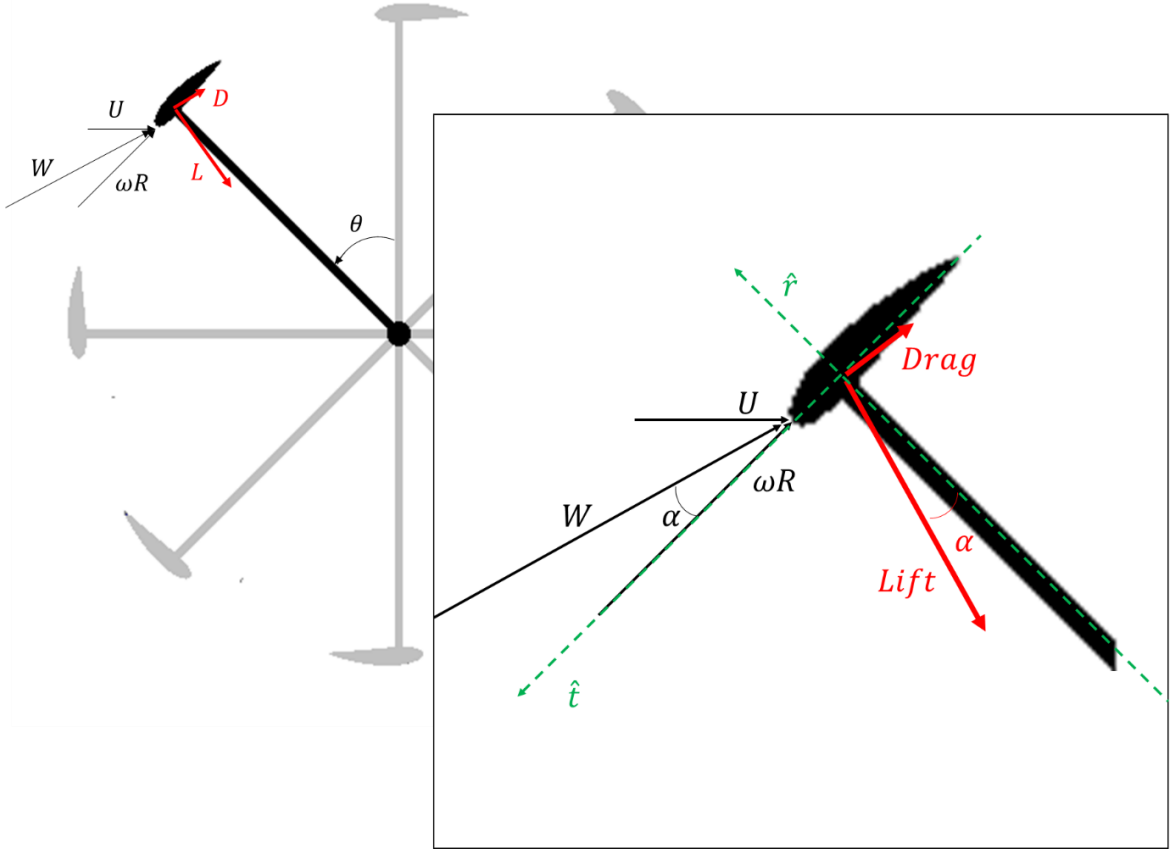

Figure 1.5 - Kinematic scheme and aerodynamic force on a blade

Simply from trigonometric considerations immediately we obtain:

$$W_{\hat{r}} = -U\sin\theta \qquad [1.1]$$

$$W_{\hat{t}} = U\cos\theta + \omega R \qquad [1.2]$$

$$tan\alpha = \frac{W_{\hat{r}}}{W_{\hat{t}}} \quad [1.3]$$

$$L = \frac{1}{2}\rho C_l W^2 c \quad [1.4]$$

$$D = \frac{1}{2}\rho C_d W^2 c \quad [1.5]$$

$$F_{\hat{t}} = L\,|sin\alpha| - Dcos\alpha \quad [1.6]$$

$$F_{\hat{r}} = (L\,|cos\alpha| + D|sin\alpha|)smg(\alpha) \quad [1.7]$$

The forces experienced by the fluid along the x and y axes, from the action-reaction principle, are:

$$F_x = F_{\hat{t}} cos\theta + F_{\hat{r}} sin\theta \quad [1.8]$$

$$F_y = F_{\hat{t}} sin\theta - F_{\hat{r}} cos\theta \quad [1.9]$$

The total trust exerted by the turbine on the flow averaged over a revolution, for a N-bladed turbine, is:

$$T = \frac{N}{2\pi}\int_0^{2\pi} F_x\, d\theta \quad [1.10]$$

The single streamtube adopts the results of the Betz analysis that are rigorously valid only for an ideal actuator disk, but are here extended to this turbine. So, according to figure 1.4, it is:

$$V_1 = \frac{V_0 + V_2}{2} \quad [1.11]$$

And the momentum balance, therefore:

$$\rho V_1 A(V_0 - V_2) = T(V_1) \quad [1.12]$$

The 1.11 and the 1.12 must be both satisfied and this is made by means of a simple iterative approach.

The single streamtube model has poor accuracy for it does not consider the speed variation across the rotor.

1.3 Multiple streamtube model

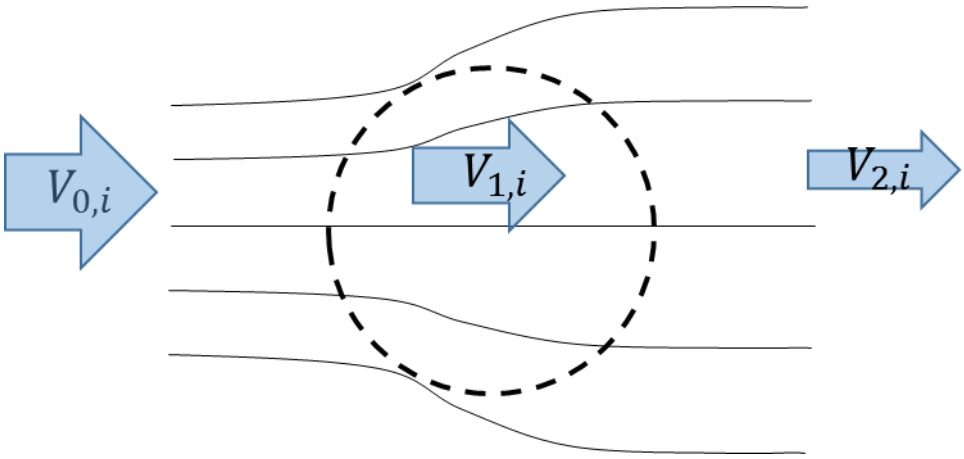

Figure 1.6 - Multiple streamtube

Introduced by Milson and Lissaman [11], is an evolution of the previous model, since it considers velocity variation along the rotor frontal area, but neglects the difference between the upwind and the downwind part. The essential concept is the application of the momentum balance to discrete number of independent streamtubes crossing the turbine. In its original formulation, the only lift force is considered and is evaluated via potential flow theory as:

$$C_l = 2\pi \sin(\alpha) \qquad [1.13]$$

Introducing very strong approximations, they even obtain a closed form for the momentum balance:

$$\frac{V_{1,i}}{V_{0,i}} = 1 - \frac{c}{2R}\frac{\omega R}{V_{0,i}}|\sin(\theta)| \qquad [1.14]$$

Vertical gradient can easily be included to account for the wind shear. However, this model does not provide satisfactory results, especially for heavy-loaded and slow rotors.

Many improved version of this model have been proposed by Stricktland [12] (drag inclusion), Muraca [13] (struts losses), Sharpe [14] (Reynolds number effects), Read et al. [15] (flow expansion).

1.4 Double-multiple streamtube model

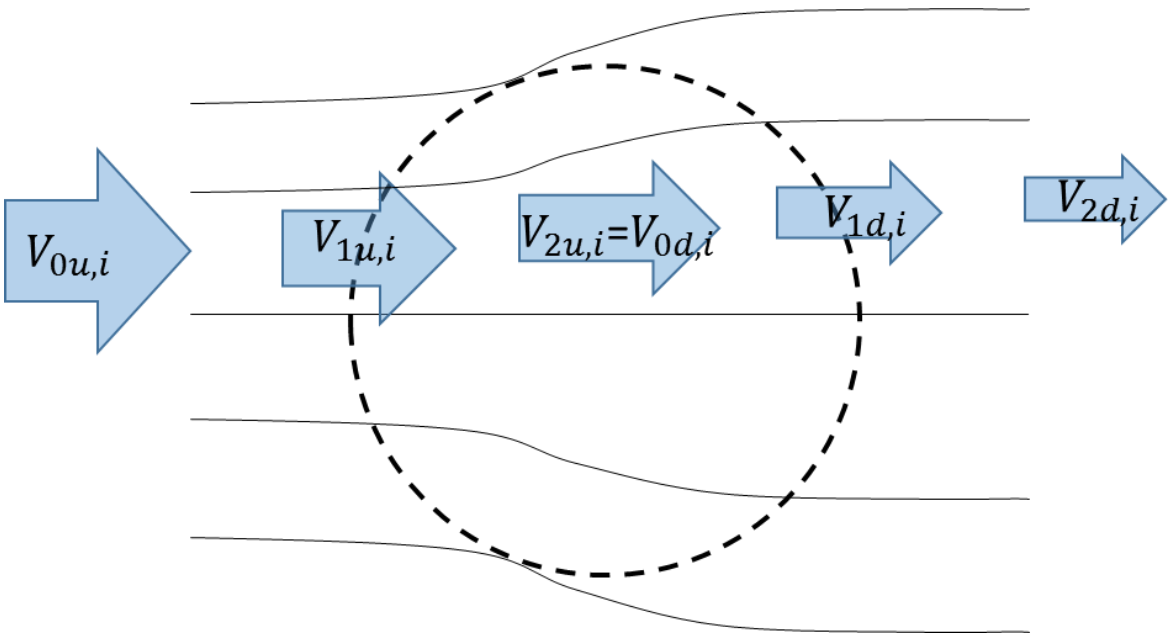

Figure 1.7 - Double multiple streamtube

In a real Darrieus rotor, the blade in the downwind passage experience a much weakened flow because of the power extraction during the upwind passage. For this reason improved modelling accuracy can be achieved by adopting the tandem actuator disk approach [16] as the double multiple stream tube actually makes. This model from Pasachivou [17] was originally formulated as a double stream tube. The approach is the same of the single streamtube with the difference that the fluid passes through two virtual actuator disk that represent the momentum sinks due to the blade-flow interactions with the upwind half and the downwind half in series. It has successively been improved with the adoption of variable induction speed as a function of the azimuthal angle [18], taking the universally known name of "double-multiple streamtube". Its predictive value is the best of the 1D momentum approaches, but it can exhibit problematic convergence for high induction cases [19].

1.5 Vortex model

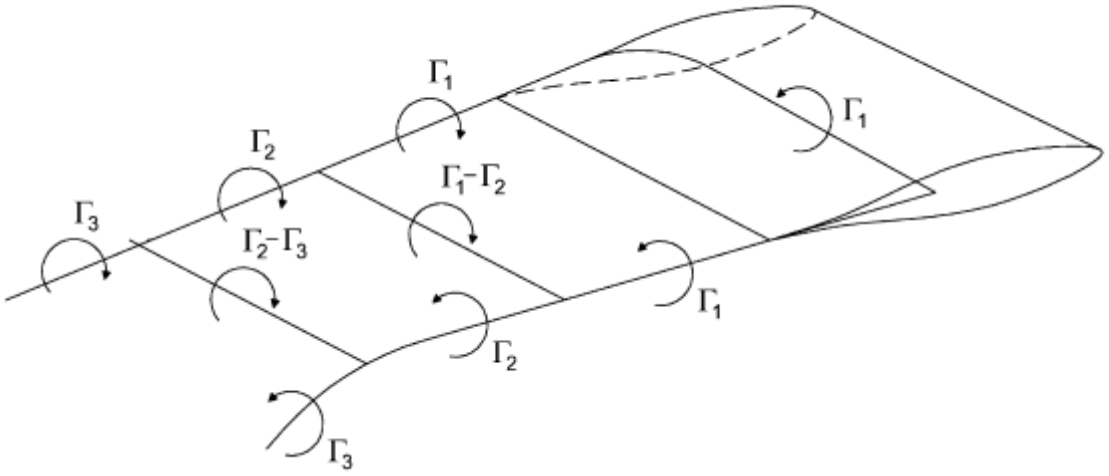

Figure 1.8 - Vortex model

A lifting wing in attached flow regime can me modeled as a continuous distribution of potential vortex arranged in so-called vortex filaments. They can be distinguished in:

- bound vortex, enclosing the wing and giving rise to the lifting force
- tip vortices, that always appear for a finite span wing in 3D
- shed vortices, having opposite verse of the bound vortex and originating every time the AoA of attack (and therefore the lift) change

As consequence of the Helmotz's theorem, a vortex filament must have a constant strength and cannot end in the fluid [20]. From this, it is possible to correlate the vortices intensity to the lift evolution of the blade. The flow field solution is the superposition of the undisturbed flow and the vortex-induced velocity, that are calculated numerically in each position in the domain via Biot-Savart's law. Originally applied to turbines in 2D by Larsen [21], they have achieved a resounding success between aerodynamicists. Improved version can be founded in [22-25], but new version, even including corrections for viscous effects and dynamic stall, are continuously proposed. Their accuracy is good in many cases [19], but the computational effort is not negligible.

1.6 Cascade model

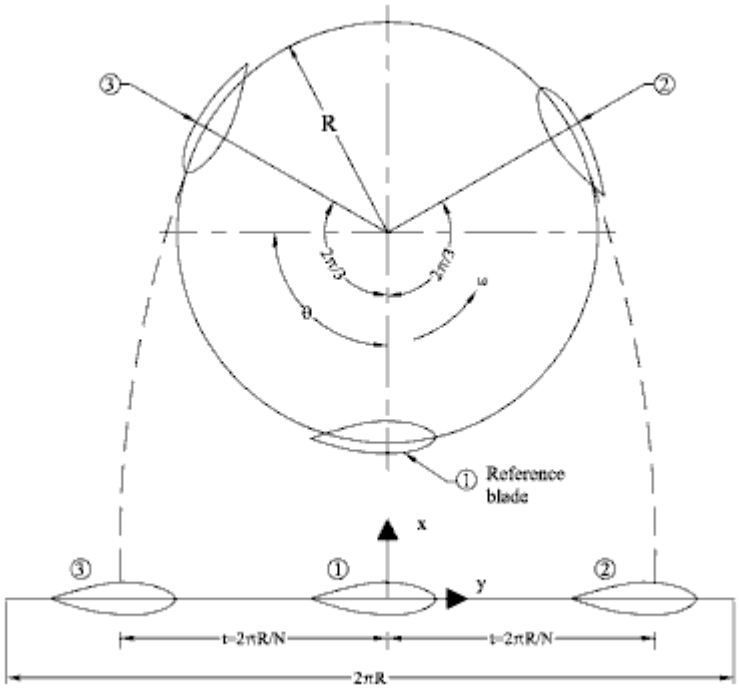

Figure 1.9 - Cascade model from Ref. [19]

This type of model deserves just a mention, since they are encounter seldom in literature. They descend form the cascade theory applied in turbomachinery and they exploit the periodic condition that can be applied to each blade. The relationship between the wake velocity and the free stream velocity is established by using Bernoulli's equation while the induced velocity is related to the wake velocity through a particular semi-empirical expression. After determination of the local relative flow velocity and the AoA, the VAWT is developed into a cascade configuration that is shown in fig. 1.9. A detailed description of this model can be found from Hirsh et al. [26]. The performance of this model are comparable to those of vortex model [19].

1.7 CFD

The computational fluid dynamic has gained a great success for the simulation of wind turbine in recent years. In particular, the amount of works relative to H-Darrieus rotors is enormous, by virtue of the simplicity of the 2D approach that can be adopted. Despite of the relatively simple the new commercial solver (i.e. Fluent) allow, some of the most complex and less understood phenomena in the field of numerical simulations are involved in the analysis of the flow past rotating blades [27]. So, a careful choice of the simulation parameters is required to catch the dynamics of the flow field.
Although a 3D approach is the only one providing consistent results, a 2D model can be successfully applied to the analysis of many relevant issues connected to the functioning of Darrieus rotors, like the dynamic stall, the flow curvature effects and the wake interaction with the downwind half of the revolution.
Concerning the unsteadiness of the problem, the URANS (Unsteady Averaged Navier-Stokes, see Appendix I) formulation with sliding mesh interfaces is widely preferred [28]. This method adopts a rotating mesh for the rotor zone, therefor allowing for a realistic description of the blades' behavior.
The following picture from Ferrari et al. [28] represents the universally accepted domain arrangement for the simulation of Darrieus turbine.

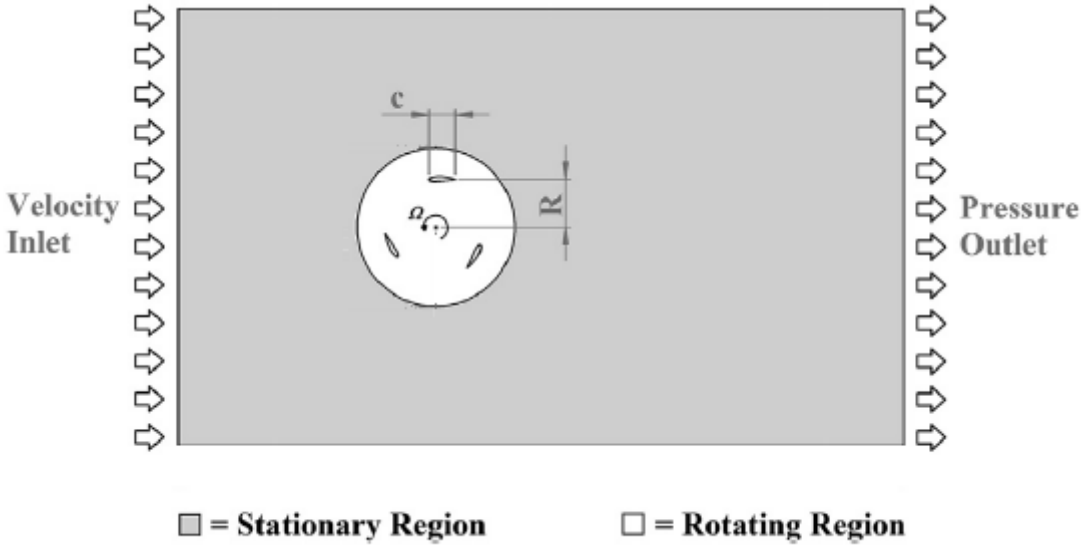

Figure 1.10 - 2D domain for CFD

Concerning the other settings (mesh type, domain dimensions, convergence criterion, turbulence model, solution algorithms) there is no a clear agreement between the different researchers, and this makes the work for the beginner quite complicated. As discussed from different eminent authors [29, 30], an accurate modeling of these machines cannot disregard anymore the recent developments in CFD simulations.

in the end, the CFD approach, even if it requires a large computational time, has been considered the most suitable for the present work. Not to get lost in the intricate multitude of literature examples, the experimental-numerical study by Ferrari et al. [28] has been adopted as reference article, for it appears to be the most complete, rigorous and detailed CFD study for Darriues turbine. The last but not least reason for choosing this reference study was the possibility of meeting the authors.

I References

[1] Reuter JR. *Torque ripple in a Darrieus wind turbine*, SAND80-0475

[2] Sidney F. Johnston Jr., Editor, *Proceedings of the Vertical Axis Wind Turbine (VAWT) Design Technology Seminar for Industry*, SAND 80-0984, Sandia Laboratory, Albuquerque,(1980).

[3] Malipeddi AR, Chatterjee D. *Influence of duct geometry on the performance of Darrieus hydroturbine*, Renewable Energy 43 (2012) 292-300

[4] Migliore PG, Wolfe WP, Fanucci JB. *Flow curvature effects on Darrieus turbine blade aerodynamics*. J Energy (1980);4(2):49-55.

[5] Balduzzi F, Bianchini A, Ferrara G, Ferrari L, Maleci R, *Blade design criteria to compensate the flow curvature effects in H-Darrieus wind turbines*, J. Turbomach. 137 (1) (2015) 1e10.

[6] Mertens S, van Kuik G, van Bussel G. *Performance of an H-Darrieus in the skewed flow on a roof*, J Solar Energy Eng 125 (2003) 433-40.

[7] Simão Ferreira CJ, van Bussel G, van Kuik G, *An analytical method to predict the variation in performance of an H-Darrieus in skewed flow and its experimental validation*. In*:* Proceedings of the european wind energy conference 2006; February 27-March 2, Athens (Greece); 2006.

[8] Mertens S, van Kuik G, van Bussel G. *Performance of an H-Darrieus in the skewed flow on a roof*, J Solar Energy Eng 125 (2003) 433-40.

[9] Li Y, Sanderc MC. *Three-dimensional effects and arm effects on modeling a vertical axis tidal current turbine*, Renewable Energy 35 (2010) 2325-2334

[10] Templin RJ, *Aerodynamic performance theory for the NRC vertical-axis wind turbine*. NRC Lab.report LTR-LA-190, (1974)

[11] Wilson RE, Lissaman PBS. *Applied aerodynamics of wind power machines*. Oregon St. Univ. (1974)

[12] Strickland JH. *A performance prediction model for the Darrieus turbine*. In: International symposium on wind energy systems, Cambridge,UK; September 7-9, 1976.p.C3-39-54.

[13] Muraca RJ, Stephens MV, Dagenhart JR. *Theoretical performance of cross-wind axis turbines with results for a catenary vertical axis configuration.* USA: NASA TMX-72662;1975.

[14] Sharpe DJ. *A theoretical and experimental study of the Darrieus vertical axis wind turbine*. School of Mechanical, Aeronautical & Production Engineering. Kingston Polytechnic. Research report. October, 1977.

[15] Read S, Sharpe DJ. *A next ended multiple streamtube theory for vertical axis wind turbines*. Cranfield, UK: 2nd BWEA workshop;1980;65-72(April).

[16] Lapin EE. *Theoretical performance of vertical axis wind turbines*. ASME paper, 75-WA/Ener-1, The winter annual meeting, Houston, TX, USA, 1975.

[17] Paraschivoiu I. *Double-multiple streamtube model for darrieus wind turbines. Second DOE/NASA wind turbines dynamics workshop*, NASA CP-2186, Cleveland, OH, February, 1981. p. 19-25.

[18] Paraschivoiu I, Delclaux F. *Double multiple streamtube model with recent improvements*. J Energy 1983; 7:250

[19] Islam M, David SKT, Fartaj A. *Aerodynamic models for Darrieus-type straight-bladed vertical axis wind turbines*. Renewable and Sustainable Energy Reviews 12 (2008) 1087-1109

[20] Wu JC, *Elements of vorticity aerodynamics*, Springer (2005) p.20

[21] Larsen HC. *Summary of a vortex theory for the cyclogiro*. Proceedings of the second US national conferences on wind engineering research, Colorado state university, 1975. p. V8-1-3.

[22] Fanucci JB, Walter RE. *Innovative wind machines: the theoretical performance of a vertical-axis wind turbine*. In: Proceedings of the vertical-axis wind turbine technology workshop, Sandia laboratories, SAND76-5586, iii-61-95, USA, 1976.

[23] Holme OA. *Contribution to the aerodynamic theory of the vertical axis wind turbine. International symposium. on wind energy systems*, September 7th-9th, Cambridge, England, 1976. p. C4-55-71.

[24] Wilson RE. *Wind-turbine aerodynamics*. J Wind Eng Ind Aerodynam 1980:357-72.

[25] Strickland JH, Webster BT, Nguyen T. A Vortex model of the darrieus turbine: an analytical and experimental study. J Fluids Eng 1979;101:500-5.

[26] Hirsch H, Mandal AC. *A cascade theory for the aerodynamic performance of darrieus wind turbines.* Wind Eng 1987;11(3):164-75.

[27] Paraschivoiu, *Wind Turbine Design with Emphasis on Darrieus Concept*, Polytechnic International Press, Canada, (2002).

[28] Balduzzi F, Biachini A, Maleci R, Ferrara G, Ferrari L, *Critical issues in the CFD simulation of Darrieus wind turbines*, Renewable Energy 85 (2016) 419e435

[29] C.J. Simao Ferreira, *The Near Wake of the VAWT: 2D and 3D Views of the VAWT Aerodynamics,* Technische Universiteit Delft, The Netherlands, 2009 (PhD thesis).

[30] Raciti Castelli M, Englaro A, Benini E, *The Darrieus wind turbine: Proposal for a new performance prediction model based on CFD, Energy* 36 8 (2011) 4919e4934

Part II - CFD experimental validation

To check the CFD code accuracy in the simulation of the flow field induced by a Darrieus turbine during normal operation, the experimental set up reported by Ferrari et al. [1] has been simulated. The turbine was tested in an open jet wind tunnel, with a very large testing section compared with the machine swept area, thus making the blockage negligible. In the following chart the experimental set up details are summarized.

Test site	Open jet wind tunnel
Testing section	> 40 m^2
Max wind velocity	70 m/s
Test velocity	8 m/s
Blockage correction	Negligible
Turbine model	H-Darrieus, 3 blades
Rotor radius	0.85 m
Airfoil	NACA0018 with virtual camber
Shaft diameter	< 0.05 m
Blades' chord	0.246 m
Blades' aspect ratio	12

Table 2.1 - Experimental setup by Ferrari et al. [1]

The chosen experiment was particularly appropriate for a simulation by means of 2D CFD solver. In fact, the high aspect ratio, the presence of rounded end plates at the blade tips are expected to have greatly reduced the tip losses [2]. Moreover, the experimenters declared that the parasitic torque due to struts was subtracted from the total torque.

Nevertheless, an annoying misunderstanding has caused the early simulation to be quite troublesome. In fact, in spite of the correct design of the machine, the tested prototype presented a small but not negligible mismatch with the declared geometry. More specifically, the blades were mounted with a wrong pitch angle, thus almost nullifying the benefit coming from the virtual camber. Thanks to the close collaboration with the author of the paper the problem has been successfully fixed and the simulated geometry made equal to the tested one.

It is worthwhile to repeat that the paper to which the present validation refers is "Critical issue in CFD simulation of Darrieus wind turbine" by Ferrari et al. [1], containing not only the essential experimental data but also precious information about the simulation setup used by the authors to justify their CFD approach. Moreover, the above mentioned CFD study, adopts some of the most challenging discretization criteria (for both space and time dimensions) in the scientific literature as far is known. A complete and very useful sensitivity analysis is also reported in the paper. Unfortunately, for the consequent huge computational effort, the simulations required for many weeks even on supercomputers, as the authors stated. So, for the present purposes, the results of Ferrari et al. have been considered as an almost unaffordable benchmark, for the very expensive computations time requested, making these methods unsuitable for the optimization process that is the final goal. In fact, after the validation, a coarser mesh and timestep have been tested, aiming at defining a time-effective setting for the continuation of the work. To conclude, the following paragraphs will focus on the most important issues concerning the CFD validation carried out.

2.1 Turbulent flow modelling

The adopted turbulence model is the k-ω model SST by Menter [3, 4] (see Appendix I). It is a 2-equation model, combining the advantageous features of the standard k- ω model (robust and accurate modeling of the near-wall regions) and the k-ε (weak dependence of the free stream turbulence intensity from boundary conditions). This makes the k-ω suitable for the simulation of flows affected by adverse pressure gradients and consequent boundary layer separation [5]. Thanks to the capability to solve the ω inside the laminar sublayer, the model shows a great accuracy in the description of the wall strain when very fine mesh ($y^+ \sim 1$) are adopted for the near wall treatment. However the so-called Enhanced wall treatment, that is a default option for this model in Fluent, is claimed to provide good results even for coarser near-wall meshes [6]. This features have made it one of the most widely used approach for Darrieus turbines' simulation [1, 7, 8]. For the full equations set please refer to [6]. In the present validation, for also the flow compressibility is modeled, to be more rigorous the resulting scalars are not Reynolds-Averaged but Favre-Average [9], but since the compressible effect are negligible [1], even this slight theoretical discrepancy will be neglected.

2.2 Physical convergence criterion

The physical convergence criterion definition is a crucial and often underestimated issue in this case. In fact, starting from an undisturbed flow condition, the simulated air mass needs a certain time to "relax" and adapt to the aerodynamic forces exerted by the whole turbine. The fact the aerodynamic forces on the blades themselves are function of the outer flow field makes all the phenomena strictly coupled and the evolution absolutely not trivial. The scientific literature gives dissonant suggestion about it.

Some authors, simply define a number of iteration after that the solution is considered asymptotic [10, 11].

An apparently more robust criterion consists in the measurement of the average torque relative variation between a turbine revolution and the previous ("torque residual"), for which a threshold (usually 1%) is fixed before stopping the calculation. Castelli et al. [12] averaged over 1/3 of revolution because of the presence of three identical blades. Ferrari et al. [1] decided to reduce the threshold value until a very safe 0.1%.

For the present work, what was really of interest was to obtain a solution with a negligible overall trend, disregarding the possible small fluctuation in the average torque that however can be observed. Thus, a criterion involving the torque variation between two subsequent periods has been adopted, but some specific choices have been made and are justified below.

First of all, concerning the period to average over, a slight difference between the 360° average torque and the 120° has been observed , especially for low TSR. In fact, in this cases, because of the great complexity of the flow, caused by the vigorous vortex shedding from the blades due to dynamic stall conditions, small unavoidable differences in the near wall mesh could led to discrepancies in the instantaneous torque for each blade.

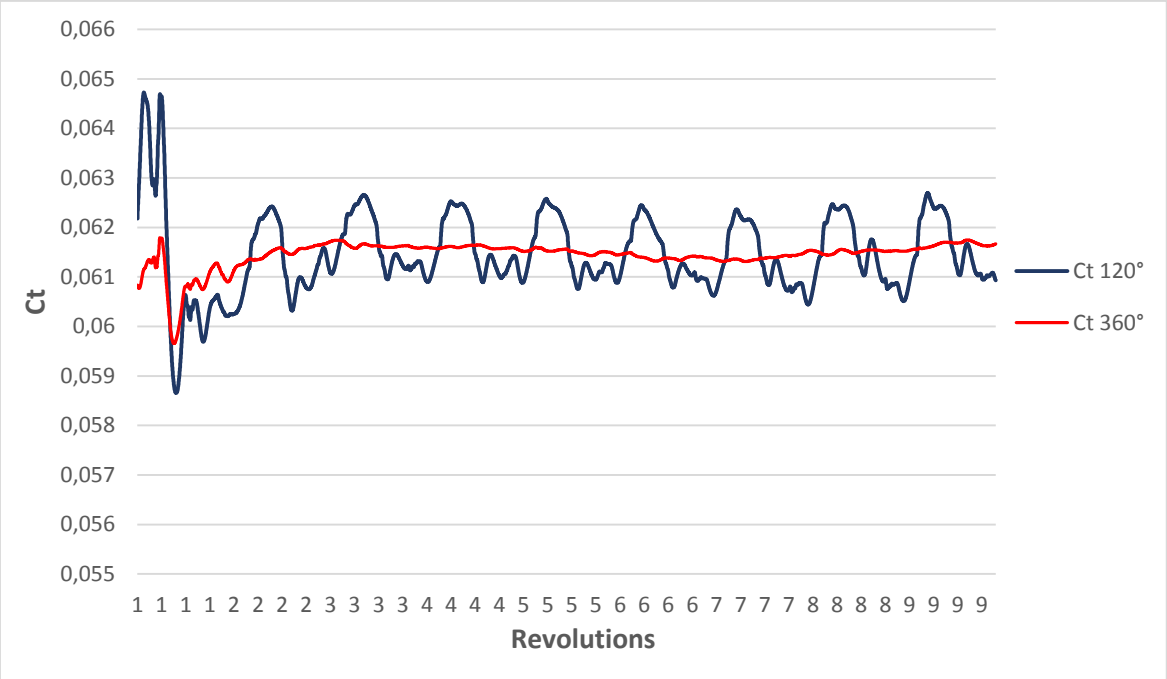

Graph 2.1 - TSR 1.1: 120 and 360 degrees averaged total torque coefficient

The amplitude of these fluctuations is negligible for the calculation of the power output (~ 2%) but could have caused a troublesome convergence.

For higher TSR, however, the trend is much more regular.

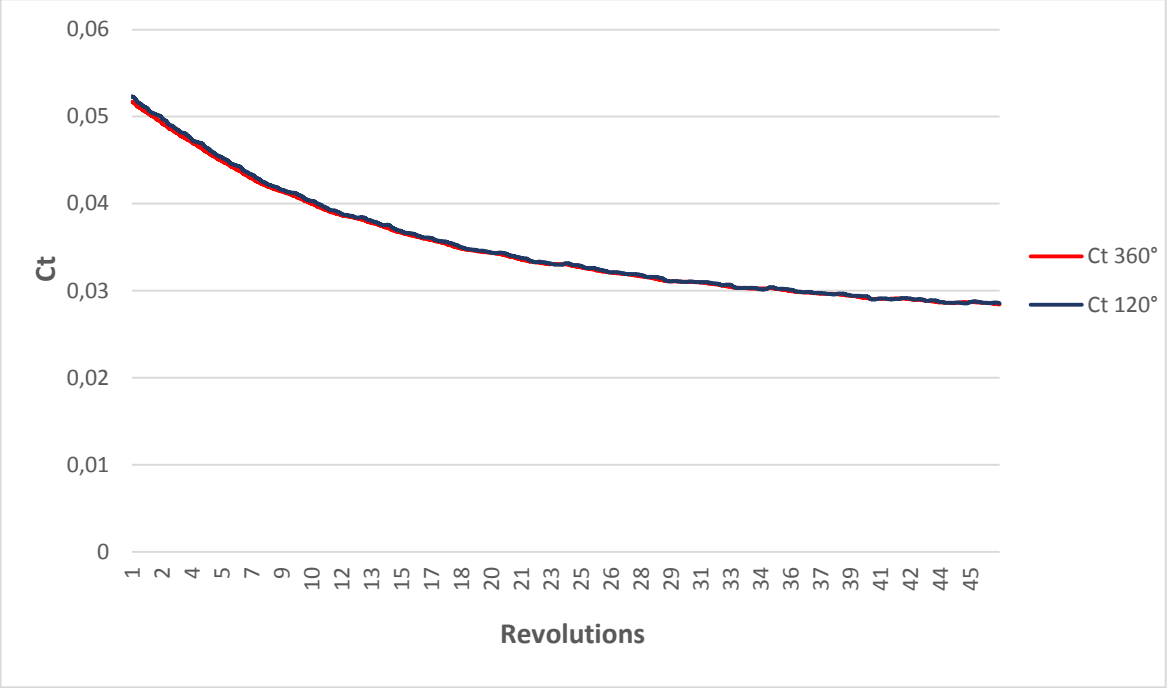

Graph 2.2 - TSR 3.3: 120 and 360 degrees averaged total torque coefficient

To sum up, two different situation have been observed: the low TSR cases, in which the torque evolution is chaotic and the high TSR cases, in which the torque has a defined trend.

The adopted criterion, at the light of the previous considerations, can thus be formalized as follows. Introducing a moving average operator:

$$MA_{(i,N)}(T) = \frac{1}{N}\sum_{i-\frac{N}{2}}^{i+\frac{N}{2}-1} T(i) \qquad [2.1]$$

Where $T(i)$ is the i-th value of the torque in the time series.

The torque residuals are:

$$\Delta T = \frac{MA_{(i,N)}(T) - MA_{(i+N,N)}(T)}{average(MA_{(i,N)}(T); MA_{(i,+N\,N)}(T))} \qquad [2.2]$$

For low TSR (chaotic residuals) must be ΔT < 0.5% for at least 3 revolution.

For high TSR (oscillating residuals) must be $MA_{(i,M)}(\Delta T)$ < 0.5%, where the moving average applied to the residuals is able to purge them from the shedding-induced oscillations that are evident in graph 2.4.

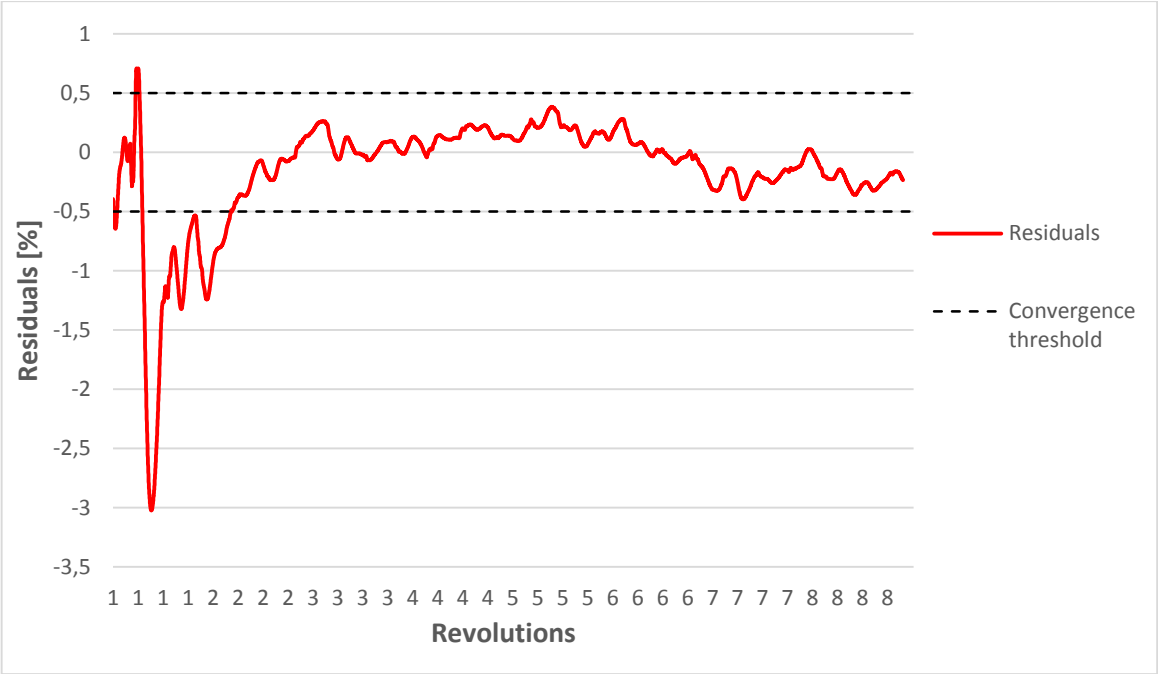

Graph 2.3 - TSR 1.1: Residuals history

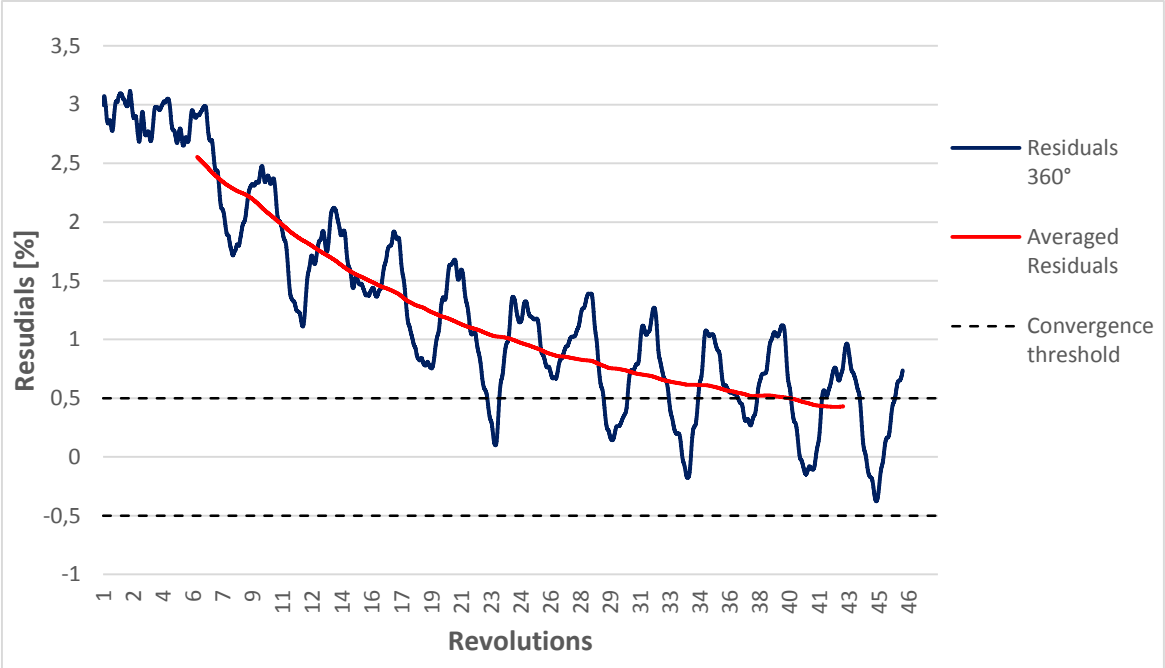

Graph 2.4 - TSR 3.3 - Residuals history

The analysis of the torque residuals at high TSR showed an evident fluctuating pattern, with a period that exceeds the revolution time. A plausible explanation for this phenomenon that appears only for high TSR is that the great vortices shed in the turbine's far wake can influence the torque convergence and in particular the residuals. In fact, a sort of von Karman vortex sheet appears behind fast rotating turbines (see fig. 2.8). The relative shedding frequency is similar to the one observed for the residuals (1.35 Hz vs 1.65 Hz). This justify the choice of adopting the moving average of the residuals in the convergence criterion. This criteria will be adopted throughout this work, except for some special cases that will be presented further.

2.3 Outer domain size

A notable effort has been spent by Ferrari et al. to verify the sensitivity of the solution to the outer domain size. They stated that for a convergent and independent result the domain should be at least 60 D (turbine diameter) wide, 40 D long in front of the turbine and 100 diameter behind it to capture the wake effects. The adopted domain is slightly different and is here reported.

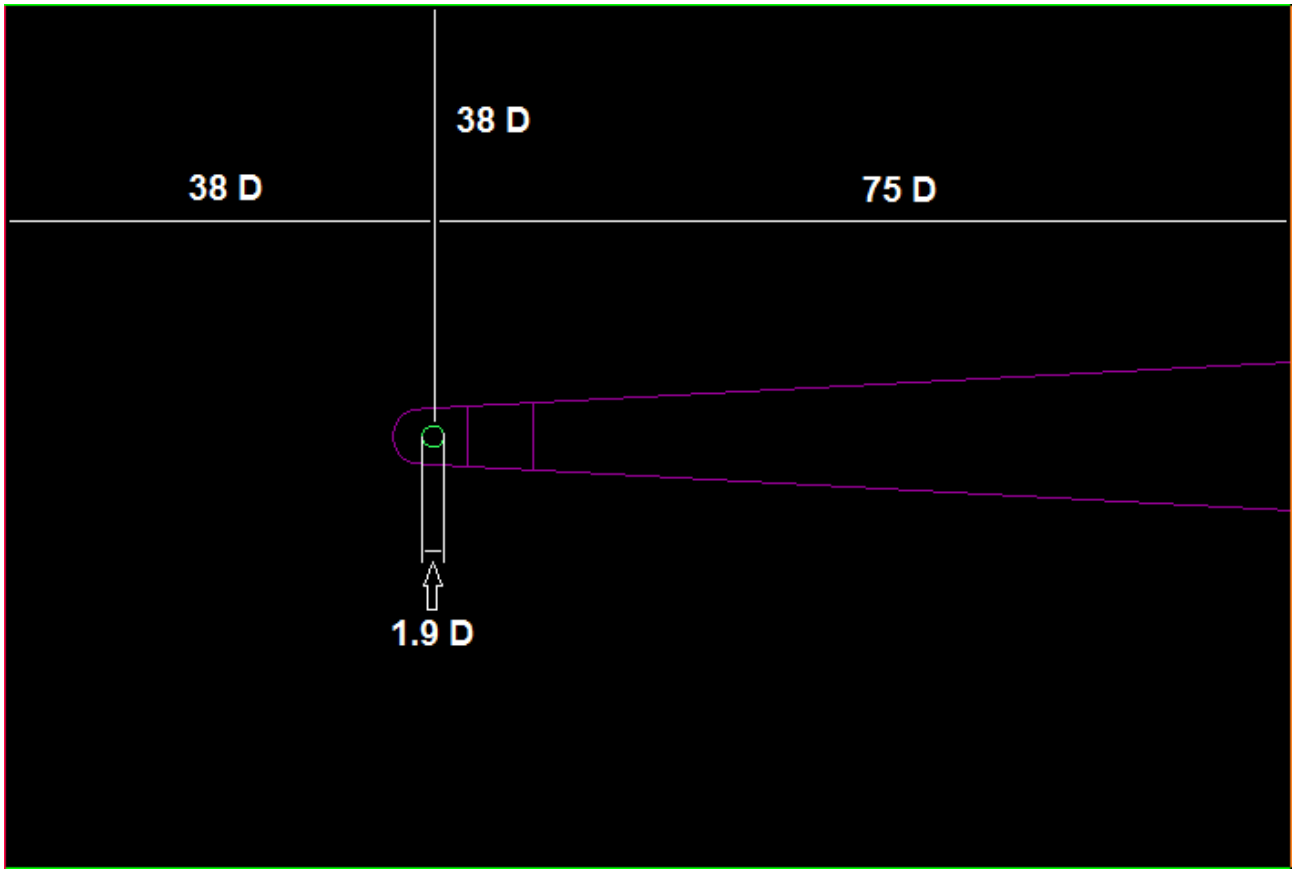

Figure 2.1 - Outer domain size

This are very cautious size when confronted with the other example found in literature. Its dimension are a little different in mainly in the wake region but this should not affect the solution for more than 0.3% as Ferrari et al. stated. The boundary conditions are:

- velocity inlet for the inlet
- pressure outlet for the outlet
- symmetry for the side boundaries

2.4 Mesh

The following meshing criteria were adopted, in complete analogy with the reported setup.

Software	ICEM CFD
Element type	All TRI unstructured + prismatic layers
Max near wall cell length	0.001 m
Number of prismatic layers (PL)	50
PL growth factor	1.065
First PL height	3e-05 m (y^+<5)
Cell dimension along the sliding interface	0.02 m
Number of cells in the rotating domain	341000
Number of cells of the outer domain	189000
Minimum orthogonal quality	0.3

Table 2.2 - Mesh setup

The following figures compare the present mesh (blue and black) with the reference mesh (grey and yellow). The slight difference are due to the different mesh generator but are supposed not have greatly affected the final solution.

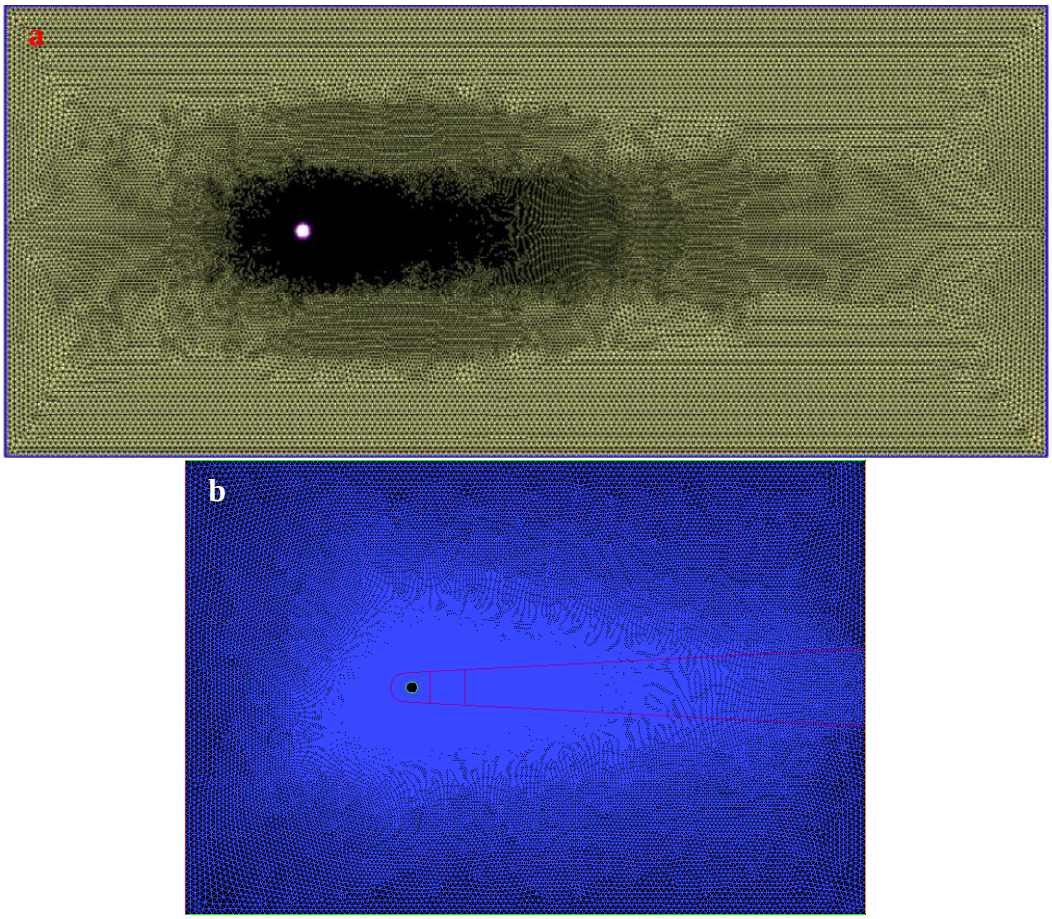

Figure 2.2 - Outer domain: **a**-Reference mesh, **b**-Present mesh

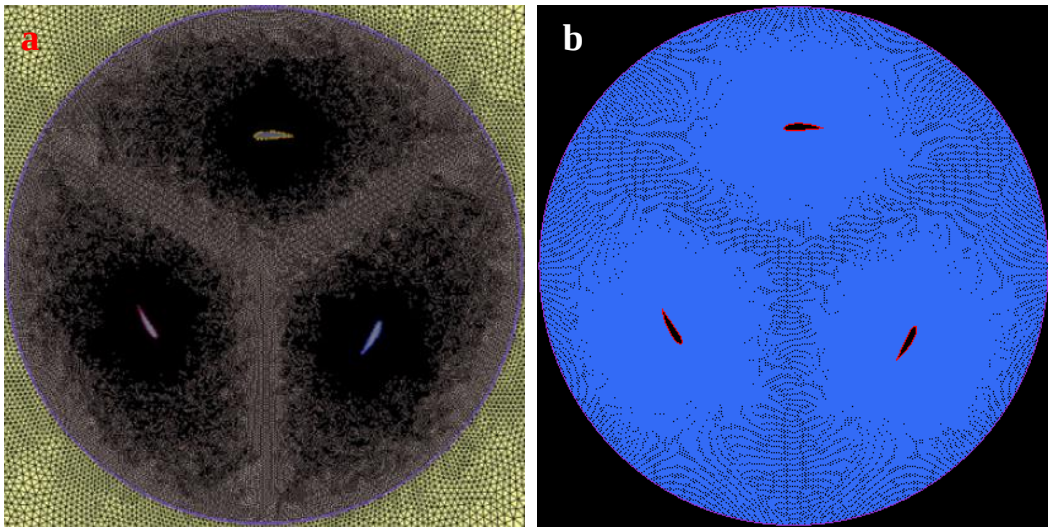

Figure 2.3 - Rotating domain: **a**-Reference mesh, **b**-Present mesh

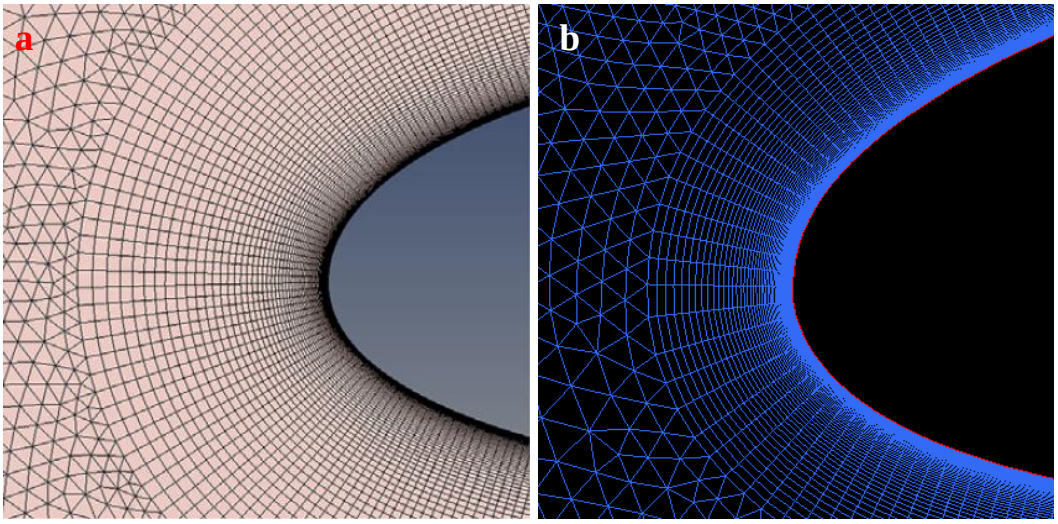

Figure 2.4 - Blade's leading edge: **a**-Reference mesh, **b**-Present mesh

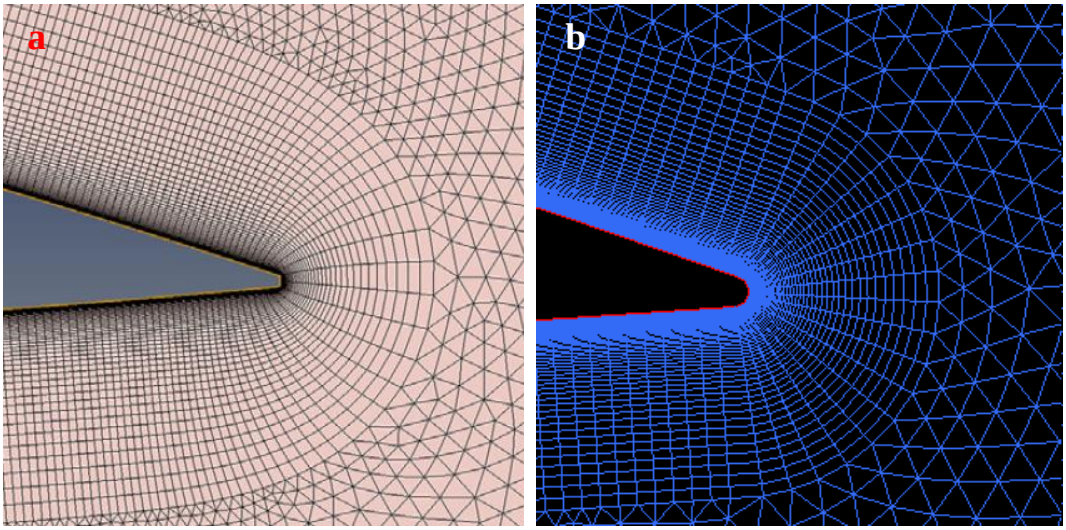

Figure 2.5 - Blade's trailing edge: **a**-Reference mesh, **b**-Present mesh

2.5 Solver settings and strategy

The solver setup was equal to the one reported in the reference.

Simulation type	Transient
Solver	Pressure Based
Turbulence model	k-ω SST
Fluyd	Air as ideal gas
Space discretization scheme	II order upwind
Time discretization scheme	II order implicit bounded
Gradient scheme	Minimum squares
Pressure velocity coupling	Coupled
Pressure algorithm	PRESTO!
Timestep	Varibable
Numeric residuals	1.00e-04

Table 2.3 - Solver setup

As already mentioned, the convergence is an expensive target for this kind of simulation. This is mainly matter of different characteristic timescales between the near blade phenomena and the far field, as will be analyzed later.

Several studies confirmed that to get a full description of the aerodynamics of the rotating blades a timestep corresponding to a rotation angle less than 1 degree is appropriate [13, 14, 15], that for the actual rotational speed means less than 0.001 seconds. So, to get a faster convergence, a coarse timestep has been adopted for the first part of the simulation, to have a first attempt estimation of the wake dynamics, and then it has been refined to obtain a more accurate forces calculation. In particular:

- 10 revolutions with a timestep corresponding to 2.14°
- 5 revolutions with 0.71°
- Undetermined revolution until convergence with 0.35°

As it could have been guessed from the particular angles values, the choice of the timestep is not free, because for practical reasons a proper correspondence between the cells on the sliding interface should be granted, and this also limits the minimum timestep size.

2.6 Results

2.6.1 Low TSR

For low TSR, the high angle of attack experienced by the blades and the consequent stall regime result in an irregular flow pattern with negligible shedding. The following figures refer to the lower TSR case simulated.

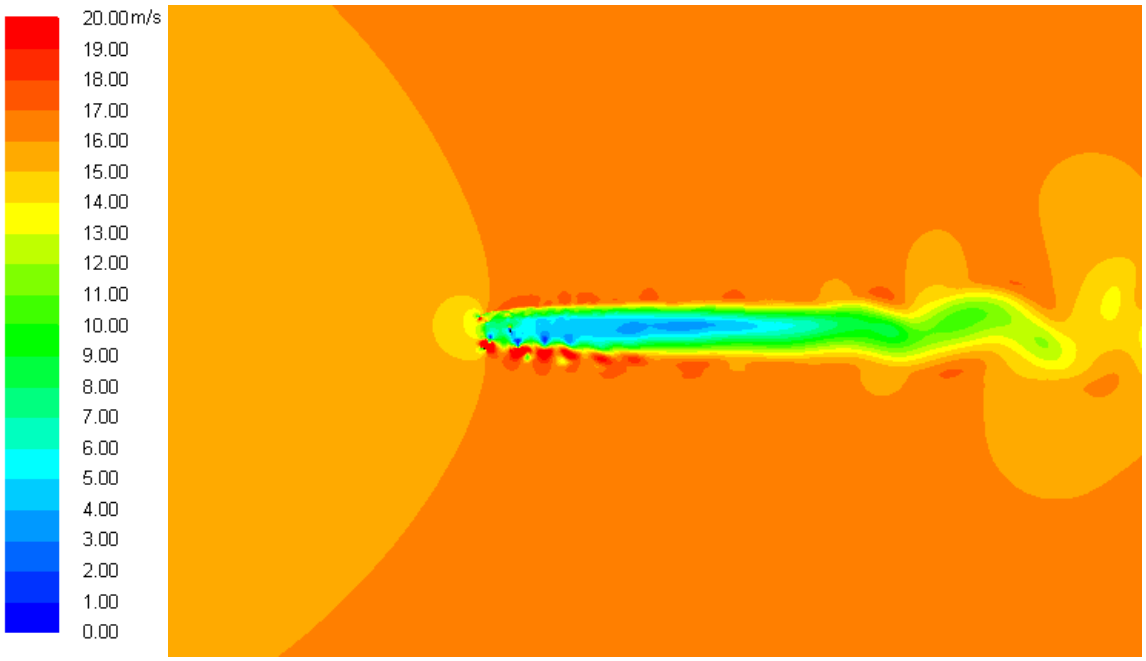

Figure 2.6 - TSR 1.1: Contours of velocity magnitude

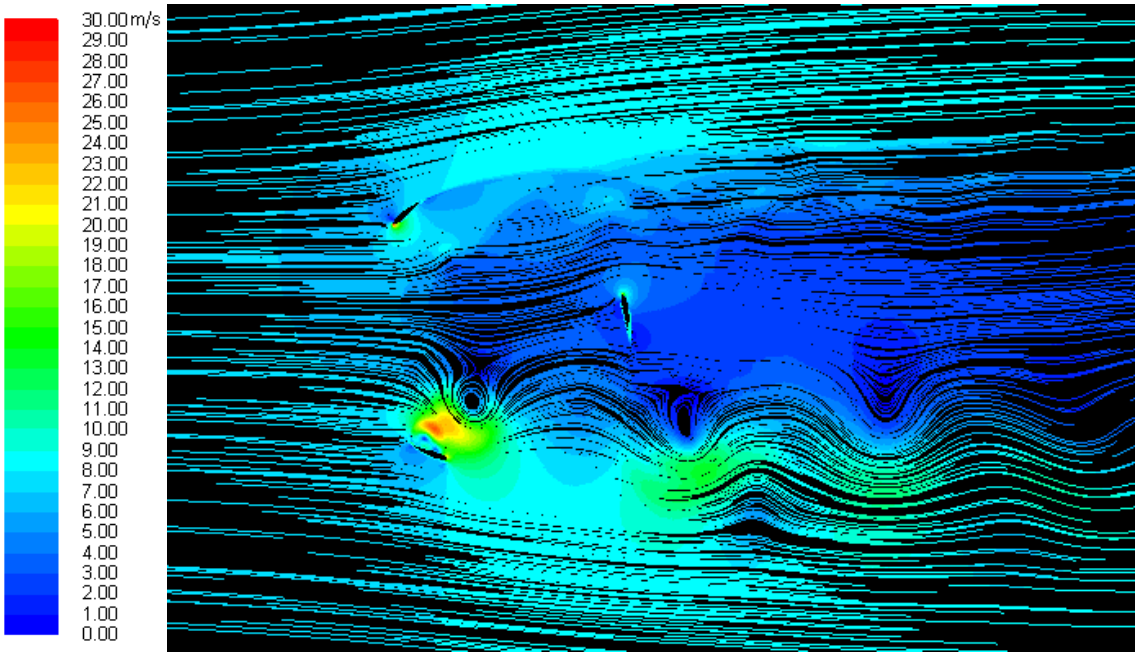

Figure 2.7 - TSR 1.1: Streamlines colored by velocity magnitude

Zooming in the rotor zone, the strong vortex shedding from the blades in an azimutal angle between 90 and 180° become evident. There are a consequence of the dynamic stall, that will be analyzed in chapter 4.4.

2.6.2 High TSR

Beyond a certain TSR, the boundary layer does not separate from the airfoil surface. The flow pattern is uniform in the rotor area, while the far wake undergoes a regular big vortex shedding. This is a consequence of the increased rotor speed and the high relative velocity experienced by the blades, thus enhancing the lift force, which in turn makes the rotor less permeable to the fluid. Even if the occurring phenomena are much different, the high blockage makes the turbine more similar to a solid cylinder, which is the best-known example of vortex shedding generator.

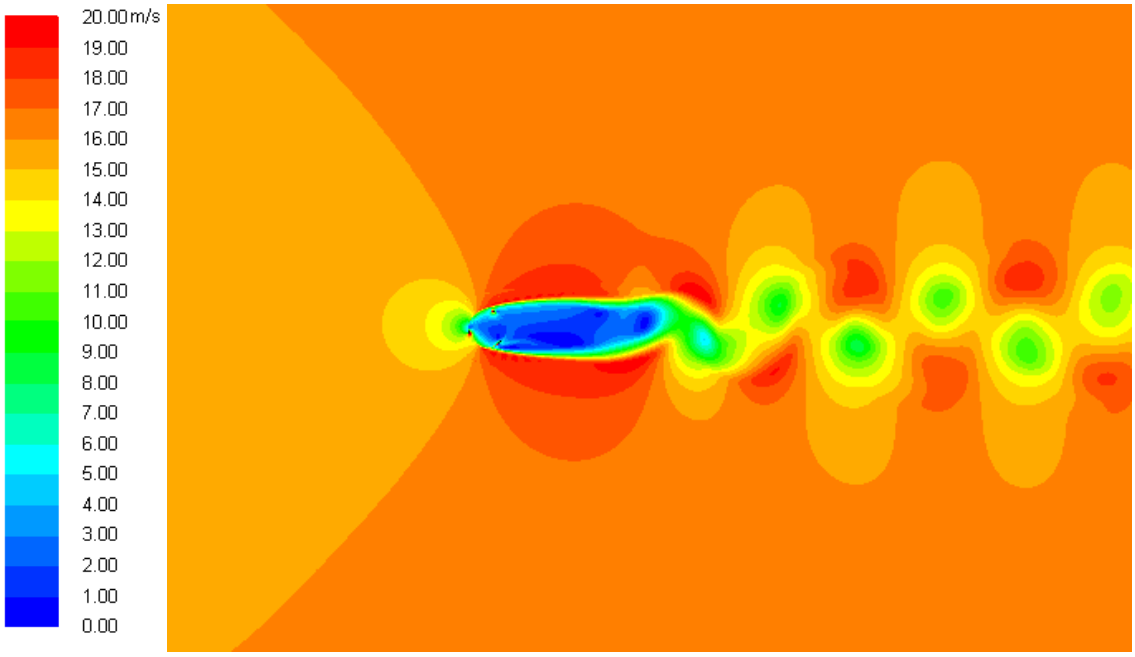

Figure 2.8 - TSR 3.3: Contours of velocity magnitude

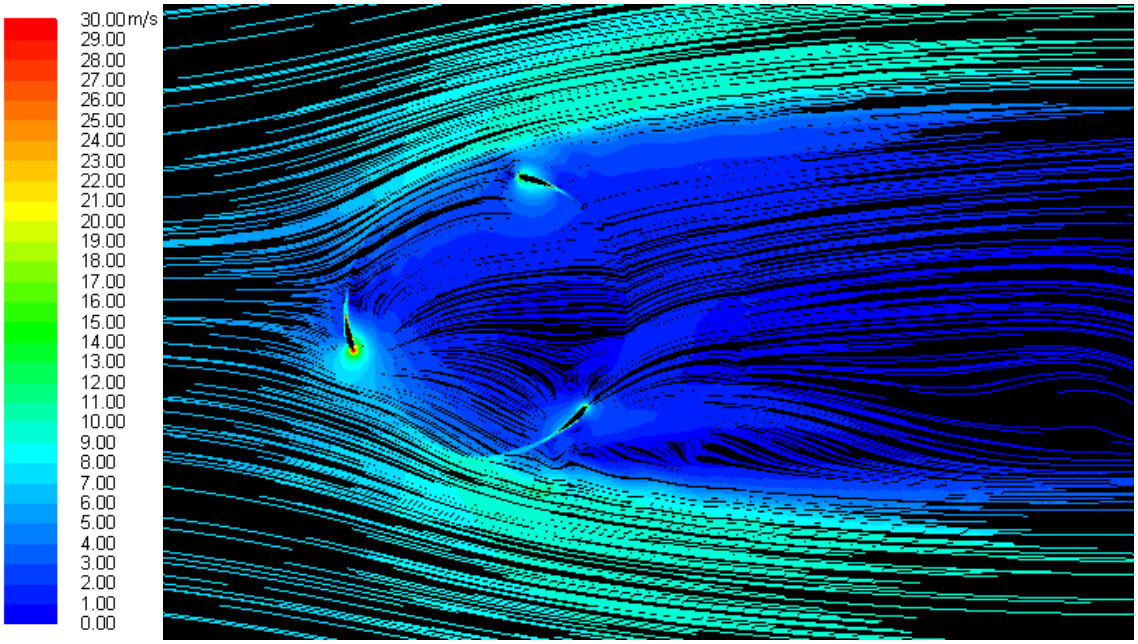

Figure 2.9 - TSR 3.3: Streamlines colored by velocity magnitude

2.7 Comparison with experimental data

The Cp/TSR curves from the present and the reference study are compared with the experimental data provided by Ferrari et al.

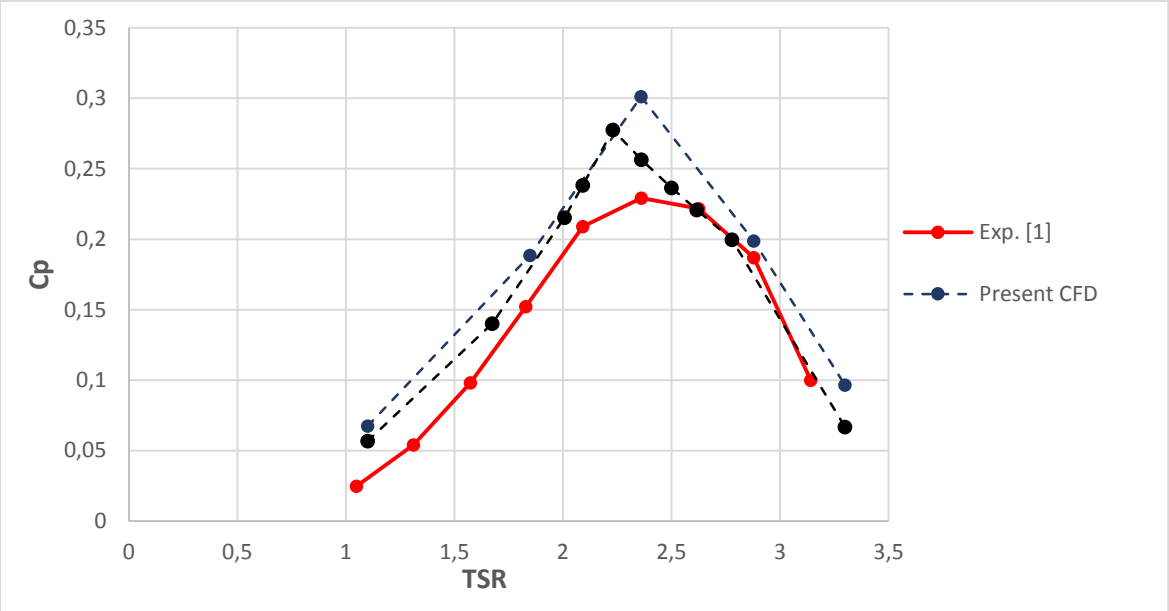

Graph 2.5 - CP-TSR curves from present CFD, reference CFD and reference experiment

The agreement is slightly worse than in the reference for comprehensible reasons related to the coarser convergence criterion and unavoidable difference in the mesh. The present CFD overestimates the peak power of 30% with respect to the experimental data, whereas the reference study commits an error of 11%. So, although a very fine mesh and a small timestep have been adopted and a calculation time of several week have been employed, the modelling of a real VAWT remains a very challenging purpose. However, the present result have been considered satisfactory, since the overall trend has been reproduced.

2.8 Comparison with the reference study

The agreement between the present and the reference Ct curve has been verified for two values of the TSR. This comparison gives a more tangible idea of the disagreement with the reference study.

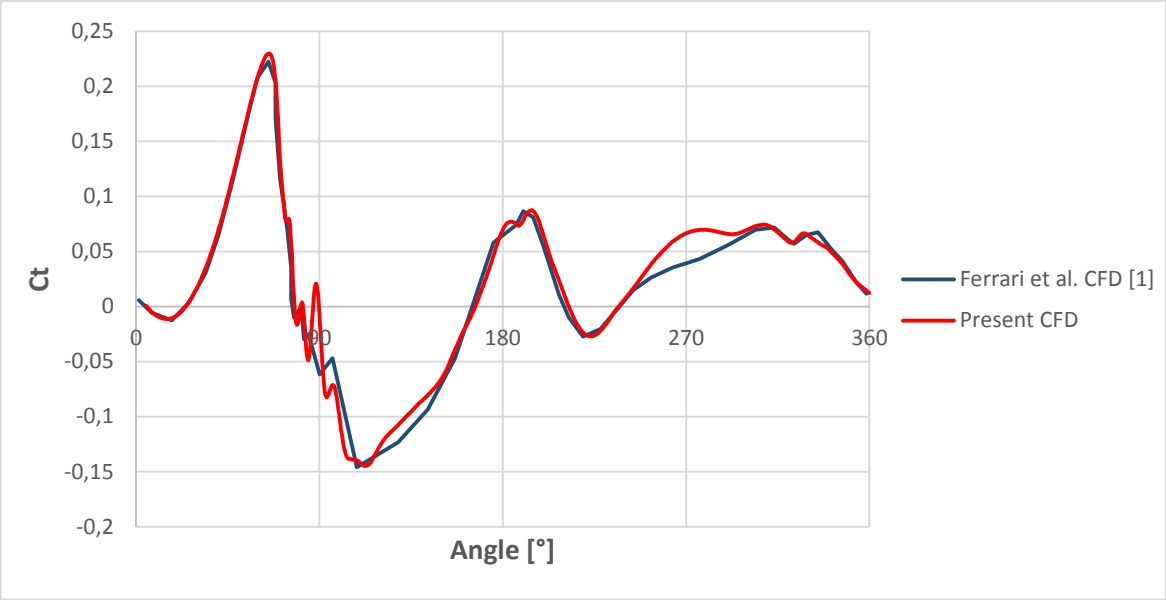

Graph 2.6 - TSR 1.1: Ct curves from present and reference CFD

In the graph above, a satisfactory correspondence between the two plots is shown, with the only exception of the downwind part ranging from 250 to 300 degrees, maybe due to the slightly finer timestep adopted by the authors and the different convergence criterion.

Observing the plot it is possible to understand very well what the blade at this extremely low TSR condition is experiencing: a first attached BL regime is abruptly interrupted by the dynamic stall onset, which causes the performances to decay, after a brief reconstitution of the BL a new torque plunge appears in the downwind path. No doubt about the fact that this complex phenomenon has been successfully reproduced even by the present CFD study

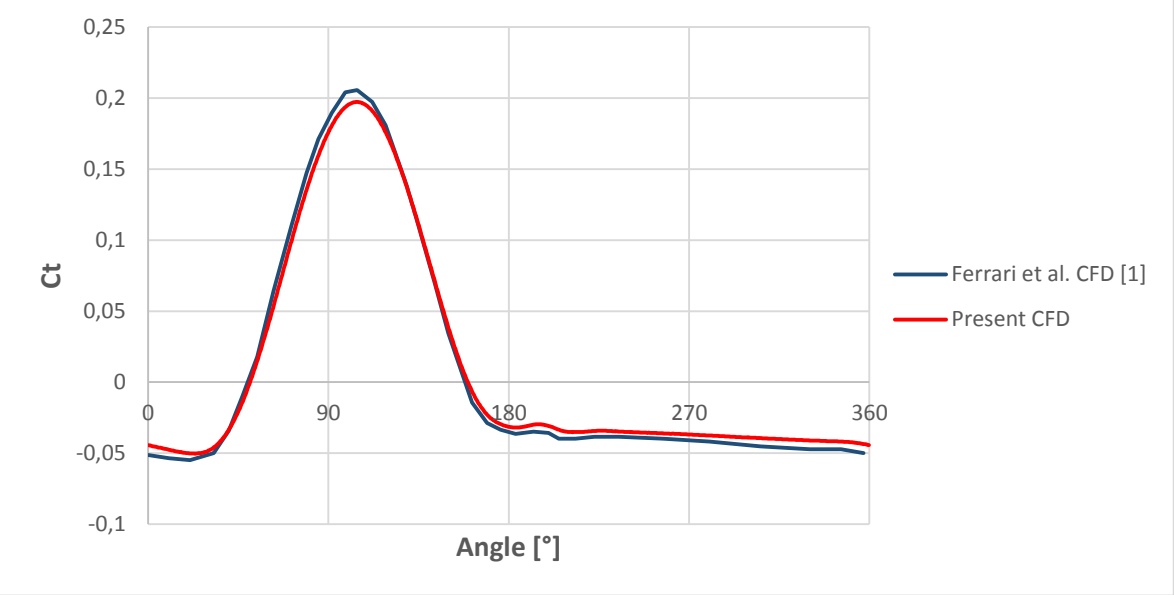

Graph 2.7 - TSR1.1: Ct curves from present and reference CFD

For high TSR, an overall good agreement can be seen, even if some differences still appear and make the Cp value quiet higher with respect to the reference. This is probably caused by the unavoidable small mesh discrepancies and the troublesome convergence affecting these simulations (it is worthwhile to remind that the convergence criteria are different).

In this case, the BL separation does not occur, because of the low angles of attack, but the great blockage effect due to the high relative speed in the upwind path, limits the power extraction in the downwind half.

2.9 Influence of the convergence threshold

To limit the computational time (which has been however very large) it has been necessary to define a slightly higher threshold in the convergence criterion with respect to the reference article. Ferrari et al. [1] had chosen 0.1% but this would have resulted in an almost unaffordable calculation time, so for the present work 0.5% has been set. Despite the great number of revolutions simulated, a slow but not negligible trend was observed, this highlighting once more the huge computational effort that the complete solution of these problems requires.

The graph below shows the convergence history for three different TSR, as a function of the convergence threshold.

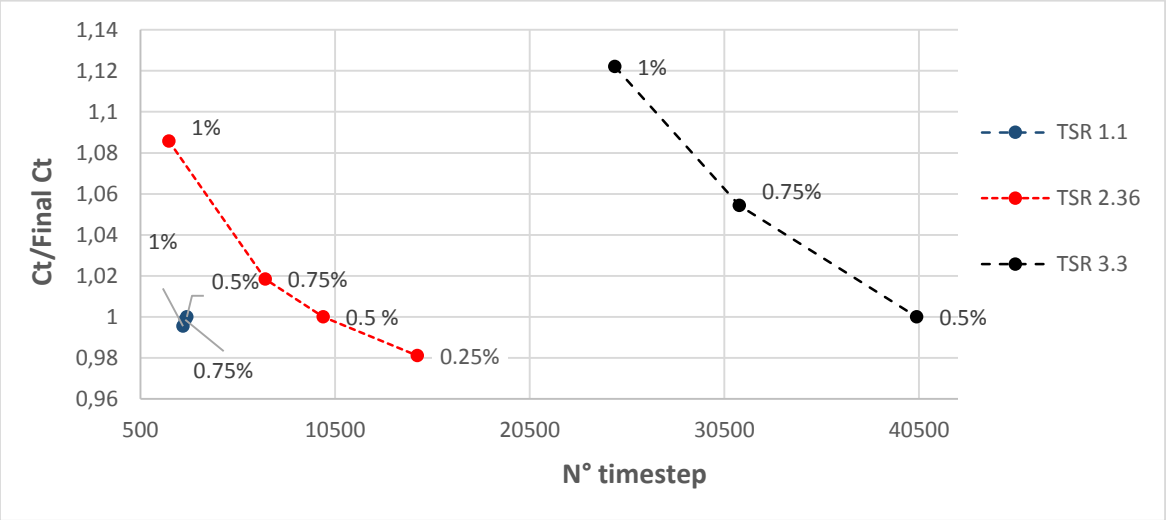

Graph 2.8 - Convergence threshold influence

As it can be noticed, in case of low TSR the torque experience a weak positive trend, probably due to the progressive reduction of the dynamic stall severity with the decreasing incoming velocity. In fact, as the stream velocity slows down because of the turbine trust, the maximum angle of attack reduces. This is an unstable condition and is very far from the operating one for a well-designed machine.

For high TSR the trend is negative and does not fade even after a great number of timesteps. In this case, the trust is much higher, thus producing a deepest wake and the velocity perturbation induced by the turbine is larger. Moreover, a reduction of incoming flow velocity, by lowering the angles of attack, also reduces the torque and the trust and this explains why the trend exponentially decays.

The next graph shows the different torque curve that would have been obtained with a higher threshold. The disagreement is evident for high TSR, so that the difference of the final curve with the reference one can be explained as matter of physical convergence.

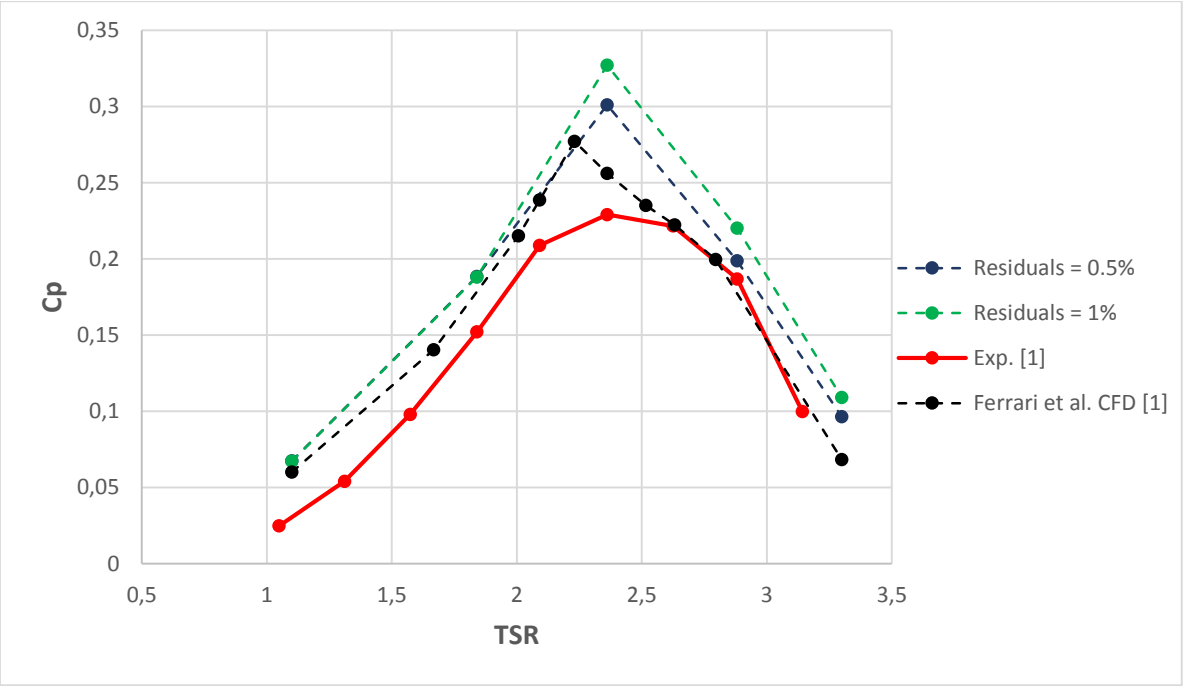

Graph 2.9 - Effects of the convergence criterion on the Cp/TSR curve

2.10 Timestep sensitivity

It is useful to state beforehand that a timestep refinement should improve the simulation accuracy for the following reasons:

1. The time derivative terms in the solver's equation is here discretized with a second order scheme, thus implying that the related error approaches 0 as DT^3
2. It makes possible to investigate phenomena with a progressively smaller timescale (e.g. the Kolmogorov scale as lower limit)
3. The numeric convergence within a single timestep could be achieved faster

There are also two negative aspects:

1. A larger number of timesteps is required before physical convergence
2. A too small revolution angle per timestep causes the cells along the mesh sliding interface to share a small portion of their face with the adjacent ones, thus creating some problem for the interpolating algorithm with consequent convergence problems

For low TSR, the torque is highly timestep-sensitive, because the BL separation and the consequent small vortex around the blades need a fine time discretization to be captured. However the global trend does not deteriorate too much. Note that the degrees the legend refers to are the rotation increment per timestep.

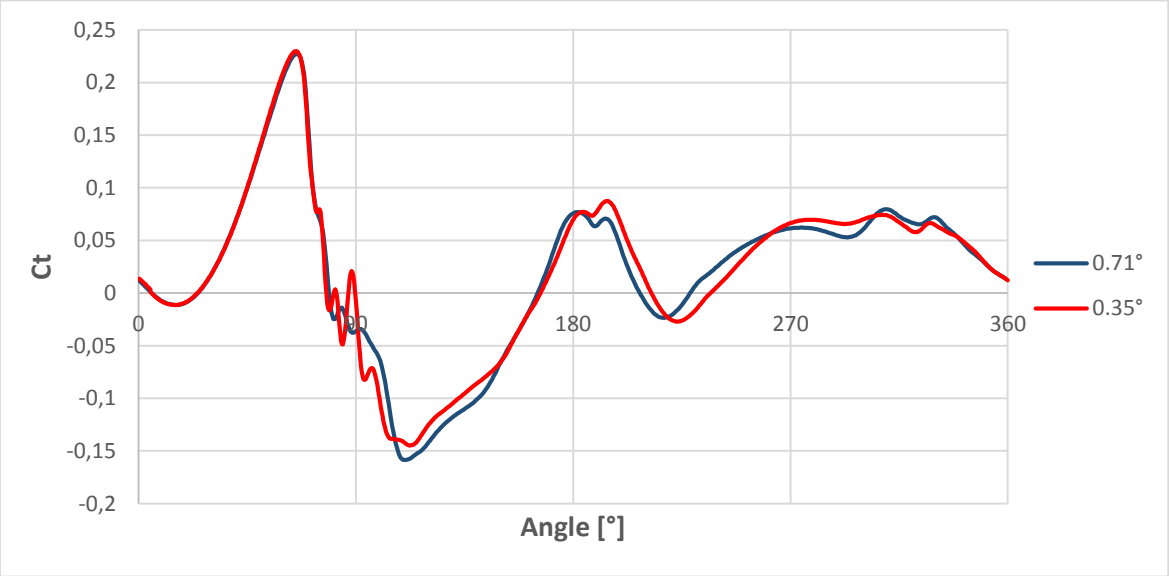

Graph 2.10 - TSR 1.1: Effects of timesteps corresponding to different azimuthal angle increment

For higher TSR de discrepancies are quite negligible, as could be theoretically justified for attached flow regime.

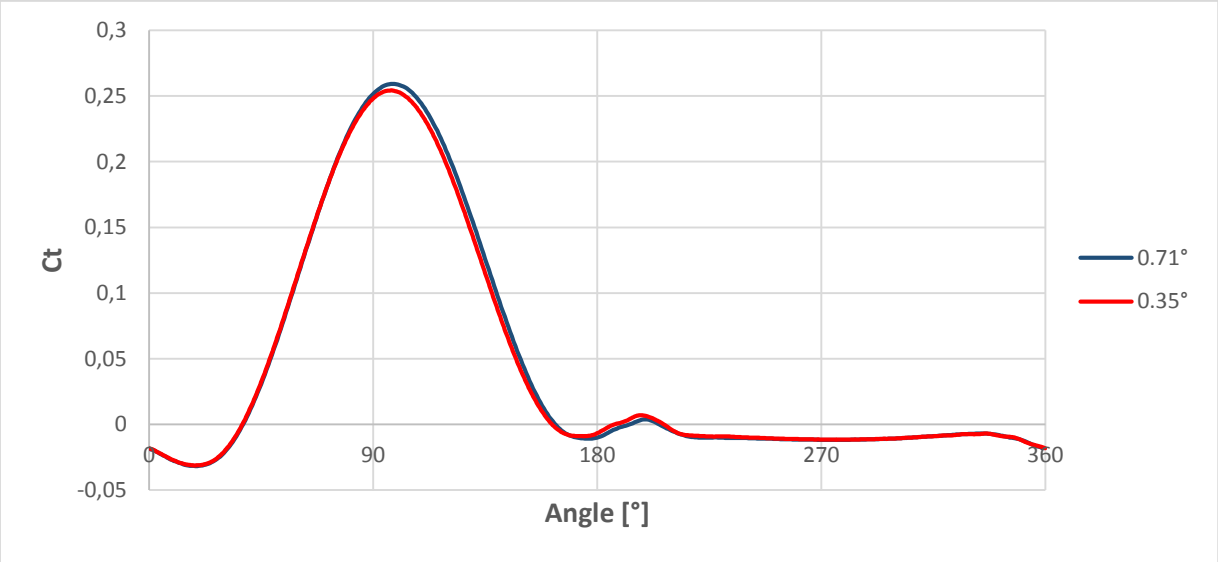

Graph 2.11 - TSR 3.3: Effects of timesteps corresponding to different azimuthal angle increment

2.11 Mesh sensitivity

The mesh adopted for the validation part of this work provided very accurate results but was very far from been time effective for the present purposes. For example, to obtain a convergent torque curve for TSR 3.3, which represent however a single point on the Cp/TSR curve, were necessary more than 20 days of unstopped calculation on a 12-core computer. For the final goal of the work was the definition of an optimal configuration of a shrouded turbine operating hopefully in attached flow condition, a coarser mesh was generated and the new result were compared with the previous ones. The mesh characteristic are summarized in table 2.4, while the other setting are unchanged.

Software	ICEM CFD
Element type	All QUAD unstructured + prismatic layers
Max near wall cell length	0.00135 m
Number of prismatic layers (PL)	25
PL growth factor	1.13
First PL thickness	3e-05 m (y^+<5)
Cell dimension along the sliding interface	0.015 m
Rotating domain diameter	1.5 D
Number of cells in the rotating domain	154000
Number of cells of the outer domain	70000
Minimum orthogonal quality	0.3

Table 2.4 - Coarse mesh setup

The results are plotted below. The low TSR case (graph 2.12) exhibits a higher sensitivity, but for it is not an operative condition, this fact has been considered uninfluential.

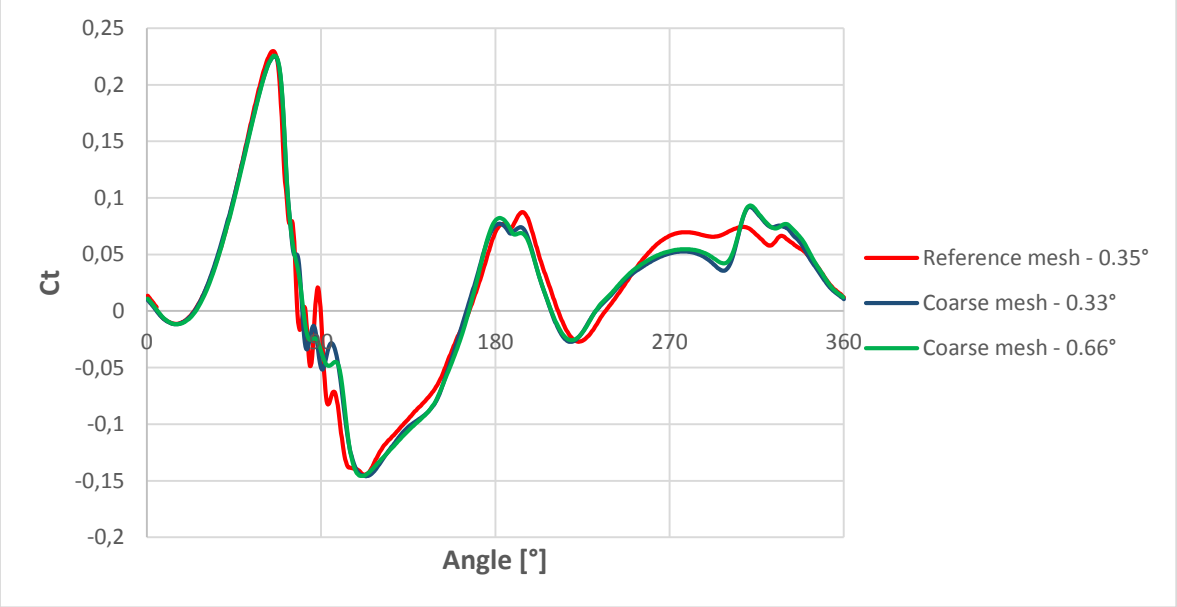

Graph 2.12 - TSR 1.1: Mesh and timestep sensitivity of the Ct curve

For high TSR (graph 2.13) the discrepancies are far negligible for the present purposes and, therefore, this mesh set up has been adopted throughout the rest of the work.

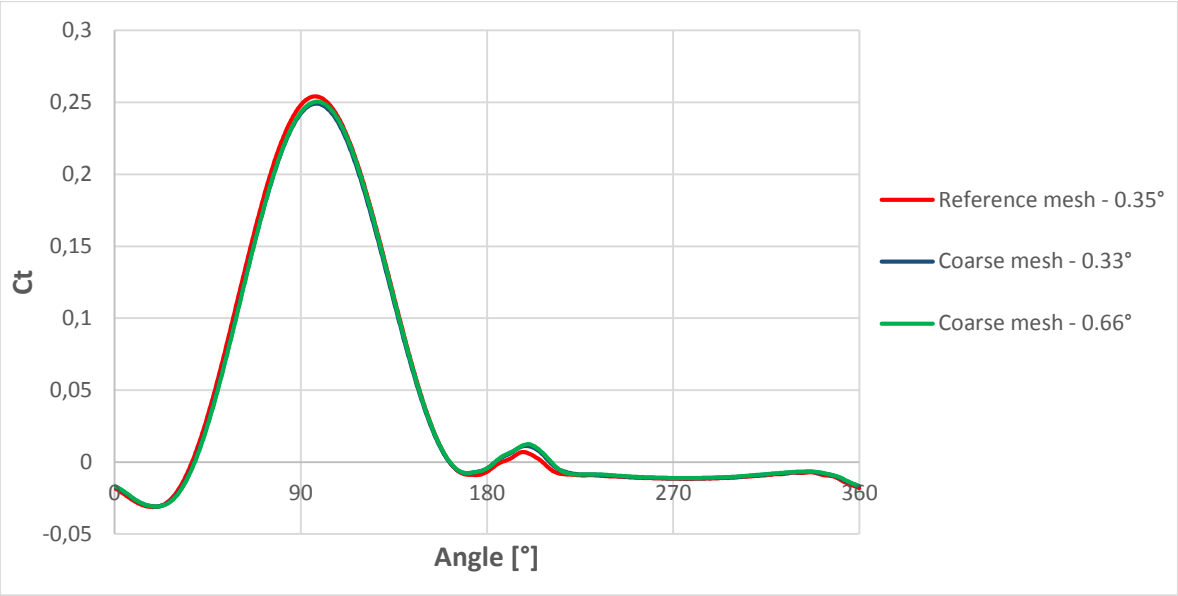

Graph 2.13 - TSR 3.3: Mesh and timestep sensitivity of the Ct curve

II References

[1] Balduzzi F, Biachini A, Maleci R, Ferrara G, Ferrari L, *Critical issues in the CFD simulation of Darrieus wind turbines*, Renewable Energy 85 (2016) 419e435

[2] Li Y, Sanderc MC. *Three-dimensional effects and arm effects on modeling a vertical axis tidal current turbine*, Renewable Energy 35 (2010) 2325-2334

[3] Menter, FR. *Zonal two-equation k-omega turbulence model for aerodynamic flows*. AIAA Paper 1993-2906, 1993.

[4] Menter FR, (1994), *Two-equation eddy-viscosity turbulence models for engineering applications.* AIAA-Journal, 32(8), pp. 269-289, 1994

[5] Mener FR, Kuntz M, Langtry R. *Ten Years of Industrial Experience with the SST Turbulence Model*,

[6] *Fluent theory guide*, Ansys Inc., Release 14.0, (2011)

[7] T. Maître, E. Amet, C. Pellone, *Modeling of the flow in a Darrieus water turbine: Wall grid refinement analysis and comparison with experiments*, Renewable Energy 51 (2013) 497e512.

[8] S. Lain, C. Osorio, *Simulation and evaluation of a straight-bladed Darrieus-type cross flow marine turbine*, J. Sci. Ind. Res. 69 (2010) 906e912.

[9] Hinze JO. *Turbulence*. McGraw-Hill Publishing Co., New York. 1975.

[10] Mohamed, *Performance investigation of H-rotor Darrieus turbine with new airfoil shapes*, Energy 47 (2012) 522e530.

[11] Daroczya L, Janiga G, Petrasch K, Webner M, Thevenin D. *Comparative analysis of turbulence models for the aerodynamic simulation of H-Darrieus rotors*, Energy (2015) 1e11

[12] Raciti Castelli M, Englaro E, Benini E, *The Darrieus wind turbine: Proposal for a new performance prediction model based on CFD*, Energy 36 8 (2011) 4919e4934.

[13] Maître T, Amet E, Pellone C, *Modeling of the flow in a Darrieus water turbine: Wall grid refinement analysis and comparison with experiments*, Renewable Energy 51 (2013) 497e512.

[14] Raciti Castelli M, Ardizzon G, Battisti L, Benini E, Pavesi G, *Modeling strategy and numerical validation for Darrieus vertical axis micro-wind turbine*, in: Proceedings of the ASME IMECE 2010, Vancouver, Canada, November 12-18,2010.

[15] Trivellato F, Raciti Castelli M, *On the Courant-Friedrichs-Lewy criterion of rotating grids in 2D vertical-axis wind turbine analysis*, Renewable Energy 62 (2014) 53e62.

Part III - DAWT theory

The following picture represents the basic concepts of diffuser-augmented HAWT and VAWT (however almost the same design applies to hydrokinetic machines).

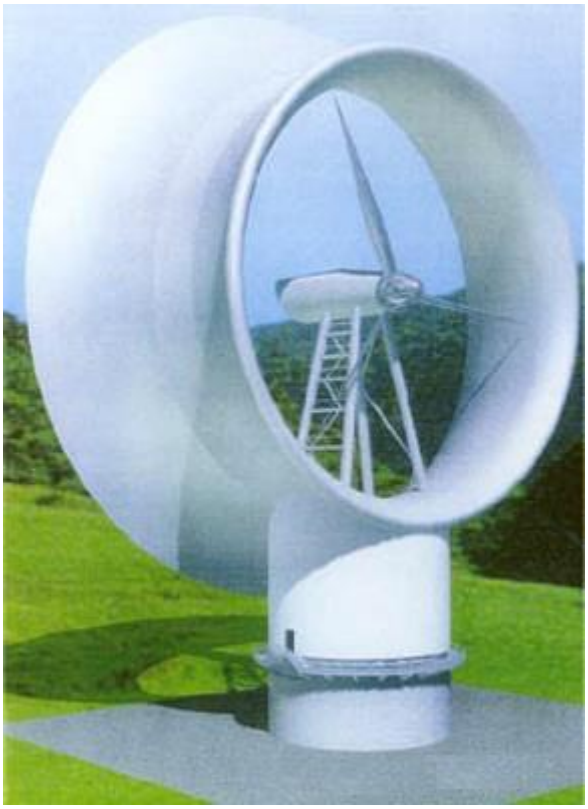

Figure 3.1 - A diffuser-augmented HAWT

Figure 3.2 - A diffuser-augmented VAWT

The principle behind these objects is simple: increasing the mass flow to the turbine in order to exploit a higher energy input keeping constant the rotor swept area. The convenience of this device is not clear since the increased energy output for a given diameter has then to be weighed against the cost increase due to the added structural elements [1]. A diffuser augmented turbine readily can exceed the Betz' limit for the Cp, if this coefficient is calculated adopting the rotor swept area. If the Cp based on the exit area is considered, the diffusers' benefits are not clear. Lilley et al. [2] stated that performances improvements in this sense could be achieved, whereas Bussel [3], through a 1-D momentum theory, affirms that if a strong back pressure originates at the exit of the diffuser, the Cp based in the exit area could break the 16/27 limit. He also states that such a high performance has not been experimentally observed yet. Even Jamieson [4] provides a simple approach to model an ideal DAWT and imposes a limit of power extraction even for VAWTs, but admits in the end that by virtue of viscous interaction between external flow some benefit could be achieved. Hjort et al. [5] claim the invention of a particular diffuser capable of inducing a Cp that exceeds the Betz limit, even referring to the exit area, but they did not provide experimental results. This brief review highlights the challenging complexity of this issue. The lack for a universally accepted simple theory, (unlike it happens for bare turbines) mainly relies on the unknown trust exerted by the diffuser even under ideal assumption [2]. This unknown force invalidate the simple 1D momentum and makes unaffordable a Betz-like approach, even if some of the cited authors persisted with this method. Besides these simple methods, there is an interesting way of regarding at the diffuser: it can be named "aerodynamic approach" and considers the flow augmentation not just like a consequence of the 1D continuity applied to the diffuser's throat, but as the contribution of the circulation due to the constitution of the Kutta condition on the diffuser's wall (see fig. 3.4)[1, 5, 6]. This can provide useful indications for the choice of the most performing geometry.
In this section, the most cited 1-D momentum theory are analyzed and, in the end, the aerodynamic approach reported by Van Beveren [6] is described.

3.1 1-D momentum theory

3.1.1 Bussel's theory

This analysis [3] starts from the study of an empty diffuser and is valid for HAWT, but the result can be extended to VAWT when regarded as single actuator ring, like in the single streamtube model.
The classic Betz hypothesis (incompressible, one dimensional, inviscid, steady flow) are valid.

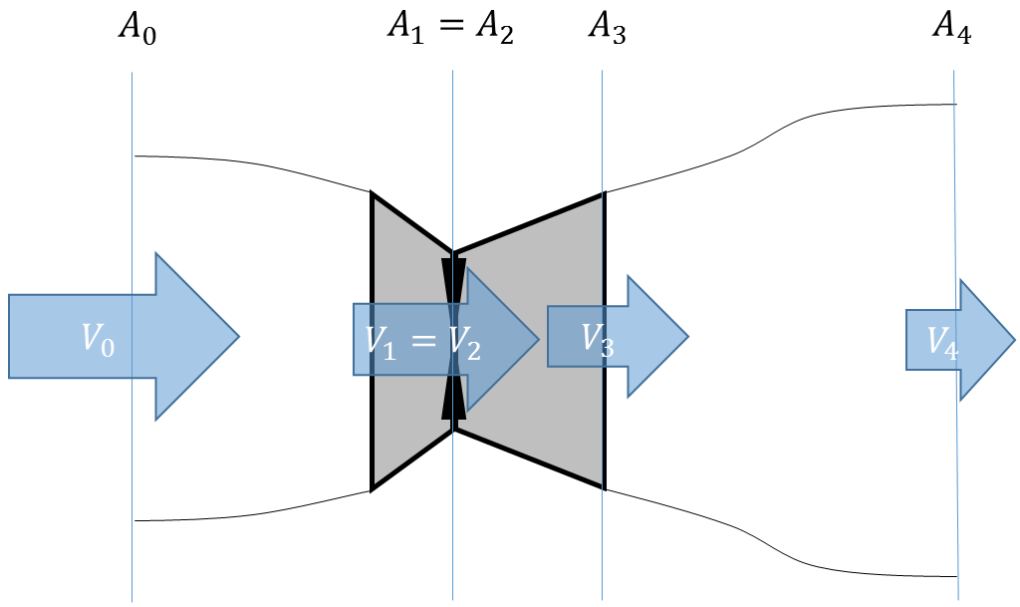

Figure 3.3 - Streamtube approach for a DAWT

From the continuity equation for a one-dimensional incompressible flow, we have:
$V_1 A_1 = V_3 A_3 = V_0 A_0$ [3.1]

Defining β as the ratio between the velocity in the exit section and the velocity in the diffuser's throat and γ the ratio $\frac{V_3}{V_0}$ for the empty diffuser, accounting for a possible under-expansion of the wake, he gets:

$V_1 = V_3 \beta = V_0 \gamma \beta$ [3.2]

Consider now briefly a bare turbine. It is now useful to remind the Froude's theorem, according to which the velocity across the actuator disk is equal to the average of the freestream and the wake velocity. This result comes immediately from the application of the energy and the momentum balance for a bare turbine:

$$\begin{cases} \frac{1}{2}\rho {V_0}^2 = \frac{1}{2}\rho {V_1}^2 + p_1 \\ \frac{1}{2}\rho {V_4}^2 = \frac{1}{2}\rho {V_2}^2 + p_2 \\ \rho V_1 A_1 (V_0 - V_4) = A_1 (p_1^+ - p_1^-) \end{cases} \rightarrow \quad V_1 = \frac{1}{2}(V_0 + V_4) \qquad [3.3]$$

In the case of a diffuser with an actuator disk in the throat (the simplest model of a DAWT) the previous result cannot be applied, because there is also the trust on the diffuser to be accounted for. So, the basic hypothesis of Bussel's theory is that the Froude theorem can be applied even for a diffuser-augmented actuator disk, simply substituting , V_1 for V_3.

He justifies the choice by supposing that the wake behind the diffuser would behave like the one of a bare turbine. So he gets:

$$V_3 = \gamma V_0(1-a) \qquad [3.4]$$

Where γ once again considers the enanced acceleration di to an additional back pressure at the exit.

$$V_4 = V_0(1-2a) \qquad [3.5]$$

The power becomes:

$$P = \dot{m}\left(\frac{1}{2}{V_0}^2 - \frac{1}{2}{V_4}^2\right) = \rho V_3 A_3 \cdot \frac{1}{2}{V_0}^2(4a-4a^2) = 2\rho {V_0}^3 A_1 \gamma\beta a(1-a)^2 \qquad [3.6]$$

Thus:

$$c_p = \beta\gamma 4a(1-a)^2 = \beta\gamma\, c_{p,BETZ} \qquad [3.7]$$

To sum up, the power is a linear function of the mass flow increase determined by the diffuser, and this is consistent with Hansen [7].

This straightforward result, as already mentioned, can be transpose in the analysis of a ducted VAWT only if the whole turbine can be modeled with a single actuator disk approach, where the average values of velocity and load are considered, thus involving a great loss of accuracy. Moreover, it adopts a very strong hypothesis to obtain the 3.4, 3.6.

3.1.2 Jamieson's Theory

Jamieson [4] adopts the usual actuator disk theory hypothesis of stationary, incompressible, one-dimensional, inviscid flow and introduces the following induction factor:

$$a = 1 - \frac{V_1}{V_0} \quad \text{rotor induction factor} \qquad [3.8]$$

$$b = 1 - \frac{V_4}{V_0} \quad \text{far wake induction factor} \qquad [3.9]$$

The Bernoulli balances between section 0-1 and 2-4 gives:

$$\begin{cases} \frac{1}{2}\rho {V_0}^2 = \frac{1}{2}\rho {V_0}^2(1-a)^2 + p_1 \\ \frac{1}{2}\rho {V_0}^2(1-b)^2 = \frac{1}{2}\rho {V_0}^2(1-a)^2 + p_2 \end{cases} \qquad [3.10]$$

So

$$\Delta p = \frac{1}{2}\rho {V_0}^2(2b-b^2) = T/A \qquad [3.11]$$

where *T* is the trust on the rotor.

To obtain a closed form solution for the far wake induction factor Jamieson argues that, for it must exist a certain section A^* having a velocity given by:

$$V^* = V_0\left(1-\frac{b}{2}\right) \quad [3.12]$$

According to continuity equation it is:

$$A^*\,V_0\left(1-\frac{b}{2}\right) = AV_0(1-a) \quad [3.13]$$

Then, as in the empty diffuser case $= 0$, must follow that:

$$A^* = A(1-a_0) \quad [3.14]$$

being a_0 the induction factor in this limit situation.

Combining 3.13 with 3.14:

$$b = 2\frac{a-a_0}{1-a_0} \quad [3.15]$$

This "simple" solution, however, is not convincing, since there is no proof that the A^* section remains constant as the operating condition change. Jamieson, however, easily concludes that:

$$Cp_{max} = \frac{16}{27}(1-a_0) \quad [3.16]$$

the same results by Bussel without the back pressure factor. The induction factor maximizing the Cp is:

$$a_{max} = \frac{1+2a_0}{3} \quad [3.17]$$

When the Cp is referred to the section A_0 it becomes:

$$Cp_0 = \frac{P_{max}}{\frac{1}{2}\rho {V_0}^3 A_0} = \frac{8}{9} \quad [3.18]$$

that is the same result of Betz. In other words, Jamieson asserts that it is possible to exploit $\frac{8}{9}$ of the power from the flow passing through the rotor, disregarding the kind of turbine (bare or ducted) adopted. For the sake of completeness, it must be said that the author admits that by virtue of viscous interaction between the wake and the outer stream this limit could be exceeded. The same considerations about VAWTs of par. 3.1.1 are valid.

3.1.3 Hjort and Sorsen's theory

Hjort and Sorsen [5] recently proposed a more rigorous approach to estimate the theoretical power gain achievable by means of an axisymmetric diffuser around a HAWT. The hypothesis of inviscid, incompressible, steady flow still hold, but in addiction the absence of uneven loads throughout the actuator disk is imposed. This allows the velocity to change in the radial direction, as it actually happens inside a diffuser, and this makes this method more realistic.

They consider overall momentum balance, including the trust exerted by the disk and the diffuser:

$$\sum \dot{m}_i \, (V_0 - V_4) = \sum A_i \Delta p \, + F \qquad [3.19]$$

Where:

- $\dot{m}_i$ is the mass flow throught an anular section of the disk
- F is the axial force on the diffuser
- Δp is the pressus drop accross the disk, supposed of been constant

The trust of the diffuser can be expanded in a McLaurin series as a function of the pressure drop:

$$F = F_{(\Delta p=0)} + \frac{\partial F}{\partial \Delta p}_{(\Delta p=0)} \Delta p + o(\Delta p) \qquad [3.20]$$

As the fluid is inviscid the first term is null (D'Alambert paradox) and so:

$$F = \frac{\partial F}{\partial \Delta p}_{(\Delta p=0)} \Delta p \, = \sigma \Delta p \, A \qquad [3.21]$$

Where σ is equal to $\sigma = \frac{\partial F}{\partial \Delta p}_{(\Delta p=0)}$. This apparently arbitrary parameter, becomes physically meaningful if the energy balance is considered:

$$\begin{cases} \frac{1}{2}\rho {V_0}^2 = \frac{1}{2}\rho {V_i}^2 + p_1 \\ \frac{1}{2}\rho {V_4}^2 = \frac{1}{2}\rho {V_i}^2 + p_2 \\ \sum \rho V_i A_i \, (V_0 - V_4) = A_1 \Delta p (1+\sigma) \end{cases} \rightarrow \quad \frac{1}{2}(V_0 + V_4)(1+\sigma) = \frac{\sum V_i A_i}{A_1} \qquad [3.22]$$

If the diffuser is empty, the wake velocity is equal to the free stream velocity, thus:

$$V_0 = V_4 \rightarrow \quad V_0(1+\sigma) = \frac{\sum V_i A_i}{A_1} = \overline{V_1} \qquad [3.23]$$

The power can be now immediately calculated:

$$P = \dot{m}\left(\frac{1}{2}{V_0}^2 - \frac{1}{2}{V_4}^2\right) = \rho \overline{V_1} A_1 \cdot \frac{1}{2}{V_0}^2 (4a - 4a^2) = 2\rho {V_0}^3 A_1 (1+\sigma) a (1-a)^2 \qquad [3.24]$$

Then:

$$c_p = (1+\sigma) 4a(1-a)^2 = (1+\sigma) \, c_{p,BETZ} \qquad [3.25]$$

That is the same Jamieson's result. The introduced apparently more complex flow field does not provide any new solution.

3.2 Aerodynamic approach

This method can be directly applied to a diffuser for a VAWT simply made of two symmetrically mounted airfoils [6].

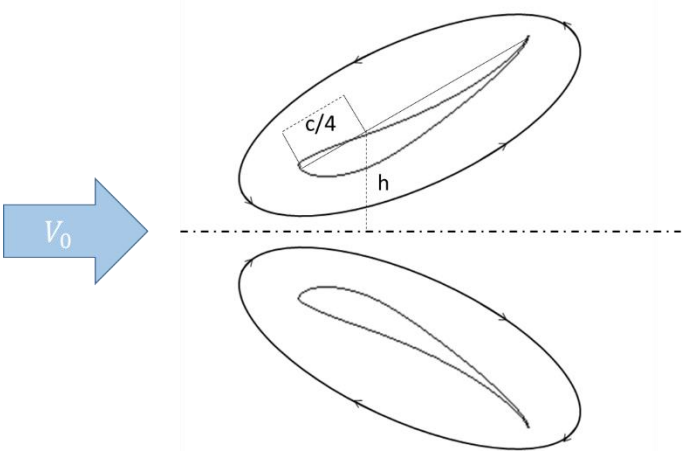

Figure 3.4 - Flow augmentation mechanism between two symmetric tilted airfoils

An easy approach to this problem derives from the lumped vortex method [8], that approximate the flow field around an airfoil as the superposition of the freestream velocity and the velocity field induced by a potential vortex representing the sum of all the bound vorticity of the wing. It can be demonstrated that for an arrangement like the one of fig. 3.4 that the circulation around each wing is:

$$\Gamma = \Gamma_0\left(1 + \frac{c^2}{16h^2}\right) \qquad [3.26]$$

where Γ_0 is the circulation of the same wing at the same incidence but in open flow, or, according to Kutta-Joukowsky:

$$\Gamma_0 = \pi\alpha U c \qquad [3.27]$$

The circulation, and therefore the lift, increases by virtue of the ground effect. As the circulation is known, the Biot-Savart formula provides the velocity field that in the central line in correspondence with the point in which the lifting vortex is assumed to be placed (quarter chord for symmetrical airfoils):

$$V_{throat} = V_0 + \Gamma_0\left(1 + \frac{c^2}{16h^2}\right)\frac{1}{\pi H} = V_0 + \frac{L}{\rho V_0 \pi h}\left(1 + \frac{c^2}{16h^2}\right) \qquad [3.28]$$

$$V_{throat} = V_0\left[1 + \frac{C_l c}{2\pi h}\left(1 + \frac{c^2}{16h^2}\right)\right] \qquad [3.29]$$

where the lift coefficient has been introduced.

Unfortunately, unless referring to the previous models, this approach does not provide an explicit formulation for the power of DAWT, but suggests what a performing diffuser should be like (see next page):

- it must be made of sections having high lift coefficient
- the throat area should be minimal
- the chord must be long, according to geometric and structural constraints

This information have been exploited in the early choice of the diffuser geometry.

III References

[1] De Vries O *Fluid Dynamic Aspects of Wind Energy Conversion*, National Aerospace Laboratory NLR Anthony Fokkerweg 2 /1059 CM Amsterdam The Netherlands (1979)

[2] Lilley GM, Rainbird WJ. 1956 *A preliminary Report on the Design and Performance of a Ducted Windmill*, Report 102, College of Aeronautics, Cranfield U.K

[3] Van Bussel, GJW. *The science of making more torque from wind: Diffuser experiments and theory revisited*. J. Phys. Conf. Ser. 2007, 75, 1-12.

[4] Jamieson P. *Innovation in Wind Turbine Design*, First Edition (2011)

[5] Hjort H, Sorsen H. *A Multi-Element Diffuser Augmented Wind Turbine*, Energies 7 (2014) , 3256-3281

[6] Van Beveren C. *Design of an urban wind turbine with diffuser*, Master Thesis, Delft University (2008)

[7] Hansen, MOL, Sørensen NN, Flay R.G.J. 1999 *Effect of placing a Diffuser around a Wind Turbine*, Proc. EWEC 1999 Conference, Nice, France

[8] Katz J, Plotkin A., *Low-Speed Aerodynamics*, McGraw-Hill, New York, 1991.

Part IV - Actuator ring model

To study the aerodynamics of a DAWT a large amount of simulations is required. Therefore it has been investigated the possibility of adopting a faster approach to simulate the behavior of the studied configuration. It is useful analyze the length and time scale of the phenomena involved in this study.

4.1 Scale analysis

Two different phenomenological scales can be distinguished in the study of the flow field induced by a VAWT.

4.1.1 Micro-scale

It involves the phenomena occurring in the near-blade zone, thus influencing the aerodynamic forces exerted by the air on the blades themselves. The characteristic dimension related to this scale can be supposed to range from the chord length (e.g. stall vortex shedding) to the boundary layer thickness, which, in attached flow regime and for the usual Reynolds number, is two order of magnitude smaller. So, for a conservative estimation:

$$L_{micro} \sim 10^{-2} c \qquad [4.1]$$

As timescale, we can consider the ratio of L_{micro} and the chordwise velocity experienced by the blade:

$$T_{micro} \sim \frac{L_{micro}}{V_{rel}} \sim \frac{10^{-2}\, c}{\omega\, R} \qquad [4.2]$$

4.1.2 Macro-scale

The far field perceives the turbine as a porous cylinder exerting an aerodynamic thrust and this makes the incoming flow slow down in front of the turbine and, even for moderate thrust values, can induce a vortex shedding. The length and time scale are quite different in this case:

$$L_{macro} \sim D \qquad [4.3]$$

$$T_{macro} \sim \frac{D}{St \cdot V_0} \qquad [4.4]$$

Where D is the machine diameter, V_0 the undisturbed flow velocity and St is the Strouhal number (usually around 0.2 [1]).

According to an order of magnitude point of view, we obtain the following estimations:

$$\frac{L_{micro}}{L_{macro}} = \frac{c}{D} \cdot 10^{-2} = \frac{\pi\sigma}{N} \cdot 10^{-2} \qquad [4.5]$$

Where σ is the turbine solidity and N the number of blades. For the solidity is usually around 0.1 and the blades are 2 or 3, we can state:

$$\frac{L_{micro}}{L_{macro}} \sim 10^{-3} \quad [4.6]$$

Applying the same method to the timescale we get:

$$\frac{T_{micro}}{T_{macro}} = \frac{St \cdot \pi\sigma}{N \cdot TSR} \sim 10^{-2} \quad [4.7]$$

It follows that a great saving of calculation time can be obtained by avoiding the explicit solution of the flow field around the blades. As the complex flow field induced by the diffuser needs for a numerical solution via CFD, the type of model required belong to the category of "hybrid CFD-BEM models". These models calculate by means of more or less sophisticated procedures the aerodynamic forces on the blades that are not solved by the CFD. To account for the blades' influences on the fluid, appropriate sources terms are inserted into the momentum equations. The domain partition in which the sources terms are added is called actuator disk. These models are quite common in the HAWT analysis [2] and a commercial tool for Fluent called "Virtual Blade" is even available [3]. For VAWT the concept of "actuator cylinder" have been introduced [4] (that becomes actuator ring in 2D), but there are only few examples of this approach coupled with CFD [5, 6, 7, 8]. The turbine sub-model can be BEM-derived [5, 6] or can descend from a CFD analysis of straightforward a bare turbine [7, 8]. The modeling of the aerodynamic forces is not trivial for a Darrieus, since the AoA is unsteady, but it provides a deepest insight of the physics underlying a VAWT's operation. Therefore the present model adopts a semi-empirical aerodynamic sub-model for the solution of the turbine's load, whereas the external flow field is solved via CFD.

4.2 Model summary

The basic idea of the hybrid CFD-BEM model is summarized in the following flowchart:

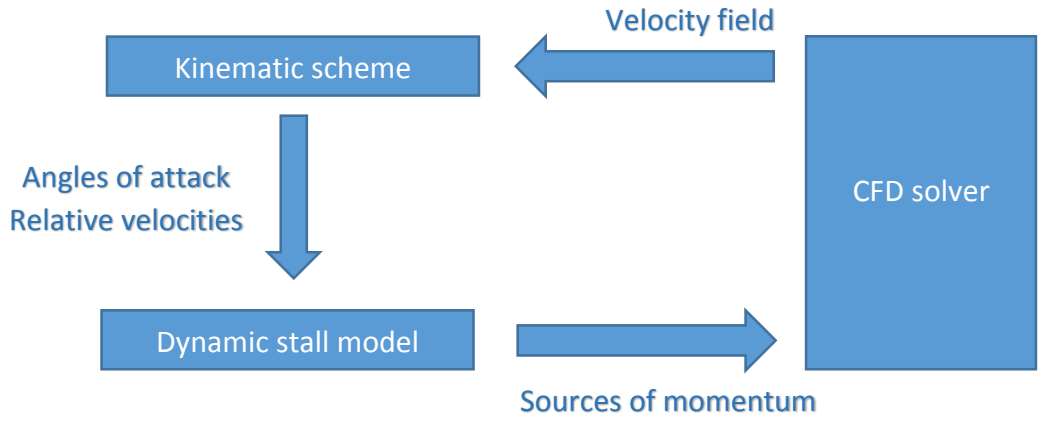

Flow chart 4.1 - Working principle of the hybrid BEM-CFD model

The sources of momentum are applied on a ring in the mesh that replaces the rotor swept area. The strong two-way coupling between blades load and velocity impose an iterative approach as explained in the next paragraphs. The imperfect assembly of the turbine used in the validation phase would have make its modeling very challenging. Therefore a new turbine geometry have been adopted. The following table summarizes the characteristics of the adopted machine.

Turbine model	H-Darrieus, 3 blades
Rotor Radius	1 m
Airfoil	NACA0012 with virtual camber
Chord lenght	0.2 m

Table 4.1 - Characteristics of the new turbine

The virtual camber, as already mentioned, almost eliminates the influence of the circular motion of the airfoil so that they can be treated as a symmetrical airfoil in translational motion, and it is expected to give an overall higher performances [8]. It is shown in fig. 4.1 where and consist of an airfoil whose camber-line fit the trajectory. Introducing only slight modifications, however, a blade without camber correction could have modeled.

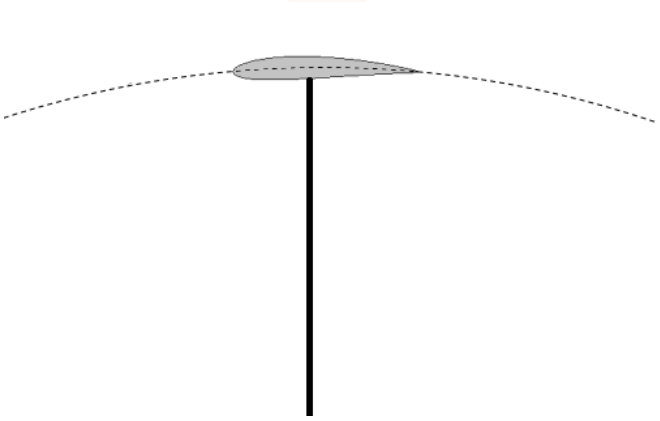

Figure 4.1 - NACA0012 with virtual camber for VAWT

It follows the detailed analysis of the single block from flow chart 4.1.

4.3 Kinematic scheme

Even though the calculation performed for the estimation of the angle of attack, relative velocity and Reynolds number relative to the blades are very simple, the hypothesis underlying this approach are crucial for the formulation of a physically coherent model.

As already mentioned, a well-known method to easily calculate the most important parameters influencing the forces experienced by a blade in a VAWT is to consider it analogous to an airfoil moving in a rectilinear flow field experiencing a velocity equal to the relative velocity resulting from the local absolute velocity and the rotation velocity. This method is widely used in the streamtube models and BEM theory (see par. 1.2). In spite of the straightforwardness of this approach, a main critical issue can be found. In fact, the relative velocity (W) cannot immediately be considered equal to the undisturbed velocity that can be measured in a wind tunnel test (as the adoption of conventional drag and lift coefficient imposes), because the flow field in the case of a VAWT is complicated by the rotational motion and, so, it is not easy to find a location in the domain in which the velocity can be considered "undisturbed". Moreover, what the CFD solves is a time-averaged flow field and not the instantaneous one induced by the blades. Thus, in continuity with the classic and widely validated streamtube approach, the relative velocity for a given azimuthal angle will be taken in the exact point of the blade path corresponding to the given position. This would be incorrect in a stationary flow field, but the fact that a time-averaged velocity is considered, smooth this inconsistency.

The scheme and the analytical expression of the kinematic model are the same already mentioned in par. 1.2 and it is not worth to repeat them. The only differences relies on the two-dimensional approach, so the equation 1.1 and 1.2, in this case, slightly change as follows as consequence of the introduction of the y-velocity (V):

$$W_{\hat{r}} = -U\sin\theta + V\cos\theta \qquad [4.8]$$

$$W_{\hat{t}} = U\cos\theta + \omega R - V\sin\theta \qquad [4.9]$$

4.4 Dynamic stall model

With dynamic stall they usually refer to a complex series of phenomena, occurring around an airfoil located in a stream where the relative angle of attack is non-stationary. In the case of oscillating airfoil, in particular, a hysteresis curve for lift, drag and pitching moment coefficient can be observed. The next original figure, taken from Ref. [9], shows the main feature of unsteady airfoil aerodynamics.

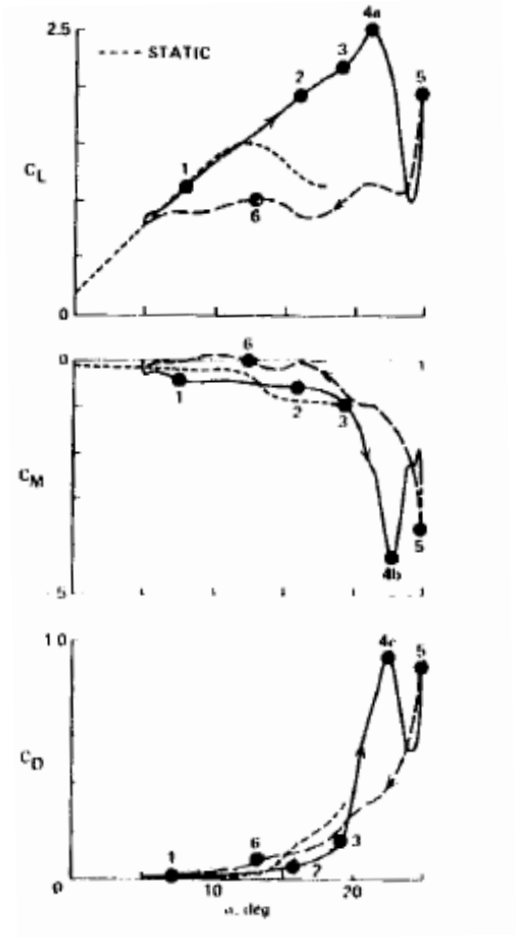

Figure 4.2 - Typical pattern of lift, drag and pitching moment of an oscillating airfoil [9]

The dotted line represents the static curve. The numbers refer to the following events:

Point	Flow condition	Effect
1	Thin attached BL	Static characteristics, with a slightly lower lift
2	Flow reversal within BL	Lift coefficient exceeds static Cl
3	Detaching of the Leading Edge Vortex	Lift continues to grow, negative moment and drag increase
4	Vortex leaves airfoil surface	Lift, drag and moment decay
5	Secondary vortex	Left, drag and moment show a rapid peak
6	Slow reattachement of BL	Return to linear characteristics

Table 4.2 - Events associated with dynamic stall

The main differences between static and dynamic characteristics can be summarized as follows:

1. Retard in the constitution of the circulation necessary for lift in the attached flow condition
2. Added mass effects
3. Delay in BL separation and reattachment
4. Building up and shedding of the Leading Edge Vortex (LEV)
5. Secondary Vortex

With the exception of the pitching moment (which has a slow influence) and the secondary vortex (not relevant) all this phenomena have to be taken into account in the formulation of the dynamic stall model.

There are several factors influencing the dynamic stall behavior [9]:

1. airfoil geometry, which cause the BL separation to occur from leading edge (sharp nose airfoil) or from trailing edge (blunt nose and cambered airfoils), is relevant mainly in a light stall regime
2. the reduce frequency of oscillation ($k = \frac{\Omega c}{2\,W}$), causing severe unsteady effect at high values; in particular, for k >0.05 the LEV becomes evident and for k >0.15 it already reaches the maximum intensity
3. the Reynolds number, affecting even the static behavior and thus the maximum angle before BL separation
4. the amplitude of oscillation, determining a light or deep stall regime
5. the Mach number, because for supersonic flows the shock waves can occur, but for small VAWTs can be neglected

There are different approach to the modeling of dynamic stall. The simplest models try to empirically reproduce the hysteresis cycle of lift (and eventually drag) by means of experiment-based correlations. Many models used for VAWT belong to this category (Gormount [10], Strickland [11], Berg [12]). Higher order model adopt differential equation with unknown coefficients that are tuned on experimental data (e.g. ONERA [13]). The more complete models are named ”indicial” and are strictly related to the physics underlying the dynamic stall, since they try to describe separately all the most important phenomena occurring in the unsteady flow (Beddoes-Leishman [14], Oye [15], Risø [16]).

The adopted model has been inspired by the work by Larsen et al. [17], that can be seen as a simplified version of the more sophisticated Beddoes-Leishman model. In this context, modifications were made to make it suitable for the VAWT analysis, in which drag and high angle of attack effect have to be considered. The model, basically, tries to reproduce the behavior of the attached flow, BL separation/reattachment and LEV dynamics by summing these different contributions in the lift and drag coefficients.

4.4.1 Lift model

The complete expression for lift coefficient is the following:

$$Cl_{tot} = (Cl_0 + Cl_{nc})\, f + Cl_{min}(1 - f) + Cl_v \qquad [4.10]$$

Where:

- Cl_0 is the lift coefficient in attached BL regime (potential flow), affected by delay in the building up of circulation
- Cl_{nc} is the added mass terms, accounting for air inertia
- f is a normalized coefficient interpolating the lift from a maximum value (corresponding to the sum of the two previous ones) to Cl_{min}; it reproduces the effect of the BL progressive detachement
- Cl_v is the contribution to lift caused by the LEV

In the next sections, the expressions used for each terms are explained.

4.4.1.1 Static lift modeling

The static lift data from the ref. [18], providing a great selection of experimental results in a wide range of angles of attack and Reynolds, has been used in this work. A simple double linear interpolation scheme has been adopted for angles and Reynolds values not corresponding to the given ones. The observation of the lift curves has highlighted some common features that have been modeled to improve the accuracy of the procedure by Larsen et al. [17].

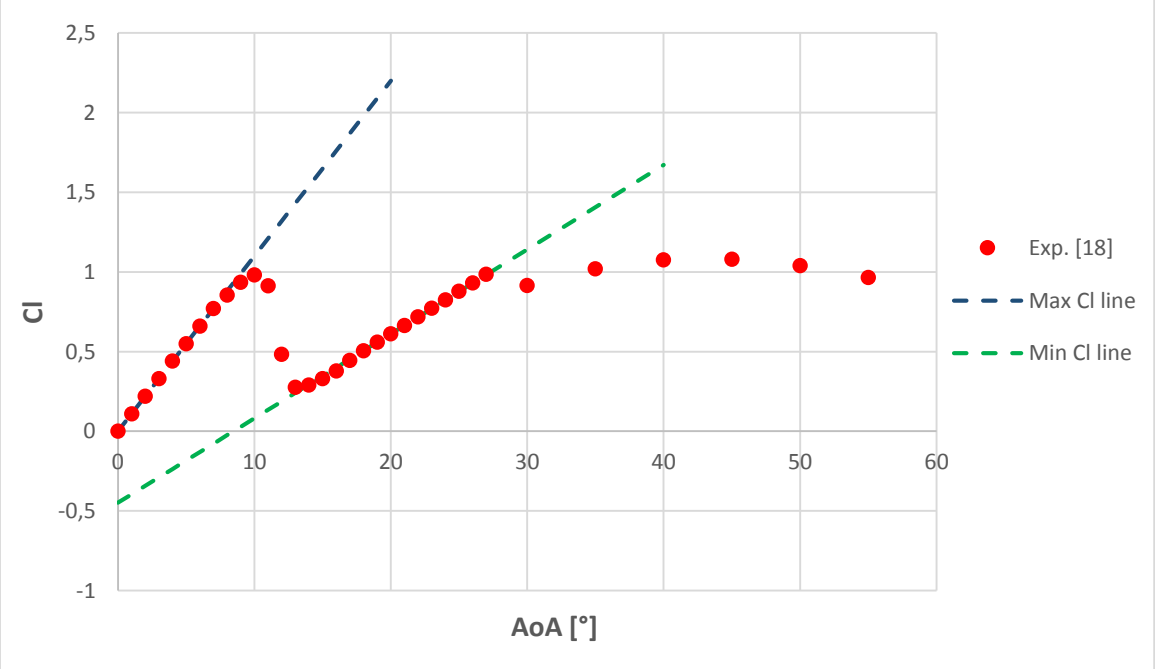

Graph 4.1 - Static lift data, NACA0012, Re =3.6·10^5 [18]

In the previous graph, the static lift experimental data show clearly the aerodynamic regimes experience by the airfoil at different pitches:

1. From 0 to 10 degrees the lift is almost equal to the ideal one ($\sim 0.11\ \alpha$), the BL is therefore attached
2. From 10 to 13 degrees the lift decays because of the stall onset and BL separation
3. From 13 to 27 degrees the lift appears still linear, but greatly reduced, indicating a fully detached flow
4. For very high angles of attack the lift start to diminish, and this is coherent with the fact that for a 90 degrees pitched airfoil only a drag force should appear

This simple analysis has shown important features that will be included with appropriate modification in the dynamic stall modeling.

4.4.1.2 Attached flow lift

In this case a Green-type function is used to model the delay for circulation building up.

$$Cl_0(\mathrm{t}) = \int_0^t \dot{Cl_{max}}(\tau)\ \overbrace{(1 - 0.5\exp((t-\tau)\boldsymbol{\omega_1}))}^{\varphi}\, d\tau \qquad [4.11]$$

Where Cl_{max} is the linear lift according to thin airfoil theory [19] and $\boldsymbol{\omega_1}$ a tuning parameter.

The non-circulatory lift can be approximated by the analytical formula by Theodorsen [20], as suggested:

$$Cl_{nc} = \frac{\pi \dot{\alpha} c}{2W} \qquad [4.12]$$

4.4.1.2 BL separation dynamics

To reproduce the effect of the retard in the destruction and reconstruction of the attached BL, Larsen suggests a simple first order differential equation:

$$\dot{f} = \boldsymbol{\omega_2}(f_s - f) \qquad [4.13]$$

Where f_s is the static value of the coefficient, calculated as:

$$f_s = \frac{Cl - Cl_{min}}{Cl_{max} - Cl_{min}} \qquad [4.14]$$

Where Cl, Cl_{min} and Cl_{max} are taken from linear fitting of the static characteristic as shows graph 4.1.

The tuning constant $\boldsymbol{\omega_2}$ needs in this case a careful analysis. In fact, thanks to the possibility of acceding to the experimental data contained in the study [21], different dynamic behaviors of the BL during a hysteresis cycle have been observed.

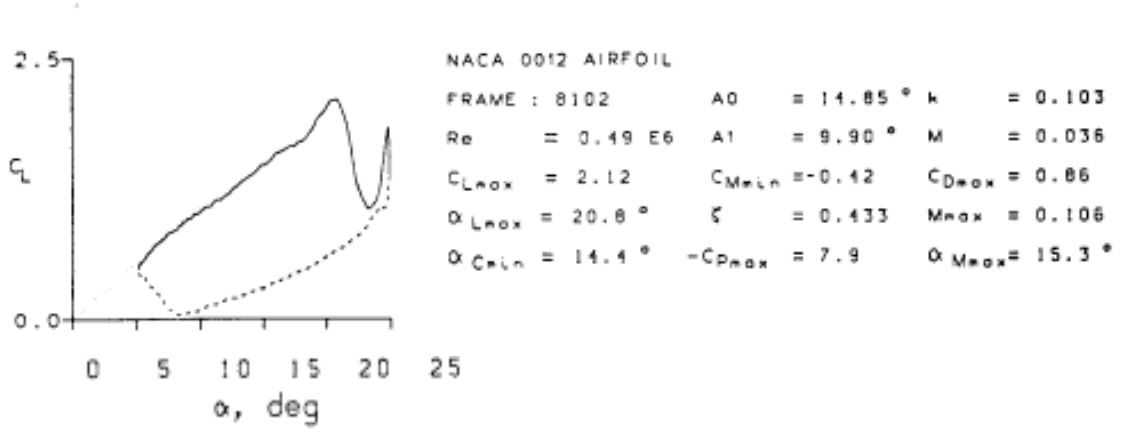

Figure 4.3 - Lift hysteresis cycle for an airfoil in oscillatory motion [21]

Considering the shown experimental results for a given oscillatory motion and stream velocity, it can be seen that from 5 to 17 degree the lift coefficient exhibits a linear characteristic, suggesting an almost attached BL, even exceeding the static maximum lift angle (14 degrees). This indicates a slow BL separation dynamics.

After the downwind convection of the LEV (causing the lift to rise up until 20 degrees), the lift plunges down to his minimum value, and it seems to follow a linear characteristic that can be considered as a fully detached flow lift (the curve is very similar to the one of graph 4.1). So, the flow passes from being almost attached to a fully separation in a short time when the LEV is shed.

The reconstruction of the BL, from 25 to 7 degrees, proceeds slowly.

For small angles, however, the reattachment is faster, so that from 7 to 5 degrees the flow returns to his initial state.

This hypothesis have been confirmed by the pressure coefficient's history.

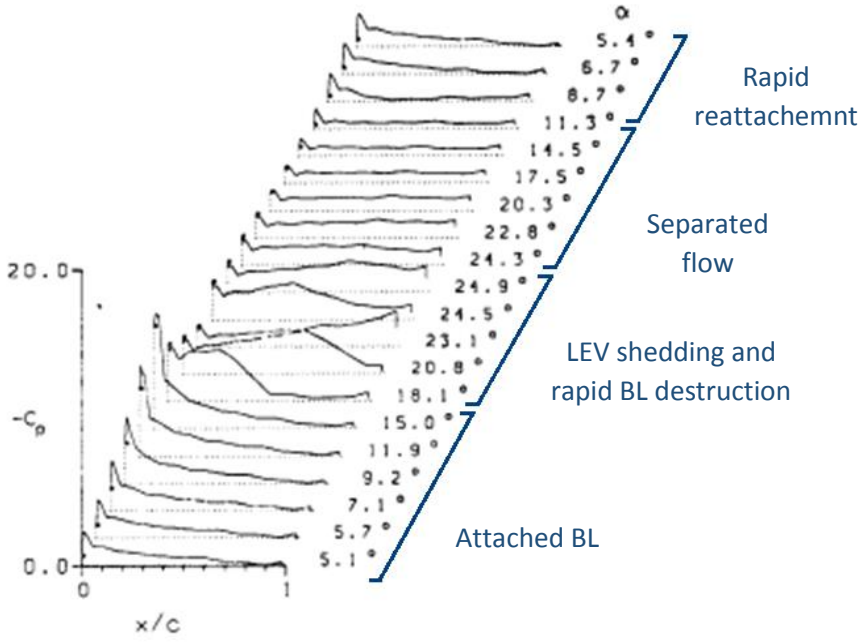

Figure 4.4 - History of pressure coefficient on the suction edge of the airfoil of figure 4.2 [21]

This analysis has suggested the adoption of two different time constant, one for the slow BL attachment/detachment regime ($\omega_{2,slow}$), and another one for the fast dynamics ($\omega_{2,fast}$).

4.4.1.3 LEV dynamics

The experimental tests indicate that at least two phase can be distinguished in the LEV history:

1. When the LEV is placed on the airfoil and keeps on building up lift
2. When the LEV is shed far downstream and cause a deep lift decay

Larsen et al.[17] model this different situation as follows

$$\begin{cases} \dot{Cl_v} = \boldsymbol{\omega_3} \overbrace{(Cl_0 + Cl_{nc} - ((Cl_0 + Cl_{nc})f + (1-f)Cl_{min})}^{\Delta Cl} - Cl_v) & if\ LEV\ is\ on\ the\ profile \\ \dot{Cl_v} = \boldsymbol{-\omega_3} Cl_v & if\ LEV\ has\ been\ shed\ away \end{cases} \quad [4.15]$$

Where is evident that the LEV induced lift tends to reduce the deficit of lift due to BL separation (ΔCl), thus restoring a linear characteristic.

The choice of the instant in which simulating the LEV detachment from leading edge is crucial, for it influences the lift peak value. So, a robust experimental-based approach as adopted, in contrast with fixed shedding angle chosen by Larsen et al.[17].

Thanks to the great number of wind tunnel data available and the particular weak "concavity" that the lift curves exhibit when LEV starts to travel, referring from 10 different experimental cases a linear dependence from Reynolds number and reduced frequency of the LEV detachment angle α_{LEV} has been extrapolated.

After that, again according to the reference model, it has been imposed:

$$\begin{cases} \dot{x}_{LEV} = \frac{V}{3} \ se\ \alpha > \alpha_{LEV} \\ \dot{x}_{LEV} = 0\ otherwhise \end{cases} \quad [4.16]$$

Where x_{LEV} is the LEV position un the airfoil (0 at the leading edge and 1 at the trailing edge). In this way the instantaneous position of the LEV on the profile can be simulated and this makes easy to switch between the two equations 4.15 when x_{LEV} becomes 1.

4.4.2 Drag modeling

The drag modeling is not present in the original model, but it has been easily formulated starting from the previous definition of BL separation grade and LEV dynamics. It is:

$$Cd_{tot} = Cd_{max}\,(1-f) + Cd_{min}\,f + Cl_v \tan(\alpha) \quad [4.17]$$

The Cd_{max} and Cd_{min} have been once again obtained respectively, from a linear and quadratic fitting of the static values.

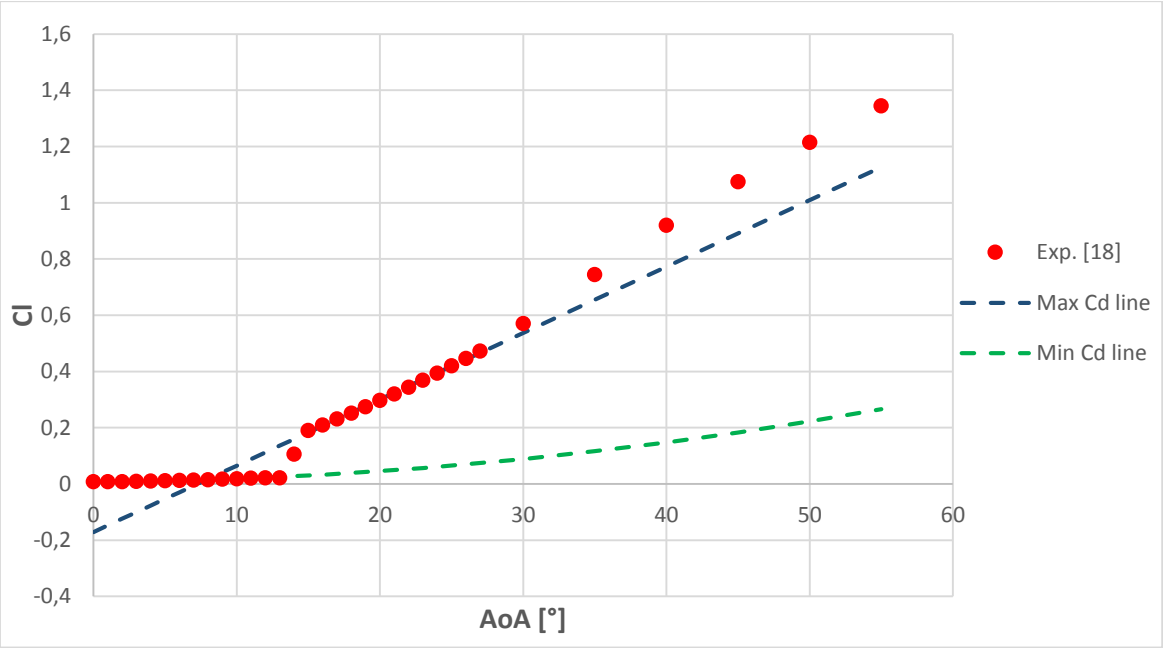

Graph 4.2 - Static drag data, NACA0012, Re = 3.6 ·10^5 [18]

Also in the case of drag, the four regimes shown for the lift curve can be observed.

The f value is the same of the one used previously for the lift modeling, so the Cl_v. The tangent term has been introduced in analogy with the well-known flat plate approximation [22]

4.4.3 Tuning and validation

To set the three tuning parameter introduced, the lift previously reported in figure 4.3 has been qualitatively reproduced. The next plot shows the result.

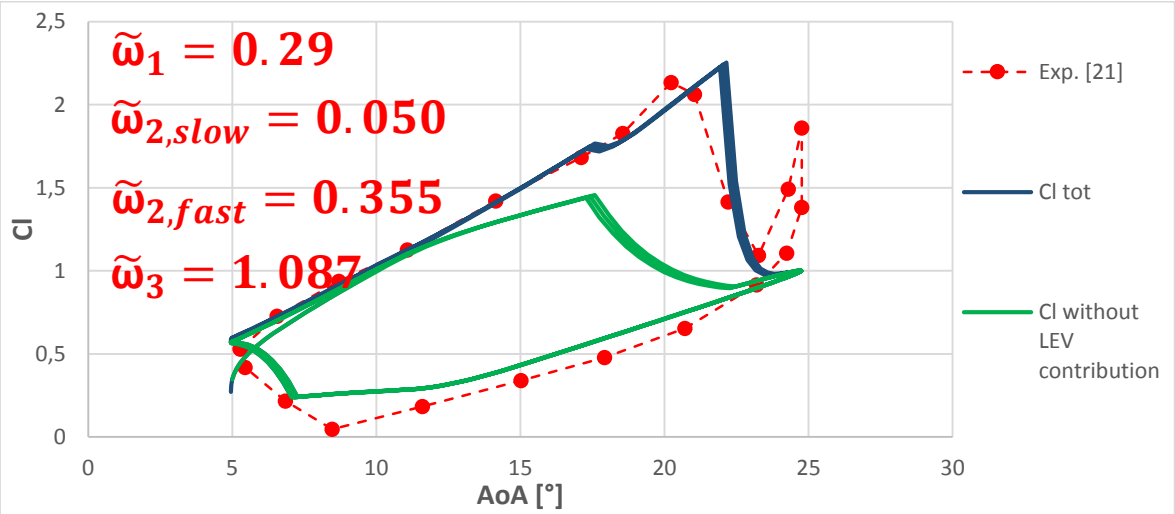

Graph 4.3- Oscillating NACA0012, M = 0.035, k = 0.103, Re = 4.9 ·10^5 : lift hysteresis cycle [21] used for the tuning

The reported time constant are in their non-dimensional form $\tilde{\omega}_i$, thus multiplied by the airfoil characteristic time $\frac{c}{2W}$, to grant them a more general applicability. There is a good

agreement, as it could be easily predicted. The linear attached and detached flow lines taken from the static experimental data seem to fit good the dynamic one. In the next page is provided a set of eight experiments (including the one used for the tuning) showing the accuracy of the proposed model. It is important to emphasize the great physical sensitivity of the dynamic stall, which cause the lift curve to be completely different from case to another. In particular, the LEV shedding can be considered as a catastrophic and discrete phenomenon and greatly influences the results, so it must be included even in a simplified analysis.

Concerning the drag, the results are also encouraging, and the fact that the drag model has been derived by the lift's one, confirms the validity of the overall approach.

The differences between the model and the experiments seem to be unavoidable, and would need a more accurate experiment-based model.

4.4.4 Differences and innovations of the present model

The main innovative feature of the presented approach, respect with the Larsen et al.[17] model are:

- The introduction of the linear characteristic for minimum lift extrapolated from static data, instead of the simplified form chosen by Larsen et al. where it was simply a quarter of the maximum lift
- The straightforward linear coefficient f (as the Risø model[16]), instead of the cosinus function based on polar coordinates
- The introduction of two different time constants for BL reparation
- The whole drag modeling

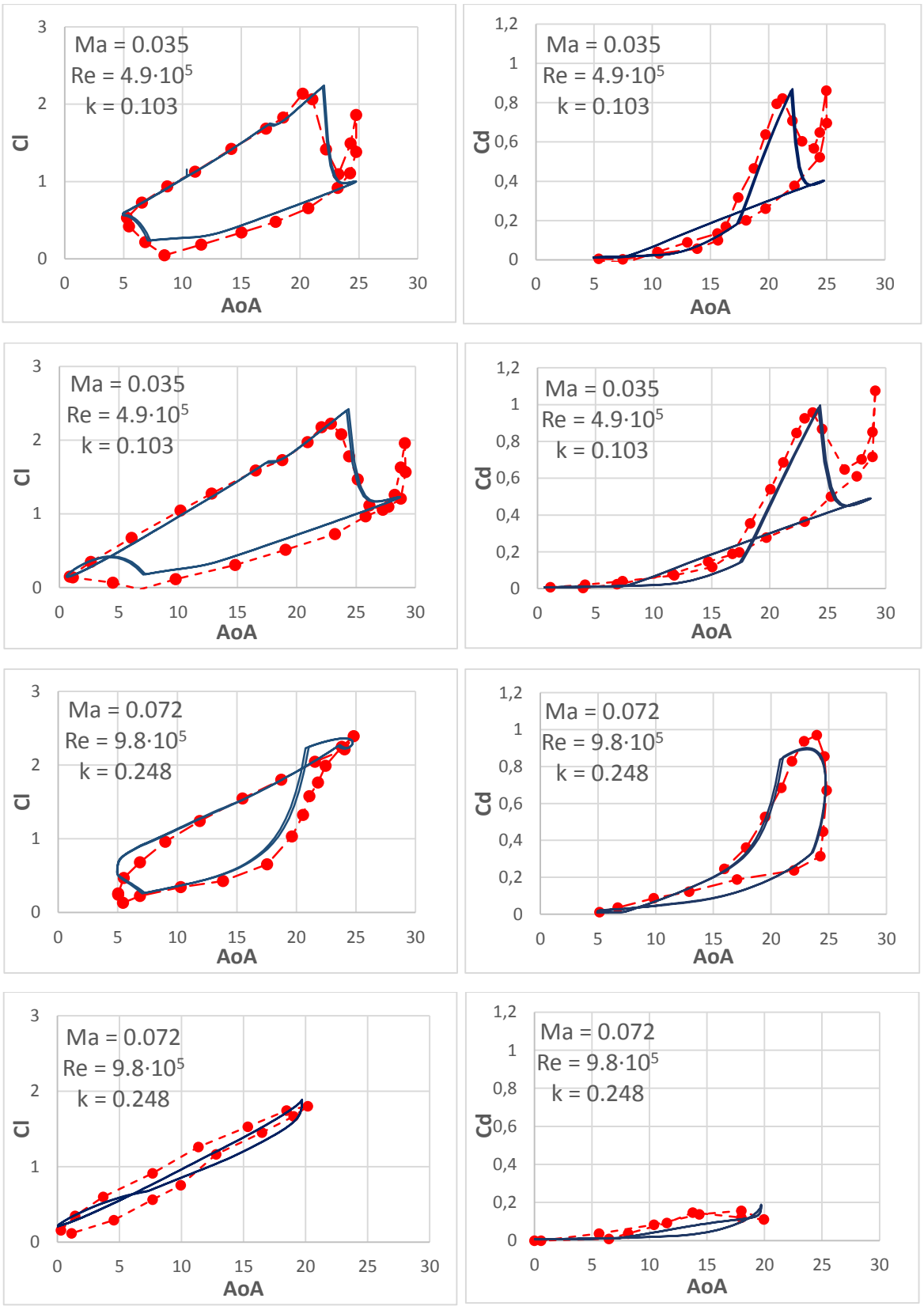

Graph 4.4 - Comparison between the result of proposed model (blue) and experimental data [21] (red)

4.5 Programming notes

The above model has been fully implemented into an Excel VBA macro at first, and , after the validation, a Fluent User Defined Function has been written in C++ language (see Appendix 2). All the differential equations have been solved with a first order Euler time discretization. The full codes (which are almost equivalent) are reported in Appendix 2.

The convergence between the AR and the CFD can be achieved through three methods:

- steady iterative: the CFD are steady: at the end of each simulations the new flow field is passed to the AR that calculates new forces that are sent to the CFD to perform a new simulation, until a convergence criterion is met. This procedure applies to case with negligible transient phenomena in the whole domain (i.e. moderately loaded bare turbine)
- transient iterative: the CFD simulation are transient; the forces in the actuator ring are upgraded periodically (the time interval is arbitrary) and the convergence is met when the velocity in the actuator ring exhibit negligible fluctuations. This procedure applies to situations where the transient phenomena are not negligible, but the solution in the rotor zone is roughly steady (i.e. vortex shedding in the far wake)
- pure transient: in this case the force are recomputed by AR every timestep, thus reproducing the behavior of a real turbine. The convergent solution will be periodic. This method is a forced choice when the fluctuation in the flow field affect also the rotor zone (i.e. strong vortex shedding attached to diffuser exit).

4.6 Bare turbine: CFD vs. AR

As preliminary validation of the AR, the just introduced turbine have been simulated by means of both models. The wind speed has been chosen according to a typical value for rated wind speed in analogous applications[23].

4.6.1 CFD

The domain dimensions, solver and mesh settings are the same obtained in the last phase of the validation (par. 2.11). The mesh characteristics are presented below.

Software	ICEM CFD
Element type	QUAD dominant unstructured + prismatic layers
Max near wall cell length	0.00106 m
Number of prismatic layers (PL)	25
PL growth factor	1.13
First PL thickness	3e-05 m (y^+<5)
Cell dimension along the sliding interface	0.017 m
Rotating domain diameter	1.5 D
Number of cells in the rotating domain	154000
Number of cells of the outer domain	95000
Minimum orthogonal quality	0.3

Table 4.3 - Mesh setup for the new turbine

4.6.2 AR

For this easy configuration, the shedding was so weak that the adoption of the steady iterative algorithm was successful. An under-relaxation factor of 0.3 on the source terms was necessary to prevent divergence. The iterative procedure was considered concluded when the mean squared error of the torque coefficients between two consecutive iteration without under relaxation where less than 5% of the mean torque. It is easy to demonstrate that this criterion imposes also a 5% difference between the so calculated Cp, but is more severe concerning the curve shape. For the sake of clarity, a typical torque and Cp evolution during the process have been reported.

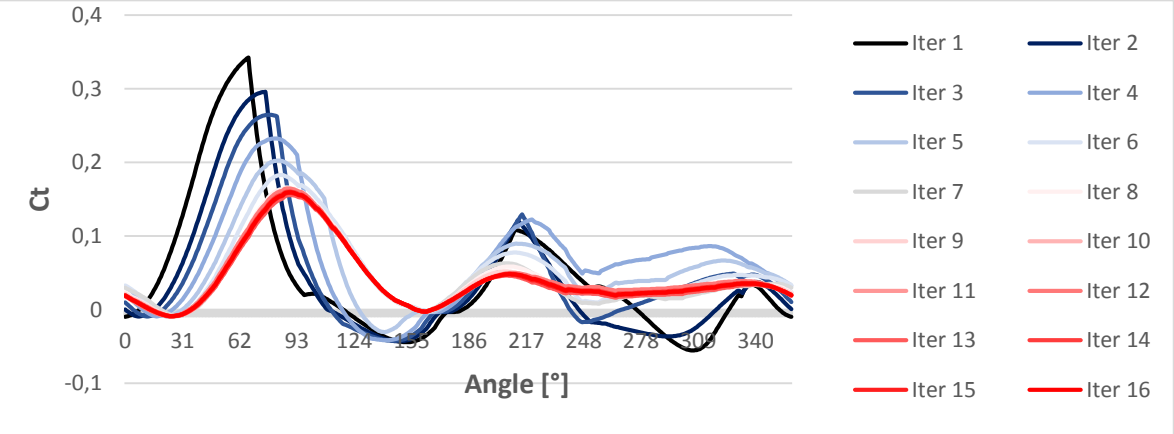

Graph 4.5 - TSR 2.7: Ct evolution during the iterative procedure

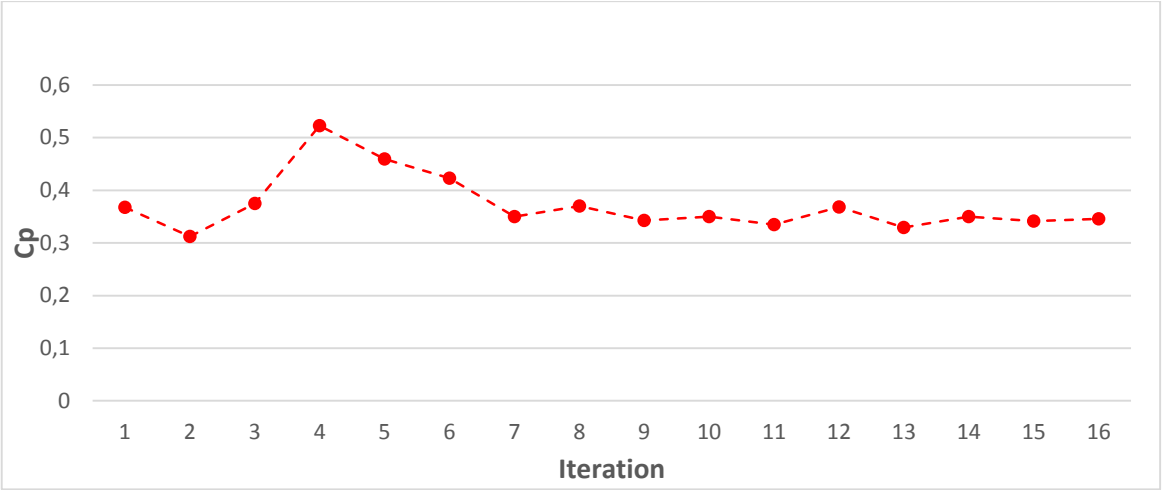

Graph 4.6 - TSR 2.7: Cp evolution during the iterative procedure

4.6.2.1 Mesh

Since the main aim of this part was to validate the model for the simplest case of a bare turbine, it has been considered not worth to carry a wide sensitivity analysis of the mesh. However a finer mesh was tested and proofed that the first attempt discretization was far enough accurate. A complete sensitivity analysis is provided in par 4.7.2 for the case of the shrouded turbine, confirming that for this case the mesh insensitiveness can be reached even with a coarser mesh.

The domain dimensions are the same of the ones adopted for the previous CFD. The final mesh (see fig. 4.5) was made up of 40000 (vs. the 250000 of the CFD) quadratic and triangular element. Figure 4.6 shows the detail of the source area, in which a very regular mesh was adopted by means of 160 quadratic cells. The source area consist of an annular ring with inner diameter 0.95 D and outer diameter 1.05D.

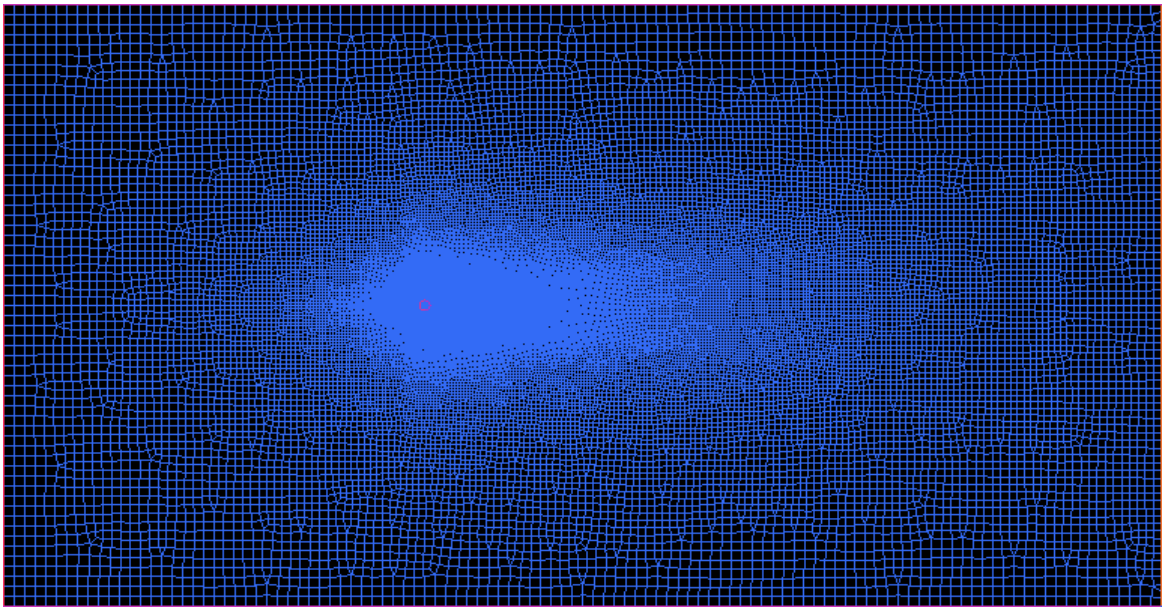

Figure 4.5 - Mesh for the AR model

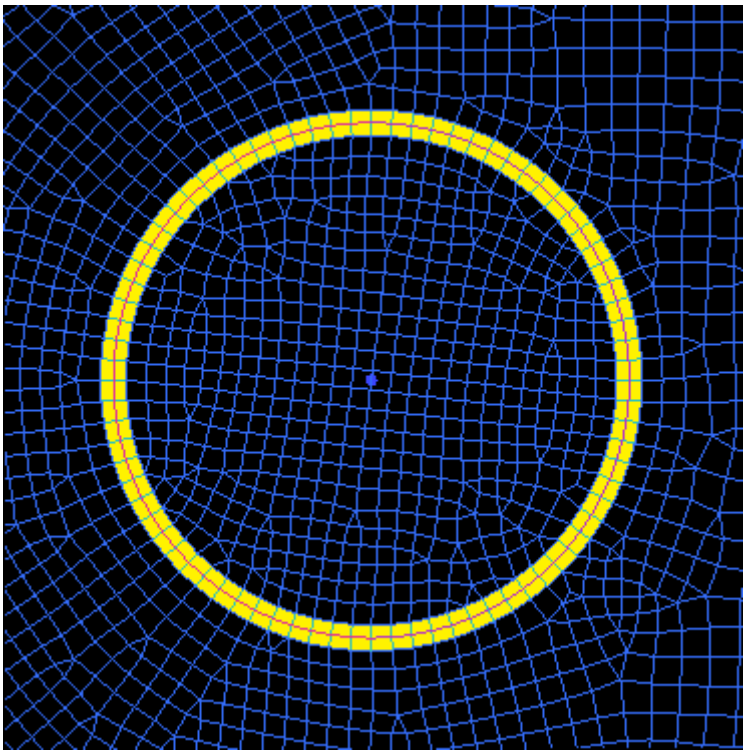

Figure 4.6 - Mesh near the actuator ring

4.6.2.2 Solver setup

To achieve a fast and robust convergence straightforward settings have been adopted.

Simulation type	Steady
Solver	Pressure Based
Turbulence model	k-ω SST
Fluid	Incompressible air
Space discretization scheme	I order upwind
Gradient scheme	Minimum squares
Pressure velocity coupling	Simple
Pressure algorithm	Second order
Numeric residuals	1.00e-04

Table 4.5 - Solver setup for AR

4.6.3 Results

4.6.3.1 Low TSR

For low TSR the blades experience a deep stall regime. The consequent decay of the lift greatly reduces the trust exerted by the turbine and high velocity can be observed across the rotor. Fig. 4.7 shows the velocity contours for the full CFD and the AR. Even though the blades rotation in the full CFD case makes the flow field unstedy, the velocity pattern around the turbine is almost steady.

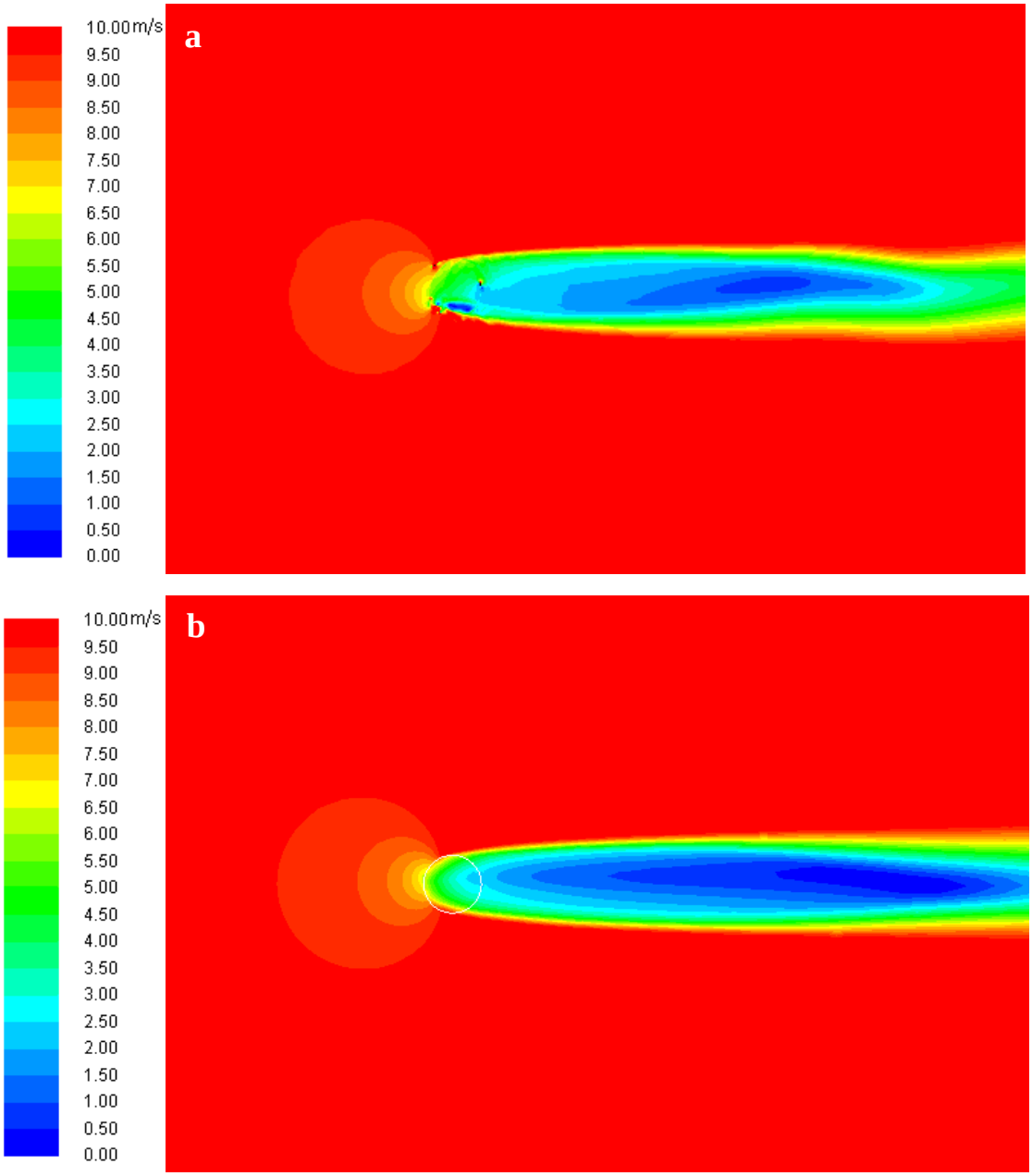

Figure 4.7 - TSR 2.3: contours of velocity magnitude: **a**-CFD, **b**-AR

The following graph compares the torque coefficient evolutions for a single blade over a revolution for the two models. The CFD curve is instantaneous because for a bare turbine his pattern does not change appreciably when the solution is converged. A satisfactory agreement was found. Obviously, for the AR is steady model, it cannot capture the irregular pattern due to the vortex caused by the stall. The Cp are quite similar with a relative

difference of about 2% (0.259 for the CFD vs 0.254 for the BEM). This comparison confirms the validity of the proposed dynamic stall model that successfully simulates the effect of the lift fall in the upwind half.

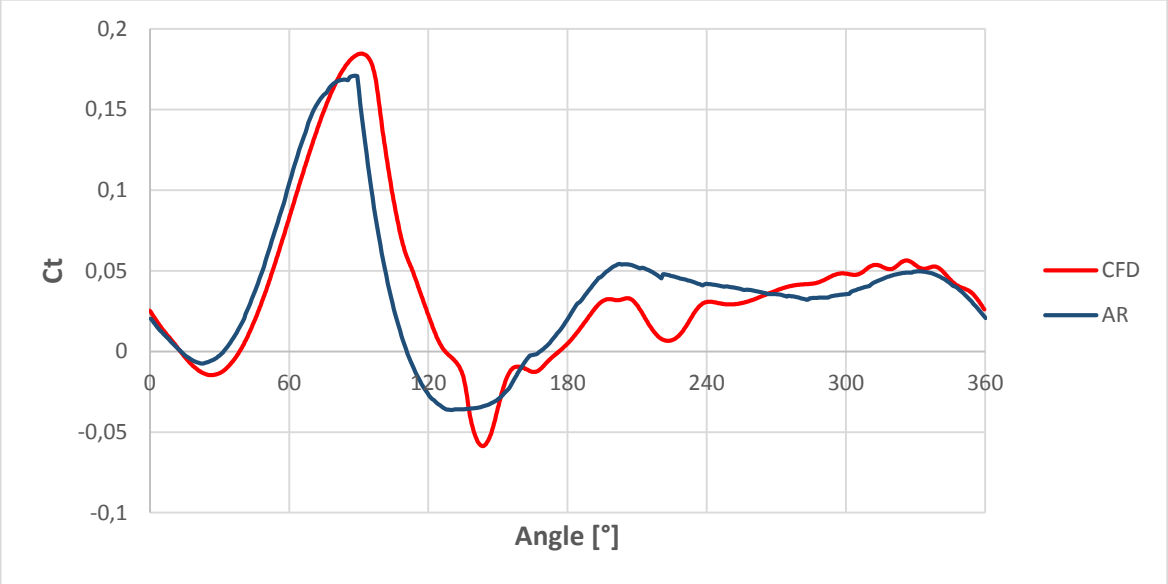

Graph 4.7 - TSR 2.3: Ct curves from CFD and AR

4.6.3.2 High TSR

When the TSR is high, the turbine exerts a high blockage on the incoming flow, this resulting in a deeper wake. The angles of attack remain under the dynamic stall threshold and the torque have a more regular pattern. This feature can be easily found in the contours of both CFD and AR.

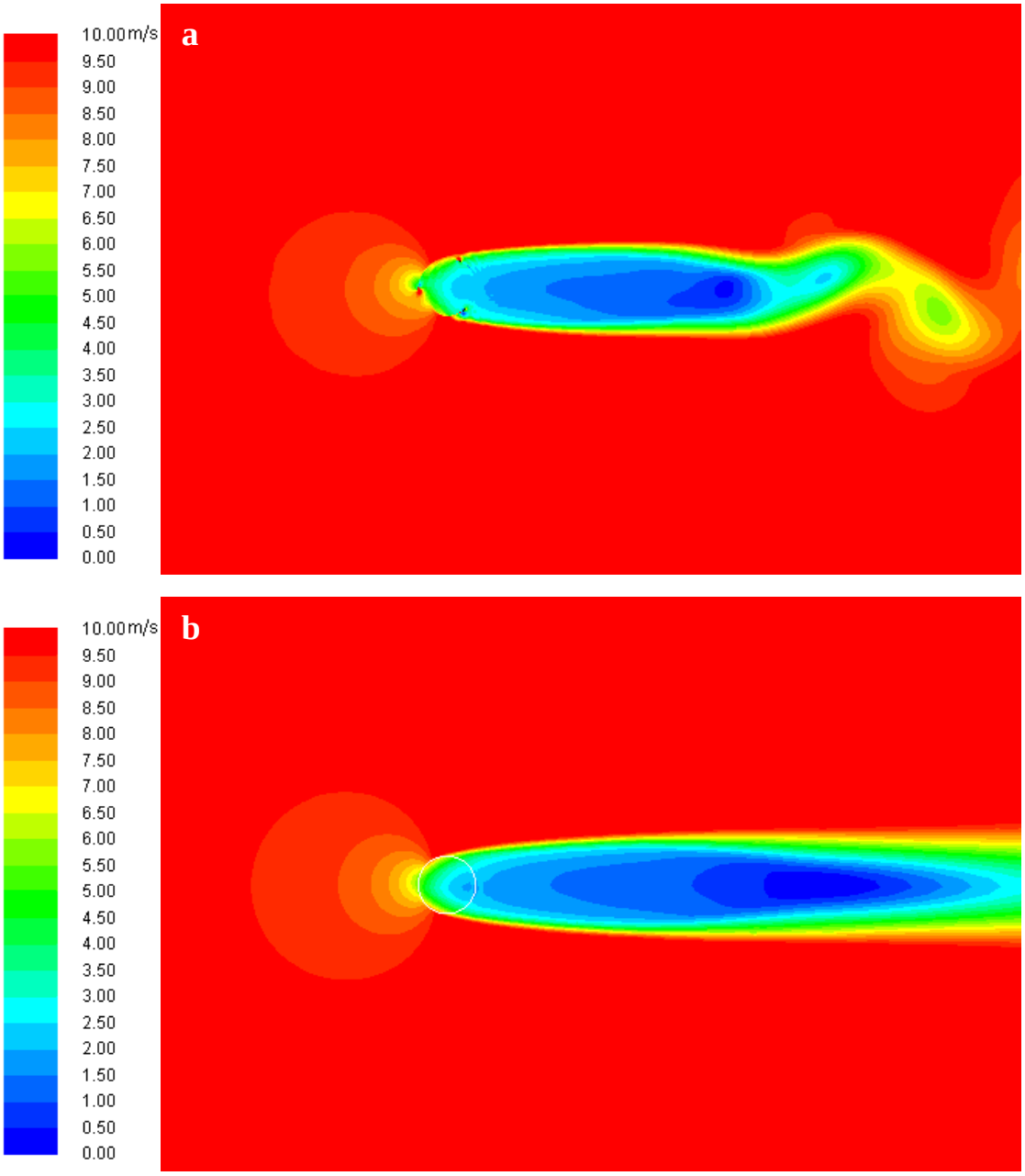

Figure 4.8 - TSR 3.1, contours of velocity magnitude: **a**-CFD, **b**-AR

The most evident difference is the absence of the vortex shedding because of the steady iterative approach adopted.

The torque graph 4.8 shows a slight difference in the peak value and in the first part of the downwind path. This last disagreement can be ascribed to an overestimation of the non-circulatory lift contribution made by the dynamic stall model (the blades experience a rapid

change of the angle of attack in this region). The difference in the peak value has not such a straightforward explanation and can be considered an unavoidable consequence of the steady modeling adopted for the aerodynamic forces. Many other factors can however be involved, such as the dynamic stall model or the incomplete convergence of the CFD (it is useful to remind that for high TSR the torque experience a slow downward trend). Nevertheless, in spite of the complete different approaches, the two model show also in this case a satisfactory agreement with a 2% difference in the CP value (0.309 for CFD vs 0.316 for AR). However, beyond a shadow of doubt, the torque curve comparison is the most robust way to evaluate the effective agreement between the two models, for the Cp is an averaged value that does not consider the effective evolution of the torque during a revolution.

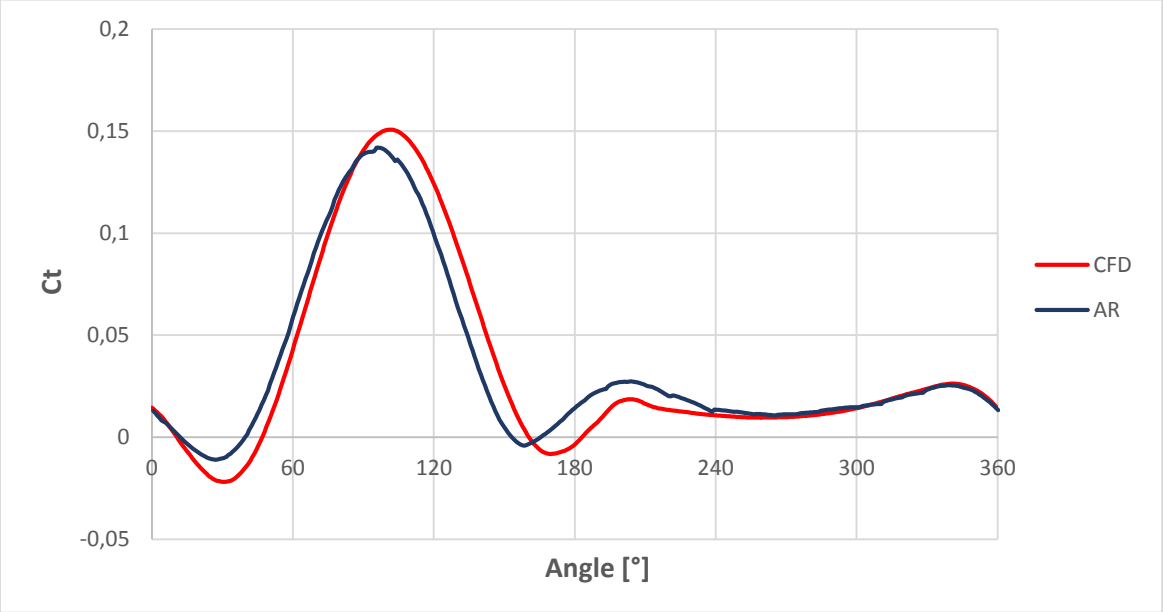

Graph 4.8 - TSR 3.1: Ct curves from CFD and AR

4.6.3.3 Maximum Cp TSR

Analogous considerations holds for this case.

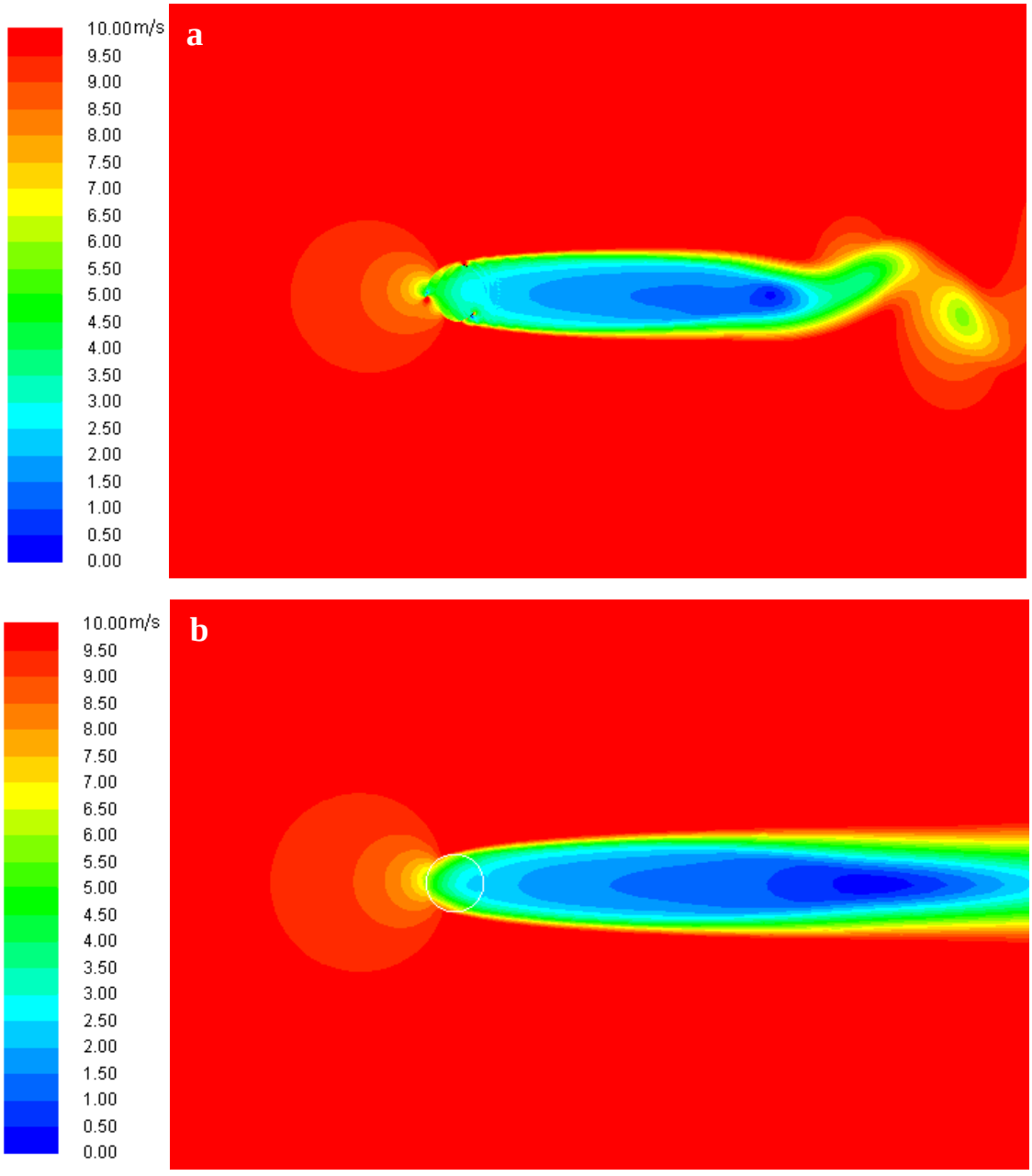

Figure 4.9 - TSR 2.7, contours of velocity magnitude: **a**-CFD, **b**-AR

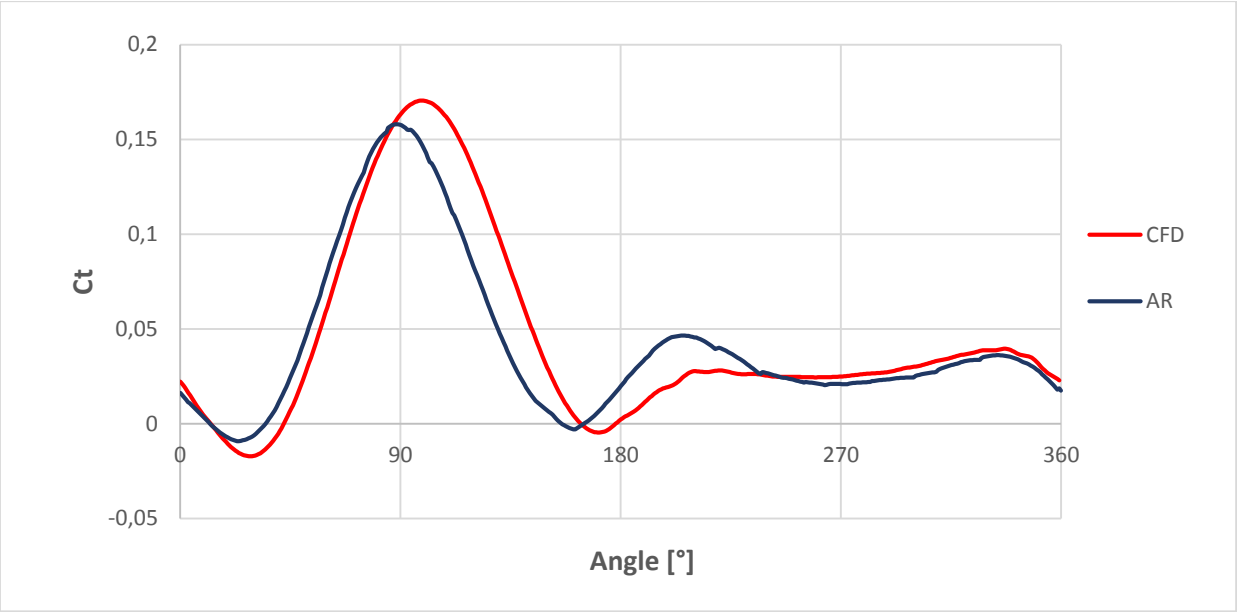

Graph 4.9 - TSR 3.1: Ct curves from CFD and AR

The error on the Cp is almost 5% (0.363 for CFD vs 0.343 for AR).

4.6.3.4 Overall trend

Since the AR model was created to perform a fast optimization of a diffuser geometry, it was very important to test its capability to capture the main changes occurring in the torque curve shape under different operative condition. The graphs below show the torque curve evolution for different TSR values.

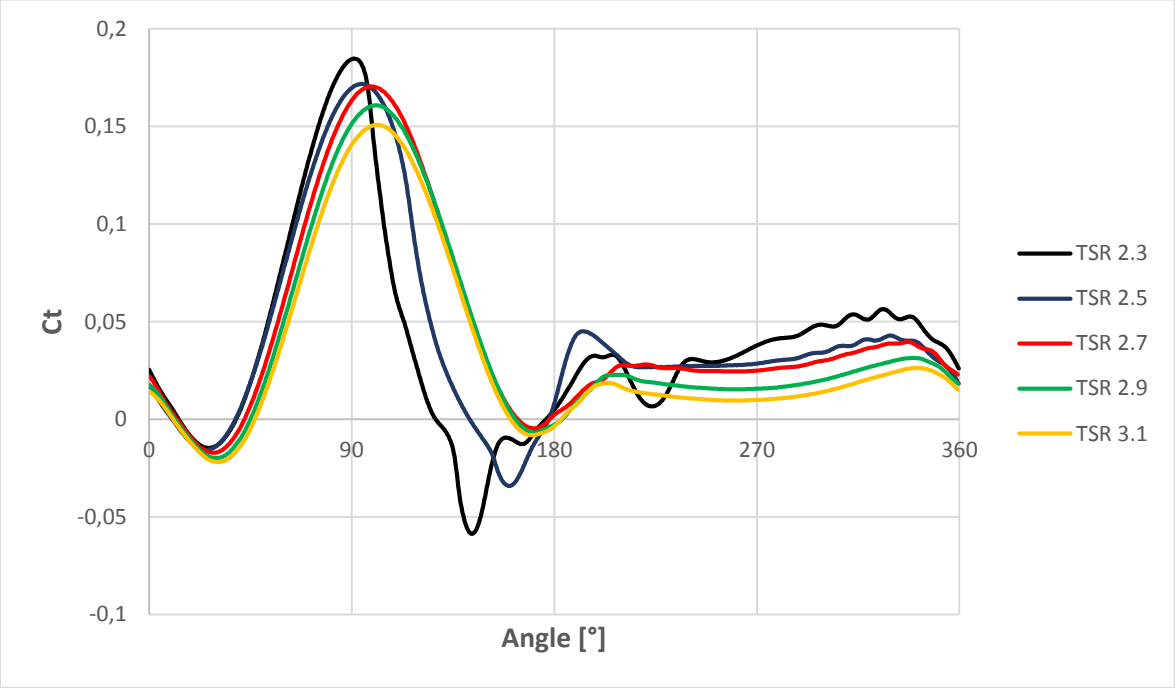

Graph 4.10 - Overall trend of the Ct curves from CFD

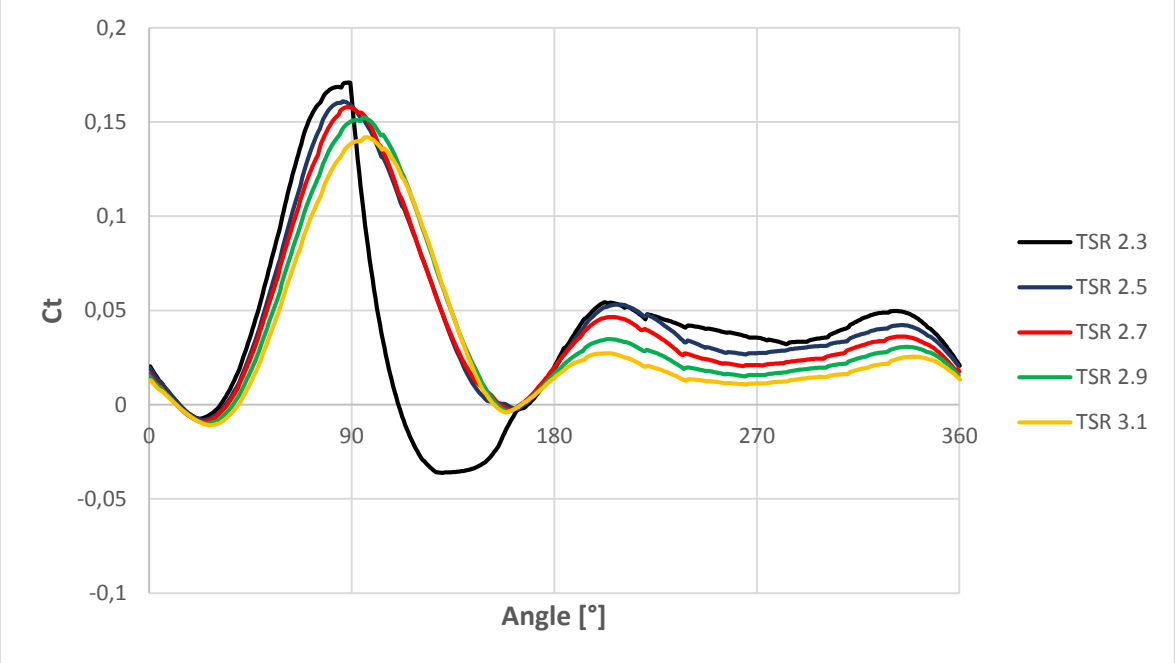

Graph 4.11 - Overall trend of the Ct curves from AR

The AR was able to reproduce the torque reduction and the slight rightward shift with the increasing TSR and the fall at low TSR. It only failed in the 2.5 TSR case, where just in the

last iterations the BL underwent a reattachment. So, this particular condition, where the maximum angle of attack becomes very near to the LEV shedding angle, represents a very sensitive case. However, a correction in the model was not introduced (although a simple blending or smoothing formulation would have worked) for the following reasons:

1. Beyond this numerical sensitiveness, there is a physical sensitiveness, as the experimental data on dynamic stall and the CFD simulations showed. A sort of threshold TSR under which the BL abruptly separates really exist
2. This is not an optimal operation point
3. A "backward" correction of the model based on the CFD results could have partially vitiate the experimental validation previously exposed and would have weakened the confront

To sum up the AR and the CFD predict the BL separation at a slightly different threshold TSR (2.5 for CFD and 2.45 for AR) as the graphs 4.12 and 4.13 show.

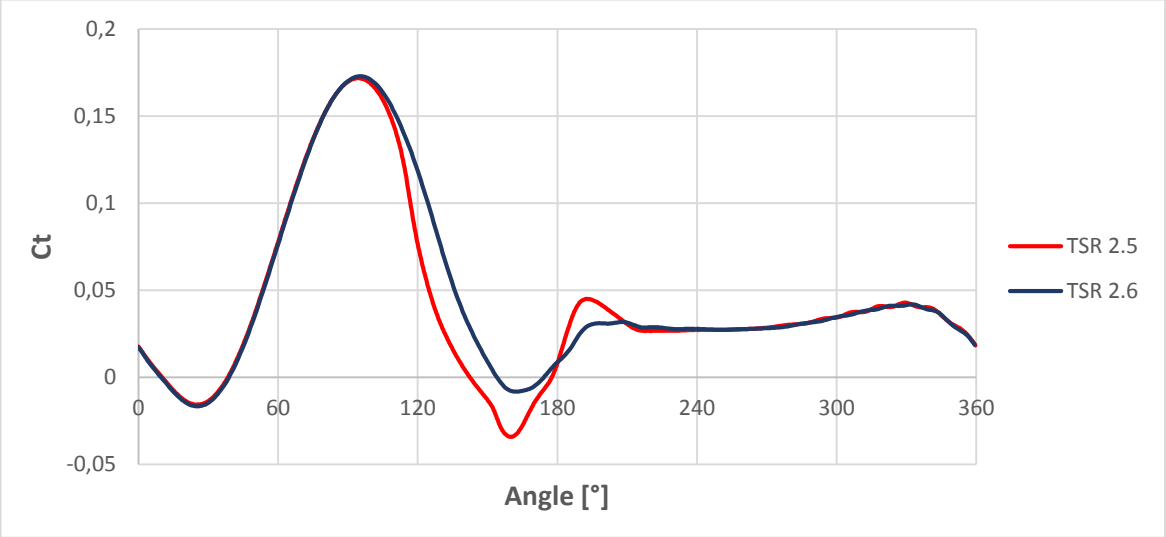

Graph 4.12 - Ct curve near the critical TSR from CFD

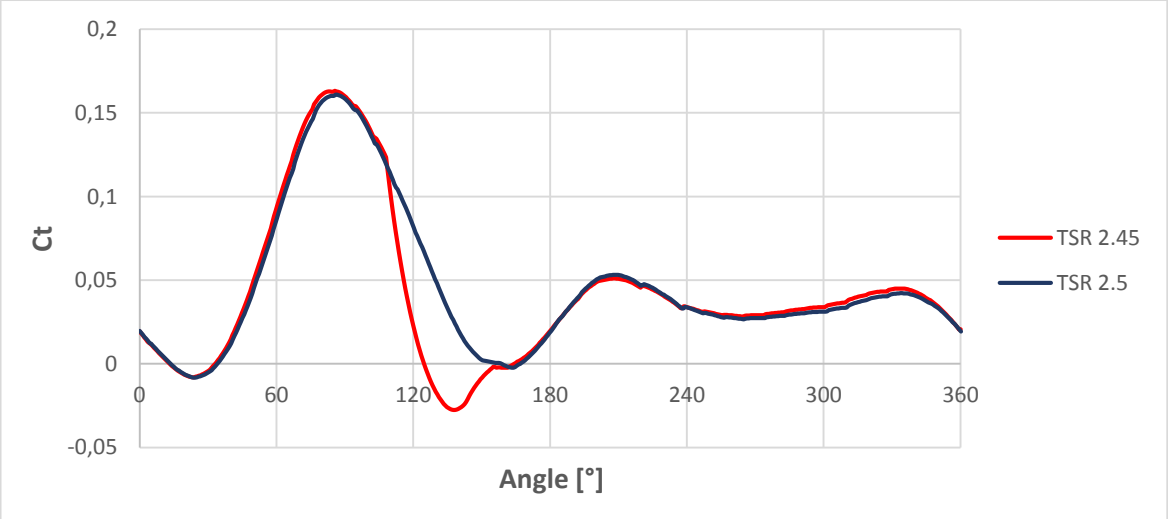

Graph 4.13 - Ct curve near the critical TSR from AR

4.6.3.5 Cp/TSR curve

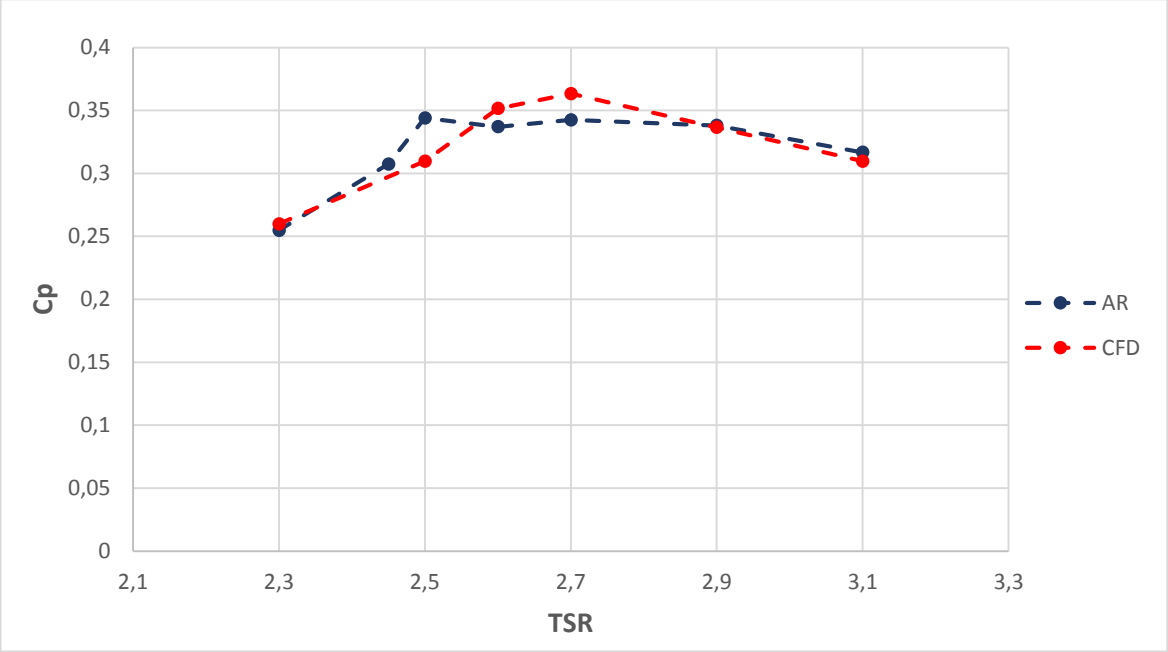

Graph 4.14 - Cp/TSR curves from CFD and AR

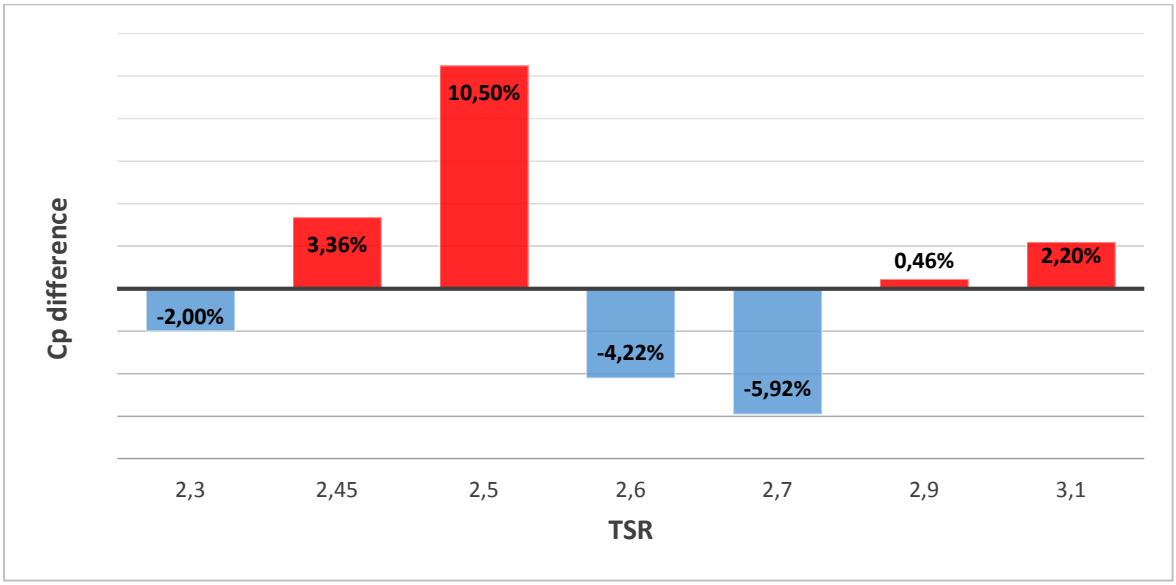

Graph 4.15 - Relative difference in Cp prediction of AR in respect to CFD

A satisfactory overall agreement can be observed. The small differences were an order of magnitude than the expected Cp increase due to the diffuser (~100%) and this encouraged to carry on a validation on the more complex case of shrouded turbine.

4.6.4 Sensitivity analysis

The sensitivity for the case of TSR 2.7 have been against various parameters.

4.6.4.1 Number of sources

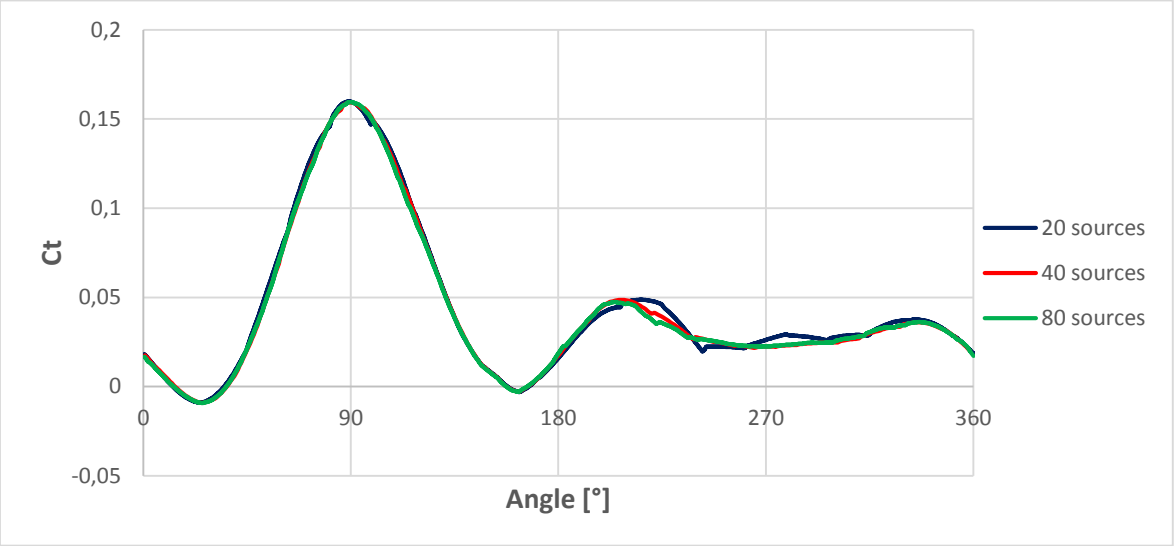

Graph 4.16 - Ct curves for different discretization of the actuator ring

The results have a very weak sensitivity to the number of source. A reasonable number of 40 sources per actuator ring has been adopted throughout the following simulations.

4.6.4.2 Mesh

A finer mesh made up of about 80000 cells was tested with the AR model and gave almost identical pattern, thus confirming the relatively coarse space discretization that the simplified domain requests. This early results suggested that a very time-sparing mesh could be used with AR.

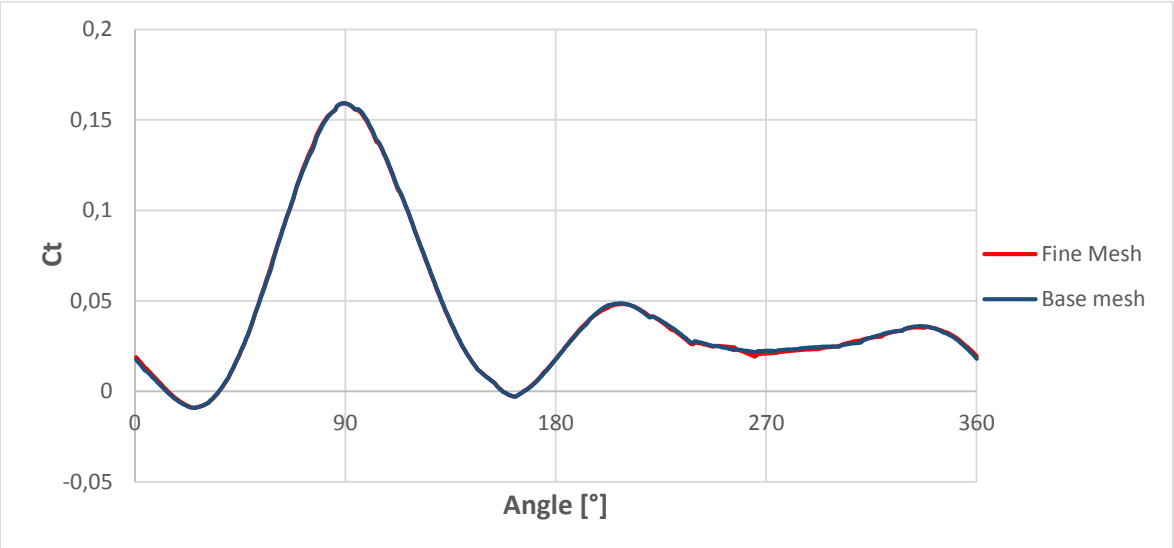

Graph 4.17 - Ct curves for meshes of the actuator ring

4.6.4.3 Timestep of the dynamic stall model

The solution becomes insensitive to the timestep adopted by the AR ring model for the calculation of the source terms when it approaches 0.001s. A cautious value of 0.0005s has been adopted, since for the diffuser augmented turbines a higher TSR and thus a smaller time per revolution should be expected.

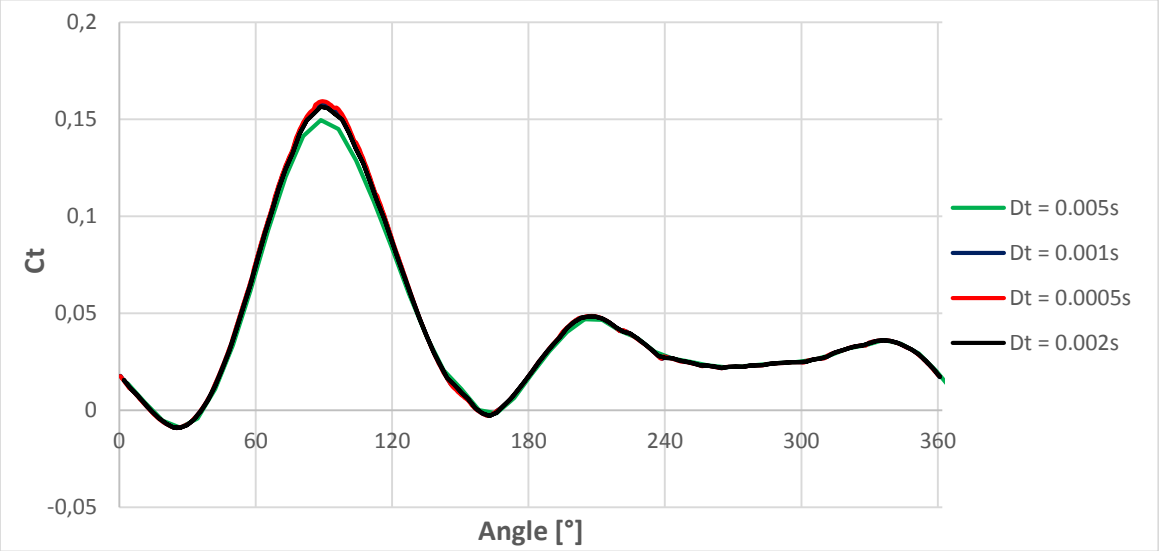

Graph 4.18 - Ct curves for different timesteps in dynamic stall model

4.6.4.4 Thickness of the actuator ring

Three different rings were adopted and tested for the case of 2.7 TSR. A far negligible difference was observed in the torque curve, thus proofing the insensitiveness of the results to this parameter.

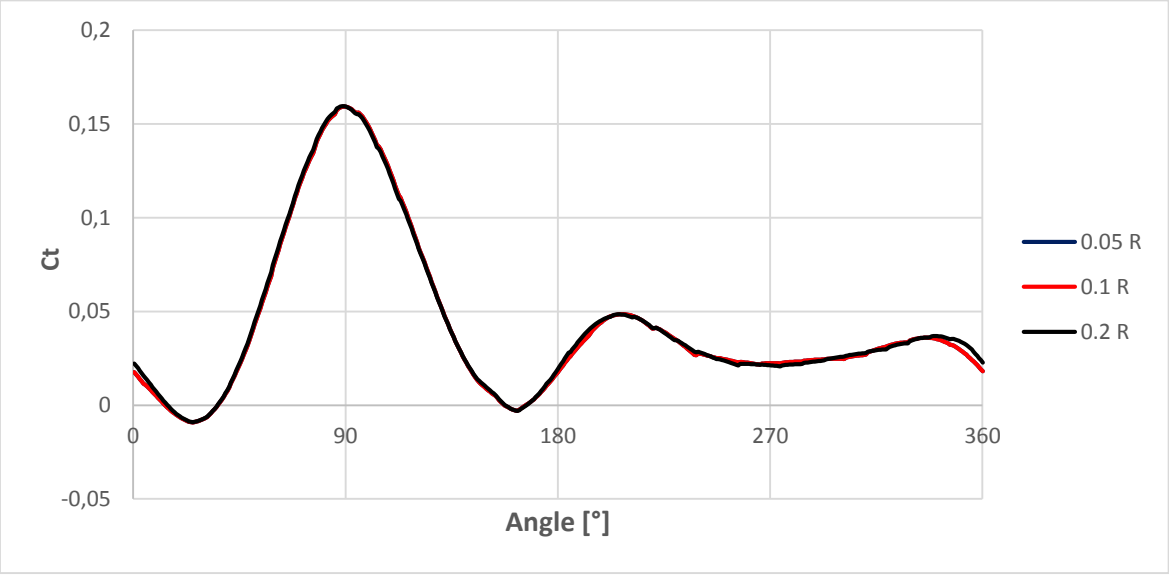

Graph 4.19 - Ct curves for different thickness of the actuator ring

4.7 Diffuser augmented turbine: CFD vs. AR

In order to validate the AR for the case of the shrouded turbine a diffuser with null angle of attack was placed around the machine and its flow filed simulated on both CFD and AR models. The diffuser geometry was inspired by considerations made in par. 3.2 deriving from the lumped-parameter aerodynamic study. In order to get a strong circulation, the high-lift Selig 1223 [24] airfoil (graph 4.20) has been adopted. This section has a very high lift coefficient even at moderate Reynolds.

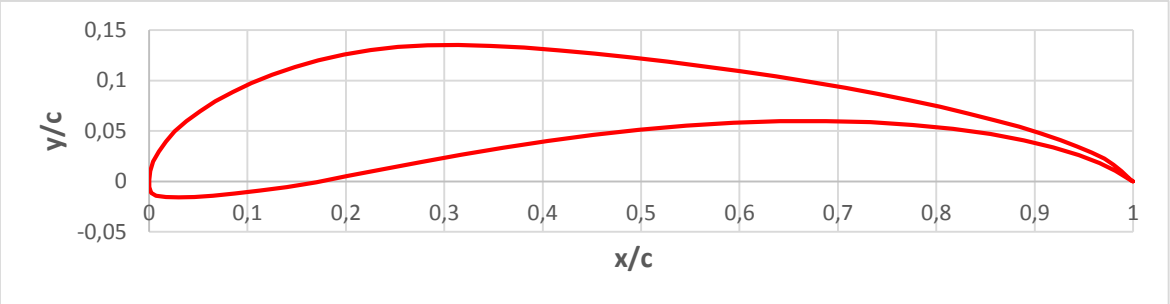

Graph 4.20 - S1223 geometric coordinates

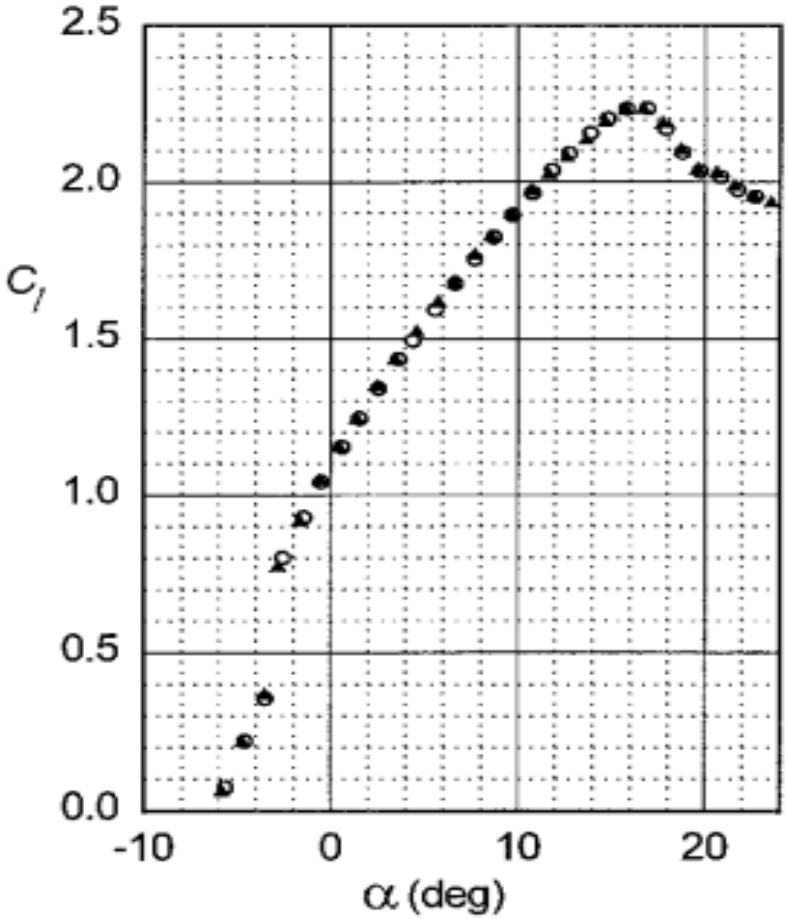

Figure 4.10 - Selig S1223 lift curve, Re=2 ·10^5[24]

A hypothetical geometrical constraint have been imposed, limiting the chord to 5 m or 2.5D. In this phase the AoA was null and the throat width had an arbitrary value of 1.3 D. The turbine was placed in the mid-chord position. The AoA, the throat area and the turbine position have been in the next phase.

4.7.1 CFD

A fast check was made, to evaluate whether the rotating domain diameter size affected the results. The following graph makes a comparison between the rotating domain with diameter 1.5D used in the previous section (where D is the turbine diameter) and a very small one. As can be easily seen the difference is negligible, thus a small rotating domain can be used without any trouble for the diffuser-augmented turbine.

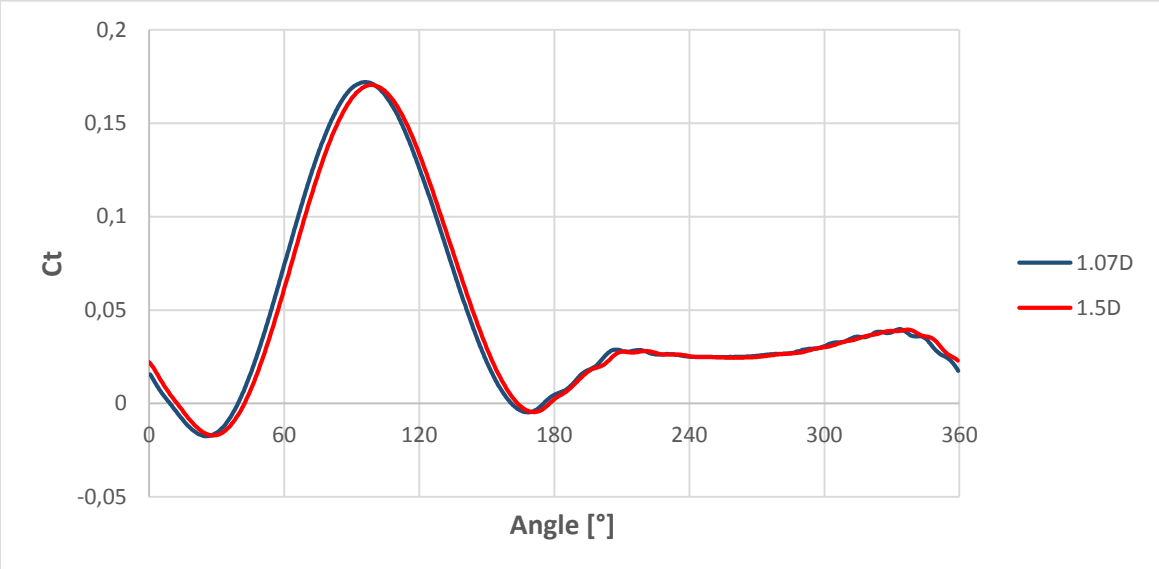

Graph 4.21 - TSR 2.7: Ct curves for two different size of the rotting domain

4.7.1.1 Mesh

The domain dimensions, the solver setup and convergence criterion adopted were the ones obtained by the previous validation. The discretization of the zone near the diffuser deserved a more in-depth analysis.

Below are reported the results of a brief sensitivity analysis carried out to evaluate the influence of the near-wall discretization for the diffuser. Three mesh were built and tested with the empty diffuser. Stationary flows were obtained.

Mesh	First layer thickness [mm]	Cells	Growth factor	Number of layers	Cells size on the diffuser [m]
G1	0.1 (y^+<4)	93000	1.25	22	0.05
G2	0.03 (y^+~1)	271000	1.17	35	0.01
G3	0.03 (y^+~1)	457000	1.13	50	0.005

Table 4.4 - Mesh for the empty diffuser case

The velocity profile along the central line of the rotor are plotted against the y-coordinate.

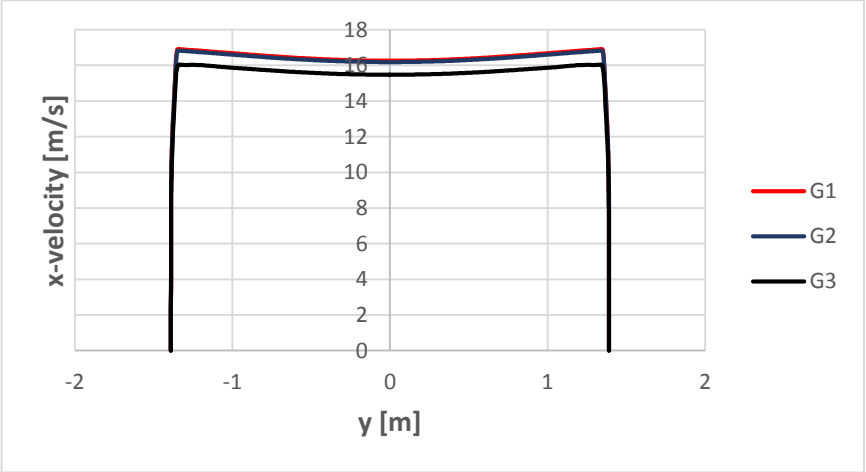

Graph 4.22 - X-velocity at mid-chord position

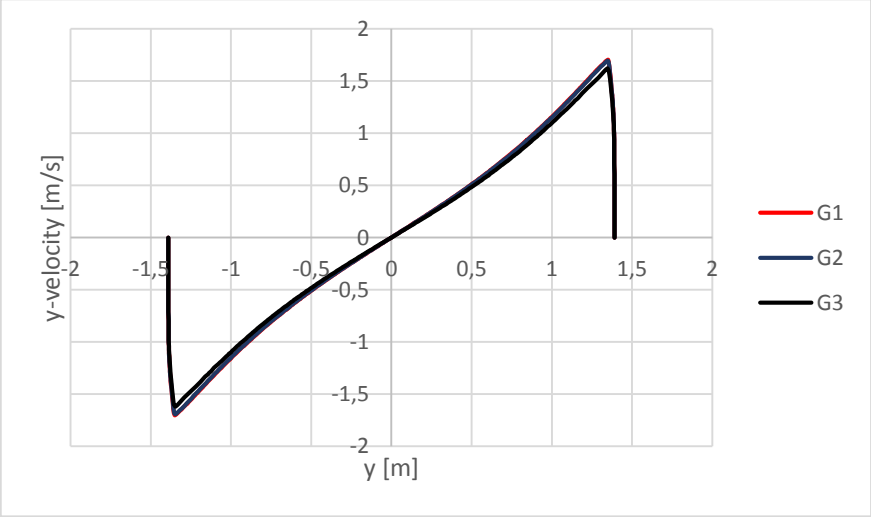

Graph 4.23 - Y-velocity at mid-chord position

The results from G1 and the G2 are almost identical whereas the third mesh underestimates (4%) the velocity increase in the rotor area.

Concerning the most critical issue, the forces on the airfoil, as the number of cells increases, the lift approaches the value obtained by means of equation 3.26, which considers the "ground effect" induced by reciprocal influence of the two airfoil. Moreover, the G2 mesh was capable in predicting with perfect accuracy the Cl value for the isolated airfoil at zero incidence.

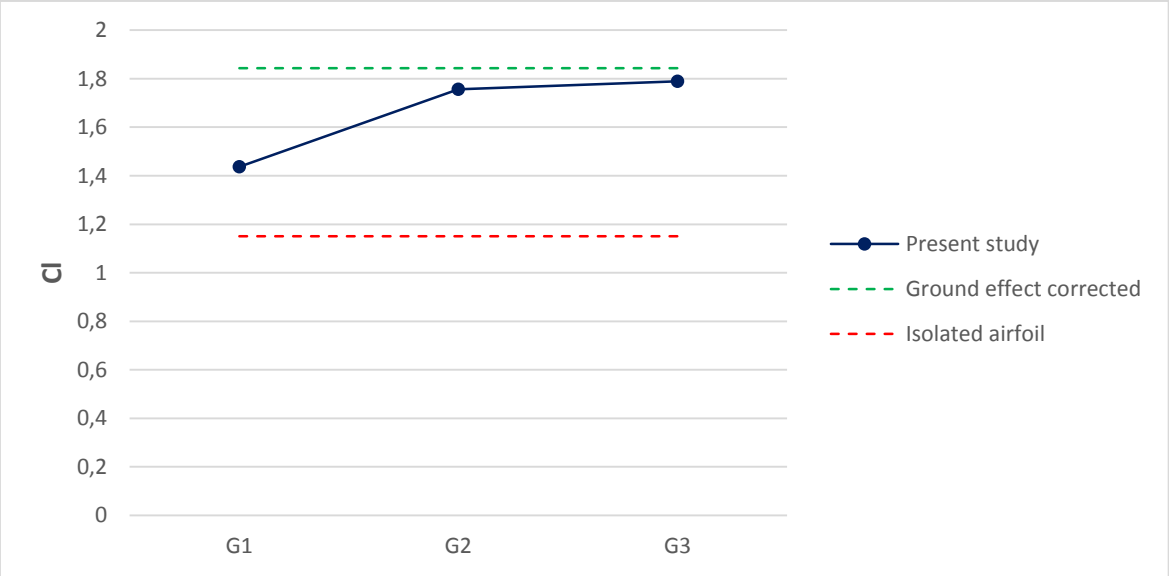

Graph 4.24 - Lift coefficient for each wing of empty diffuser

In light of the above, the G2 mesh criteria were adopted throughout all the CFD simulation involving the diffuser.

The following table reports the overall mesh characteristics.

	Rotor	**Diffuser+Esternal domain**
Software	ICEM CFD	
Element type	QUAD dominant unstructured + prismatic layers	
Max near wall cell length	0.001 m	0.01 m
Number of prismatic layers (PL)	25	35
PL growth factor	1.13	1.17
Minimum PL thickness	3e-05 m	3e-05 m
Cell dimension along the sliding interface	0.01 m	
Number of cells	120000	240000
Minimum orthogonal quality	0.3	

Table 4.5 - Mesh for diffuser augmented turbine

The following pictures display some details of the mesh.

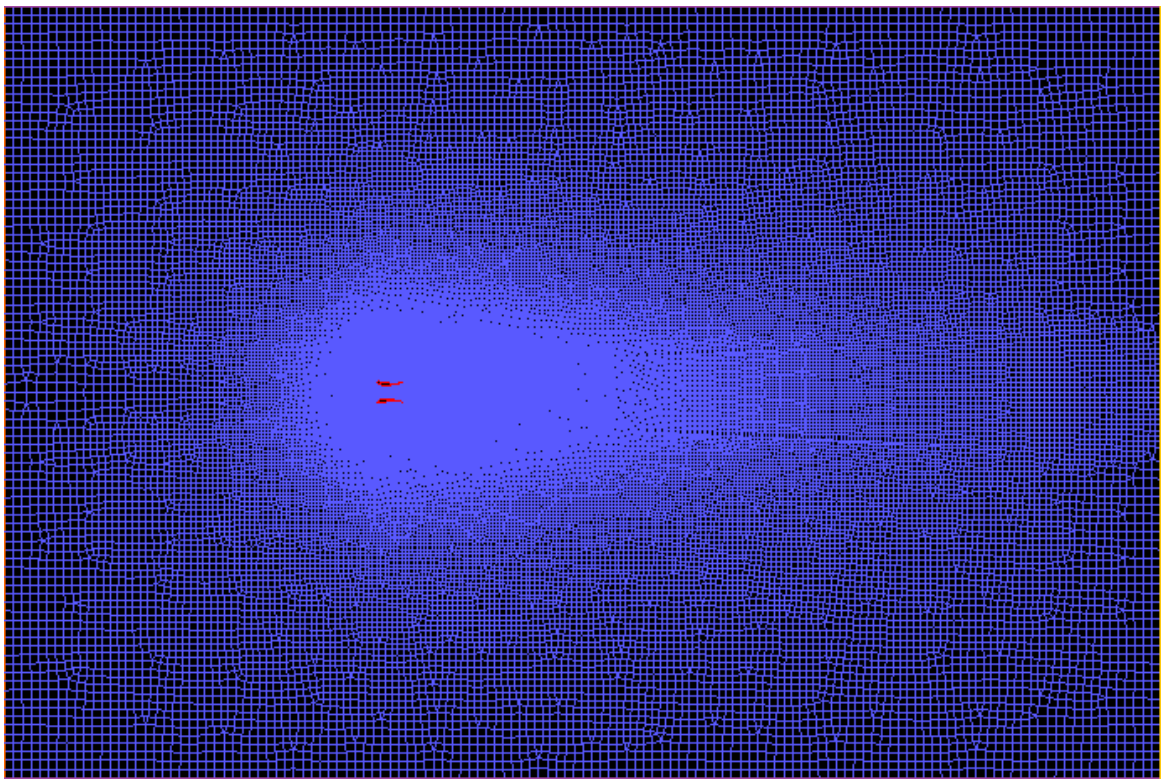

Figure 4.11 - Global mesh

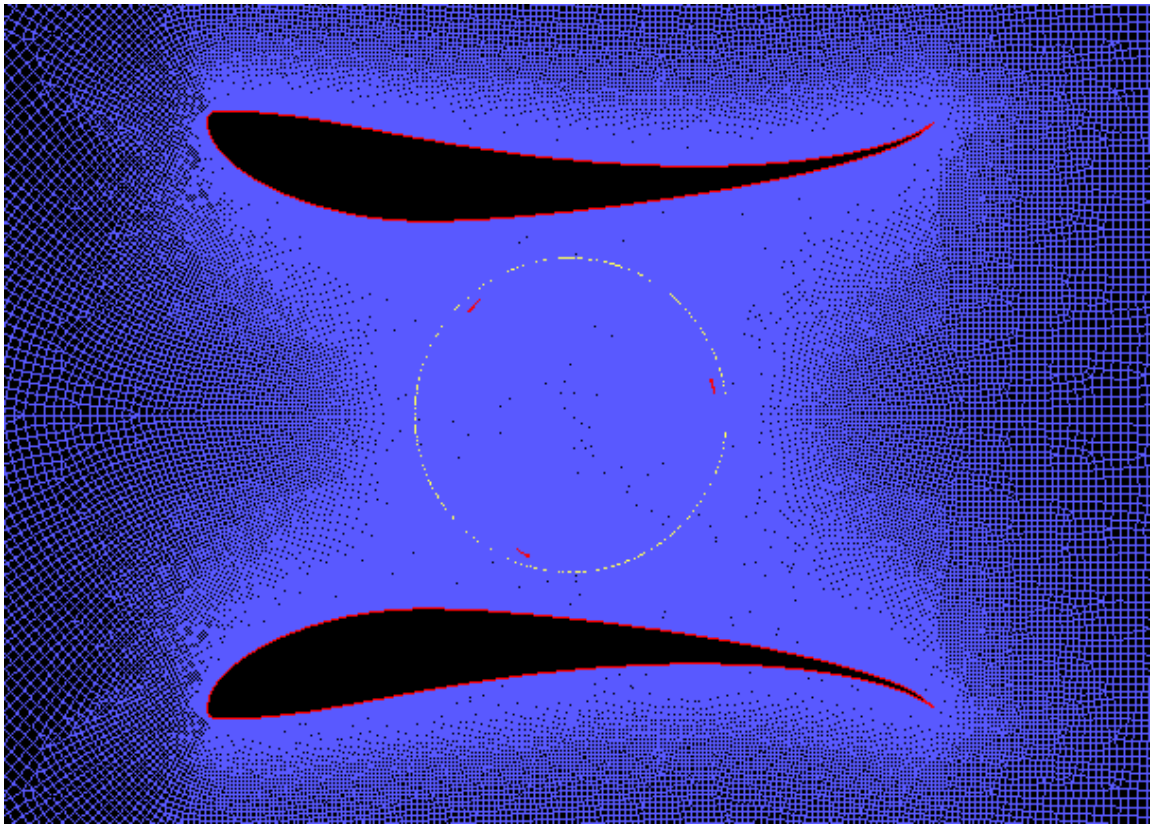

Figure 4.12 - Mesh in the diffuser zone

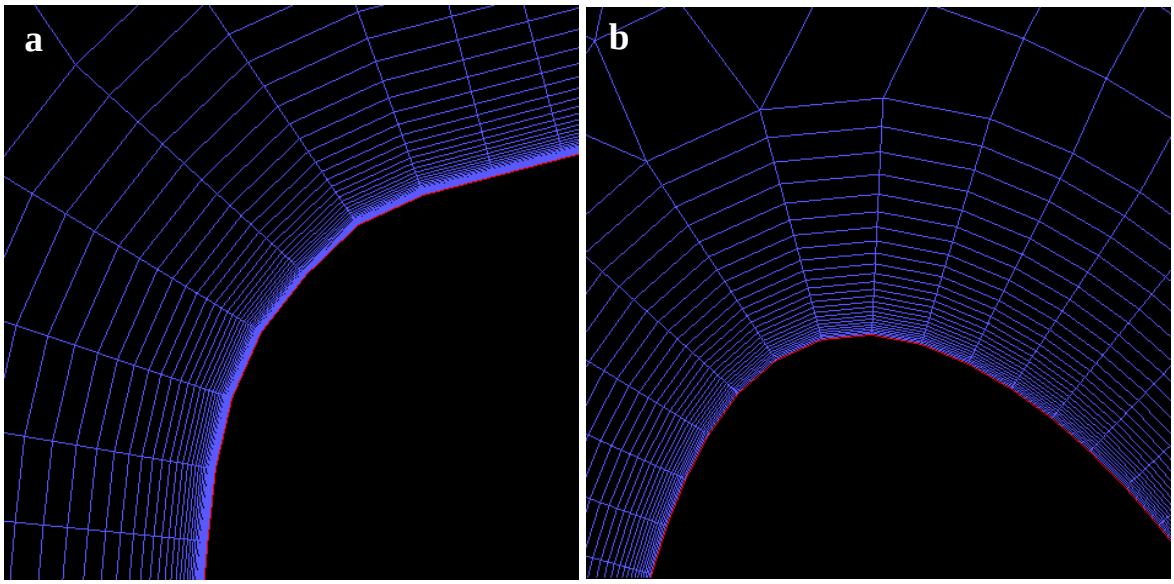

Figure 4.13 - Prismatic elements: **a**-Diffuser surface, **b**-Blade surface

4.7.2 AR

When a diffuser is introduced, the vortex shedding downstream becomes stronger and the flow field does not converge to steady solution. Fortunately, despite the unsteady vortex shedding, for a zero or moderately tilted diffuser, the velocity distribution across the actuator ring (and thus the torque curve) show negligible fluctuation. This made possible the adoption of the transient iterative scheme.

As regards the convergence criterion, it was considered the average value of the x-velocity in the downwind half-cycle, which is a reasonably reliable monitor of the flow in the rotor area. For a non-monotonic pattern was observed, a very conservative criterion was adopted, in order to prevent a local maximum or minimum from being considered a convergent solution: the calculation was stopped when the residuals of the monitor (average x-velocity in the downwind half-cycle) remained between a range of ±0.1% for at least 20 seconds, corresponding roughly to 100 revolutions. In formula:

$$R_n(t) = \frac{M(t) - M(t - n \cdot dt)}{M(t)} < 0.001 \quad \forall\, n \in [0, 20/dt] \qquad [4.18]$$

This criterion is very easy to implement, for it can be automatically set in the solver and has been applied throughout the rest of the work for transient simulations with the AR.

Before proceeding to the comparison with CFD, a sensitivity analysis have been carried out to find the optimal timestep and mesh.

4.7.2.1 Timestep sensitivity

The timestep analysis have been for the highest TSR (3.3) in order to test the capability of the solver to describe the wake vortex shedding which is expected to have his maximum intensity in this case of high blockage. The mesh adopted was the finer of table 4.6. The results are exposed in the graph below:

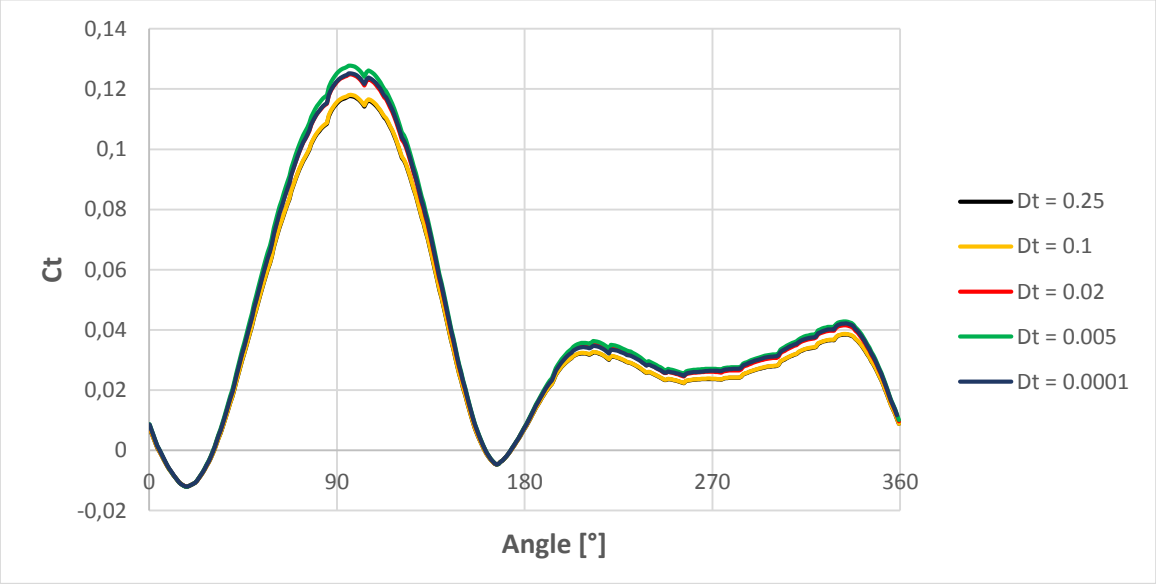

Graph 4.25 - TSR 3.3: Ct curves for different timesteps

When the timestep is very coarse, the curve is downshifted but suddenly rises up when a DT of at least 0.02s is adopted. A further refinement results in negligible changes whereas the calculation time greatly increases. The reason behind this behavior is clear when the following pictures 4.14 are observed.

When the timestep is too much coarse (as in the first two cases) the wake exhibits a lower shedding frequency compared with the finer timestep contours. In fact, to simulate a periodic phenomenon with acceptable accuracy, the timestep must be at least an order of magnitude smaller than the period of the fluctuation [25]. Below this critical threshold, the simulation can become completely invalid and misrepresent the real dynamics.

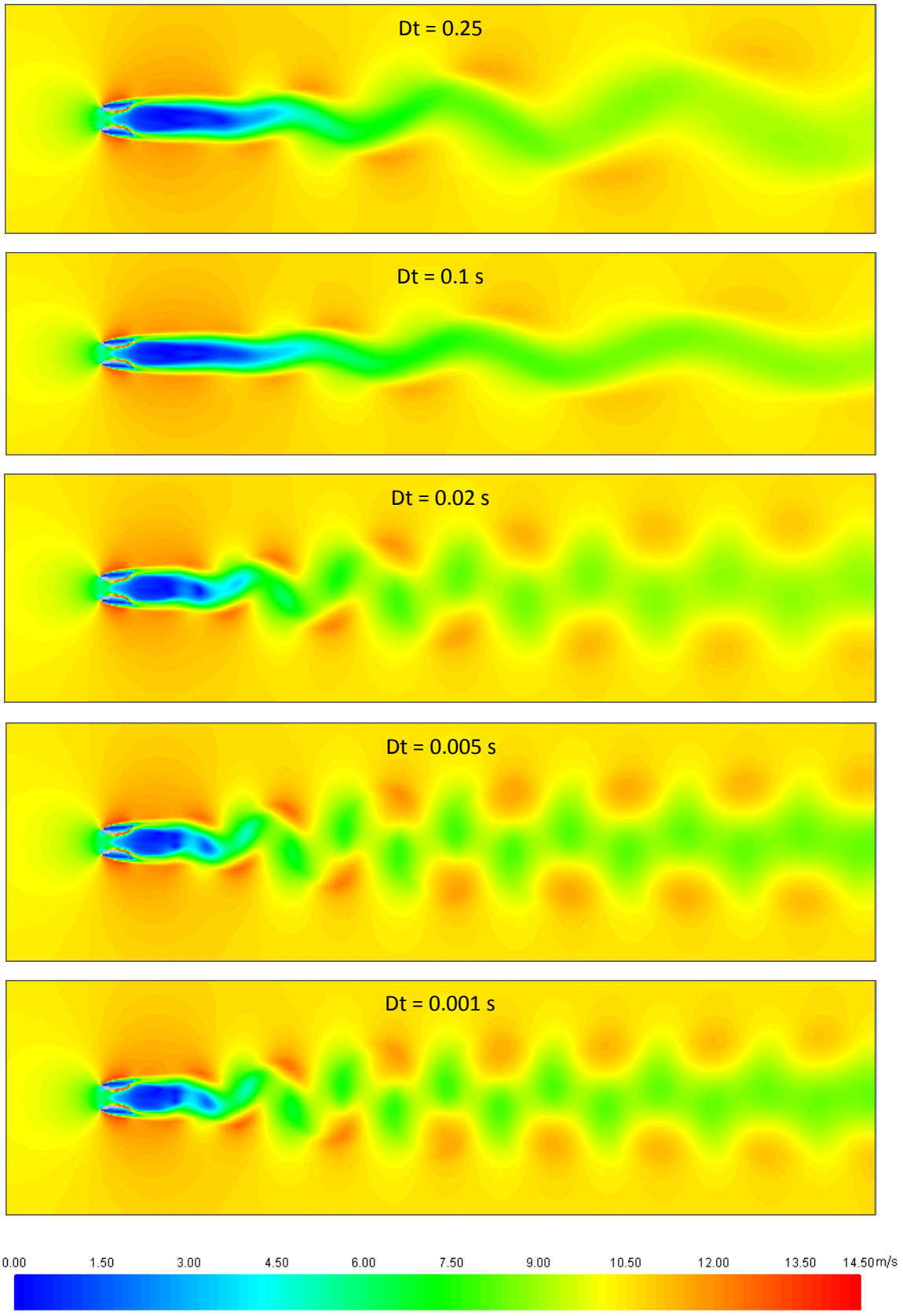

Figure 4.14 - TSR 3.3: contours of velocity magnitude for different timesteps

.

Concerning the problem of the shrouded turbine above, evidently, the larger acceptable timestep lies between 0.1 and 0.02 seconds and for a time-efficient calculation 0.02s has been chosen.

The chart below shows the relative difference due to different timestep settings.

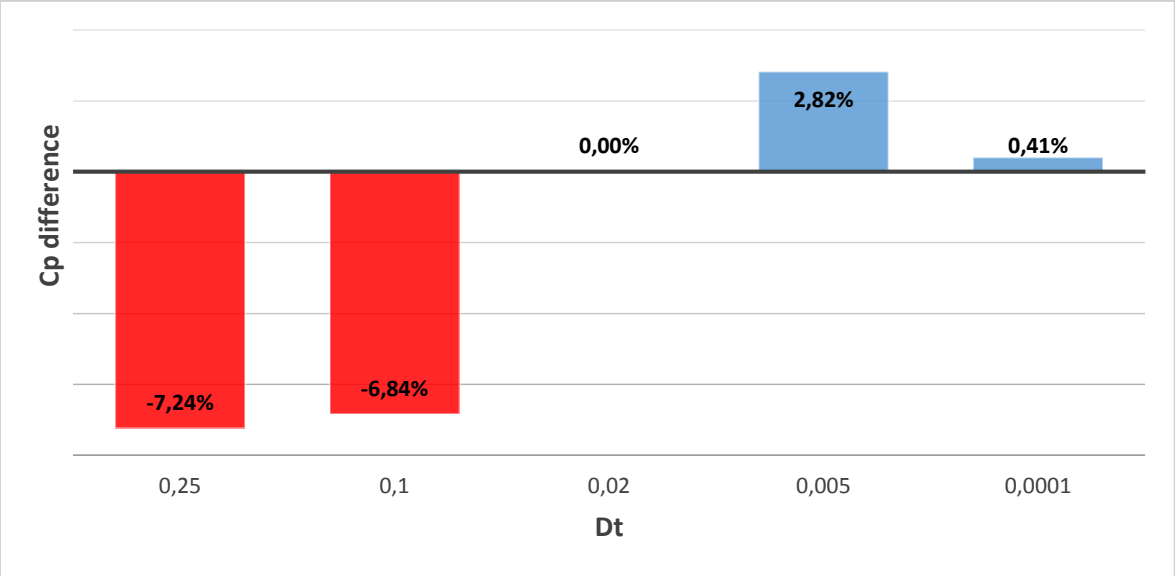

Graph 4.26 - TSR 3.3: relative difference between the Cp calculated at the nominal timestep and the others

4.7.2.2 Mesh sensitivity

Once the timestep was fixed, the sensitivity of the case to the spatial discretization was tested. Mesh with different characteristics (number of cells in the actuator ring, refinement of the wake region and discretization of the near wall region) were adopted for the case of TSR equal to 2.9, which almost corresponds to the maximum Cp condition.

Mesh	Cells	Number of layers (on the diffuser)	First layer thickness [mm]	Growth factor	Cells size on the diffuser [m]	Cells in the actuator ring
G1	16081	13	1 (y^+<20)	1.25	0.08	80
G2	34300	16	0.5 (y^+<15)	1.25	0.05	160
G3	63000	20	0.3 (y^+<10)	1.2	0.03	240

Table 4.6 - Meshes used in the sensitivity analysis

The results are shown in the next graph.

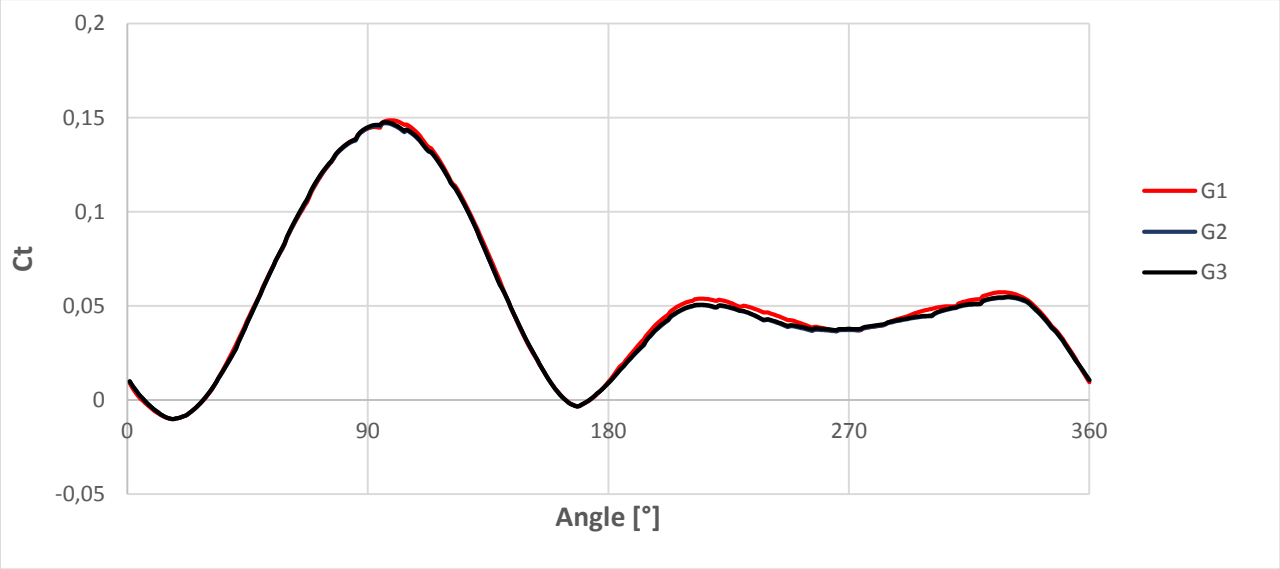

Graph 4.27 - TSR 2.9: Ct curves for different meshes

The agreement between G2 and G3 is almost perfect. G2 criteria have been chosen and used throughout the rest of this work. However, the poor near-wall mesh refinement made this discretization unreliable for the wall stress calculations.

4.7.3 Results

4.7.3.1 Low TSR

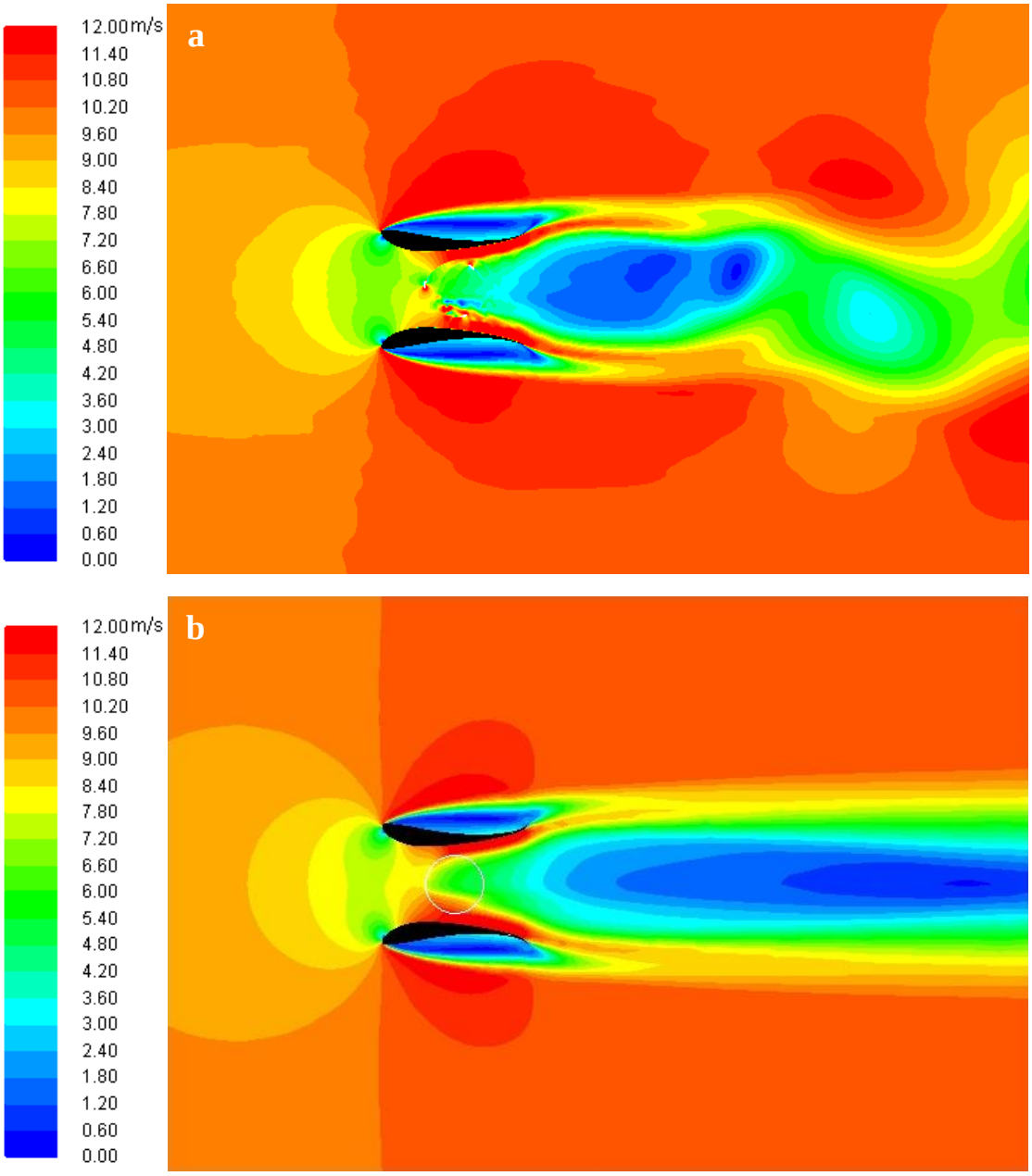

Figure 4.15 - TSR2.3, contours of velocity magnitude: **a**-CFD, **b**-AR

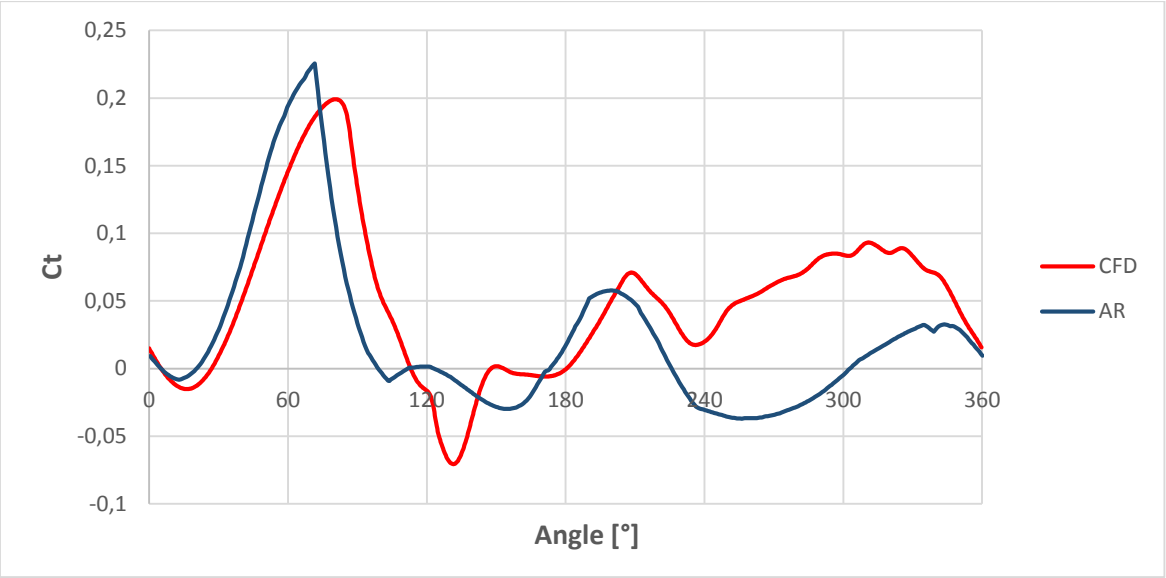

Graph 4.28 - TSR 2.3: Ct curves for CFD ad AR

The AR predicts well the torque decay in the upwind half but overestimates the power loss in downwind. This undesired disagreement, probably due to a different dynamic stall modeling in respect to the accurate CFD, makes the AR unreliable for the cases in which a BL separation in downwind occurs. However, for this condition is very far from being optimal, this possible model's failure is not expected to have influenced the following optimization analysis. The most important fact is that the AR was able to detect the dynamic stall onset and to reproduce qualitatively its effect on the power curve, even if the Cp prediction is quite poor (0.337 for CFD vs 0.159 for AR).

4.7.3.2 High TSR

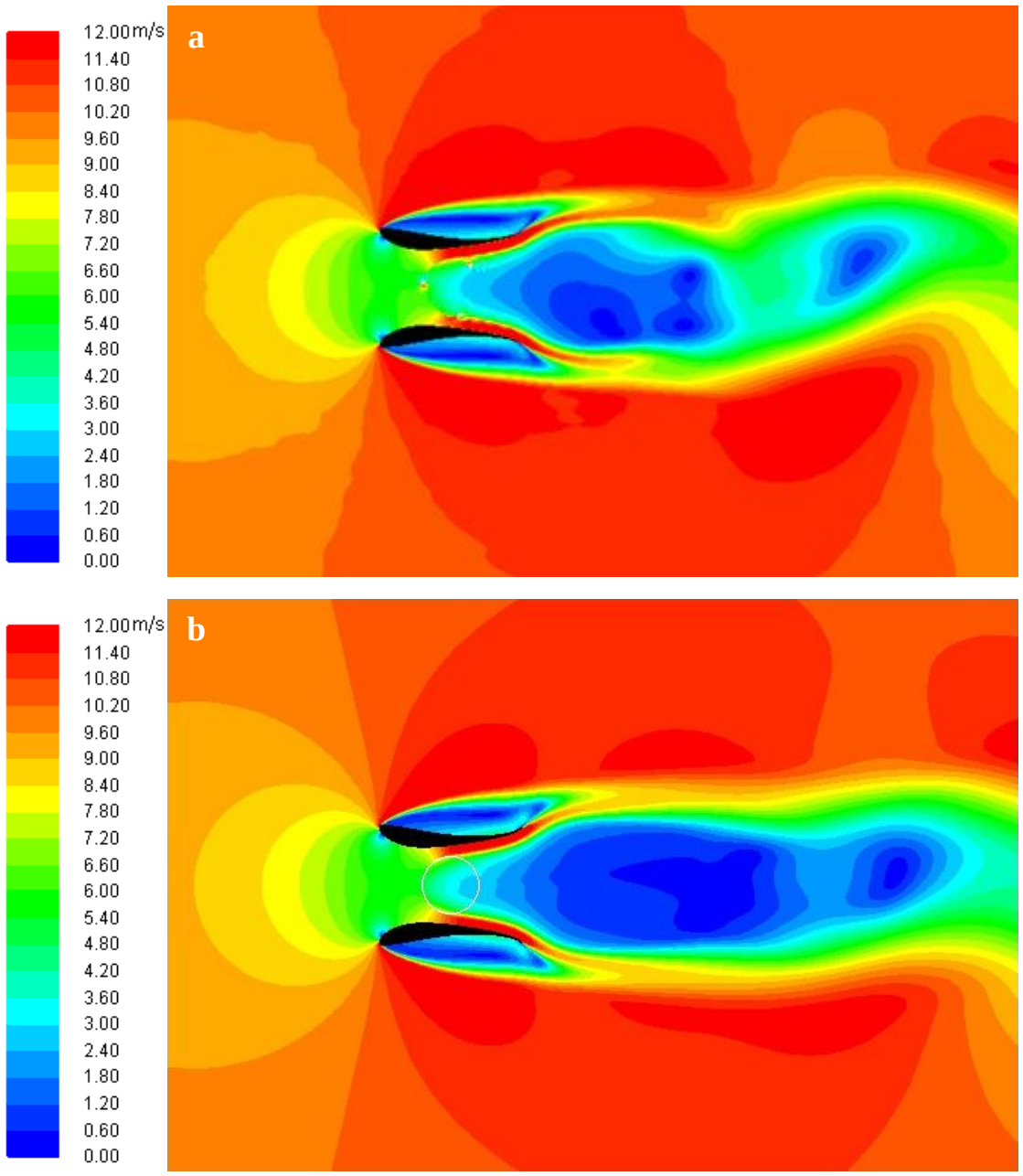

Figure 4.16 - TSR 3.3, contours of velocity magnitude: **a**-CFD, **b**-AR

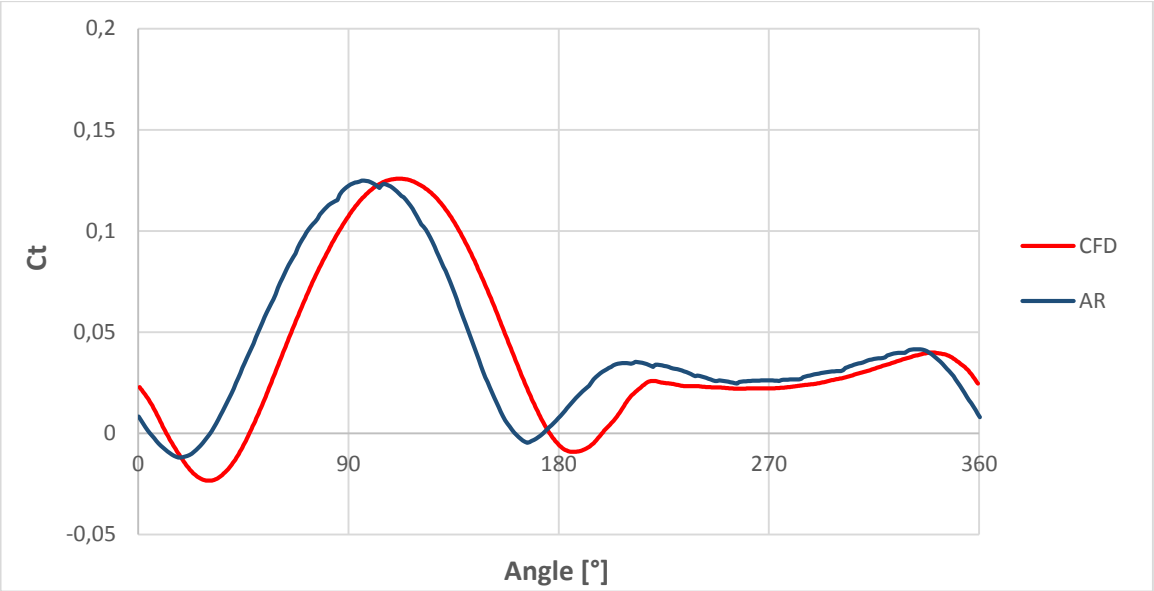

Graph 4.29 - TSR 3.3: Ct curves for CFD ad AR

In the case of completely attached BL, the model gives a result very close to the CFD. Only a slight shift (about 10 degrees) in the torque/azimuthal angle curve can be noticed, but it does not affect the overall Cp that is in acceptable agreement with the one provided by the URANS simulation (0.376 for CFD vs. 0.415 for AR)

4.7.3.3 Maximum Cp TSR

This is the an operative condition, so it is very important to check the agreement between the two models.

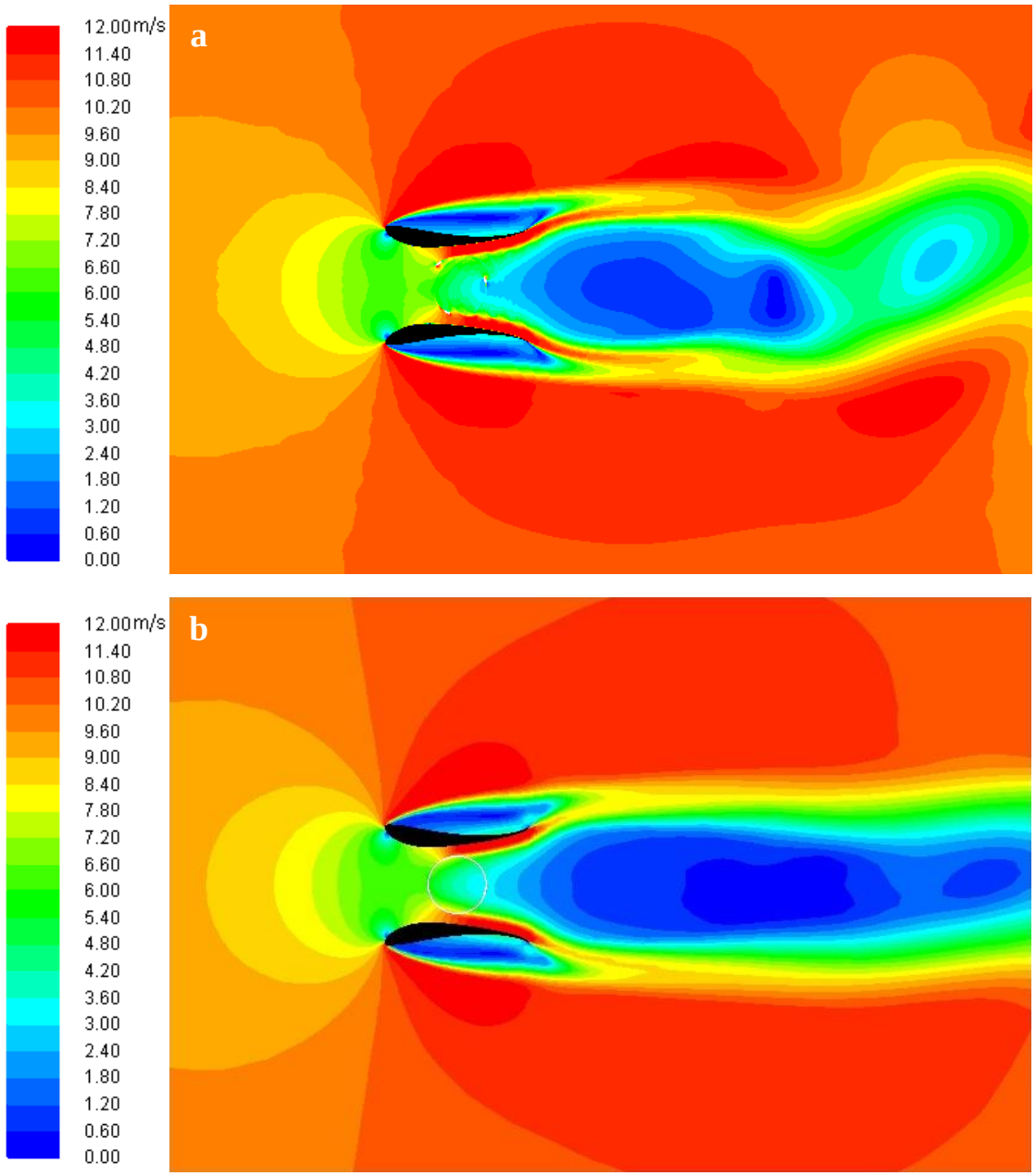

Figure 4.17 - TSR 2.7, contours of velocity magnitude: **a**-CFD, **b**-AR

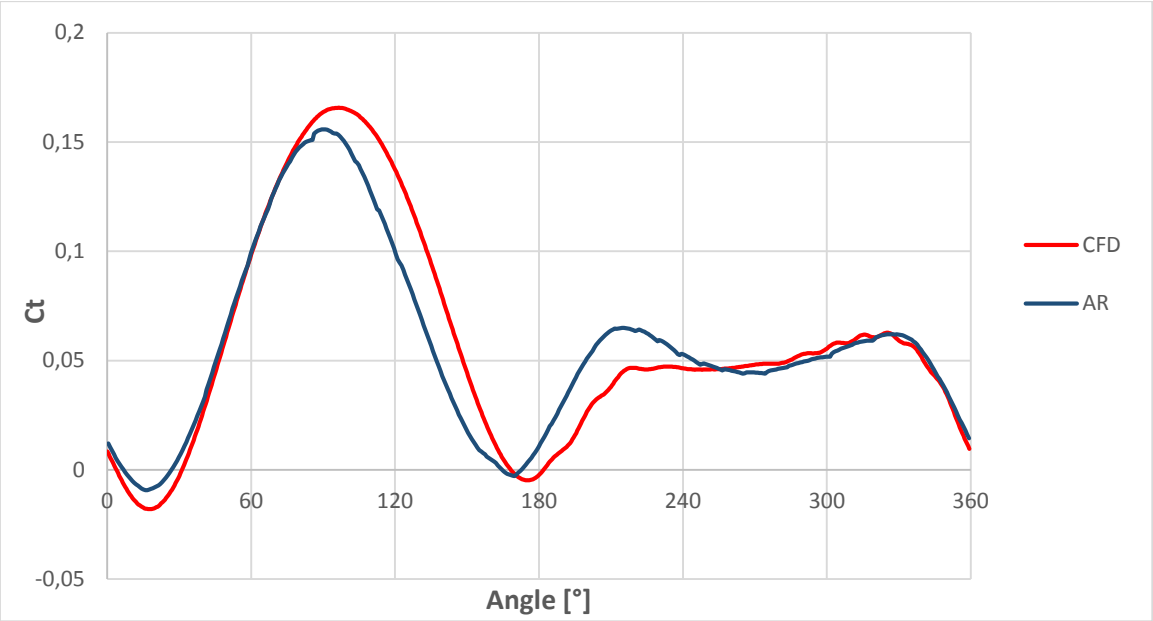

Graph 4.30 - TSR 2.7: Ct curves for CFD ad AR

The agreement is acceptable between the two curves and the Cp difference is negligible (0.469 for CFD vs 0.456 for AR).

4.7.3.4 Overall trend

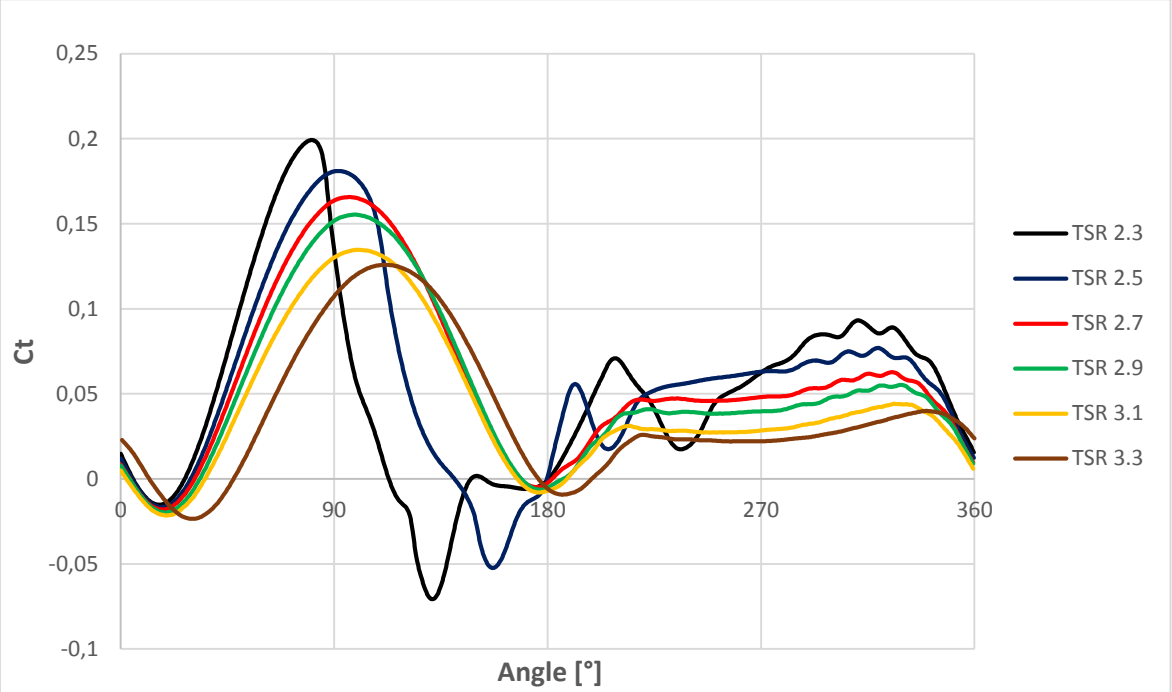

Graph 4.31 - Overall trend of the Ct curves from AR

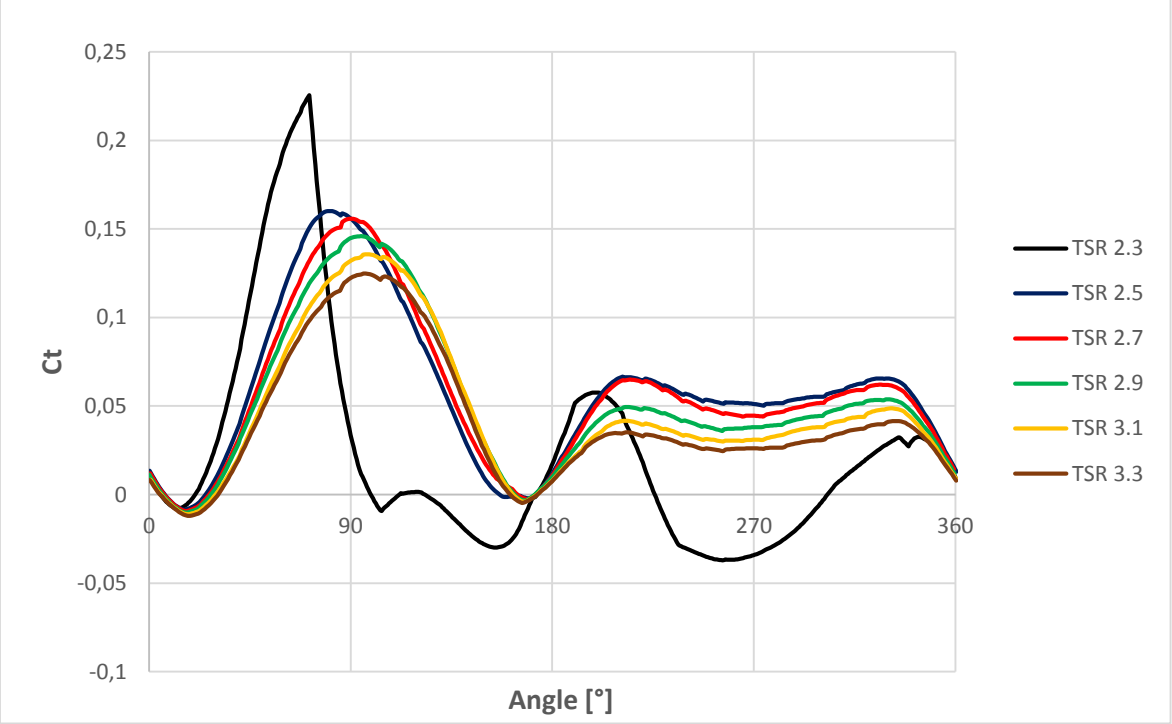

Graph 4.32 - Overall trend of the Ct curves from AR

The torque evolution caught by the AR presents an acceptable agreement with the one obtained by means of CFD, except for the low TSR cases where the BL separates. The AR shows again a lower threshold TSR concerning the BL separation.

4.7.3.5 Cp/TSR curve

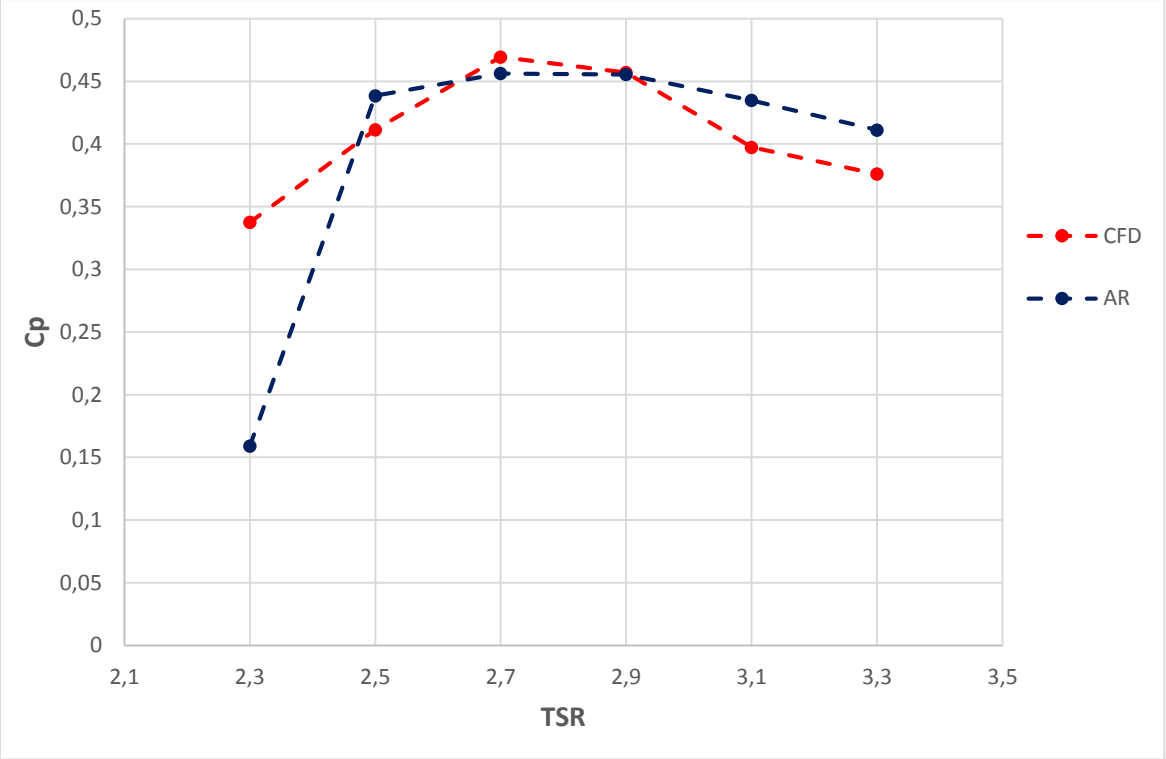

Graph 4.33 - Cp/TSR curves from CFD and AR

Except for the disastrous 2.3 TSR case, the agreement is far acceptable for the present purposes.

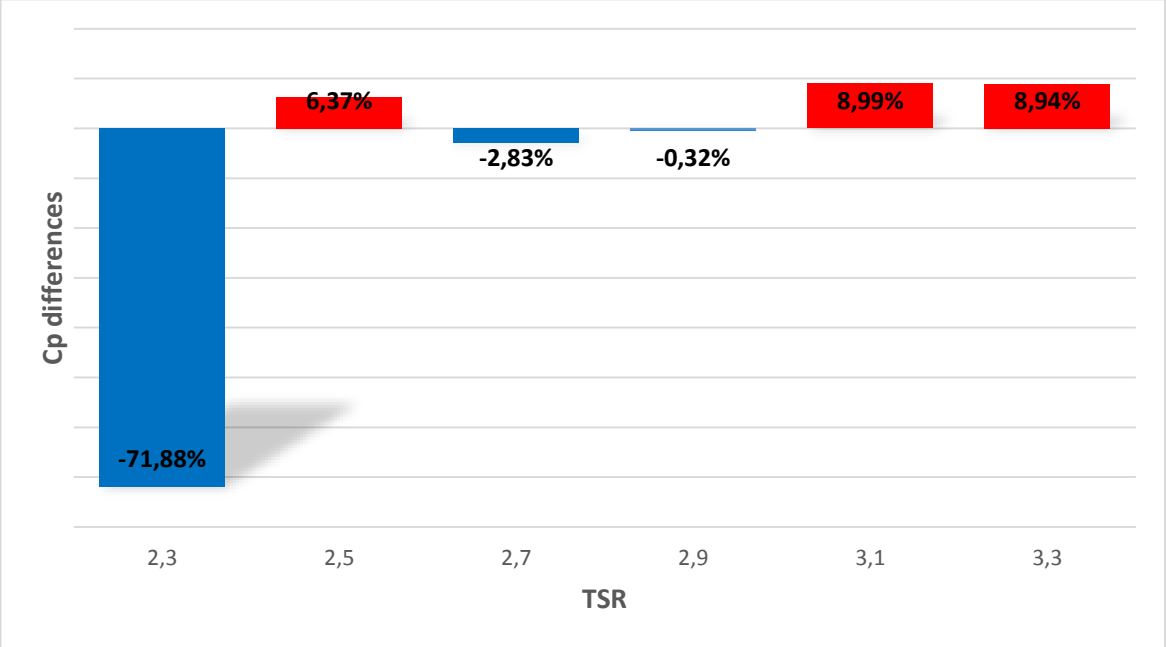

Graph 4.34 - Relative difference in Cp prediction of AR in respect to CFD

4.7.4 The diffuser effects

The AR model provides more information about the flow field around the blades so that it is possible to give an interpretation of the way the diffuser is working. The Ct curves from CFD and AR proof that the new model was able to capture well the effect of the diffuser in the turbine.

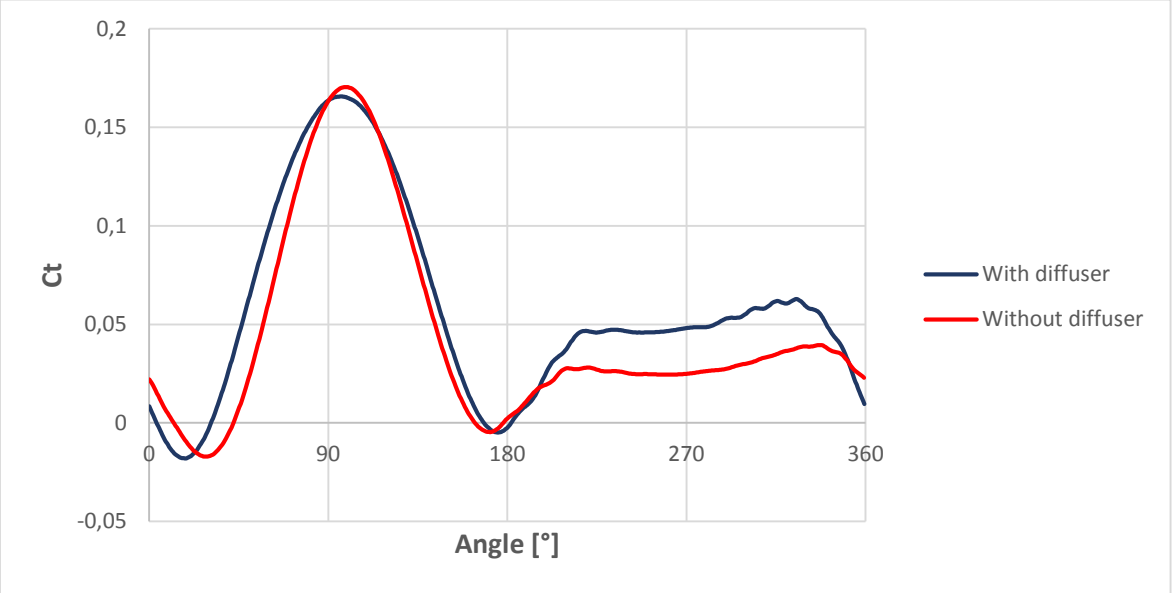

Graph 4.35 - TSR 2.7: Ct curves for bare and diffuser augmented turbine for CFD

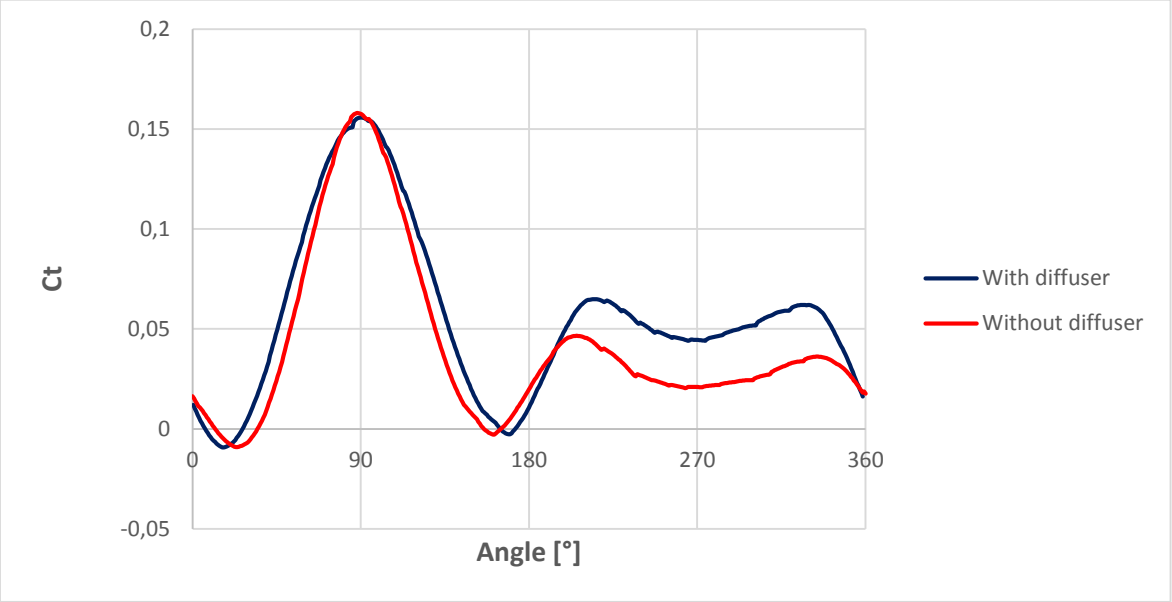

Graph 4.36 - TSR 2.7: Ct curves for bare and diffuser augmented turbine for AR

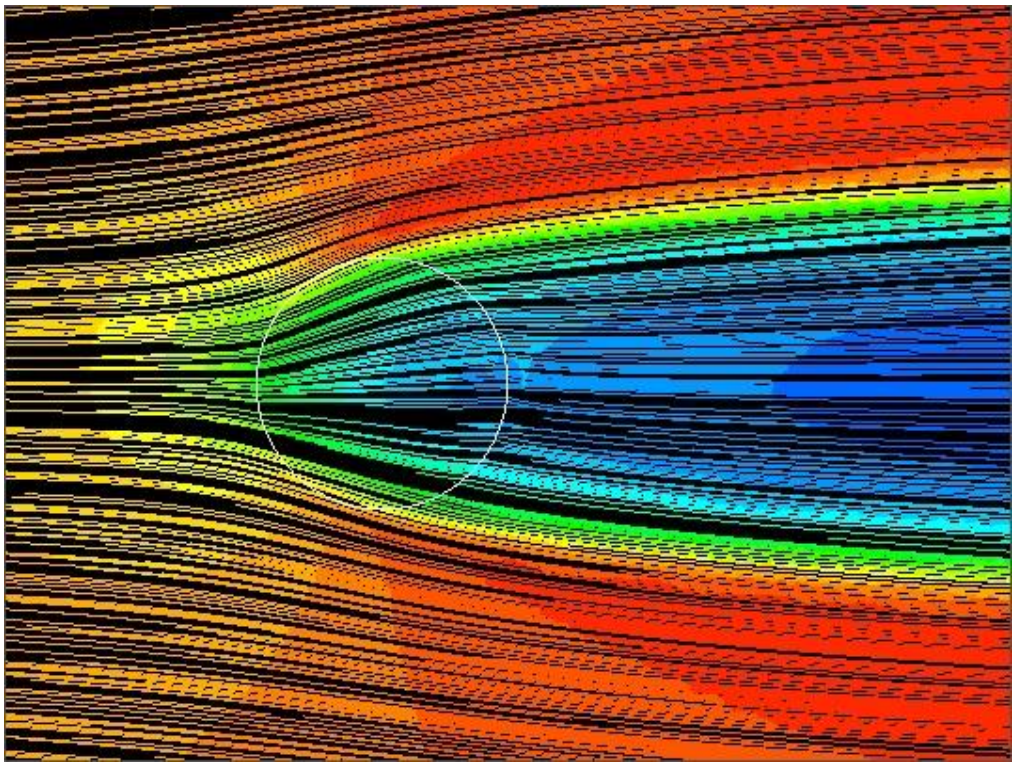

Figure 4.18 - Streamlines in the rotor zone colored by velocity magnitude for bare turbine (AR)

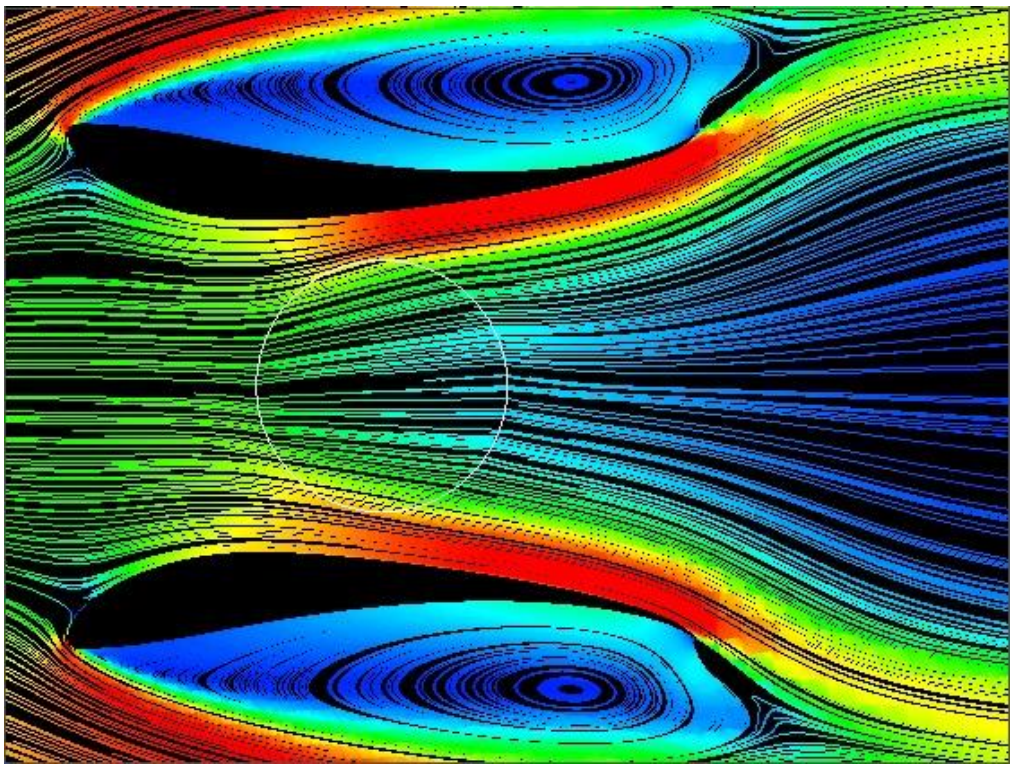

Figure 4.19 - Streamlines in the rotor zone colored by velocity magnitude for DAWT (AR)

4.7.4.1 Upwind

As graphs 4.35 and 4.36 show, the torque peak in the upwind half does not exhibit appreciable changes, while its shape becomes slightly wider. This is the consequence of the no-slip condition at the diffuser wall that reduces the streamlines expansion consequent to the flow slowing down across the rotor. The fig. 4.18 and 4.19 show this effect, which is confirmed by the profiles of the two components of the velocity vector along the ring (graphs 4.37, 4.38). In fact, whereas the x-velocity in almost the same (except for angle near 0° and 180°) the y-velocity is reduced by the diffuser and, as a consequence of this, the angle of attack is higher (graph 4.38)

4.7.4.2 Downwind

The greatest benefit of the diffuser is the enhancement of the downwind power production, that can be considered simply as the straightforward consequence of a higher x-velocity magnitude, for the y-velocity does not change.

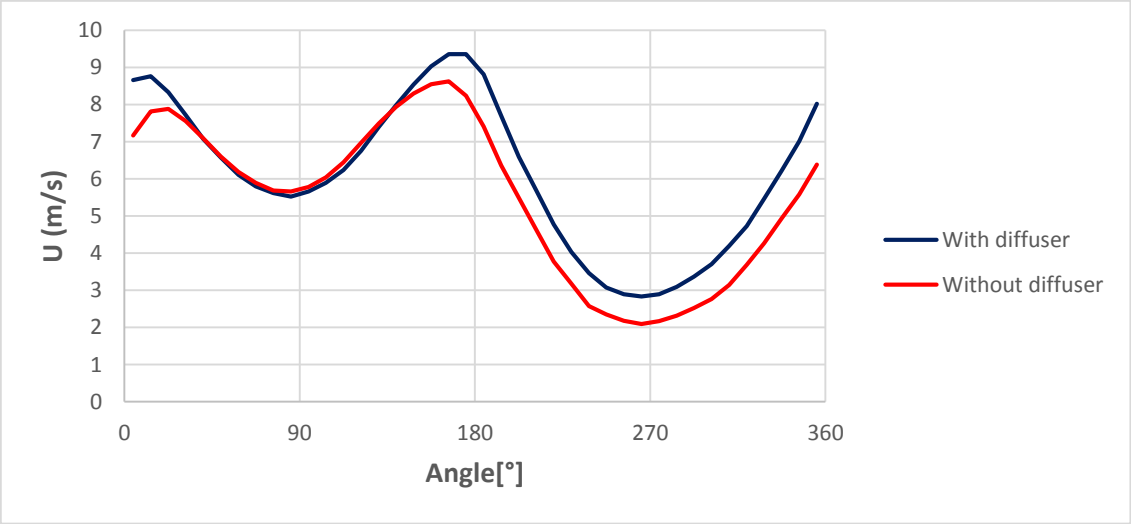

Graph 4.37 - TSR 2.7: x-velocity along the actuator ring for bare and shrouded turbine

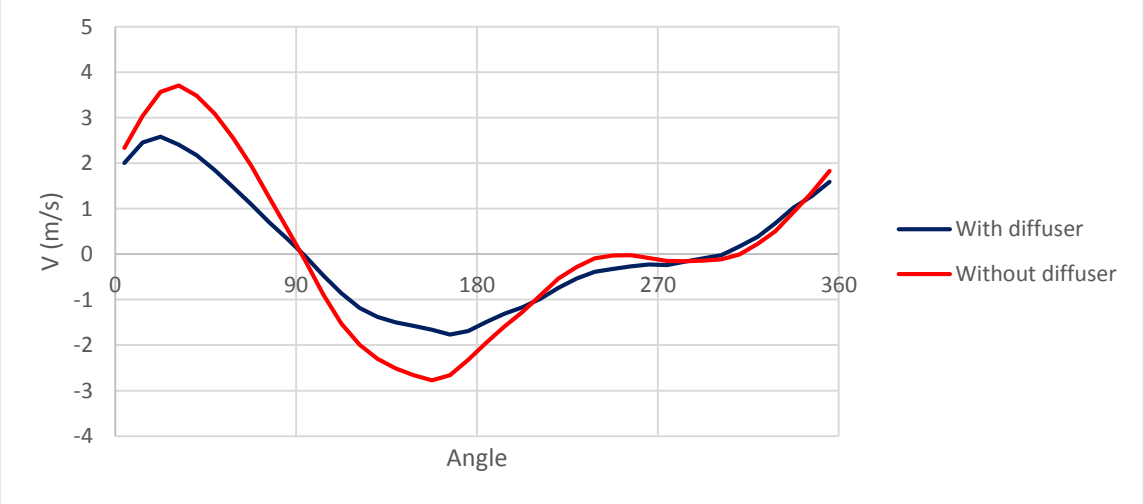

Graph 4.38 - TSR 2.7: y-velocity along the actuator ring for bare and shrouded turbine

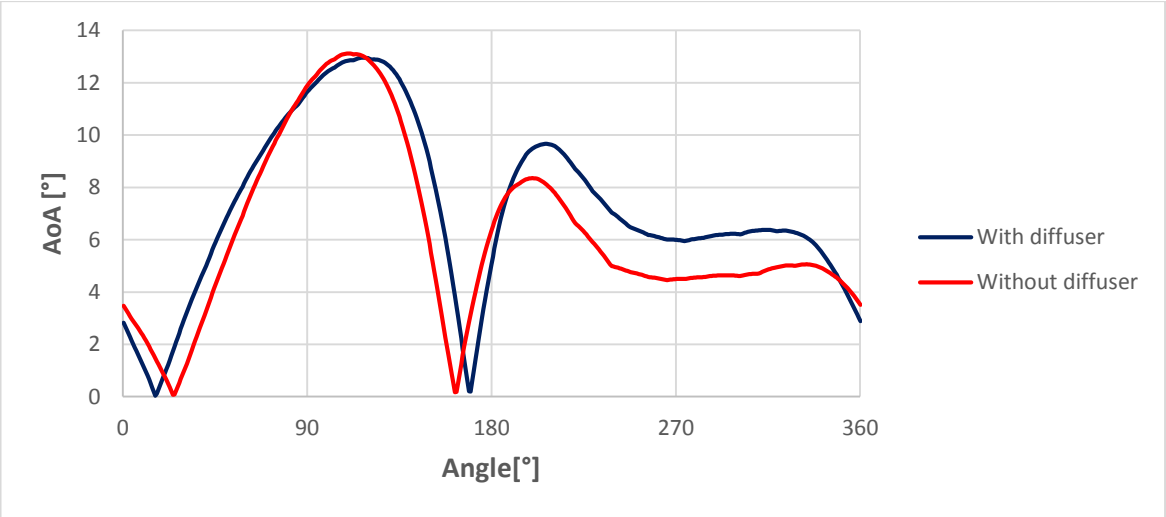

Graph 4.39 - TSR 2.7: AoA along the actuator ring for bare and shrouded turbine

This explanation match the considerations made by [26, 27] concerning their CFD studies, but it is essential to highlight the relatively simple way they were deduced from the AR results. The present model, for it immediately provides the most important quantities affecting the turbine operation, permits to have a deep insight of the phenomena.

To sum up, this wide and challenging validation campaign highlighted the limit of the AR in respect to the more complex full CFD and proofed that this very fast model can be used to perform an analysis to investigate the influence of the main geometrical parameters on the turbine power output.

IV References

[1] Trivellato F, Raciti Castelli M. *Appraisal of Strouhal number in wind turbine engineering*, Renewable and Sustainable Energy Reviews, Volume 49, September 2015, Pages 795-804

[2] Hansen MOL, Sørensen JN, Voutsinas S, Sørensen N. *State of the art in wind turbine aerodynamics and aeroelasticity*, Prog. Aerosp. Sci., 42 (2006), pp. 285-330

[3] Zori LAJ, Rajagopalan RG. *Navier-Stokes Calculation of Rotor-Airframe Interaction in Forward Flight*. Journal of the American Helicopter Society. April 1995, Vol. Vol.40.

[4] Madsen HA. *The actuator cylinder flow model for vertical axis wind turbines*. PhD dissertation, Aalborg University Centre, 1982

[5] Torresi M, Fortunato B, Camporeale S. *Modello CFD per il calcolo delle prestazioni e degli effetti di scia di turbine eoliche ad asse verticale*, La Termotecnica, Maggio 2013

[6] S. Antheaume, T. Maitre, J.-L. *Achard, Hydraulic Darrieus turbines efficiency for free fluid flow conditions versus power farms conditions*, Renew. Energy 33 (10) (2008) 2186e2198

[7] Georgescu AM, Georgescu SC, Perte AM, Badea I, *Time efficient computing of the power coefficient for a ducted Achard turbine*, U.P.B. Sci. Bull., Series D, Vol. 74, Iss. 4, 2012

[8] Balduzzi F, Bianchini A, Ferrara G, Ferrari L, Maleci R, *Blade design criteria to compensate the flow curvature effects in H-Darrieus wind turbines*, J. Turbomach. 137 (1) (2015) 1e10.

[9] McCroskey WJ. *The Phenomenon of Dynamic Stall*, NASA Technical Memorandum 81264, (1981)

[10] Gormont RE, *An Analytical Model of Unsteady Aerodynamics and Radial Flow for Application to Helicopter Rotors*, U.S. Army Air Mobility Research and Development Laboratory, 1973, Technical Report 72-67.

[11] Strickland JH, Webster BT, Nguyen T. (1980) *A Vortex Model of the Darrieus Turbine: An Analytical and Experimental Study*, SAND79-7058, Sandia National Laboratories, Albuquerque.

[12] Berg DE. (1983) *An Improved Double-Multiple Streamtube Model for the Darrieus-Type Vertical Axis Wind Turbine*, Sixth Biennal Wind Energy Conference and Workshop, pp. 231-233.

[13] Tran CT, Petot D. *Semi-empirical model for the dynamic stall of airfoils in view of the application to the calculation of responses of a helicopter blade in forward flight*. Vertica 5, 35-53, 1981

[14] Leishman, JG, Beddoes TS. *A semi-empirical model for dynamic stall*. Journal of the American Helicopter Society 34, 3-17. 1986

[15] Øye S. *Dynamic stall simulated as time lag of separation.* Technical Report, Department of Fluid Mechanics, Technical University of Denmark, 1991

[16] Hansen MH, Gaunaa M, Madsen, HA. *A Beddoes-Leishman type dynamic stall model in state-space and indicial formulations*. Risø-R-1354(EN), Risø National Laboratory, Roskilde, Denmark, 2004

[17] Larsen JW, Nielsena SRK, Krenk S. *Dynamic stall model for wind turbine airfoils*, Journal of Fluids and Structures 23 (2007) 959-982

[18] Sheldahl ER, Klimas PC. *Aerodynamic Characteristics of Seven Symmetrical Airfoil Sections Through 180-Degree Angle of Attack for Use in Aerodynamic Analysis of Vertical Axis Wind Turbines*. SANDS0-2114

[19] Batchelor GK , *Introduction to fluid dynamics*, ISBN 0 521 66396 2 paperback (2002)

[20] Theodorsen, T. *General Theory of Aerodynamic Instability and the Mechanism of Flutter*. Technical Report 496, NACA, 1935

[21] McAlister KW, Pucci SL, McCroskey WJ, Carr LW. *An Experimental Study of Dynamic Stall on Advanced Airfoil Sections*, NASA Technical Memorandum 84245, 1982

[22] Ortiz X, Rival D, Wood D, *Forces and Moments on Flat Plates of Small Aspect Ratio with Application to PV Wind Loads and Small Wind Turbine Blades*, Energies 2015, 8(4), 2438-2453

[23] *www.allsmallwindturbines.it*, On-line

[24] Selig MS, Guglielmo JJ. *High-Lift Low Reynolds Number Airfoil Design*, Journal of aircraft, Vol. 34, No. 1, January- February 1997

[25] *Introduction to ANSYS Fluent-Transient flow modeling*- ANSYS Inc (2015)

[26] Malipeddi AR, Chatterjee D. *Influence of duct geometry on the performance of Darrieus hydroturbine*, Renewable Energy 43 (2012) 292-300

[27] Zanforlin S, Letizia S. *Improving the performance of wind turbines in urban environment by integrating the action of a diffuser with the aerodynamics of the rooftops*, Energy Procedia Volume 82, December 2015, Pages 774-781

Part V - Optimization

The hybrid model is a powerful tool to perform the optimization of the DAWT. It provides sufficiently reliable results for a single configuration in a time that is roughly 100 times shorter than that of CFD. The analysis that have been carried out, however, cannot be defined an "optimization" in the strict sense, but a more appropriate term would be "parametric analysis" or OFAT analysis (one-factor-at-a-time). In fact, due to the unaffordability of a brute-force approach, the main geometrical parameters affecting the performance of the DAWT have been varied one at-a-time to detect and justify the relative effects. An OFAT analysis is strictly correct only if the two-factors effects are negligible [1]. In the present case, the so called "optimal" configuration selected in the end is more the result of careful considerations in light of the phenomena observed in the OFAT analysis than a blind product of an optimization algorithm. As already mentioned, the diffuser section and length have been fixed according to theoretical (max lift) and practical (limiting size and loads) considerations. The remaining free parameters were:

- the diffuser incidence angle
- the throat section
- the turbine position relatively to the diffuser

The following scheme visually represents the degrees of freedom considered in this phase.

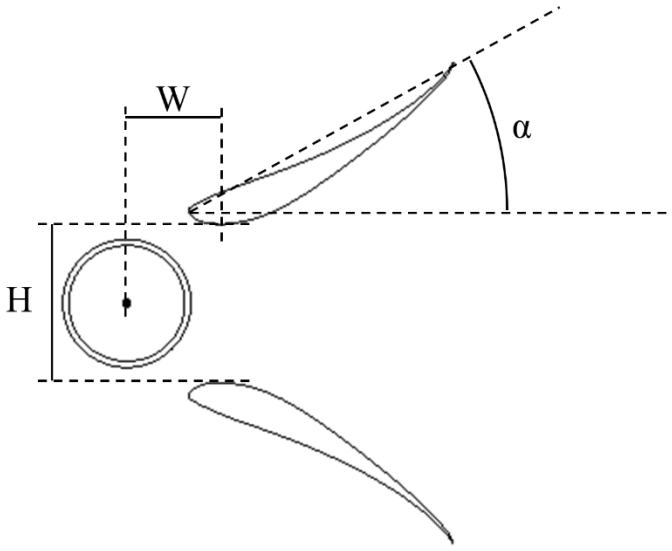

Figure 5.1 - Degrees of freedom of the selected geometry

Some *a priori* qualitative consideration have been useful to decide the correct sequence in the OFAT analysis.

In fact:

- the angle of divergence is directly related to the mass flow, both according to 1-D approach and following the lumped vortex theory (see par. 3.1, 3.2). The higher possible angle before the stall occurrence was expected to be optimal. Due to the importance of this parameter, it has been tested for first.
- concerning the throat width, literature references are dissonant [2, 3] but it is obvious that as the distance between the wings approach high values the acceleration effect must vanish. Therefore, a relatively small value for this parameter have been adopted for the first phase.
- The turbine position have been investigated in ref. [4] were it was confirmed the straightforward result that the turbine must be place in throat to achieve the highest performance. Then, the initial position of the turbine was exactly the throat.

The phases of the OFAT analysis summarized below:

1. α = variable, H = 1.3 D, W = 0
2. α = optimized, H = variable, W = 0
3. α = optimized, H = optimized, W = variable

The domain size have been held constant in this process, because it would have been impossible to perform a sensitivity analysis for each simulations. The eventual effect of blockage due to the increased diffuser frontal area have been evaluated in the end.

5.1 Angle optimization

As already stated in par. 3.2 the angle of attack of the airfoils forming the diffuser should be the higher possible before the occurrence of the BL separation, in order to induce the maximum lift and thus a strong circulation. The graph below shows the evolution of the Cp/TSR curve that greatly shifts upward (more power) and rightward (higher velocity and so higher optimal TSR).

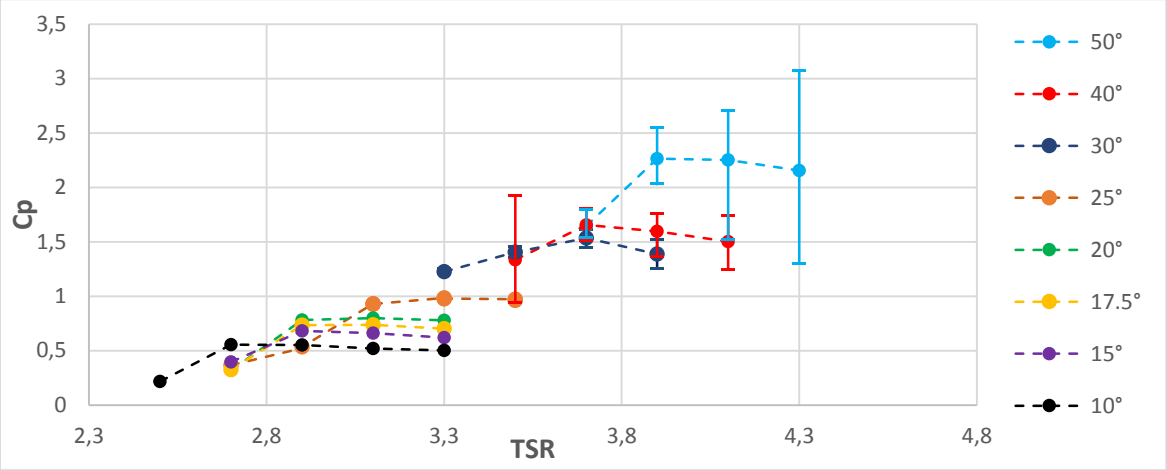

Graph 5.1 - H = 1.3 D, W = 0, Cp/TSR curves for different angles of the diffuser

For high divergence angle, the shedding became very strong and induced fluctuation in the solution. The choice of the pure transient algorithm for the AR was forced.

The results for these oscillating solutions are reported for the higher and the lower Cp instant. For the sake of clearness in the graphs of velocity and torque, is also reported the median between this two extreme conditions.

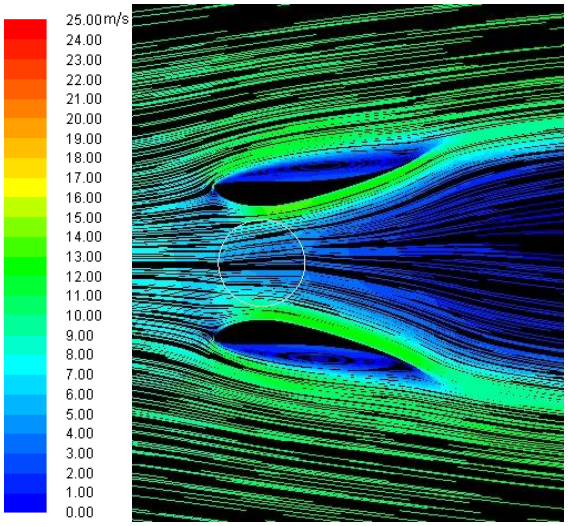

Figure 5.2 - α = 10°, H = 1.3 D, W = 0, TSR = 2.9: streamlines colored by velocity magnitude

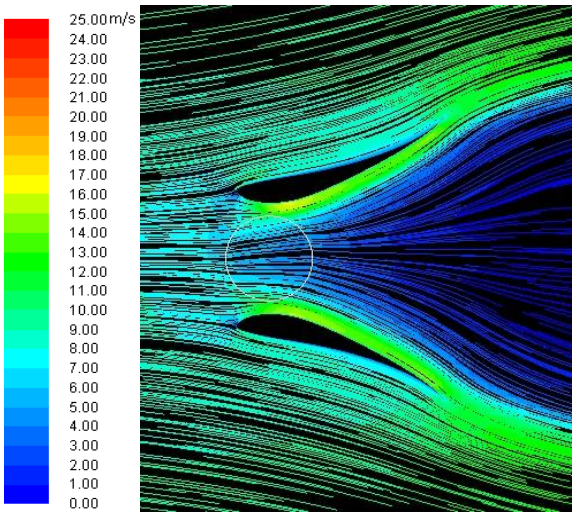

Figure 5.3 - α = 20°, H = 1.3 D, W = 0, TSR = 3.1: streamlines colored by velocity magnitude

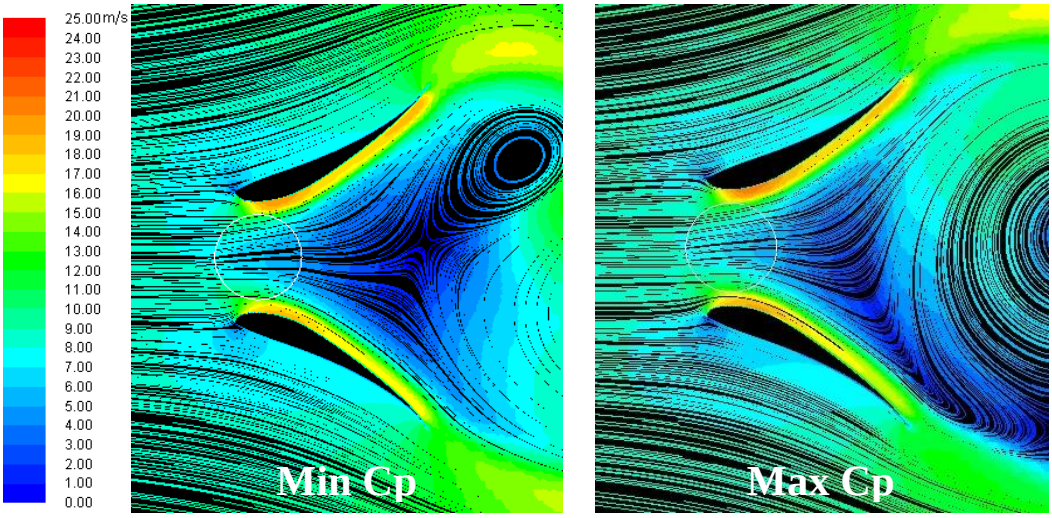

Figure 5.4 - α = 30°, H = 1.3 D, W = 0, TSR = 3.7: streamlines colored by velocity magnitude

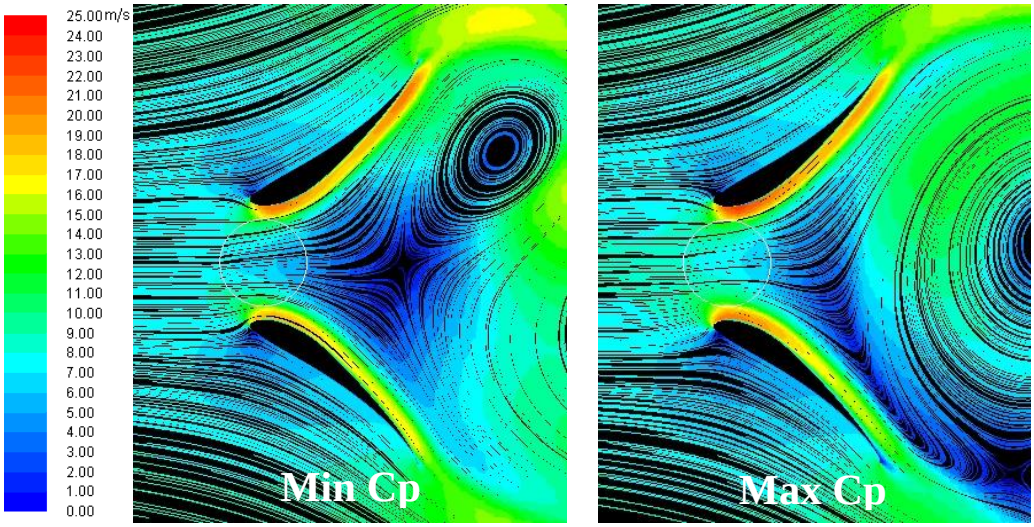

Figure 5.5 - α = 40°, H = 1.3 D, W = 0, TSR = 3.7: streamlines colored by velocity magnitude

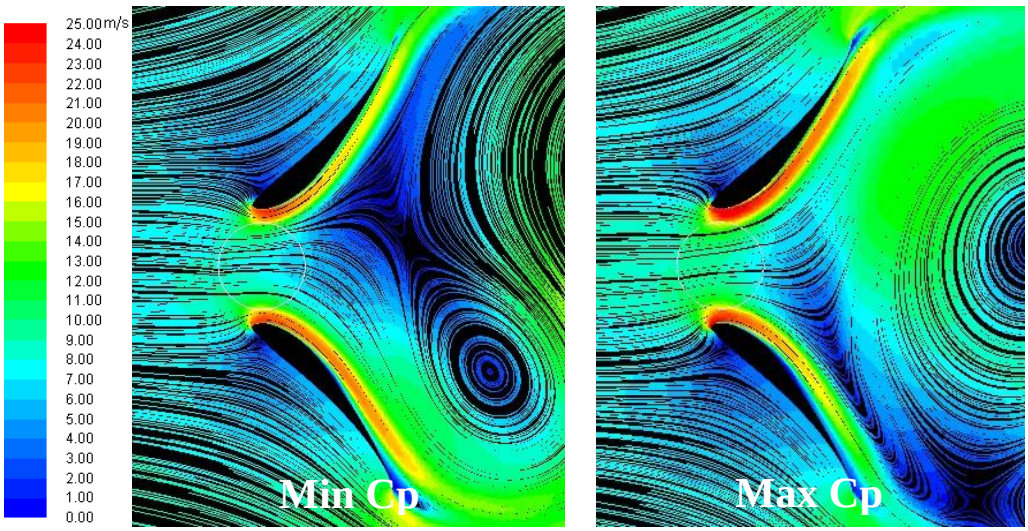

Figure 5.6 - α = 50°, H = 1.3 D, W = 0, TSR = 3.9: streamlines colored by velocity magnitude

For the stall onset for the isolated airfoil was detected around 15-17 degrees for moderate Reynolds, the BL was expected to separate at a comparable angle for the diffuser.

As the previous plot shows, however, it was necessary to increase the angle toward 50 degrees to detect an incipient stall inside the diffuser. This was a very unexpected and apparently non-physical behavior that deserves an in-depth analysis.

5.1.1 Boundary layer separation delay

The 30 degrees case, that was the first one to largely exceed the stall angle provided by the above-mentioned static data, was extensively investigated. As preliminary check, a full CFD simulation, with the same set of parameters used in par. 4.7.1, was carried out to confirm the phenomenon.

The BL did not separate even when a fully URANS approach is adopted, and this is important for two main reasons:

- the BL attachment is not a consequence of the revolution-averaged method adopted by the AR model but occurs even when the real pulsating flow-blade interaction are simulated
- the phenomenon is insensitive to the grid (330000 vs 37000 cells) and timestep ($2.5\ 10^{-4}$ vs $2\ 10^{-2}$) refinements.

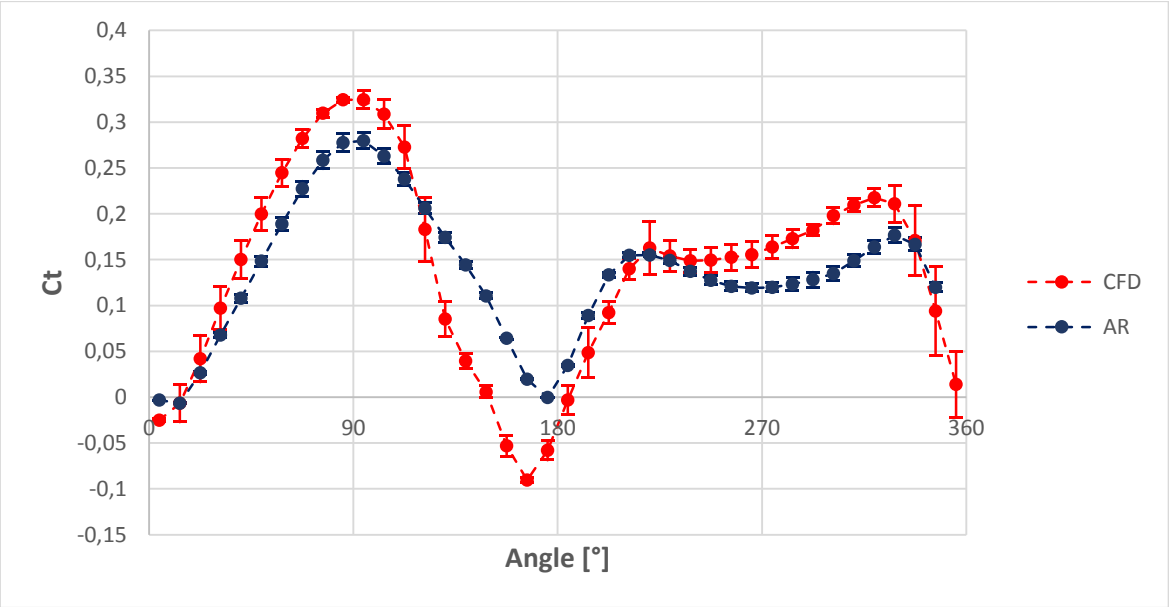

Graph 5.2 - α = 30°, H = 1.3 D, W = 0, TSR = 3.7: Ct curves from CFD and AR

The CFD confirmed once again the results of the AR. The torque curves are different because the selected TSR (3.5) was found out to be very close to the threshold TSR for the LEV detachment. However the striking Cp of 1.4 was confirmed. (1.43 CFD vs 1.4 AR). Also the full CFD captures the intense vortex shedding. The simulation lasted for about 10 days on a 24 cores unit and the simulation where stopped as the average Cp over an entire shedding oscillation exhibit a negligible trend (0.5% of relative difference between two consecutive shedding periods).

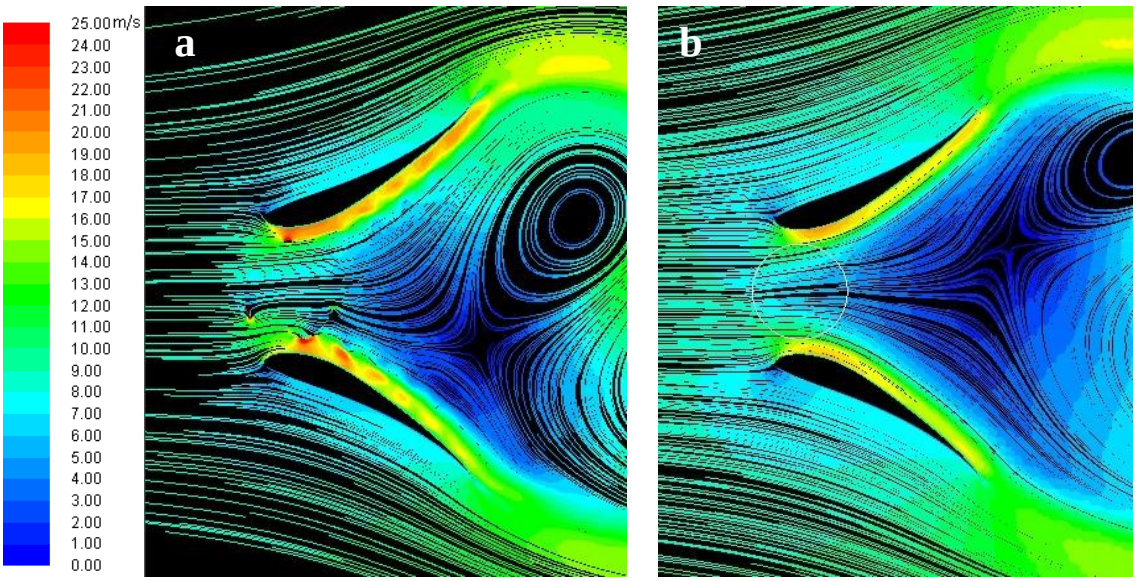

Figure 5.7 - α = 30°, H = 1.3 D, W = 0, TSR = 3.5: streamlines colored by velocity magnitude from CFD (**a**) and AR (**b**) in min Cp conditions

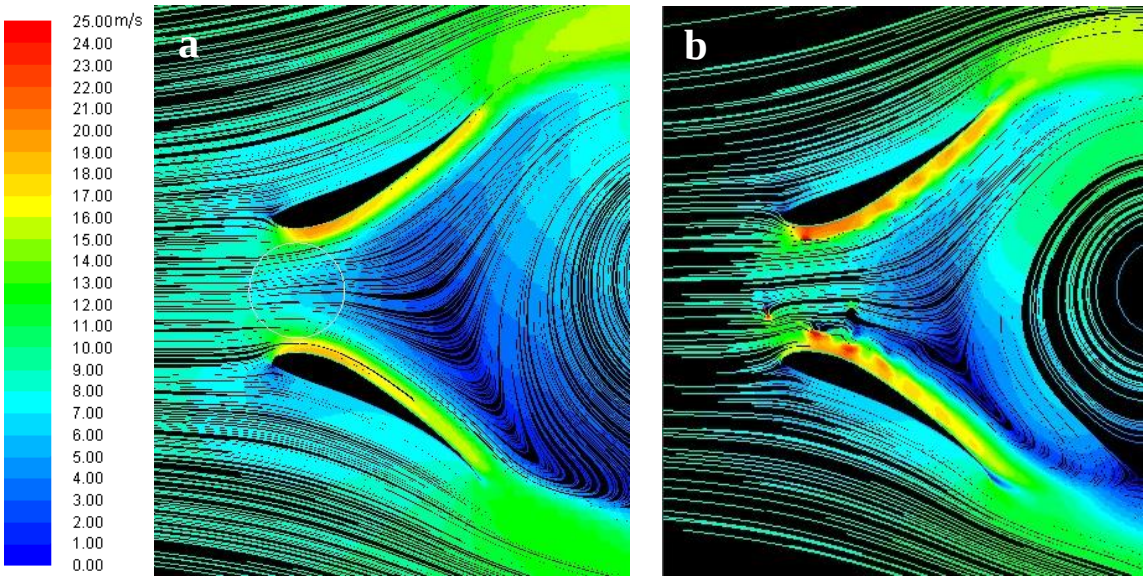

Figure 5.8 - α = 30°, H = 1.3 D, W = 0, TSR = 3.5: streamlines colored by velocity magnitude from CFD (**a**) and AR (**b**) in max Cp conditions

The streamlines plot are very close so the phenomenon occurs also in an accurate full CFD simulation.

This fringe benefit induced by the turbine presence in the diffuser throat have been already observed [5, 6]. Two main factors where seem to play a decisive role: the fluid pre-rotation and the wake negative pressure.

5.1.1.1 Fluid pre-rotation

When an empty diffuser is simulated the stall occurs almost immediately.

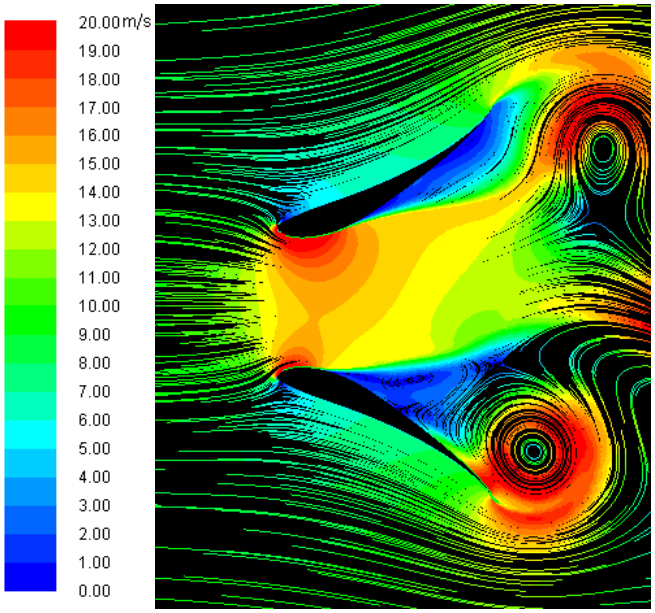

Figure 5.9 - α = 30°, H = 1.3 D, W = 0, empty diffuser: streamlines colored by velocity magnitude

The flow around a thin airfoil can be approximated by the potential solution valid for a flat plate [7]:

$$u_\theta = \frac{-c|V_0|\sin(\theta+\alpha)-\frac{\Gamma}{\pi}}{\mathrm{c}\sin(\theta)} \quad [5.1]$$

where the cylindrical coordinates where adopted and:

- u_θ is the velocity along the plate
- α is the incidence
- Γ is the circulation (which is arbitrary in 2D)
- $|V_0|$ is the undisturbed velocity magnitude

For the Kutta condition to be met, the velocity at the trailing edge ($\theta = \pi$) must be finite, hence:

$$\Gamma = \pi c|V_0|\sin(\alpha) \quad [5.2]$$

$$u_\theta = \frac{-c|V_0|[\sin(\theta+\alpha)+\sin(\alpha)]}{\mathrm{c}\sin(\theta)} \quad [5.3]$$

The second stagnation point ($u_\theta = 0$) lies near the trailing edge and more specifically:

$$\theta = -2\alpha \rightarrow x = \frac{c}{2}\cos(2\alpha) \quad [5.4]$$

This synthetic result shows that the higher angle of attack, the more the first stagnation points moves toward the rear. Thus, an approximate method to estimate the actual angle of attack that an airfoil is experiencing is to individuate the position of first the stagnation point and evaluate its distance from the leading edge.

This brief dissertation about the stagnation point is useful to demonstrate that a body inside the diffuser throat (i.e. a turbine) causes the streamlines to diverge so that the airfoils experience a "pre-rotated" flow and thus a reduced angle of attack.

The following geometry have been considered: the 30 degrees diffuser with the turbine (in particular the lower Cp case instantaneous streamlines but with the high Cp it would have been the same) and the diffuser with a solid cylinder with the same diameter of the rotor.

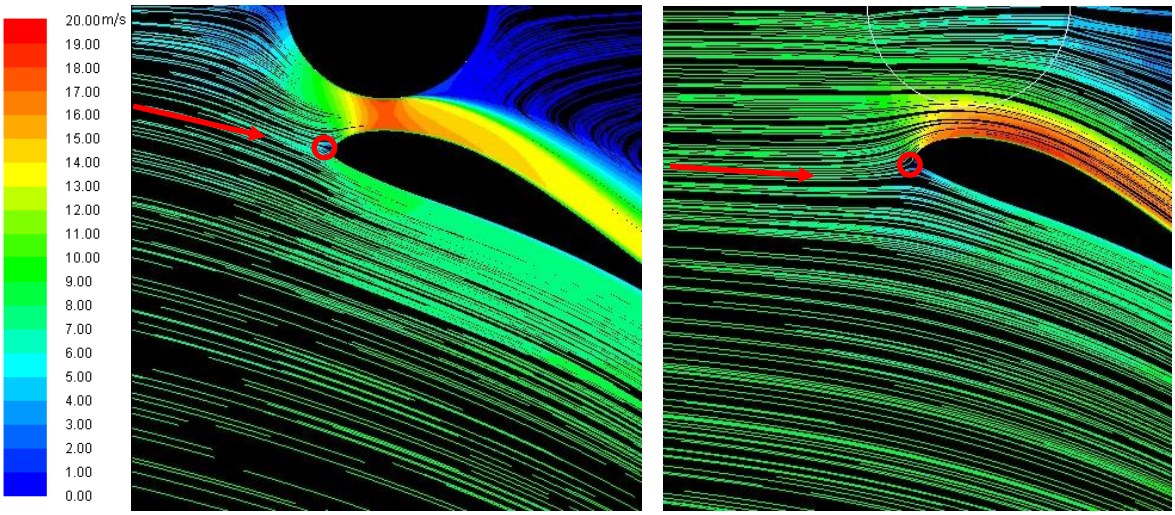

Figure 5.10 - α = 30°, H = 1.3 D, W = 0, stagnation point position: **a**-solid cylinder, **b**-AR

The stagnation point is very close to the leading edge in both the situations, especially for the cylinder. To have basis for comparison, it is worthwhile to consider the flow around an isolated S1223 airfoil with an angle of attack of 13 degrees (incipient stall).

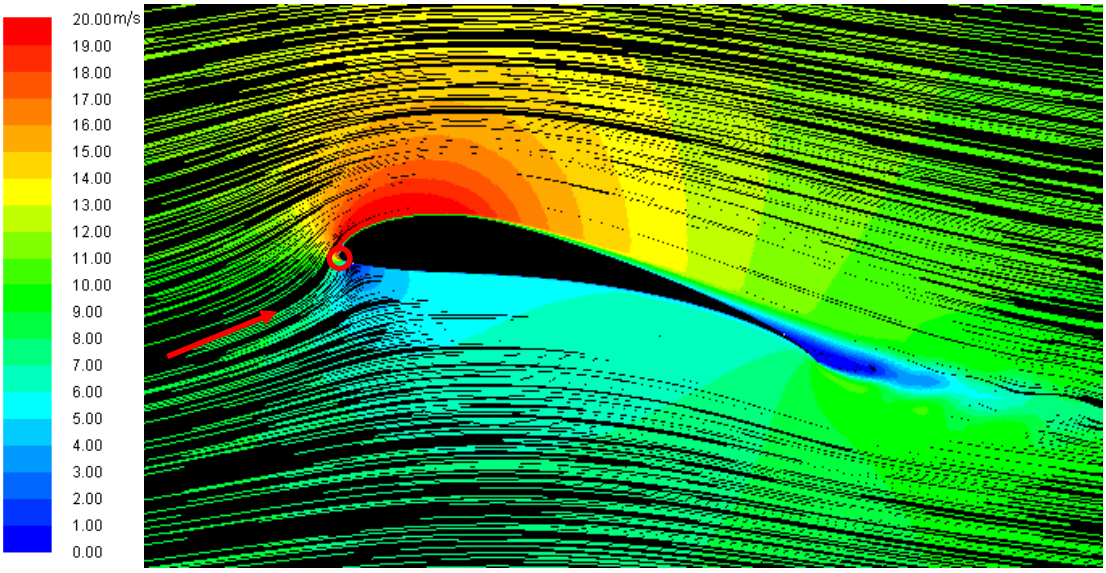

Figure 5.11 - Position of the stagnation point for an isolated S1223 airfoil, AoA =13°

Despite the angle of attack is more than halved, the stagnation point appears even more downstream. To sum up, the turbine and the cylinder, because of their trust, cause a divergence in the streamlines to occur in front of them. The airfoil, being placed very close to the body, experiences an actual angle of attack lower than the geometric one. The red arrows in the plot give a qualitative representation of the pre-rotation induced by the body.

5.1.1.2 Wake negative pressure

Pressure contours for the turbine, the cylinder and the isolated airfoil are given.

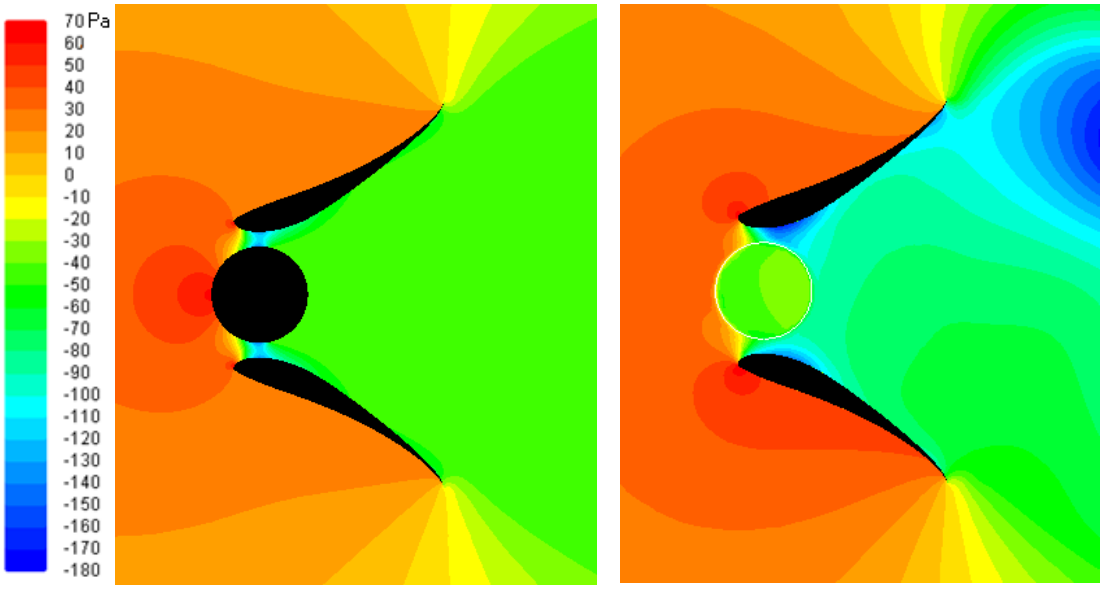

Figure 5.12 - α =30°, H = 1.3 D, W = 0, pressure contour: **a**-solid cylinder, **b**-turbine

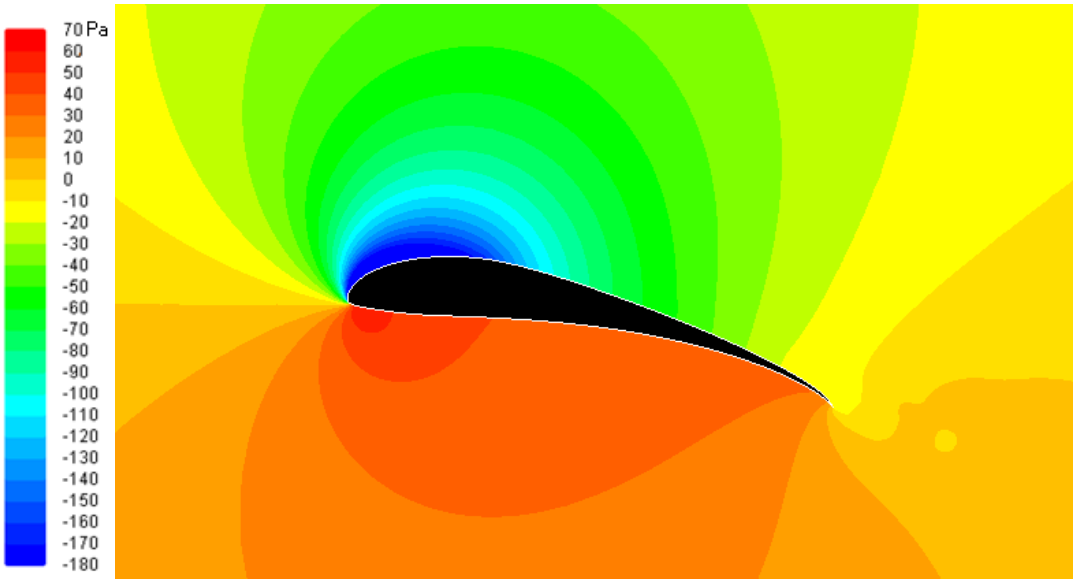

Figure 5.13 - Pressure contour for an isolated S1223 airfoil, AoA =13°

The main different that can be observed between the first two contours and the pressure map for the isolated airfoil consists in the lack of a pressure recovery at the rear of the airfoil when either the turbine or the cylinder are placed inside the diffuser. This for both the turbine and the cylinder creates a negative pressure region in their near wake. The origin of this is slightly different, but are related to the drag force experience by the body:

- The turbine, even under ideal conditions, is subjected to a drag that is a consequence of the power extraction from the stream
- The cylinder experiences a form drag that is related to the BL separation from its surface which creates a low pressure zone in the near wake

This phenomenon originates a fringe benefit on the diffuser, for it greatly reduces the adverse pressure gradient on the airfoils. The following graph represents the coefficient of pressure distribution along the wall for the present cases study.

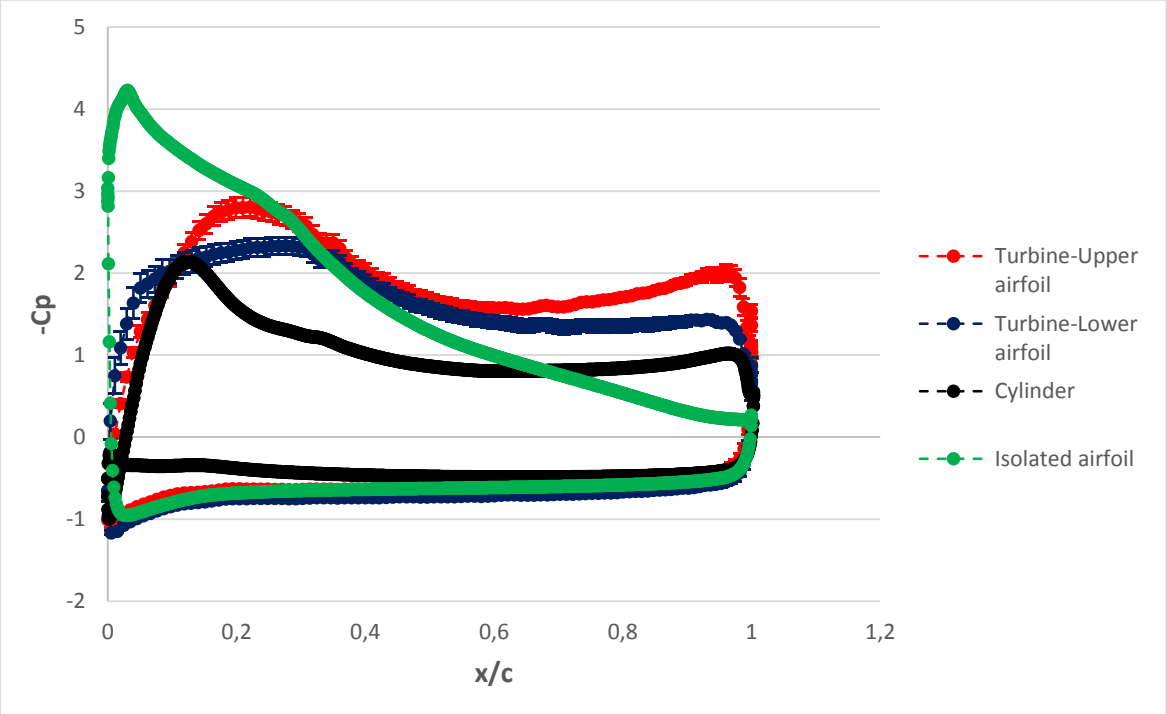

Graph 5.3 - Profile of the coefficient of pressure on the surface of the airfoil

It is evident that even if the isolated airfoil has a lower angle of attack, it operates under more critical condition because of the strong and almost constant adverse pressure gradient that BL must withstand.

5.1.3 Effects of the angle of the diffuser

The effect of the increasing angle is depicted in the following graphs

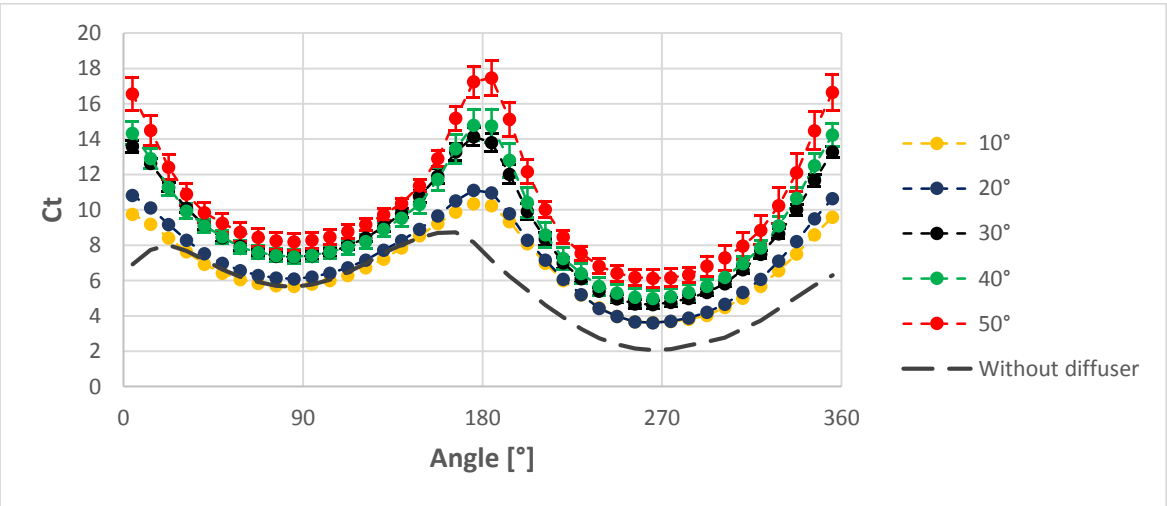

Graph 5.4 - Profiles of the x-velocity along the actuator ring

As regards the x-velocity (U) a substantial upshift of the profile can be observed and this is coherent with equation 3.29. For moderate angles (<=20°) the greater benefits affects the downwind half but when the incidence is high (>=30°) even the upwind half experience a moderate acceleration.

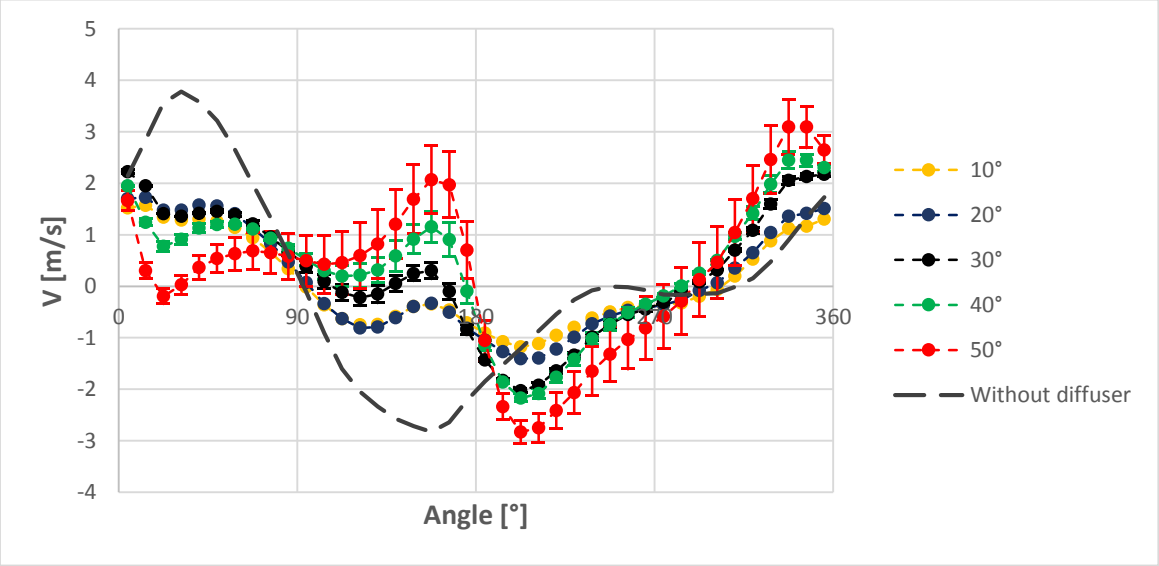

Graph 5.5 - Profiles of the y-velocity along the actuator ring

The y-velocity (V) shows a very interesting plot. As the diffuser strength increases, V exhibits completely opposite pattern especially in the upwind part. The explanation of this phenomenon is straightforward when the effect of the turbine and the diffuser on the mass flow are considered.

The turbine tends to slow down the incoming flow so an exiting mass flow across the normal boundaries must be set in order to satisfy the continuity equation; this means that the streamlines must diverge across the rotor.

The diffuser accelerates the flow in the convergent part (converging streamlines) and slows it down in the divergent part (diverging streamlines).

When the turbine operates inside the diffuser throat, the previously considered effect can be roughly superposed. This explains why the diffuser contrasts the diverging behavior in the upwind half while it enhances the streamlines divergence in downwind.

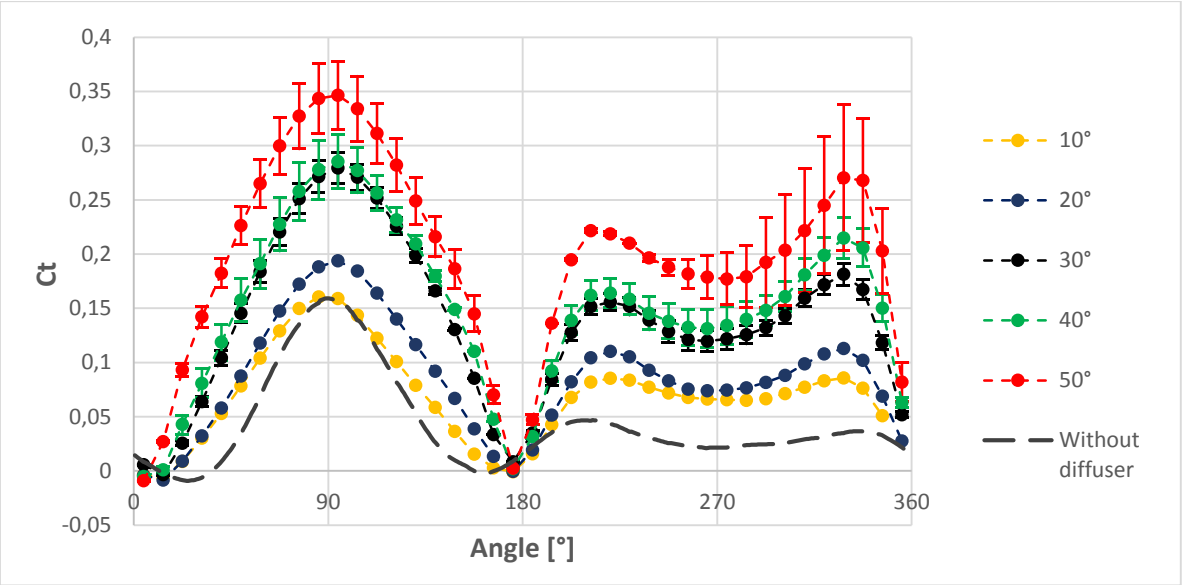

Graph 5.6 - Ct curves at different divergence angles

The effect of the modified U and V are evident when the torque curve are plotted. Beside an overall rise of the power output due to the U increase, a fattening of the upwind torque can be observed. It is due to streamlines divergence prevention made by the diffuser that increases the relative angles of attack of the blades as already observed.

5.2 Throat area optimization

The second parameter whose influence has been investigated is the throat area. Equation 3.29 indicates that the Cp is inversely proportional to the throat area. The selected angle of divergence was 40°, because higher angles leaded to BL separation in the diffuser, except for the lucky but apparently instable 50° case seen before. The results of the analysis are exposed below.

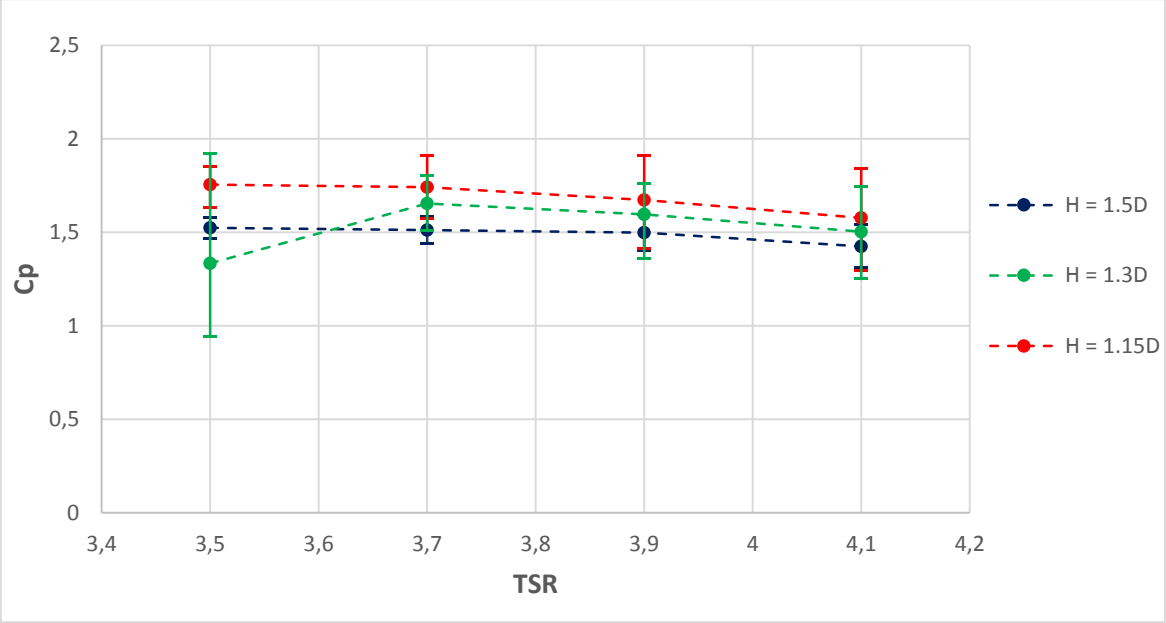

Graph 5.7 - α = 40°,W = 0, Cp/TSR curves for different throat section

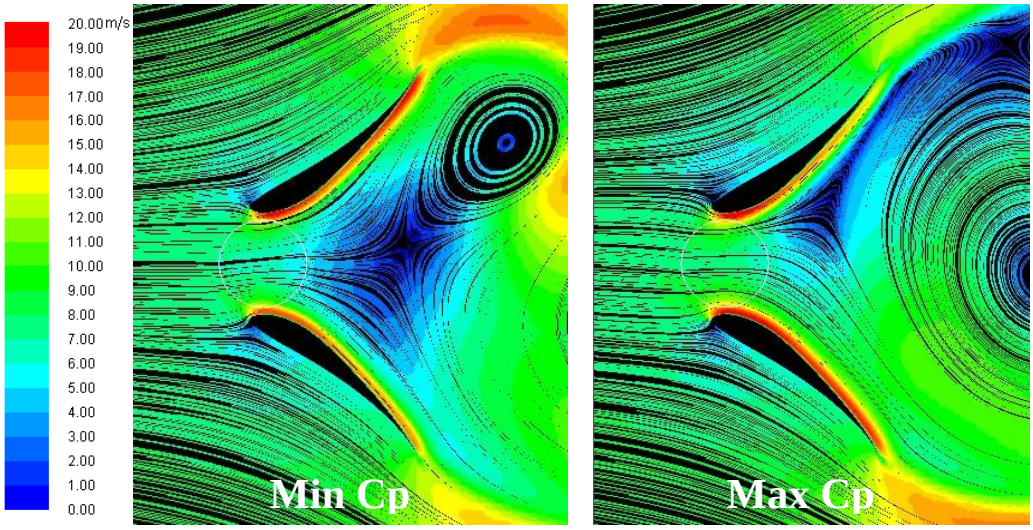

Figure 5.14 - α = 40°, H = 1.15 D, W = 0, TSR = 3.7: streamlines colored by velocity magnitude

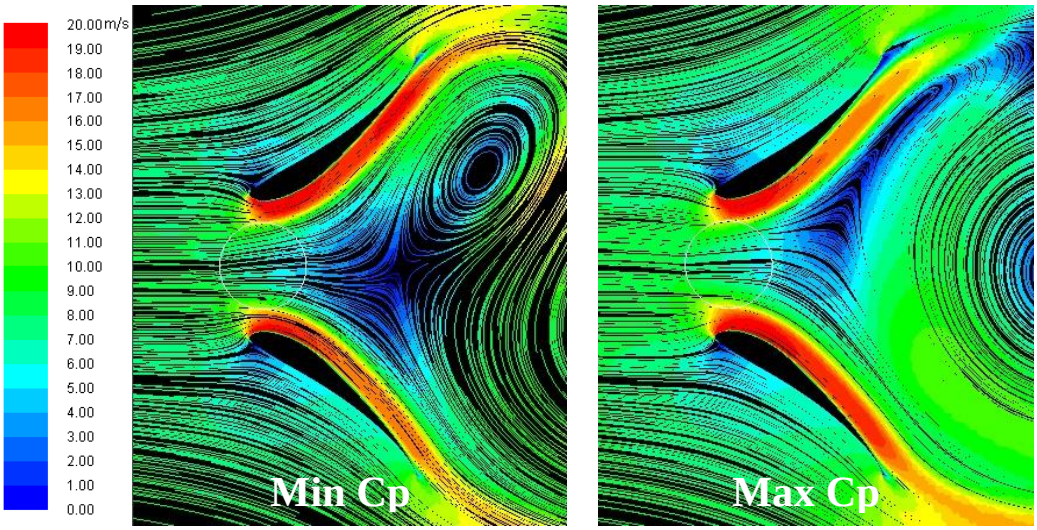

Figure 5.15 - α = 40°, H = 1.5 D, W = 0, TSR = 3.7: streamlines colored by velocity magnitude

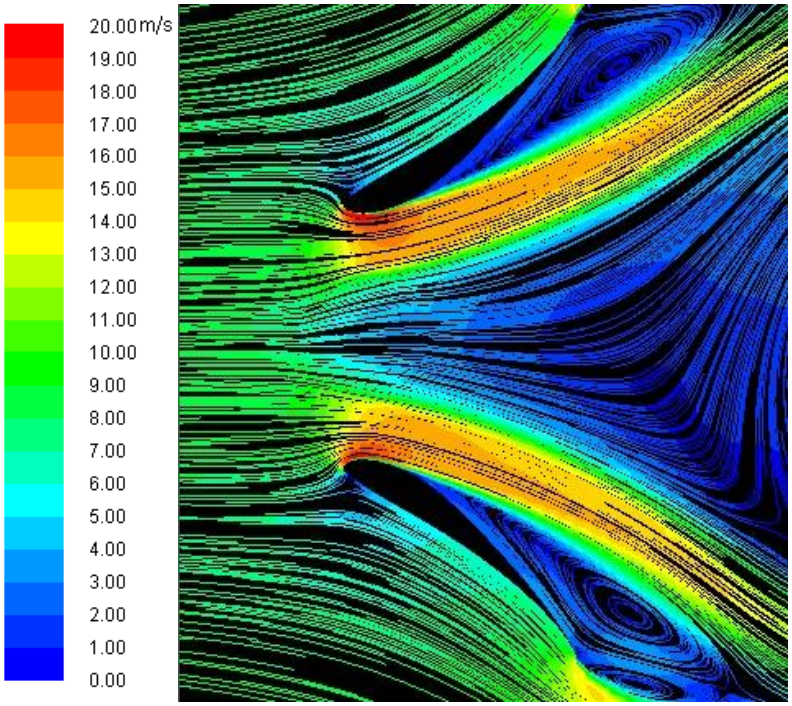

Figure 5.16 - α = 40°, H = 2 D, W = 0, TSR = 3.7: streamlines colored by velocity magnitude

As the throat area increases, the gap between the turbine and the diffuser becomes wider. This permits a larger amount of air to flow inside the diffuser. When throat becomes twice the turbine diameter the flow separates from the suction side of the airfoils and the performance greatly decay (fig. 5.16). This is trivial, since when the distance between the airfoils and the turbine is high the flow should approaches the isolated airfoil case solution, corresponding to a deeply stalled wing.

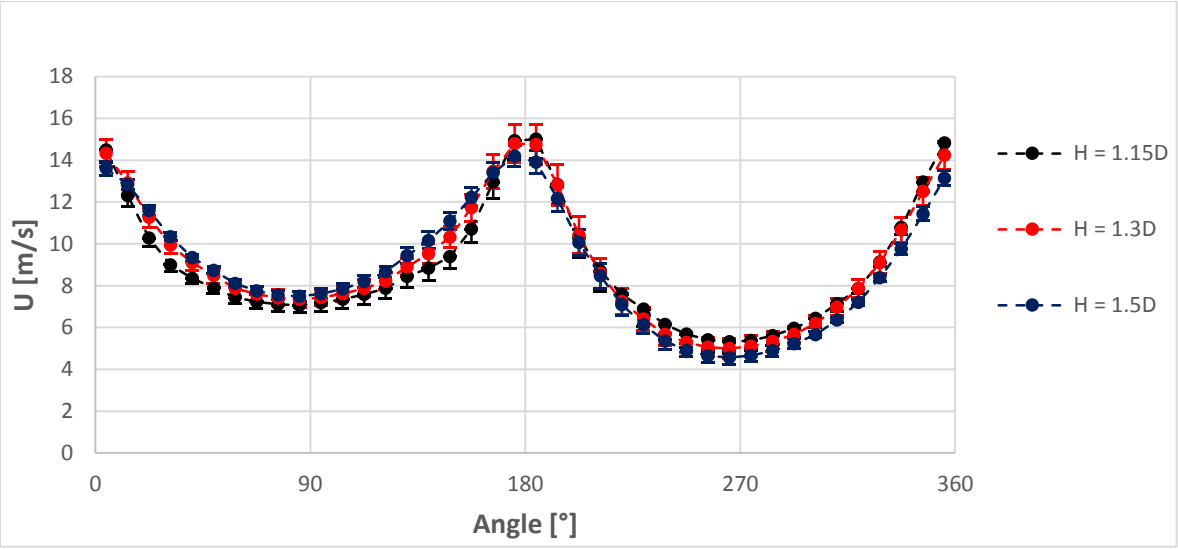

Graph 5.8 - Profiles of the x-velocity along the actuator ring

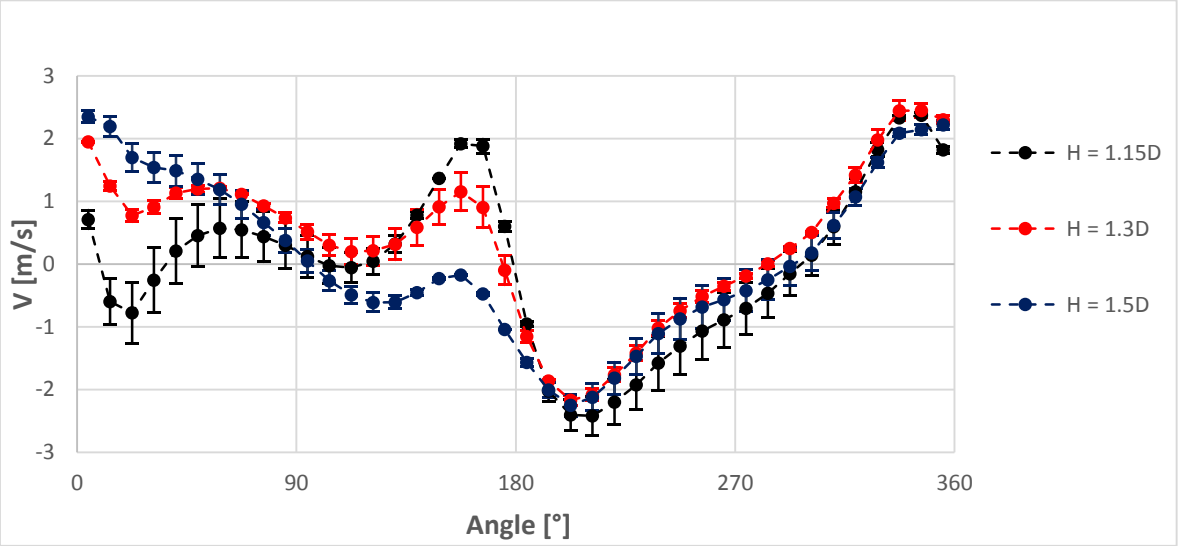

Graph 5.9 - Profiles of the y-velocity along the actuator ring

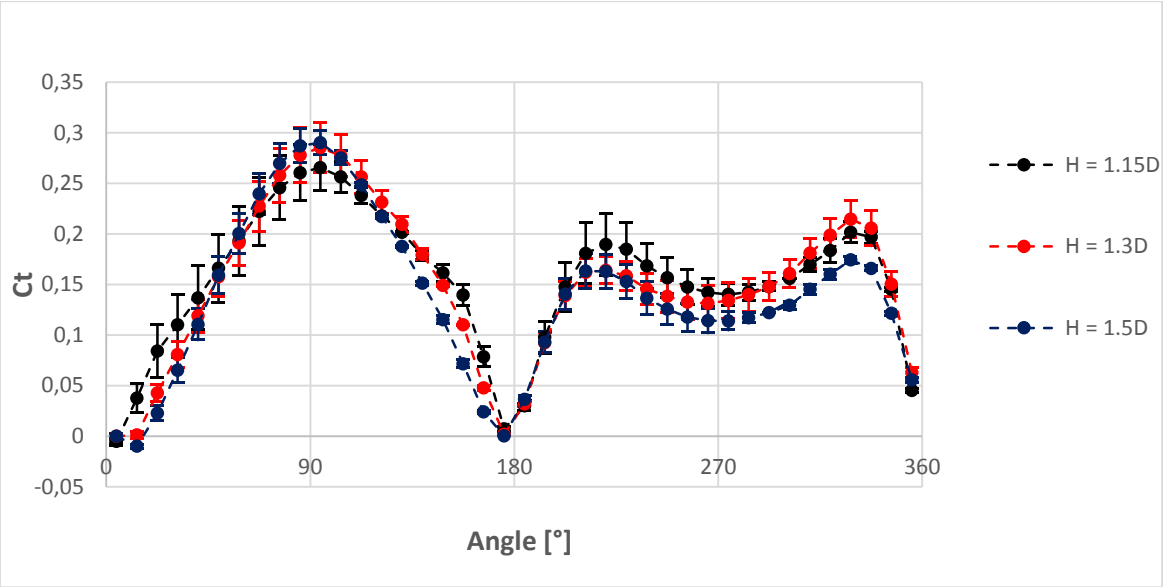

Graph 5.10 - Ct curves for different throat sections

The results show small differences. It can be noticed how with the smaller throat the diffusive process in upwind is enhanced (see graph 5.9). The most important effect of reducing the throat, however, was the BL thinning and stabilization. Therefore, an H equal to 1.15 D, that gives also better overall performances, has been chosen.

5.3 Turbine position optimization

Four different new position were tested with the previously optimized angle and throat (α = 40°, H = 1.15 D). The graphs and figures below show the results.

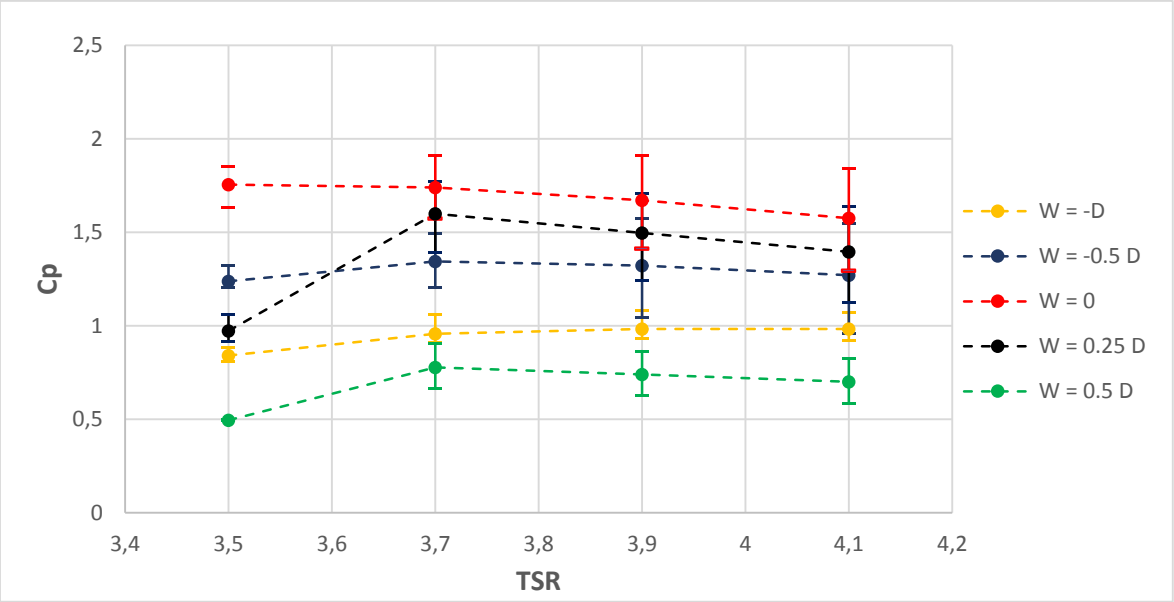

Graph 5.11 - α = 40°, H = 1.15 D, Cp/TSR curves for different positions of the turbine

None of the new configuration was able to achieve the Cp of the one with the diffuser placed exactly in the throat. For two of them, the one with the turbine placed half a diameter upwind and the one with the turbine moved one diameter downwind, the diffuser stalled, as e consequence of the increased mass flow due to the reduced "cork effect" exerted by the turbine. The streamlines are reported below.

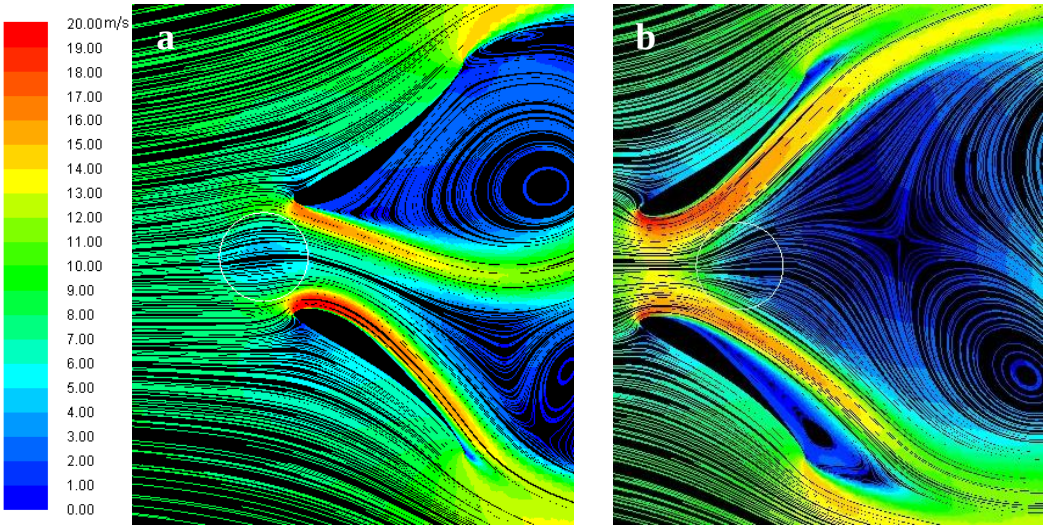

Figure 5.17 - The unfortunate configurations with W = 0.5D (**a**) and W = -D (**b**)

The other two cases, referring to smaller shift of the turbine, are more interesting and deserve an in-depth analysis. The streamlines plot relative to the mentioned configurations are here reported.

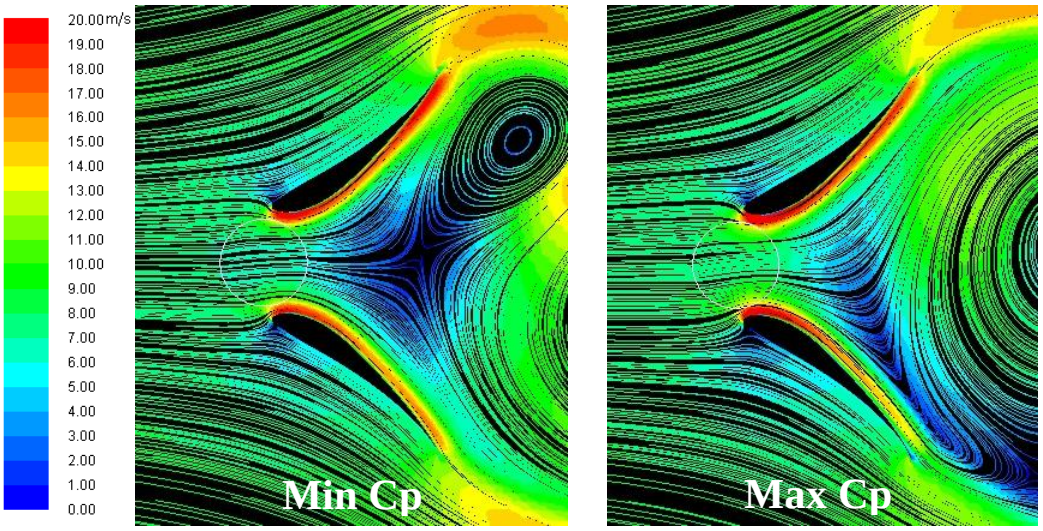

Figure 5.18 - α = 40°, H = 1.15 D, W = 0.25 D, TSR = 3.7: streamlines colored by velocity magnitude

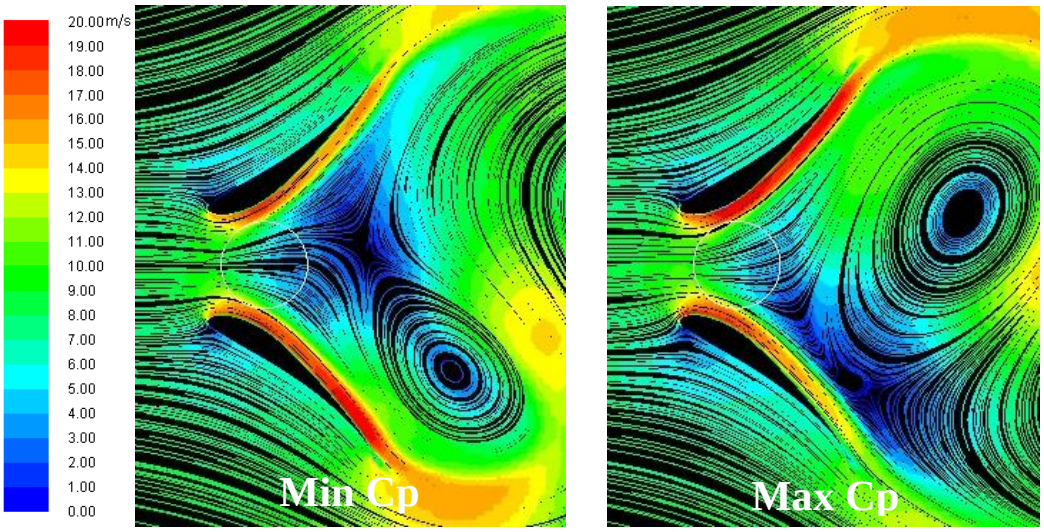

Figure 5.19 - α = 40°, H = 1.15 D, W = -0.5 D, TSR = 3.7: streamlines colored by velocity magnitude

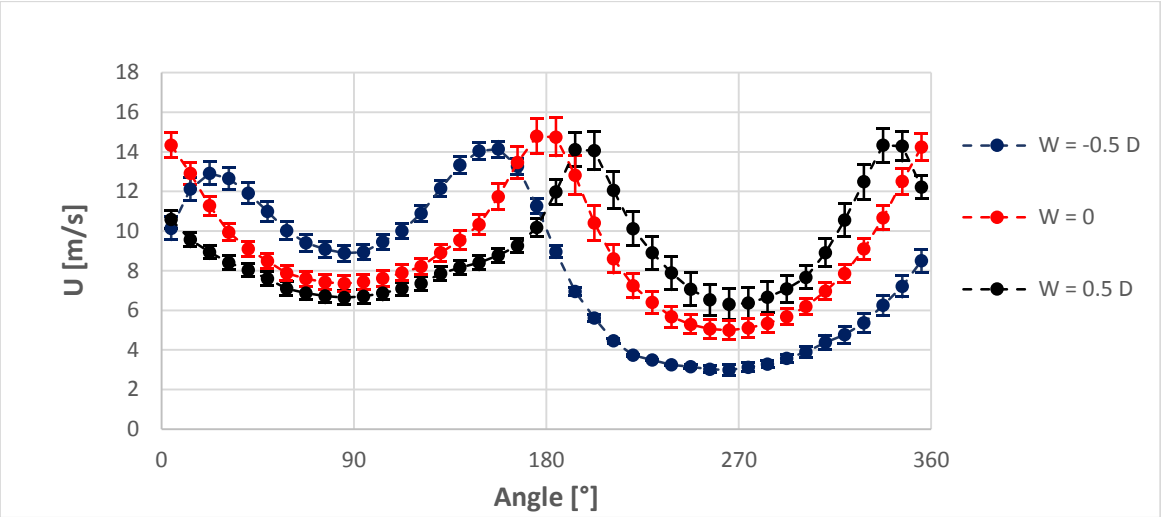

Graph 5.12 - α = 40°, H = 1.15, profiles of the x-velocity along the actuator ring

As it could have been expected, when the turbine is placed downwind in respect to the diffuser throat, the velocity unevenness between the upwind half and the downwind increases, whereas when it is placed after, the velocity is even higher in downwind. This was expectable, since the greater acceleration takes place in the throat.

The y-velocity plot confirms this trend and highlight how in the case of the turbine placed upwind the divergence of the velocity experienced by the turbine is higher, since it is placed in the divergent part of the diffuser.

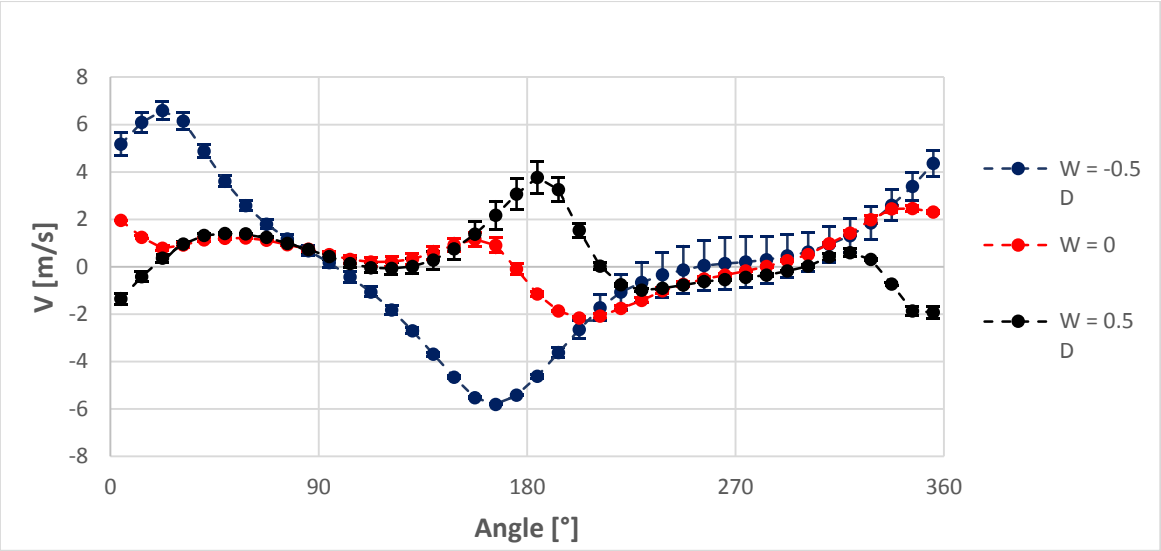

Graph 5.13 - α = 40°, H = 1.15, profiles of the y-velocity along the actuator ring

The torque curves are reported below.

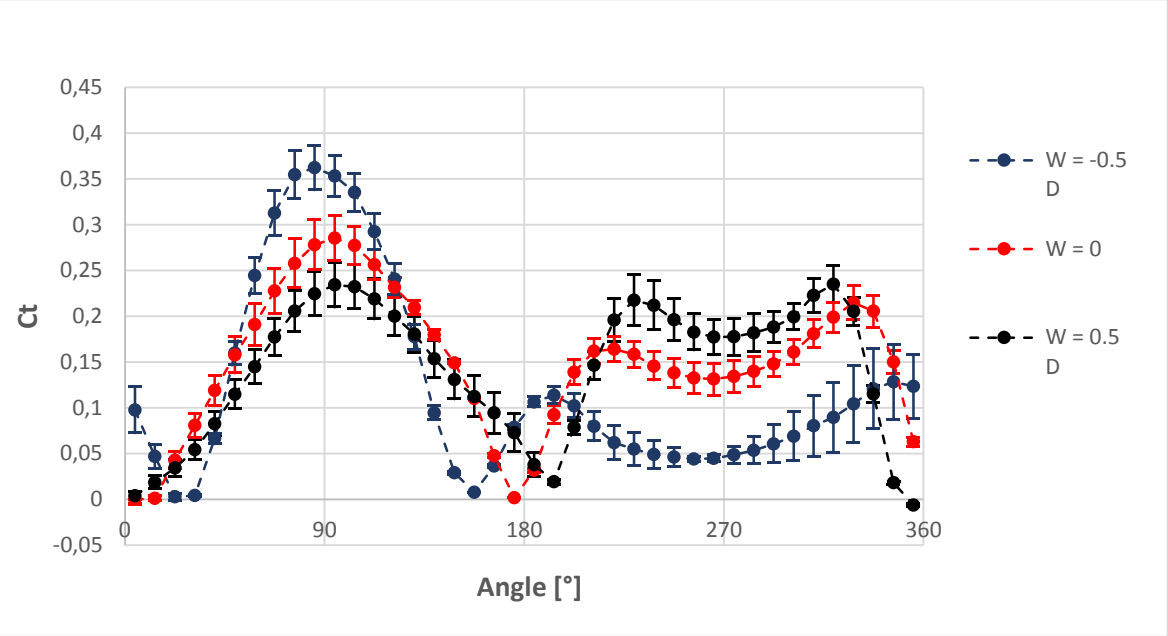

Graph 5.14 - Ct curves for different positions of the turbine

For the W = -0.5 D case, the power production takes place mainly in upwind, while for the opposite case it appears more balanced. This suggest an interesting benefit that can be harnessed by placing the turbine slightly upwind: the torque ripple reduction. However, the overall performance, even in this case, are poorer than in the base configuration. Malipeddi et al. [4] reported exactly the same behavior concerning an analogous case.

5.4 Optimal design

The benefits on the stability of the BL obtained by virtue of the throat area reduction, made attractive the possibility of exploiting this effect to have an attached flow even at higher angle. A successful attempt was made increasing the angle to 50 degrees that therefore became the optimal configuration. The following pictures show how even for this very critical incidence the BL is thin and stable.

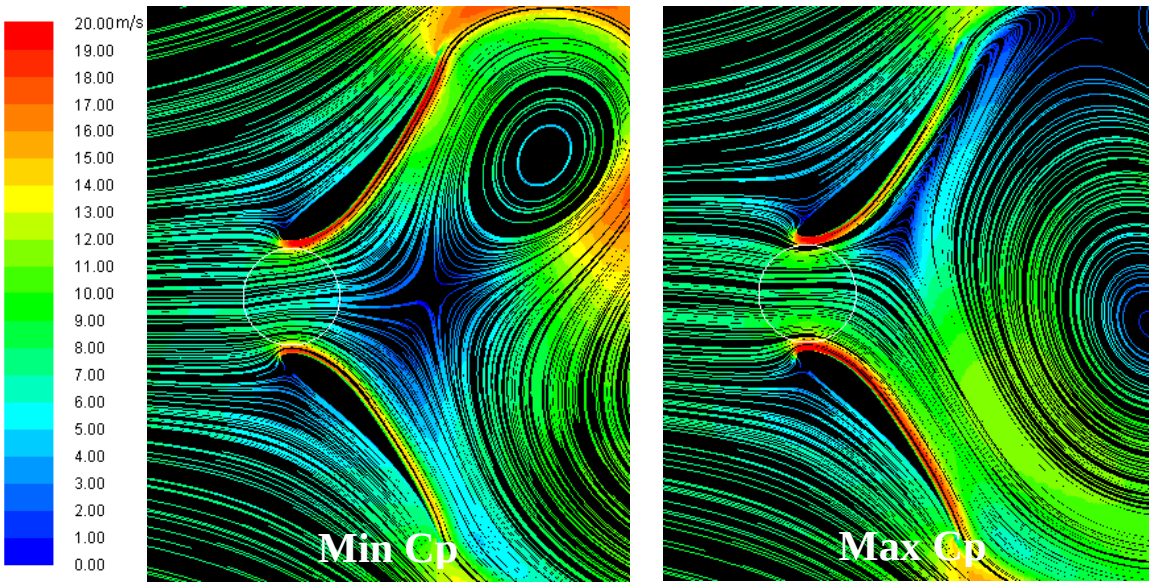

Figure 5.20 - α = 50°, H = 1.15 D, W = 0, TSR = 3.9: streamlines colored by velocity magnitude

The Cp/TSR curve approaches 2, a remarkable result.

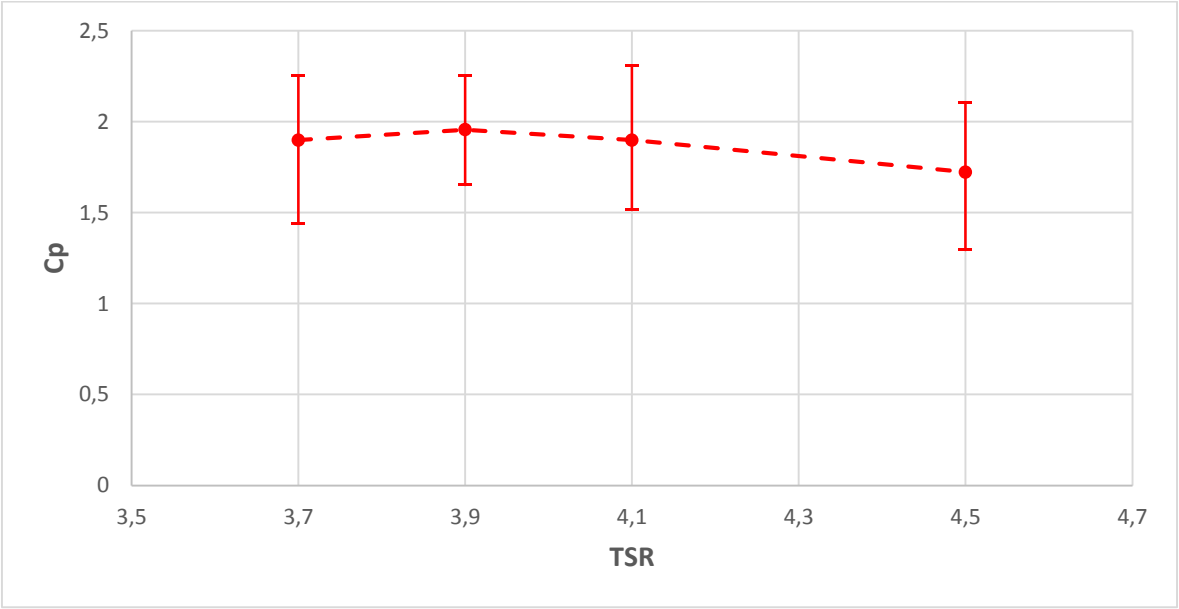

Graph 5.15 - Cp/TSR curve for the optimal configuration

V References

[1] Daniel C. *One-at-a-Time Plans*, Article in Journal of the American Statistical Association 68(342):353-360 · June 1973

[2] Coşoiu CI, Georgescu AM, Degeratu M, Haşegan L, Hlevca D. *Device for passive flow control around vertical axis marine turbine*, Earthand Environmental Science 15 (2012) 062031

[3] Geurts B, Simão Ferreira CJ, Van Zuijlen A, Van Bussel H. *Aerodynamic Analysis of a Vertical Axis Wind Turbine in a Diffuser*, 3rd EWEA Conference - Torque 2010: The Science of making Torque from Wind, Heraklion, Crete, Greece, (2010)28-30

[4] Malipeddi AR, Chatterjee D. *Influence of duct geometry on the performance of Darrieus hydroturbine*, Renewable Energy 43 (2012) 292-300

[5] Maître T, Mentxaka Roa A, Pellone C, Achard JL. *Numerical 2D hydrodynamic optimization of channeling devices for cross-flow water turbines*, U.P.B. Sci. Bull., Series D, Vol. 72, Iss. 1, (2010)

[6] Van Beveren C. *Design of an urban wind turbine with diffuser*, Master Thesis, Delft University (2008)

[7] Batchelor GK , *Introduction to fluid dynamics*, ISBN 0 521 66396 2 paperback (2002)

Part VI - Power curve

To estimate the operative efficiency of the new DAWT, some correction have been introduced to adapt the power obtained in the 2D CFD to more realistic open flow 3D domain.

6.1 Power curve

The ideal power curve of a turbine is shown below [1].

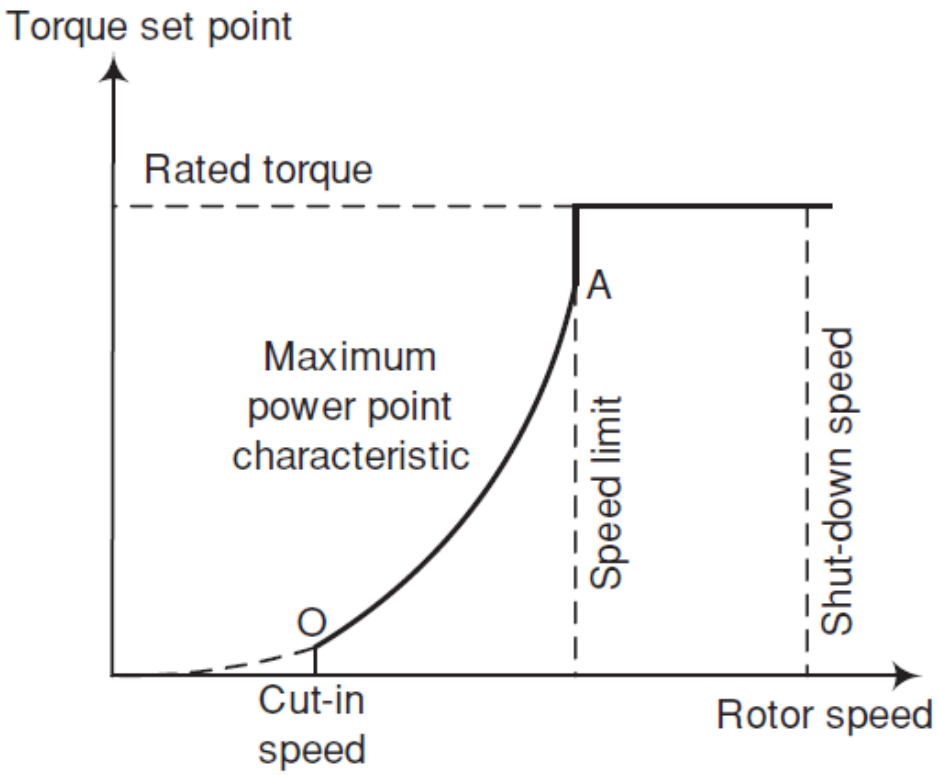

Figure 6.1 - Ideal power curve of a wind turbine [1]

The power curve ideally split in four parts:

1. Below the cut-in speed the power output is null
2. Above the cut in but below the rated wind speed the rotor operates at his maximum efficiency point
3. Above the rated wind speed and the cut off (or shut down) wind speed the power is held constant to the nominal value
4. Above the shut down wind speed the rotor is stopped for safety issues

The ideal power curve, which is the one granting the higher wind energy exploitation for a given machine size (and thus installation costs) can be approached by means of sophisticated pitch and rotor speed controls, that are supposed not to be cost-effective for the present micro-turbine.

For a small turbine, it could be feasible a variable speed control by means of a Maximum Power Point Tracker that has been applied even to small turbines rotor in different contests [2, 3]. The following controller characteristic comes from Ref. [4] and has been adopted on a 500 kW Darrieus turbine, but there are examples of MPPT for sale in the market of mini and micro wind generation.

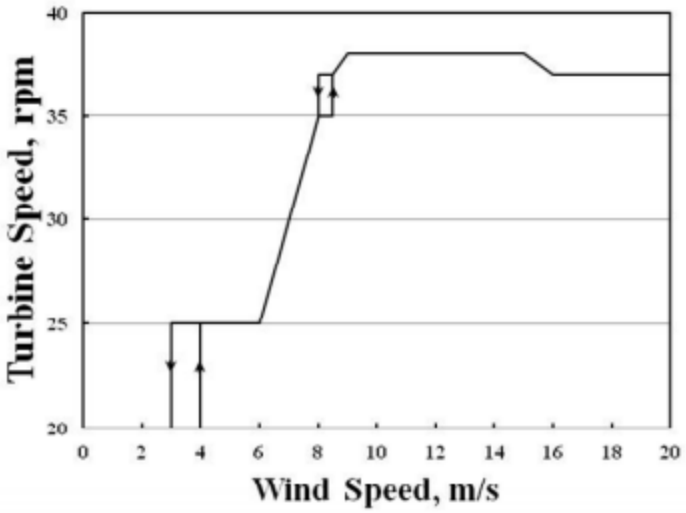

Figure 6.2 - Rotor speed control for a 500 kW Darrieus [4]

It has been consequently chosen to simulate the same control strategy on the present turbine. This method does not permit to achieve constant power once the rated wind speed is passed and so a not negligible overloading for wind speed slightly higher than the rated one must be accounted for.

In the light of the above, to build the power curve of both the bare and the diffused augmented turbine, two Cp/TSR curve at lower wind speed (5 and 7.5 m/s) have been simulated, in order to find the optimal Cp that an hypothetically perfect MPPT would track. After that, three high speed configurations (11, 12 and 14 m/s) have been simulated with fixed ω to describe the behavior of the turbine in passive stall conditions.

6.1.1 Bare turbine

Before considering the result of the simulations, it is worthwhile to estimate *a priori* the effect of the undisturbed velocity in the turbine performance by means of non-dimensional analysis and Buckingham's Theorem. The characteristics parameter for 2D approach are the following:

- P, the power
- U, the flow velocity
- ω, the rotational speed
- D, the rotor diameter
- c, the blde chord
- N, the number of blades

- μ, the fluid viscosity
- ρ, the fluid density

The fundamental units for a non-reactive, incompressible fluid in which the thermal effect are negligible are [s], [Kg] and [m]. Thus the non-dimensional group describing the system are 8-3 = 5 (they reduce to 4 since N is non-dimensional). In fact, as in common practice, we have:

- $C_p = \frac{P}{\frac{1}{2}\rho U^3 D}$, the coefficient of power
- $TSR = \frac{\omega R}{U}$, the tip speed ratio
- $Re = \frac{\rho U D}{\mu}$, the relative Reynolds number
- $\sigma = \frac{Nc}{\pi D}$, the solidity

For a given geometry, the solidity is also fixed and its effect has not been investigated in the present work. So, the overall system behavior can be described by the following equation [5]:

$$C_p = f\,(TSR, Re) \qquad [6.1]$$

The TSR effect has been widely observed in the previous simulations.

Concerning the effect the Reynolds number, since it is expected to influence mainly the blades' performance, it is worthwhile to adopt the one relative to the blades themselves:

$$Re_{rel} = \frac{\rho U_{rel} D}{\mu} \qquad [6.2]$$

This number, however, depends on the Re and the TSR and thus the relationship 6.1 still holds.

In the light of the above, the undisturbed flow velocity affects the turbine performance, for a give TSR, since it changes the Reynolds number at which the blades operate. The following graph shows the relative Reynolds number at TSR 2.7 for three wind velocities.

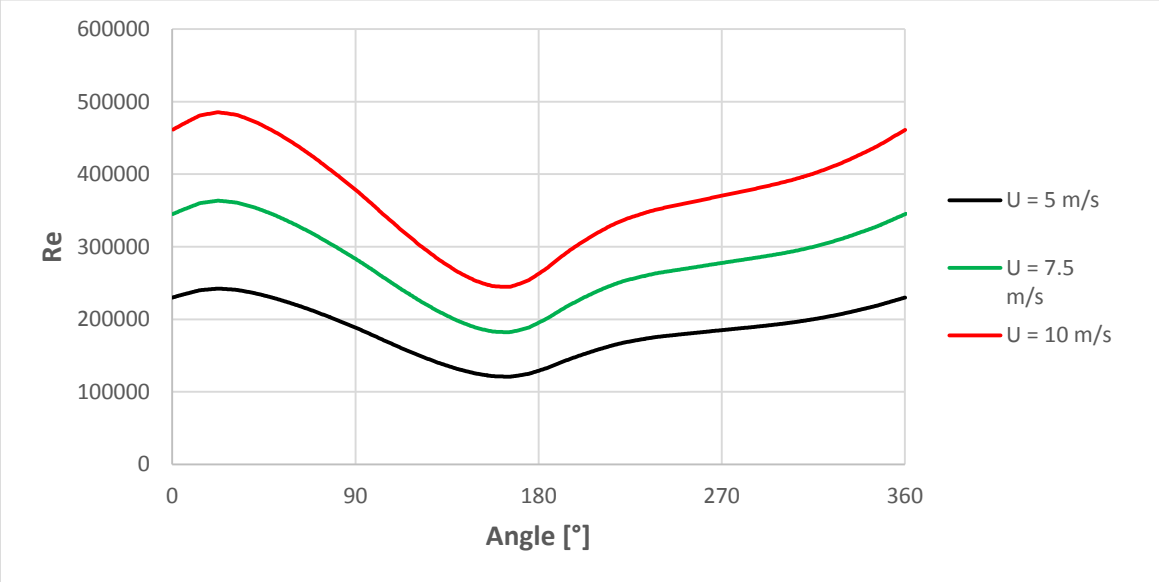

Graph 6.1 - Bare turbine, TSR 2.7: Reynolds number relative to the blades according to AR

The Cp/TSR curves for two different wind speed lower the rated velocity (10 m/s) have been simulated by means of the steady iterative method (par. 4.5) and the results are showed below.

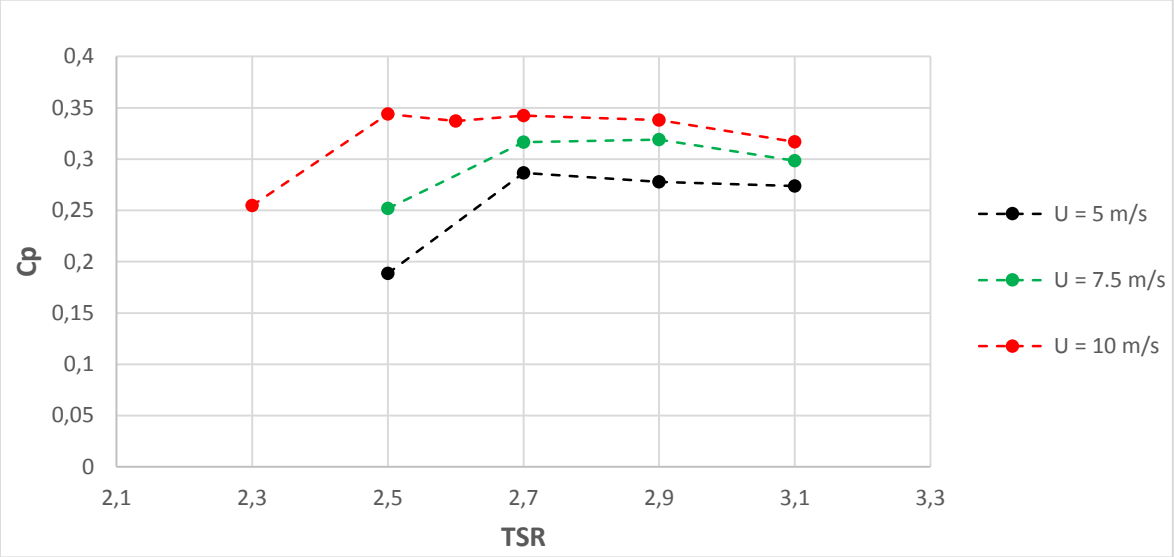

Graph 6.2 - Bare turbine: Cp/TSR curves for different wind speed according to AR

The maximum Cp decays when the wind slow down and this is consistent both with experiments [6] and the just exposed theory. It can also be noticed how the dynamic stall occurs at higher TSR (which means lower angles of attack) for low Reynolds, as a consequence of the correlation for α_{LEV} (see par. 4.4.1.3).

For wind speed higher than 10 m/s, the rotor speed have been held constant. The results are shown in the following chart.

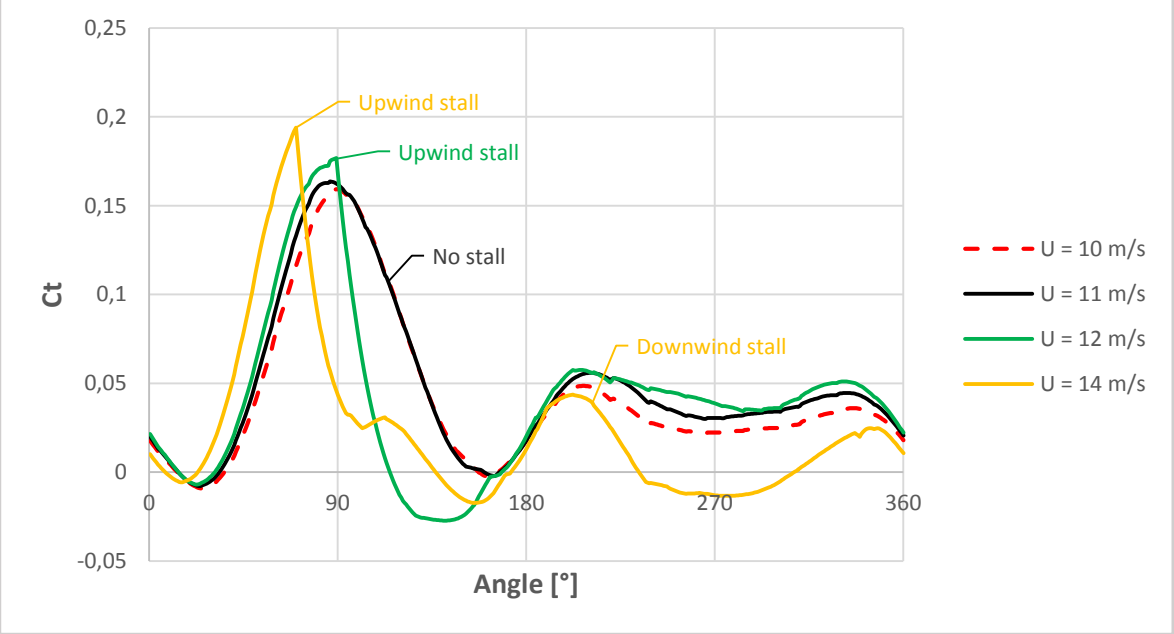

Graph 6.3 - Bare turbine, ω = 27 rad/s: Ct curves for high wind speed according to AR

The higher wind velocity, the more the stall affects the Ct curve.

The power curve, built by taking the maximum Cp point from graph 6.2 is reported below.

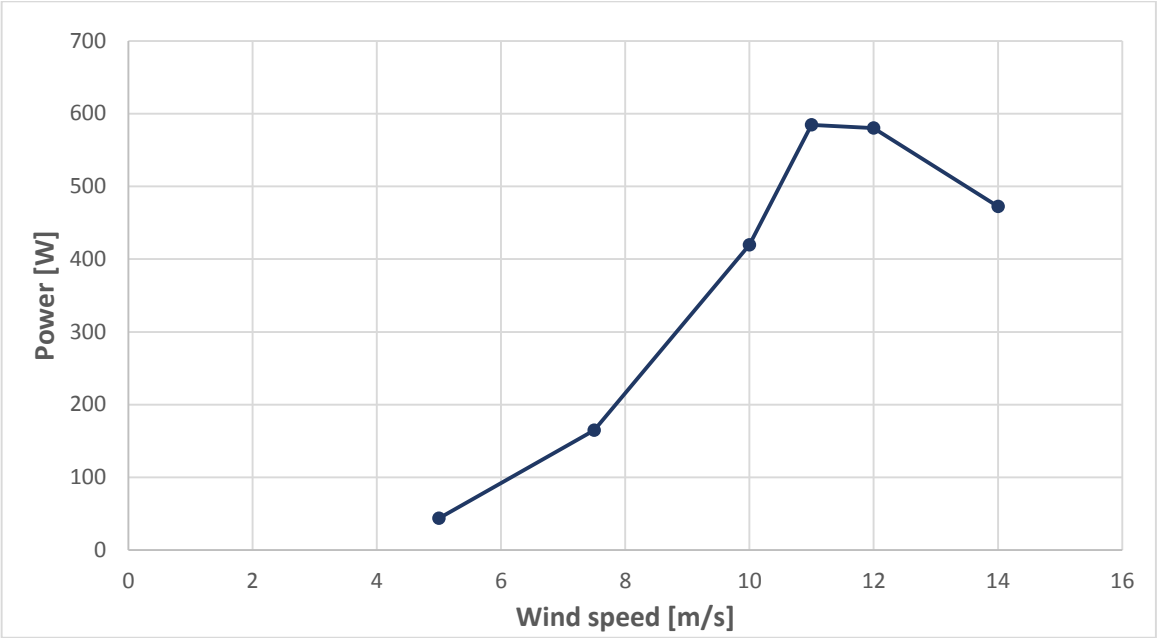

Graph 6.4 - Bare turbine, Power curve to AR

6.1.2 Diffuser augmented turbine

The same procedure has been adopted for the turbine with the diffuser. The Cp curves for low wind speed are reported below and show a behavior similar to the bare turbine ones.

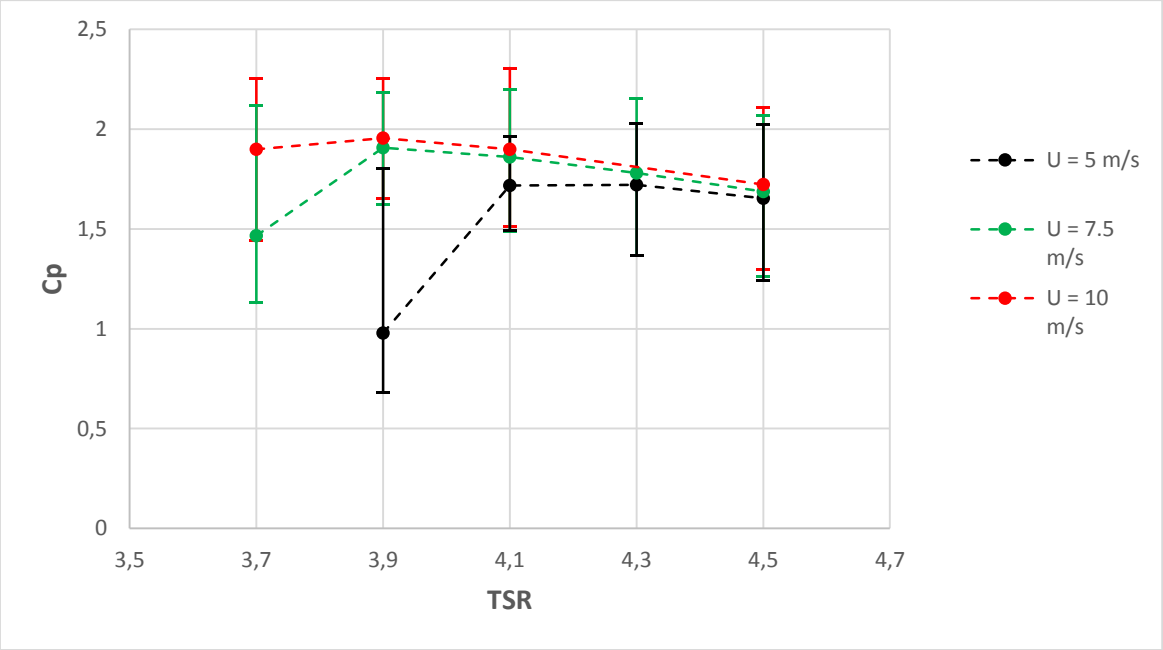

Graph 6.5 - DAWT: Cp/TSR curves for different wind speed according to AR

For the high speed cases, the presence of the diffuser greatly modifies the phenomena occurring. In fact, as the speed exceeds the nominal value, the turbine blades experience a stall because of the increased angles of attack. This cause a sudden lift decay and an overall trust reduction. This let a greater flow enter the diffuser and this is associated with a

repositioning of the stagnation point farther from the leading edge. As it was shown in par. 5.1.1.1, the stagnation point position is a good detector for the actual angle of attack in an airfoil. In other words, the diffuser experience a higher angle of attack and undergoes a disastrous stall. The following streamlines plot show the increasingly deep stall regime of the diffuser as the velocity rises. The timestep have been reduced to 0.002s for these simulations because the small vortex arising from the stall were expected to have a high frequency.

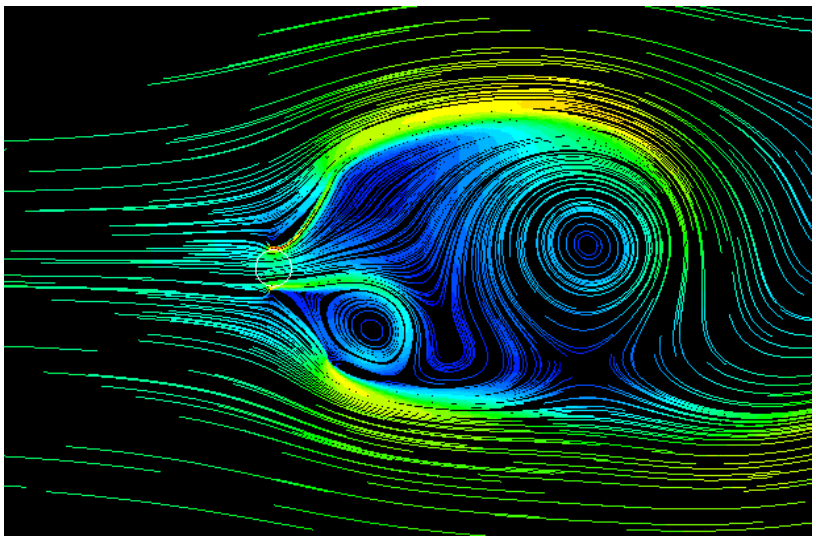

Figure 6.3 - U = 11 m/s, ω = 39 rad/s: streamlines colored by velocity magnitude

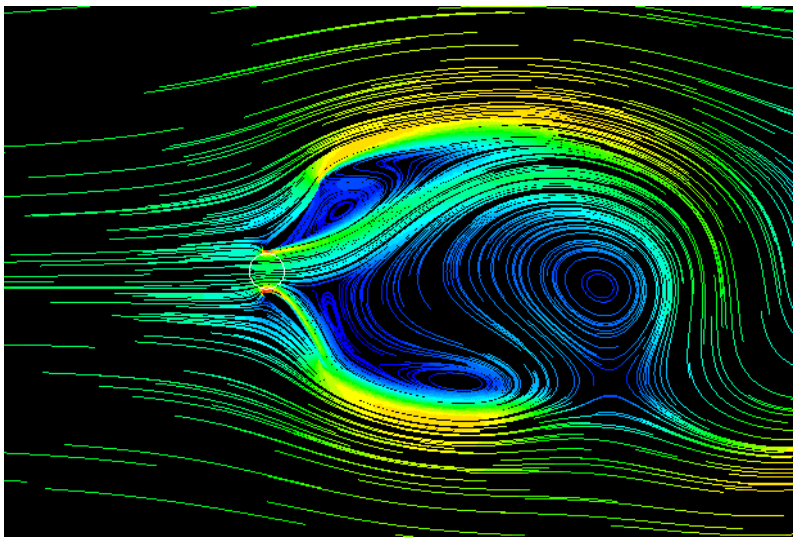

Figure 6.4 - U = 12 m/s, ω = 39 rad/s: streamlines colored by velocity magnitude

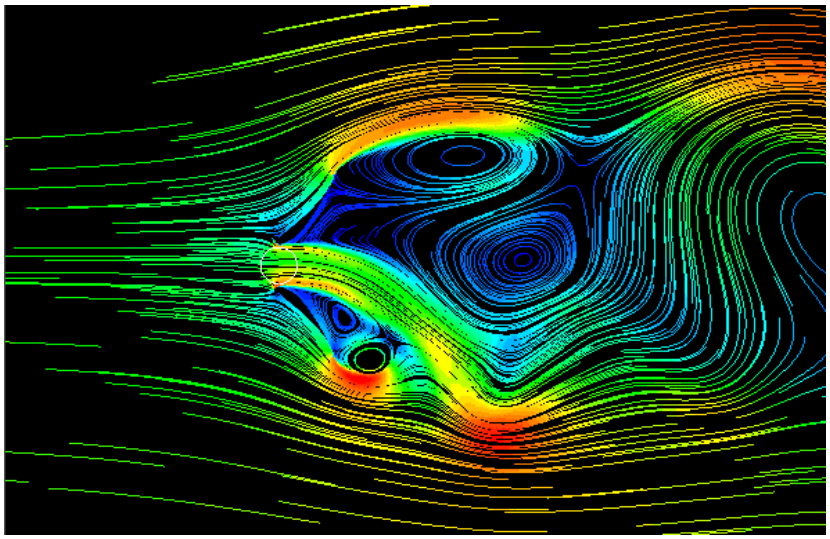

Figure 6.5 - U = 14 m/s, ω = 39 rad/s: streamlines colored by velocity magnitude

A check was made with 12 m/s to evaluate weather the stall occurred when the optimal TSR was established but it was confirmed that the diffuser works in attached flow regime as the proper rotor speed is set.

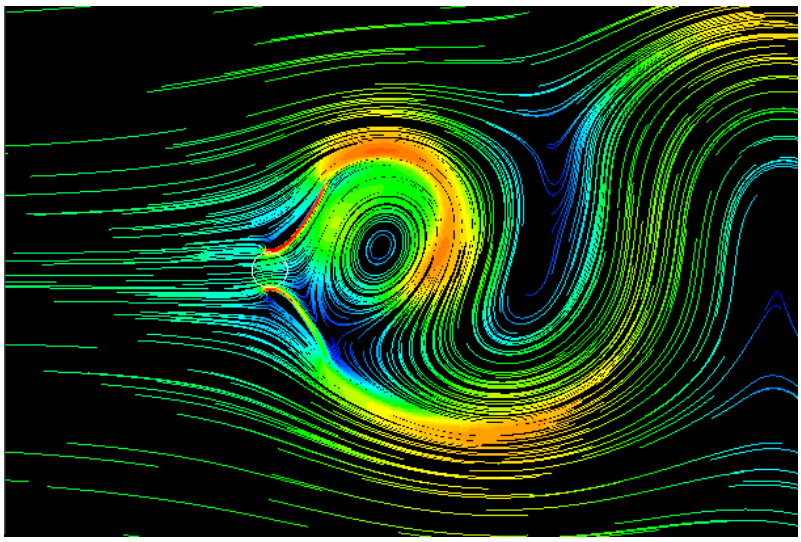

Figure 6.6 - U = 12 m/s, TSR = 3.9: streamlines colored by velocity magnitude

To conclude, the power curves for the bare and the diffuser augmented turbine are compared. The power output is roughly five times e higher when the diffuser is adopted. Unfortunately, the turbine with the diffuser exhibits a rude behavior at high wind speed.

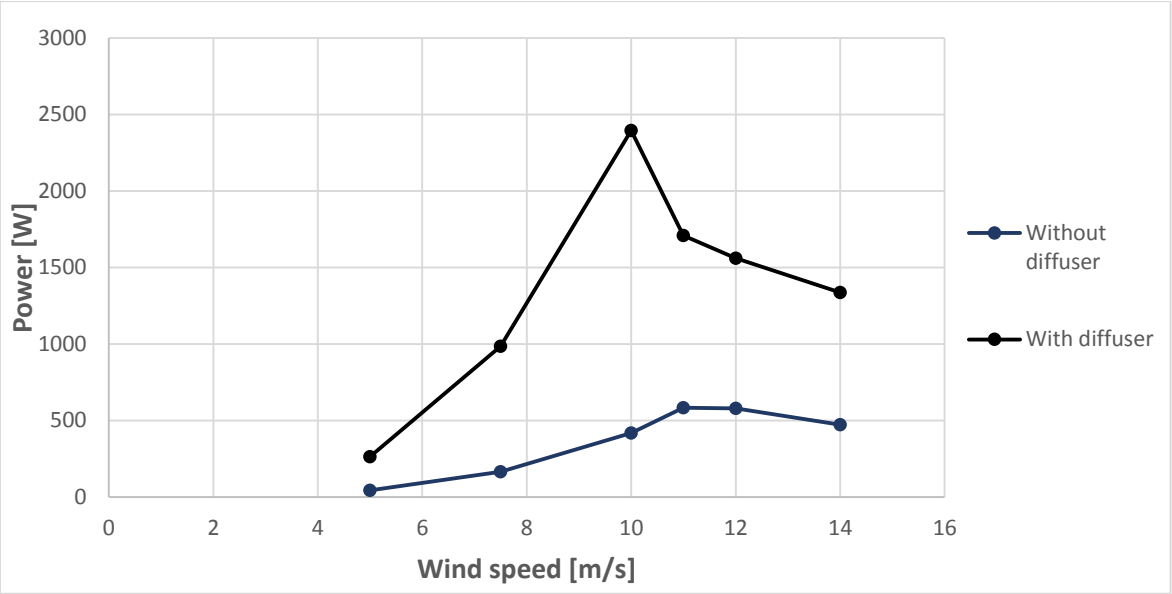

Graph 6.6 - Power curves for bare and shrouded turbine

This value needed for appropriate corrections to account for the various unideal effect occurring in a realistic 3D open domain.

6.1.2.1 CFD last check

As last check a CFD, simulation for the optimal configuration in the most critical condition of 5 m/s of wind speed have been performed with the same meshing criteria of par. 4.7.1. The compliance between the two model is not completely satisfactory, but a notable fact is that even after 500 revolutions (corresponding to many weeks of calculations on a 12 core supercomputer) the Cp trend CFD was still chaotic. Probably it would have required a very long and almost unaffordable time to reach a periodic regime.

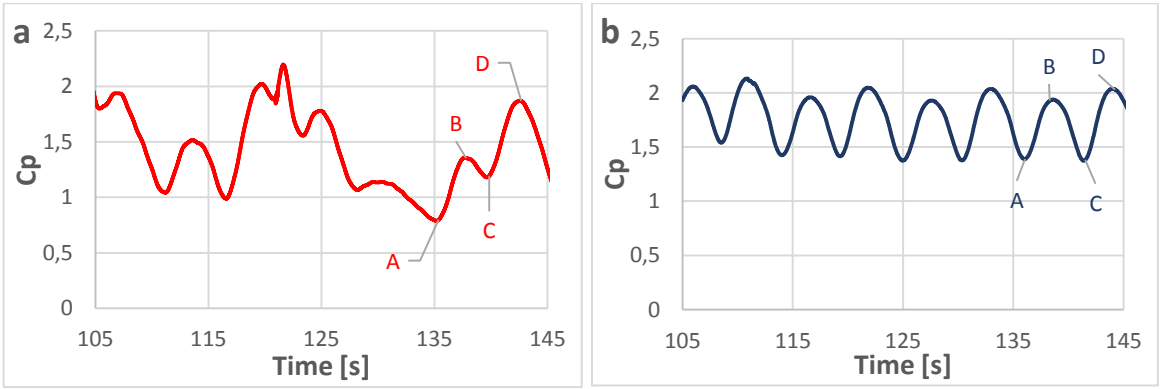

Graph 6.7 - Optimal configuration, U = 5 m/s: Time evolution of the Cp **a**-CFD, **b**-AR

The comparison of Ct curves between the CFD and the AR in different corresponding shedding moment is provided. For two cases (C, D) the agreement is poor in terms of absolute value, whereas in the other two a good compliance can be noticed.

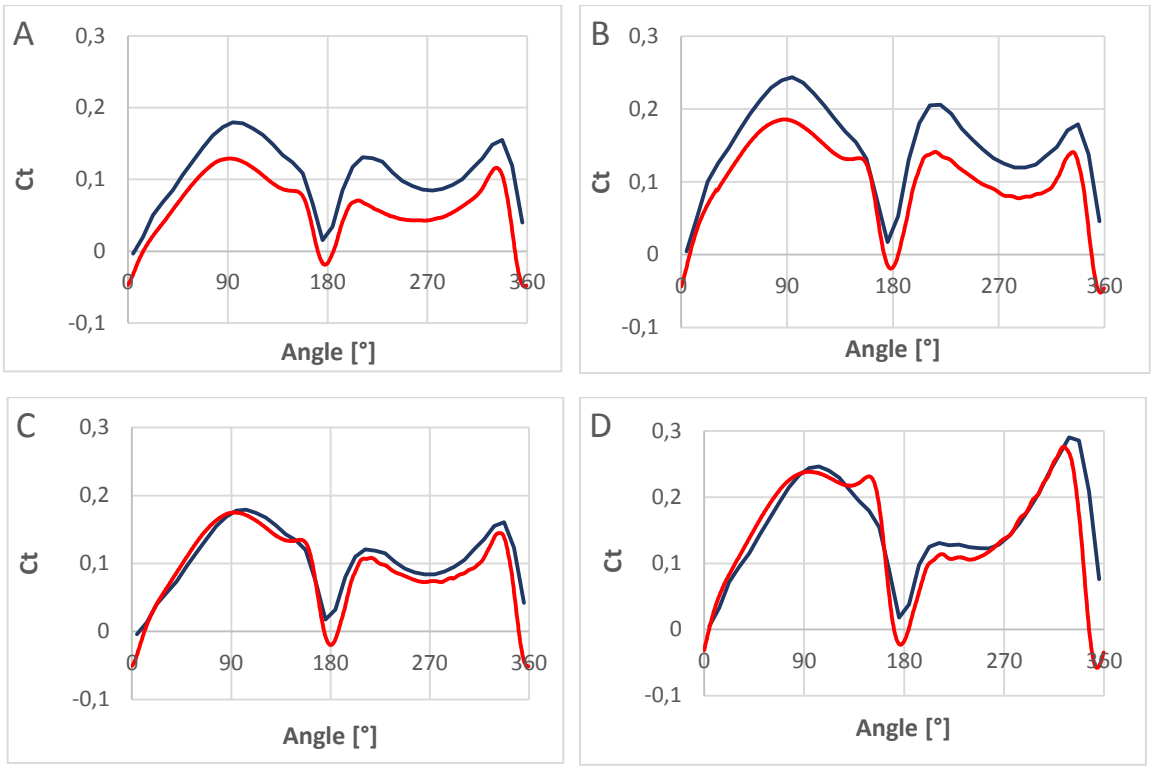

Graph 6.8 - Ct in different moment from previous graph from CFD (red) and AR (blue)

In the next page, also the flow field corresponding to the four moment selected previously are reported. Whereas the qualitative agreement is good, the velocities are quite different in terms of absolute value, with a general overestimation for the AR. However the most remarkable fact remains the BL attachment that even with an accurate CFD in very challenging conditions (50 degrees of AoA, low speed) confirmed. This accurate CFD provided also the value of the forces experienced by the diffuser. The global force coefficient defined as:

$$C_f = \frac{\sqrt{L^2+D^2}}{\frac{1}{2}\rho U^2 A} \qquad [6.3]$$

ranges from 2 to 3.5. This value can be considered valid for every case of attached BL. The highest velocity before the stall occurrence is 10 m/s, that, once inserted in the 6.3, gives an upper value of 2 kN/m, a notable load. For higher wind speed the AR detected forces of the same order of magnitude.

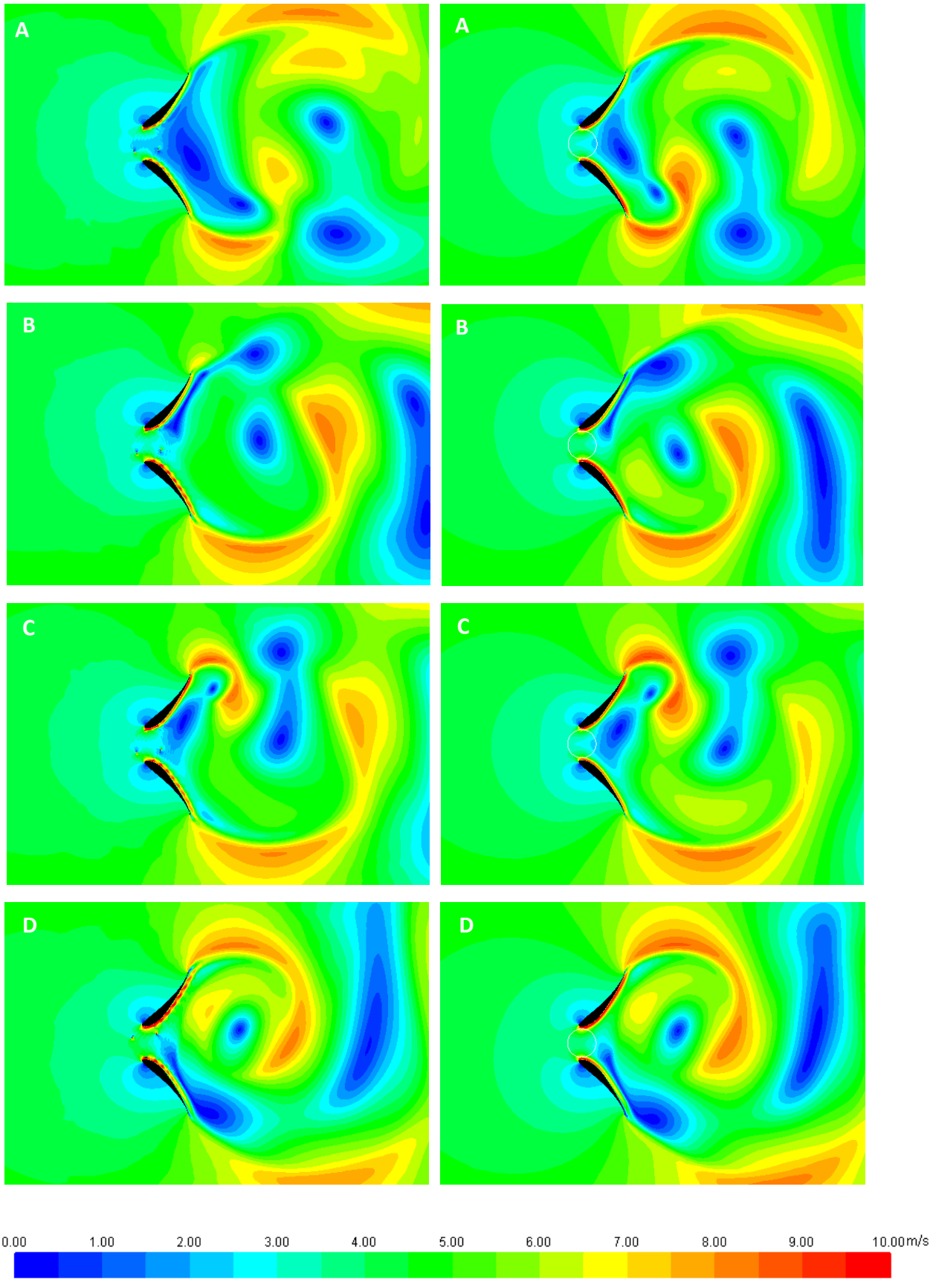

Figure 6.7 - Contour of velocity magnitude in different moment: CFD (left side) and AR (right side)

6.2 Blockage effect

Since in the optimized diffuser configuration the flow is completely different from the case of the bare turbine, it has been necessary to test the influence of the domain dimension on the solution. The size of the domain has not been changed during the optimization phase for practical reasons, as exposed in par.5.

Two new domains have been built with the same aspect ratio adopting a scale factor of 5 and 10 respectively (see the graph below). The power output was found to be very sensitive to the domain dimension and so it has been concluded that the Cp values calculated in the optimization phase needed for a correction to be considered reliable in a on open air environment. Moreover, the 5 times greater domain exhibited almost the same result of the far greater domain, so it has been considered suitable to evaluate the performance in an ideal open field. Throughout this chapter, the original domain will be called "small domain" while the second one "infinite domain" for obvious reasons.

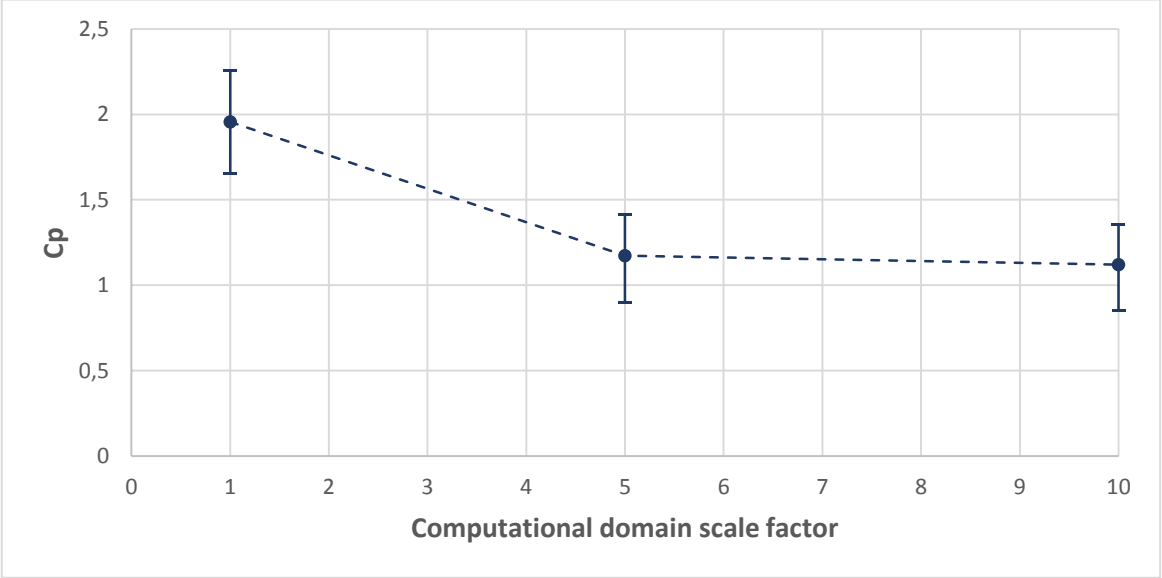

Graph 6.9 - Cp for domains of different size

Since the turbine develops a thick wake, it is reasonable to treat it like a bluff body.

The blockage effect of non-streamlined bodies have been extensively investigated for wind tunnel practice [7, 8, 9, 10, 11] For the case of a bluff body, one of the widely-accepted correction is the one proposed by Maskell [11]:

$$\frac{U_c{}^2 - U^2}{U^2} = \varepsilon C_D \frac{S}{C} \qquad [6.4]$$

where:

- U id the nominal wind speed at the inlet
- U_c is the undisturbed wind speed that, in an infinite domain, would give the same pressure distribution on the body
- $\frac{S}{C}$ is the blockage ratio between the model's frontal area and the tunnel section
- ε is an empirical factor which is almost 1 for two-dimensional flows

The fundamental hypothesis behind this model is the equivalence of the effect of the flow field on the model between the tunnel case with velocity U and the infinite domain case with U_c as undisturbed velocity. The blockage effect, as Maskell [11] argues, is essentially an acceleration of the flow with respect to the open air configuration. In this sense, the author demonstrates experimentally that:

$$\frac{p(x,y,z)-p_b}{H-p_b} \neq f(blockage) \quad [6.5]$$

where

- H is the total pressure at the inlet
- p_b is the base pressure

which means that the non-dimensional pressure shape around the body is not influenced by the wall constraints.

The blockage effect, however, is highly case-sensitive and for the present problem, the lack of a specific correction for a diffuser augmented Darrieus turbine was a source of trouble. Concerning the blockage in the case of VATW can be cited Ross et al. [12], that found the Maskell's method to be the most suitable.

It has been chosen to proof the Maskell's hypothesis also for the present case. In other words, it has been proofed that the effect of the small domain so far adopted gives the same results of the infinite domain operating with slightly higher inlet velocity or, *vice versa*, for a given wind speed in the infinite domain, a smaller wind velocity exists so that, once imposed to the small domain, provides the same turbine performances of infinite domain case.

To verify the validity of the Maskell to the present case, a Cp/TSR curve has been built by means of AR in the infinite domain for the rated wind speed 10 m/s. After that, the equivalent velocities in the small domain were estimated adopting the following graphic procedure in the Cp/TSR plane.

Being P the power calculated in the infinite domain at a specific rotor speed ω, we are interested in finding a velocity U_{eq} in the small domain providing the same power with the same ω. This can be made making some attempts on the U_{eq} and veriying the compliance of the so obtained Cp and TSR with the Cp/TSR curves of the small domain for different velocities. Formally:

1. Impose U_{eq}
2. Calculate:

$$C_p = \frac{P}{\frac{1}{2}\rho {U_{eq}}^3 A} \quad [6.6]$$

$$TSR = \frac{\omega R}{U_{eq}} \quad [6.7]$$

3. Insert the new (TSR, C_p) dot in the TSR/C_p plane relative to the small domain
4. Verify the compliance. If it is satisfying stop, otherwise go to 1.

The results of this simple procedure are depicted in the following charts.

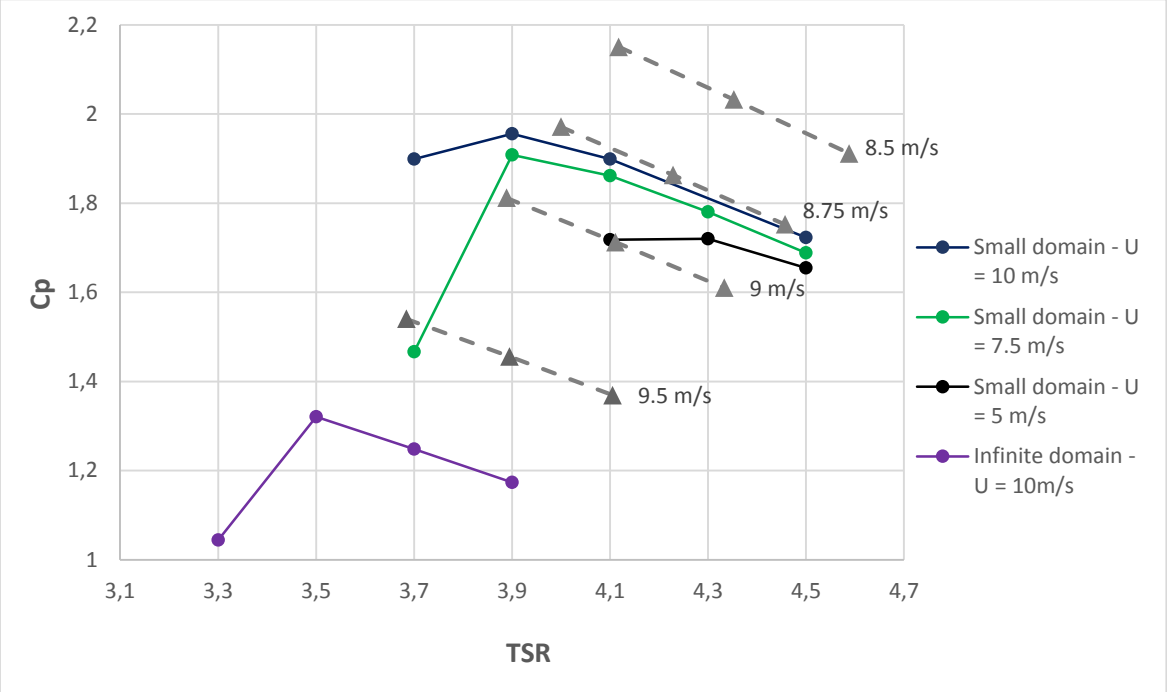

Graph 6.10 - Cp/TSR plane of the optimal design used to find the appropriate equivalent velocity

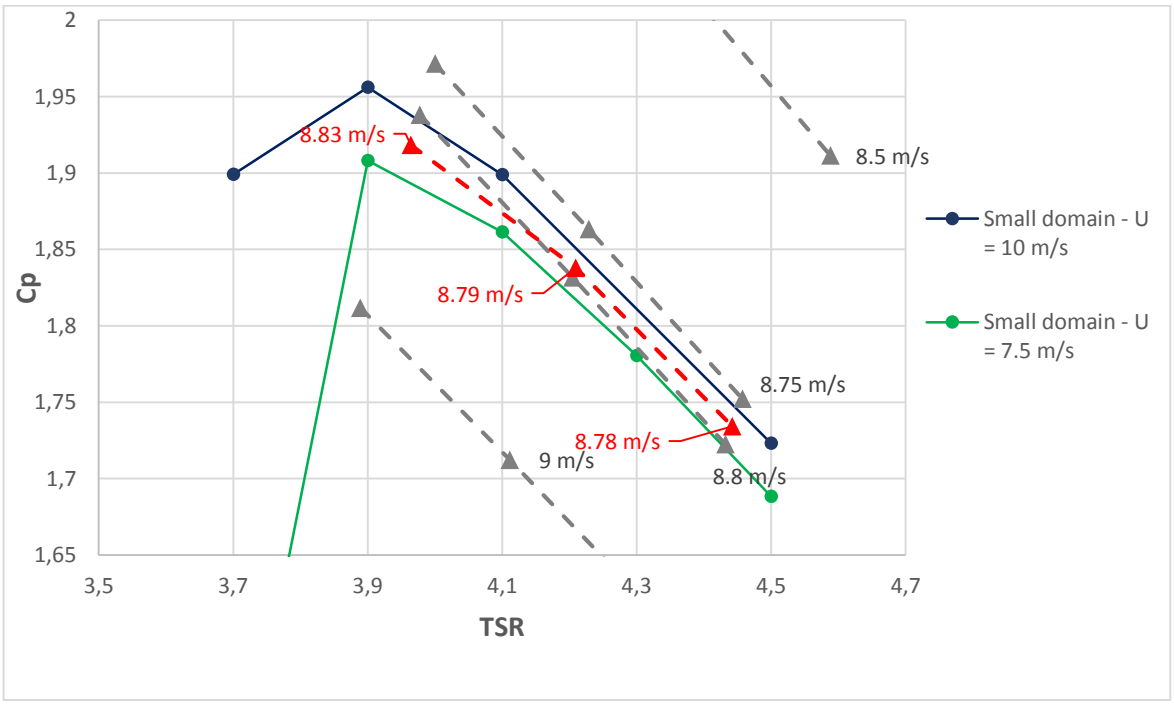

Graph 6.11 - Zoom from the precedent graph

The obtained values have a Cp curve lying in the narrow range between the 10 m/s and the 7.5 m/s and this is satisfactory.

To sum up, the new velocities corresponding to each of the infinite domain case were expected to be:

Rotor speed [rad/s]	Power [W/m]	Velocity in the infinite domain [m/s]	Equivalent velocity in the small domain [m/s]
35	1624	10	8.83
37	1525	10	8.79
39	1439	10	8.78

Table 6.1 - Equivalent velocities in the small domain

This velocities are very close to each other but they decrease slightly as the TSR increases, and this is physically correct since for higher TSR a higher blockage is expected [13]. Once found the hypotetic equivalent velocities, three simulation were performed in the small domain. The following graph show the almost percfetc agreement between the curve of the infinite domain and the one of the small domain woth the above reported corrected velocity.

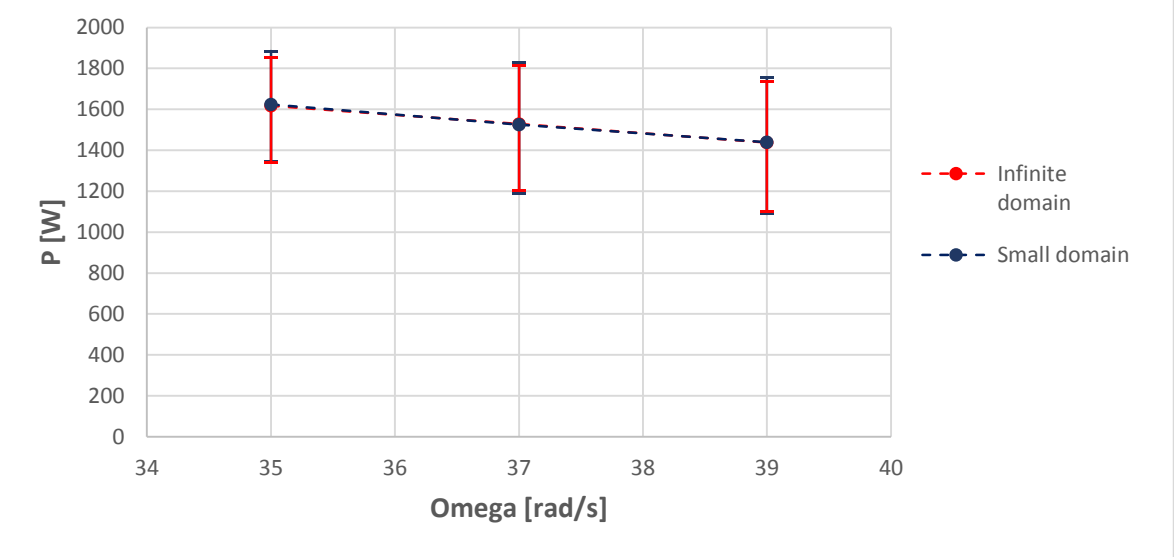

Graph 6.12 - Cp equivalence between the infinite domain and the small domain with corrected velocity

This result does not provide a sufficently hard proof that the Maskell hypotesis is correct for the present case, but it only confirms the validity of the above described graphical procedure. To evaluate the degree of equivalence between the approach the torque curve shapes have been compared.

Looking at graphs 6.13, 6.14, 6.15 the two curves are almost indistinguishable and this proofs that the blockage effect is felt by the flow field in the neighborhood of the body just like an acceleration in respect to the nominal velocity. In practice, the results obtained can be reported, with an acceptable confidence, to an open field case considering a properly corrected velocity that is slightly higher ($\sim 1 - 1.5\ m/s$) than the nominal one.

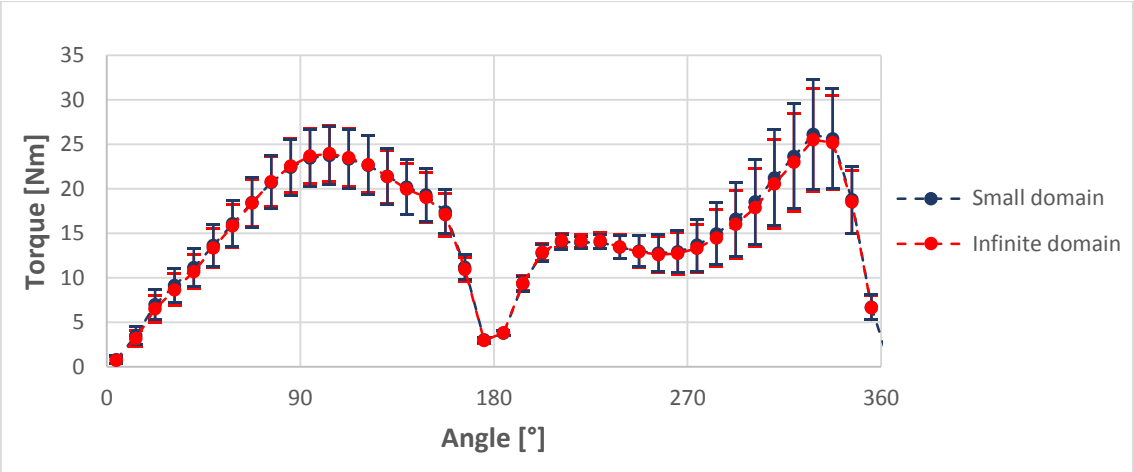

Graph 6.13 - ω = 35 rad/s: Torque curves from the infinte domain and the small domain with corrected velocity

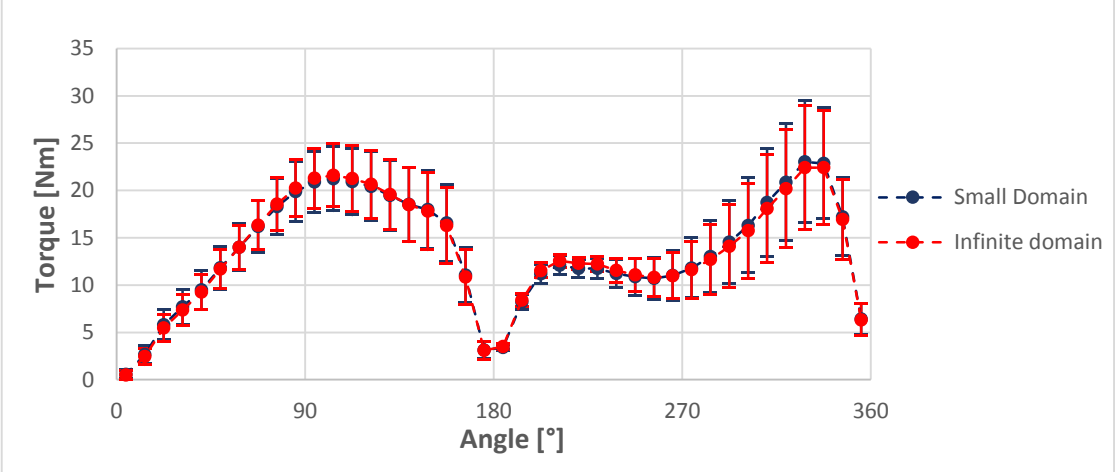

Graph 6.14 - ω = 37 rad/s: Torque curves from the infinte domain and the small domain with corrected velocity

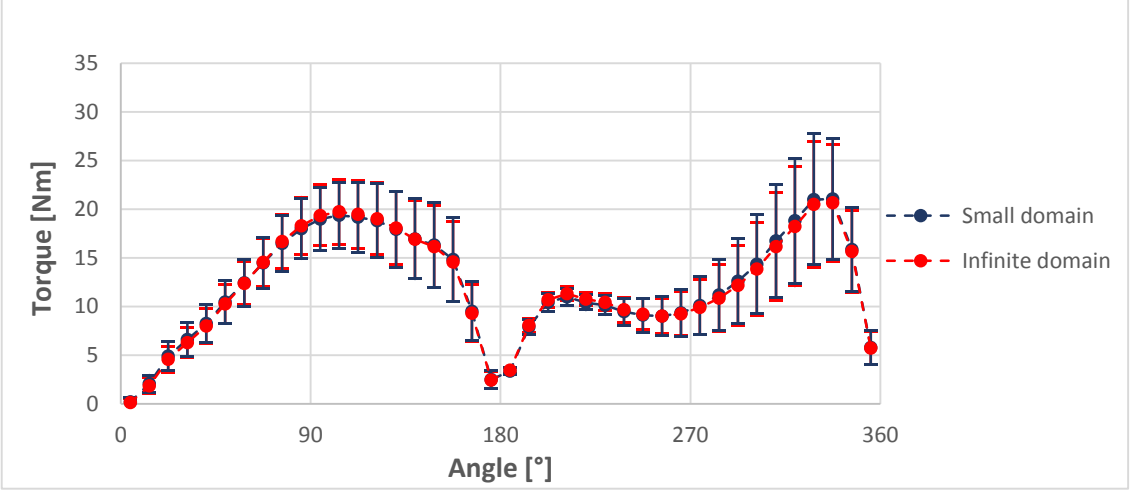

Graph 6.15 - ω = 39 rad/s: Torque curves from the infinte domain and the small domain with corrected velocity

The flow field at the maximum Cp moment for the 35 rad/s rotor speed are reported.

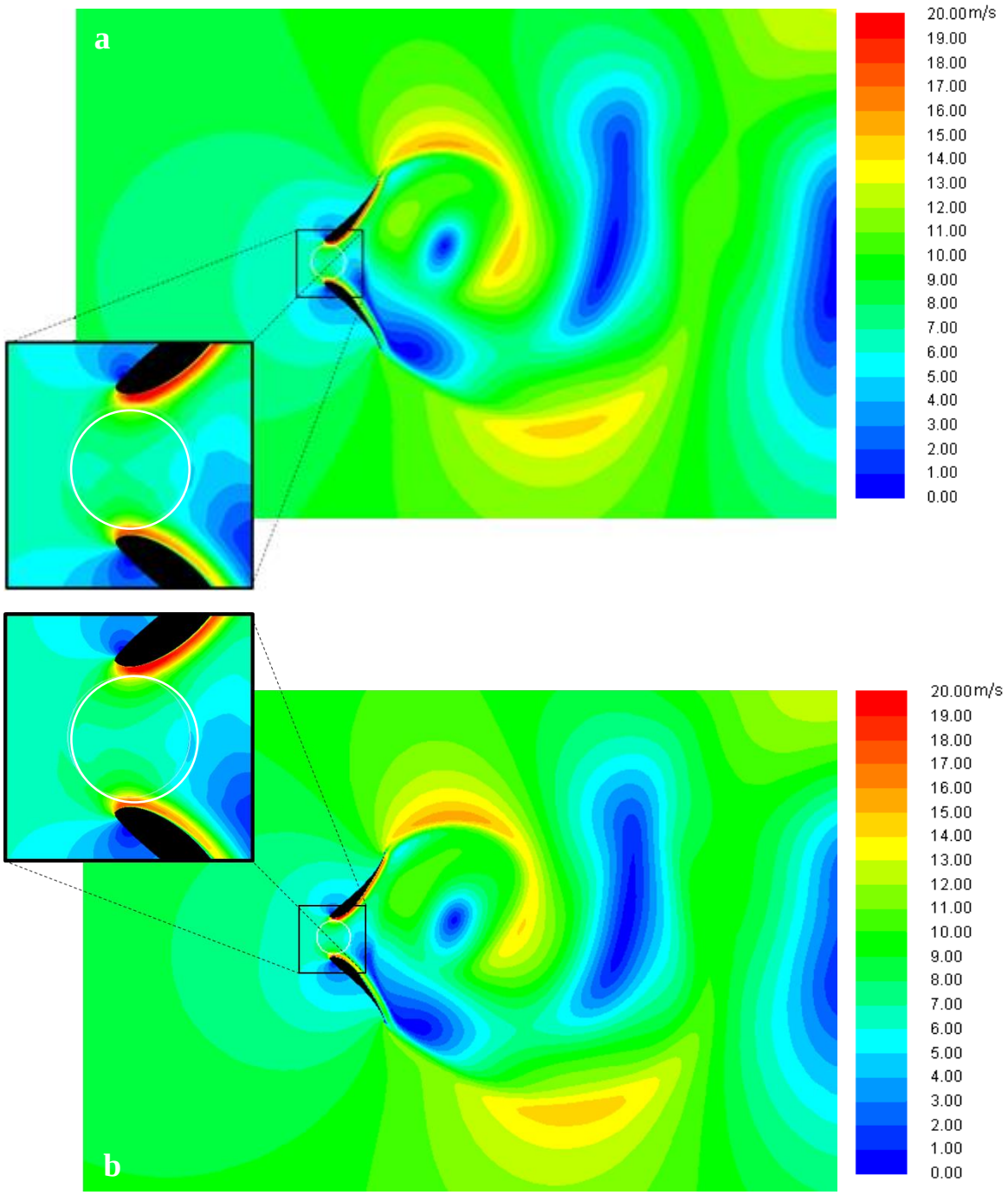

Figure 6.8 - ω = 35 rad/s, U = 10 m/s: comparison of the flow field from the small domain (**a**) domain and the infinite (**b**) with corrected velocity at max Cp instant

The velocity contour are very similar and almost identical in the rotor zone.

6.2.1. Correction

Once the correspondence between the infinite domain and the small domain results was verified the Maskell's relationship has been tested, to find the proper correction formula to adjust the power curve. In practice, the 6.4 has been applied to the small domain cases and the agreement to the infinite domain checked. The required drag here is the sum of the

diffuser's drag and the trust of the turbine. The empirical factor ε minimizing the square errors was 1.24 m/s.

Velocity in small domain [m/s]	Velocity in infinite domain [m/s]	Cd	Correction factor $\frac{U_c}{U}$	Corrected velocity [m/s]	Error
8.83	10	2.77	1.135	10.021	0.2%
8.79	10	2.8	1.136	9.988	0.12%
8.78	10	2.82	1.137	9.985	0.15%

Table 6.2 - Results of the fitting performed to find the proper correction formula

The fact that the empirical parameter is close to the unit as Maskell suggests for 2D flows [11], confirms the validity of the chosen correction. Even adopting $\varepsilon = 1$ the error does not exceed 3%.

To have a further validation of this method, a confront between the small domain with 7.5 m/s and the infinite domain with the relative equivalent speed (8.505 m/s) has been performed and the agreement is still remarkable.

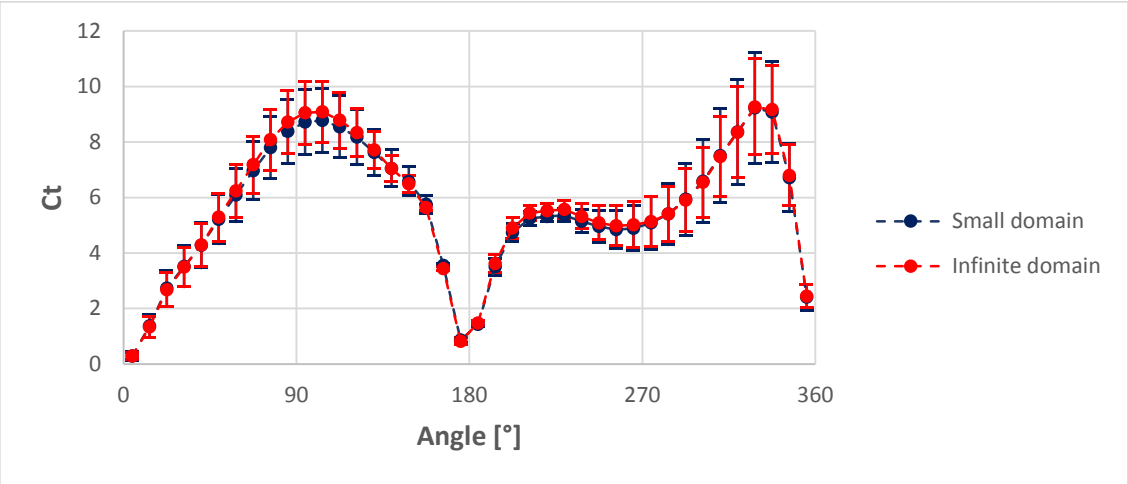

Graph 6.16 - ω = 29.25 rad/s, U = 7.5 m/s: Torque curves from the infinte domain and the small domain with corrected velocity

The presented correction has been applied to the power curve of the DAWT, whereas the bare turbine was insensible to the domain size. The following graph reports the corrected power curve.

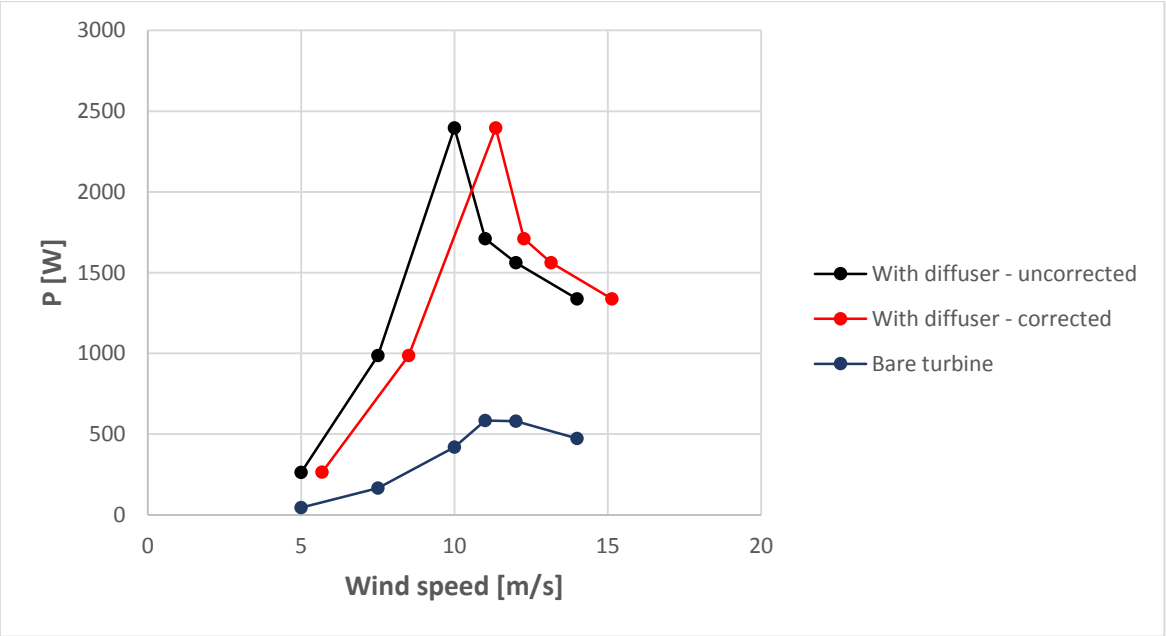

Graph 6.17 - Blockage-corrected power curve

Once fixed the blockage, the available more realistic results in the infinite domain inspired an in-depth analysis about the vortex shedding influence on the power exploitation.

6.3 Vortex shedding

The vigorous vortex shedding detected in the last phase of the optimization had great effects on the solution and deserved an in-depth analysis. In the following pictures, the velocity contours relative to five different angles of the diffuser in their maximum power conditions are reported.

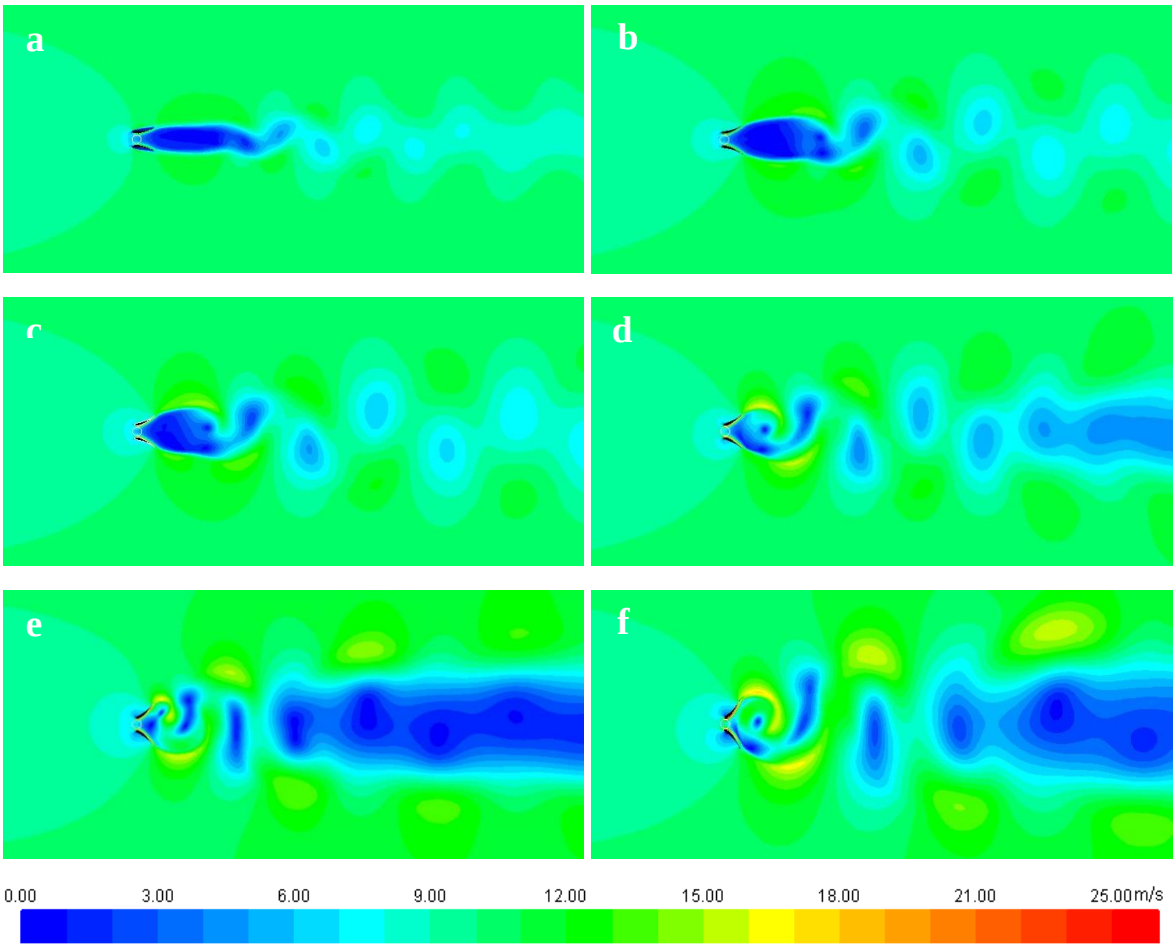

Figure 6.9 - H = 1.3 D, W = 0, Vortex shedding for different diffuser angle in maximum Cp conditions: **a**-α = 10°, **b**-α = 20°, **c**-α = 25°, **d**-α = 30°, **e**-α = 40°, **f**-α = 50°

As the angle increases, the wake becomes thicker and more instable. For high angles, the vortices shed directly from the diffuser surface, whereas for moderate angles a zone of almost stationary wake exists in the near wake. From 5.6 of the torque curves, it is evident how the flow instability influences the power coefficient that experiences periodic fluctuations for angle greater than 20°. Observing the shedding period and at the Strouhal number $\left(St = \frac{fH}{U_\infty}\right)$ a slight discontinuity can be noticed between 25° and 30°, thus confirming a possible change in the shedding regime.

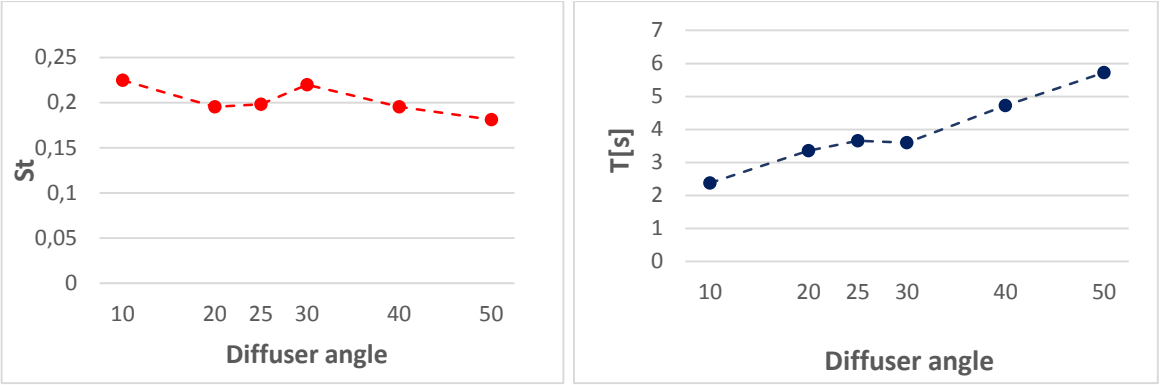

Graph 6.18 Vortex shedding: **a**-Strouhal number, **b**-Period

The shedding history for the optimal configuration at 10 m/s in the infinite domain is reported.

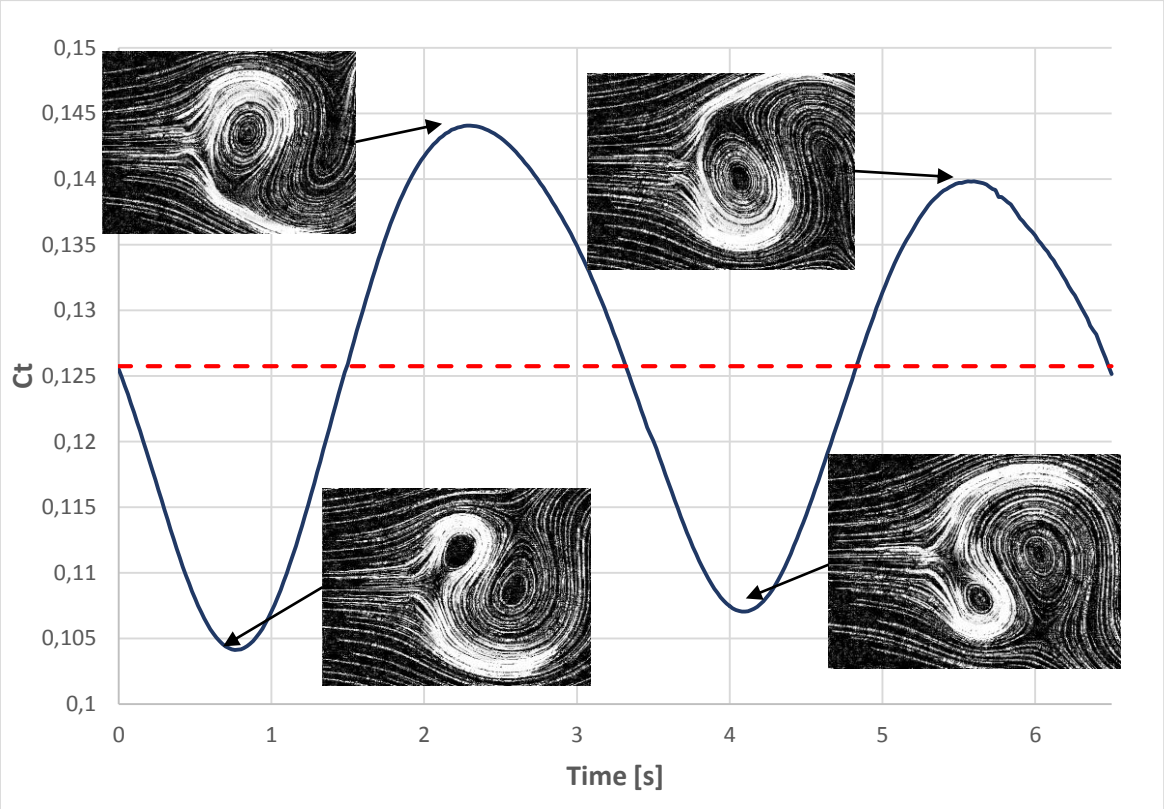

Graph 6.19 - Infinite domain, optimal configuration, U = 10 m/s: shedding history

The streamlines colored by velocity magnitude relative to the frames selected in previous graph are given below.

The streamlines colored by velocity magnitude relative to the frames selected in previous graph are given below.

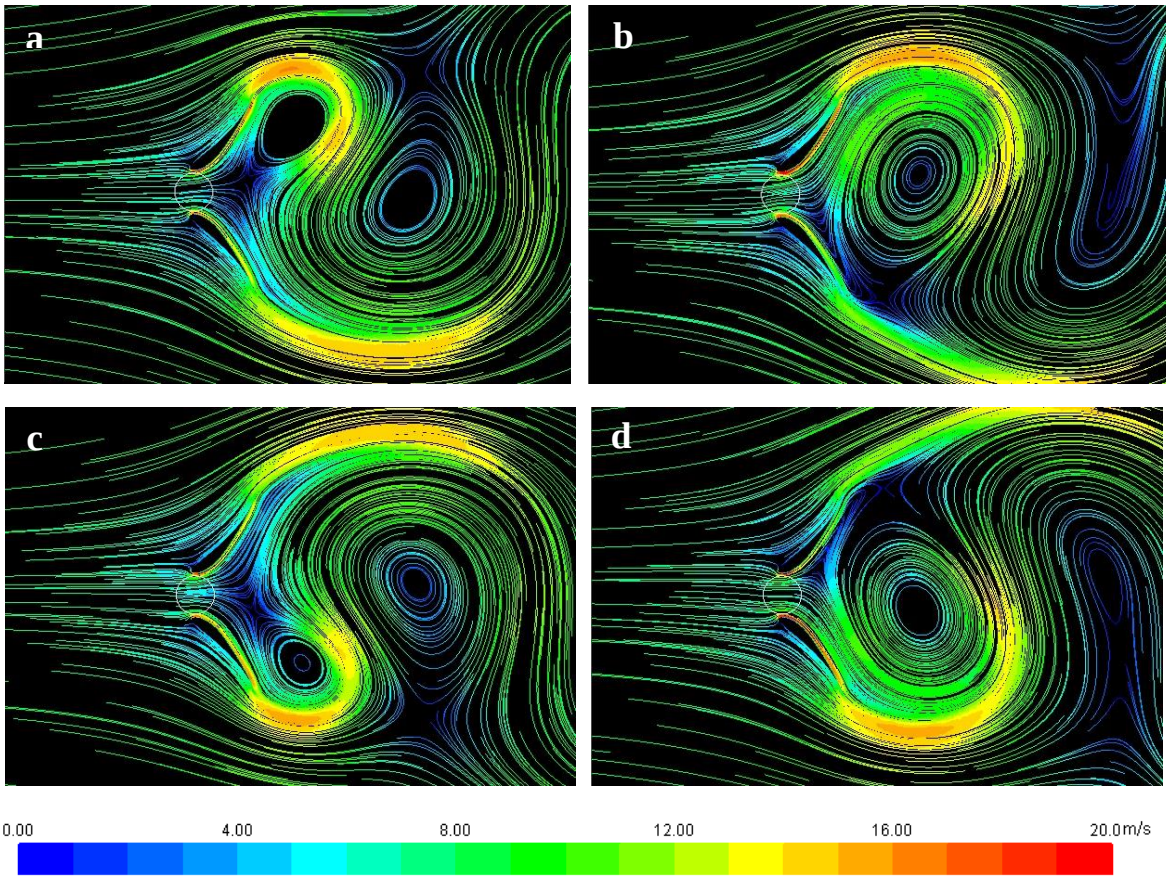

Figure 6.10 - Infinite domain, optimal configuration, U = 10 m/s, streamlines relative to vortex shedding history moments according to Cp evolution: **a**-absolute min , **b**-absolute max, **c**-relative min, **d**-relative max

It can be noticed that when the vortex is small the torque coefficient (and thus the Cp) experiences a minimum while when the vortex has grown up and it is about to detach the power output undergoes a peak. This is because the vortex induced velocity can be opposite or favorable to the main flow. This is clear when the profiles of the x-velocity are compared. The following chart is relative to the shedding from the upper side of the diffuser (Figure 6.10 **a** and **b**). It represents the x-velocity profile at the diffuser exit when the vortex is small and when it is big.

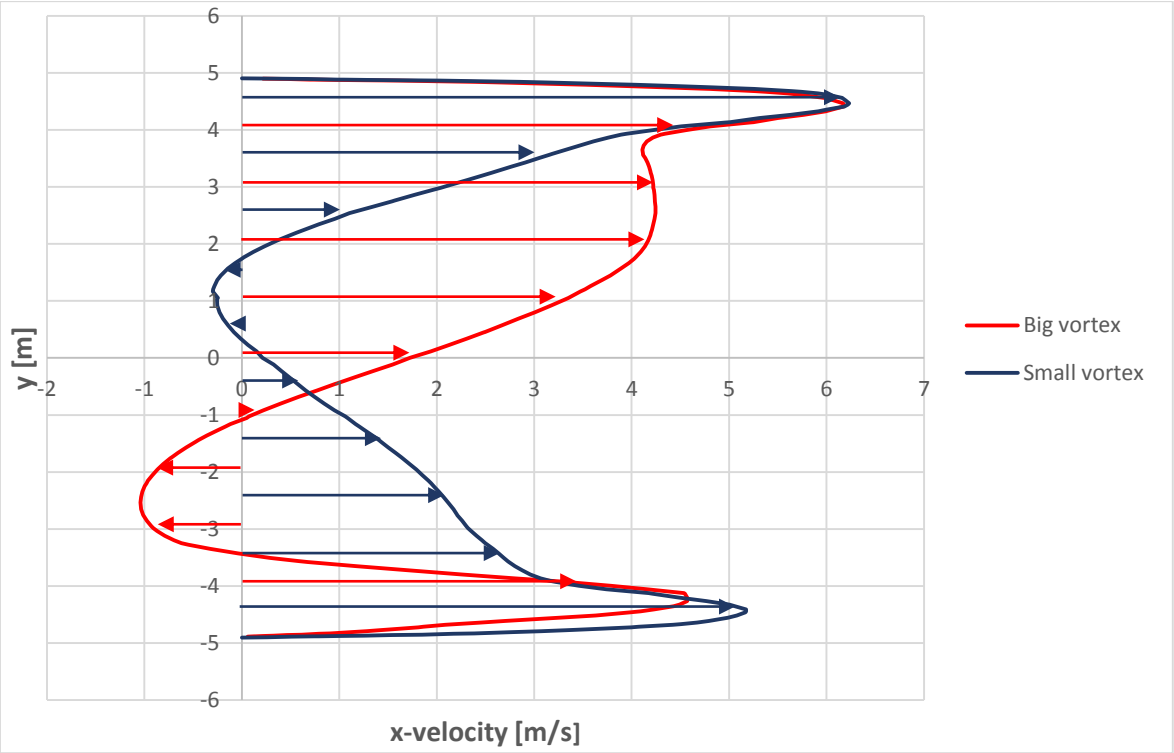

Graph 6.20 - X-velocity at the diffuser exit for shedding moment of max and min Cp

With the small vortex placed over the diffuser exit its anti-clockwise circulation induces a negative velocity at the center of the profile, thus reducing the mass flow.

Conversely, the velocity profile when the big vortex is in the middle of the diffuser exit exhibits the typical pattern of a vortex induced velocity that is positive in the upper part and negative in the lower.

Overall, the mass flow is higher in the second case of about 15%.

The different values of the peaks in the Ct/Time curve can be related to the turbine rotational verse, since it is the only source of asymmetry in the problem.

6.3.1 1D theory limits

The application of the work-energy theorem on a generic stationary domain containing the turbine leads to:

$$\frac{D}{Dt}\int_{\Omega}\frac{1}{2}\rho u^2\,d\Omega = \frac{1}{2}\rho\int_{\Omega}\frac{\partial u^2}{\partial t}\,d\Omega + \frac{1}{2}\rho\int_{A2}V^2\cdot u\,dy - \frac{1}{2}\rho\int_{A1}V^2\cdot u\,dy = P \qquad [6.8]$$

where P is the total power supplied to the system, the algebraic sum of the turbine work, friction loss and pressure work. Thus:

$$P = -P_t - P_{loss} + P_{press} \qquad [6.9]$$

where:

$$P_{press} = \int_{A1}p\cdot u\,dy - \int_{A2}p\cdot u\,dy \qquad [6.10]$$

The 6.10 can be rearranged as follows:

$$\int_{A1}\left(\frac{1}{2}\rho V^2+p\right)\cdot u\,dy-\int_{A2}\left(\frac{1}{2}\rho V^2+p\right)\cdot u\,dy-\frac{1}{2}\rho\int_{\Omega}\frac{\partial u^2}{\partial t}d\Omega-P_{loss}=P_t \qquad [6.11]$$

The sum of the kinetic energy and the static pressure is the total pressure and will be called H.

It is appropriate to time average each term of the previous relation over a time span equal to the lower frequency fluctuation period (the shedding period in this case), in order purge it from the transient term:

$$\frac{1}{\Delta t}\int_t^{t+\Delta t}P_t=\frac{1}{\Delta t}\int_{A1}\left[\int_t^{t+\Delta t}H\cdot u\,dt\right]dy-\frac{1}{\Delta t}\int_{A2}\left[\int_t^{t+\Delta t}H\cdot u\,dt\right]dy-\frac{1}{\Delta t}\int_t^{t+\Delta t}P_{loss} \qquad [6.12]$$

or: in ideal conditions (no dissipation) the average power is the difference between the incoming and the outgoing total pressure. This is a meaningful form of the energy balance provides useful estimation of the upper limit of the extractable power and will be applied in the following increasingly complicated situations:

1. bare turbine
2. turbine with diffuser with negligible shedding
3. turbine with diffuser and shedding

6.3.1.1 Bare turbine

The following scheme represent an ideal situation of moderately loaded turbine

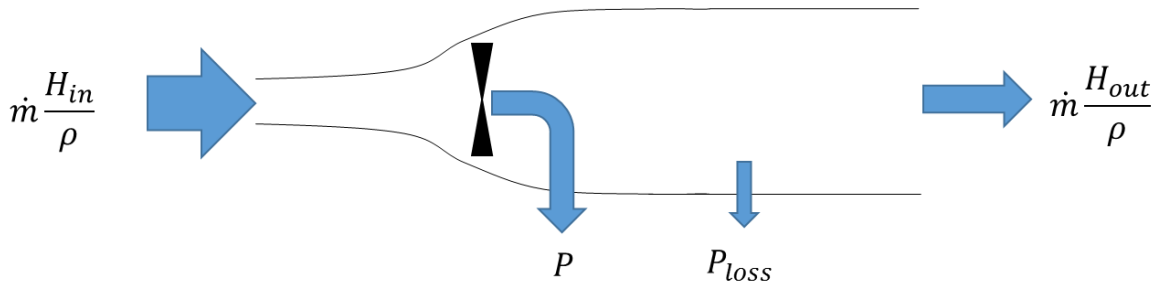

Figure 6.11 - Bare turbine energy balance

Here, the actuator disk theory can be used to find the well-known Betz-Lancaster limit $Cp \leq \frac{16}{27}$, but it requires the following fundamental hypothesis:

- inviscid, incompressible fluid
- stationary one-dimensional flow
- trust exerted only by the actuator disk
- no interaction by the fluid that does not cross the actuator disk (streamtube model)

In this conditions the maximum power output is influenced by the streamlines divergence as a consequence of the trust of the turbine and the consequent flow rate reduction.

The Betz-Lancaster limit holds for HAWT under normal condition, while for Darrieus models Newman [14] argued that a slightly higher value $\left(\frac{16}{25}\right)$ can be reached under ideal conditions.

6.3.1.2 Diffuser augmented wind turbine

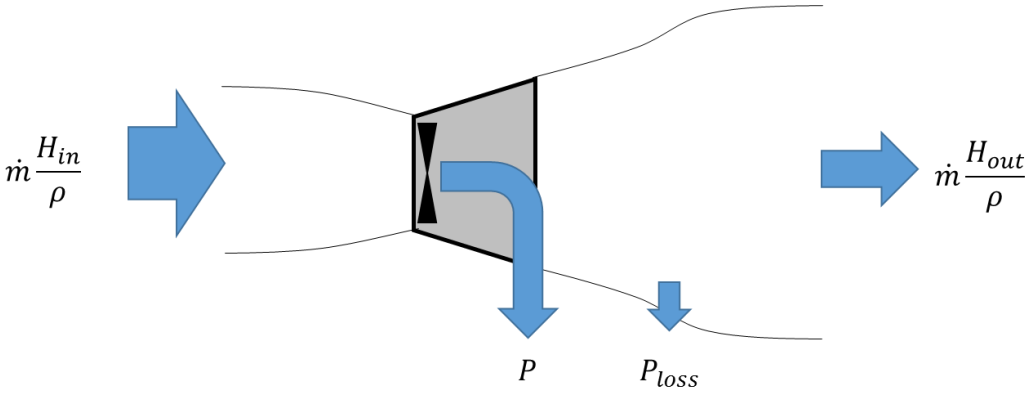

Figure 6.12 - Energy balance for a DAWT without shedding

When the diffuser is introduced, the Betz limit is no longer valid, as the diffuser itself exerts a trust that cannot be easily deduced. This is the same domain adopted by the supporters of the 1-D momentum previously discussed (par. 3.1). In that case, very strong hypothesis were formulated in order to overcome the problem of the unknown trust, but even without any kind of approximations, the model in fig 6.12 suggests an upper limit to the power output equal to the incoming total pressure flow. It can be easily showed that in the optimal configuration tested this limit does not hold. The following graphs report the mass flow rate through the turbine and the total pressure at the inlet of the hypothetic streamtube upwind the turbine.

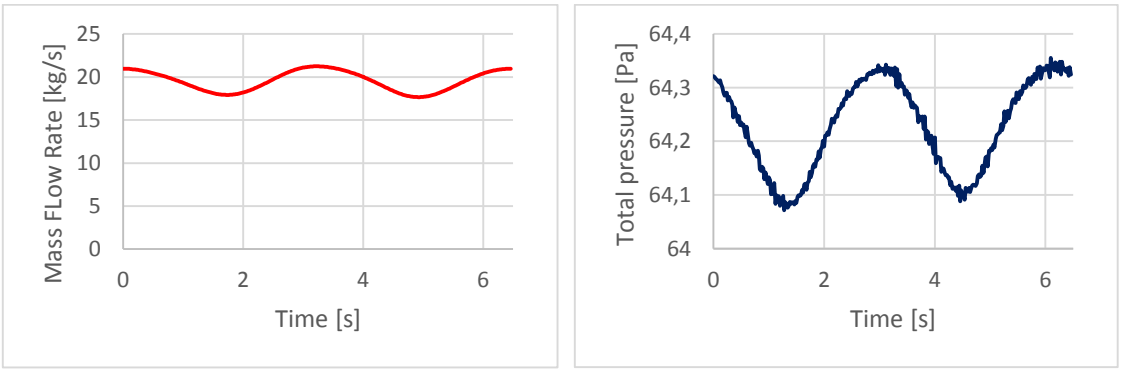

Graph 6.21 - **a**-Mass flow across the rotor mid diameter, **b**-Total pressure at the domain inlet

The mass flow fluctuates greatly because of the shedding whereas the total pressure exhibits negligible variations. Its value slightly exceeds the expected $\frac{1}{2}\rho {U_0}^2$ corresponding to 61.25 Pa because of the small suction head (3 Pa) that the solver need to drive the flow across the domain (this pressure gradient is always present in the CFD calculations because of confined domain).

Now, even hypothesizing negligible energy losses upwind the turbine, the maximum available power, according to figure 6.11 would be:

$$\frac{1}{\Delta t}\int_t^{t+\Delta t} P_t < \frac{1}{\Delta t}\int_{A1}\left[\int_t^{t+\Delta t} H\cdot u\, dt\right] dy \sim \frac{H_{in}}{\rho}\frac{1}{\Delta t}\int_{A1}\left[\int_t^{t+\Delta t}\rho u\, dt\right] dy = \frac{H_{in}}{\rho}\frac{1}{\Delta t}\int_t^{t+\Delta t}\dot{m}\, dt \quad [6.13]$$

When the actual quantities are introduced:

$$\frac{1}{\Delta t}\int_t^{t+\Delta t} P_t = \frac{1}{2}\rho {U_o}^3 A\frac{1}{\Delta t}\int_t^{t+\Delta t} Cp = 1617\ W \quad [6.14]$$

$$\frac{H_{in}}{\rho}\frac{1}{\Delta t}\int_t^{t+\Delta t}\dot{m}\, dt = 1025\ W \quad [6.15]$$

Thus the 6.13 is far from been satisfied. The this means that the coefficient of power, even when referred to the section of the streamtube infinitely upwind from the turbine, not only exceeds the Jamieson's limit $\left(\frac{16}{27}\right)$ (see par. 3.1.2) but is even greater than one. The reason behind this behavior lies in the streamtube concept. As the vortex shedding becomes strong, it cause a vigorous mixing in the wake. The mixing provides, as obvious, a momentum exchange between the freestream and the low-speed wake that would have been impossible according to a streamtube approach, where the wake develops apart from the rest of the flow. The turbulent mixing, in this way, demolishes the fictitious "fluid walls" enclosing the flow elaborated by the turbine and make a greater mass of fluid enter in the energy balance. The following figure summarizes this effect, ensuring that no fundamental principle is violated, as some early researcher hypothesized [15, 16]. This is a regime similar to the turbulent windmill state [17] that heavily loaded rotors experience. There the momentum theory of Betz breaks down, but according to the empirical formulation of Glauert [18], the trust coefficient approaches 2 in this condition. However, for a bare turbine in turbulent windmill state the power output is greatly reduced because of the excessive induction factor and the consequent low velocity across the rotor. Conversely, in the case of a diffuser augmented turbine, the high divergence angle and turbulent mixing enhance the flow concentration and permits very high power extraction. This entrainment phenomenon (in analogy to the term adopted in submerged jet theory) can be exploited to enhance power production and so do the so called Mixing-Ejector Wind Turbines or MEWT [19].

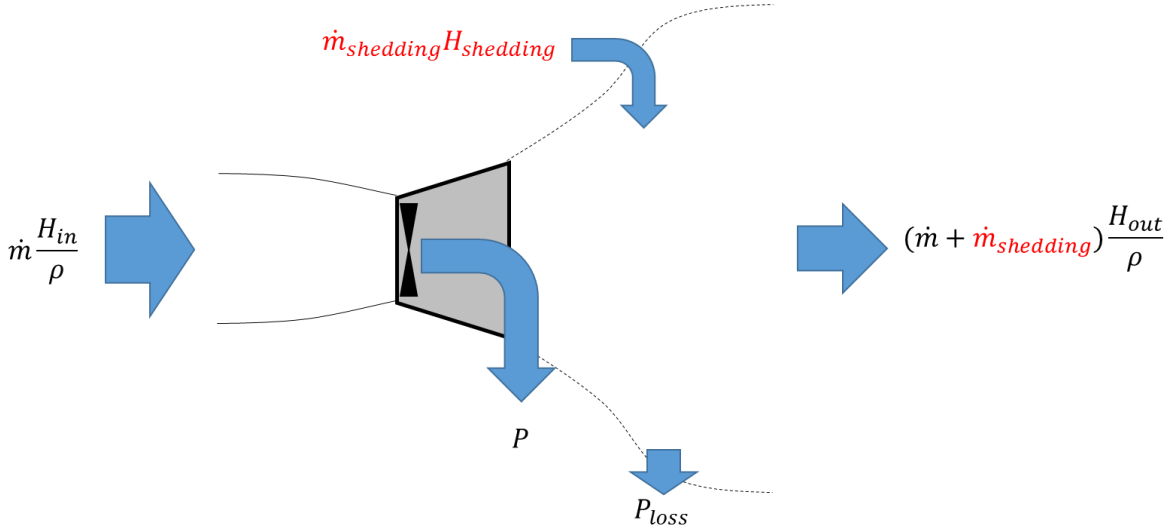

Figure 6.13 - Energy balance for a DAWT with highly turbulent wake

6.4 Three-dimensional effects

The 2D flow approach neglects important phenomena occurring in the real three-dimensional space:

1. The velocity can have also a non-null z-component. This actually happens as the flow experiences the turbine trust and bends upward and downward in front of the rotor. The turbine tips operates actually in skewed flow conditions.
2. The wake development is influenced by the three dimensional mixing that enhances the velocity recovery [20]
3. The induction field of the tip vortex can affect the velocity in downwind and in the near wake [21]
4. Because of the tip losses, as known, the overall lift diminishes and the induced drag appears

The first three effect are almost impossible to be accounted for by means of a simple model and a 3D CFD or Panel (potential) code is required. More over, their effects on the performance are not easily-understood.

The tip losses influence, however, can be considered by means of a simple correction factor as it will be explained below. Two fundamental hypothesis are required:

- the velocity magnitude and direction variation due to the 3D field are negligible, conversely their effect on lift and induced drag are considered by means of a simplified approach
- the potential theory is applied for both the 2D and the 3D case, assuming that the tip losses factor would be similar in real flow

In fact, the practical approximated Prandtl solutions for the overall lift and induced drag due to tip vortex are [22]:

$$C_l = C_{l0}\frac{AR}{AR+2} \qquad [6.16]$$

$$C_d = \frac{{C_l}^2}{\pi AR e} = {C_{l0}}^2\frac{AR}{\pi(AR+2)^2 e} \qquad [6.17]$$

where:

- C_{l0} is the lift coefficient for an infinite wing
- AR is the aspect ratio
- e is the so called span efficiency factor which is typically <1

For the hypothesis above are valid, the conventional equations of the BEM theory can be adopted.

The instantaneous torque provided by a single blade is:

$$T(\theta) = L\sin(\alpha) - D\cos(\alpha) \qquad [6.18]$$

If the angle of attack is small the average torque, when the 6.16, 6.17 are introduced, becomes:

$$T \sim \frac{1}{2\pi}\int_0^{2\pi}\left[L\alpha - D\left(1-\frac{\alpha^2}{2}\right)\right]d\theta \sim \frac{1}{4\pi}\rho c\int_0^{2\pi}(C_l\,\alpha - C_d)U^2 d\theta \qquad [6.19]$$

Adopting the potential flow results, $C_{l0} \sim 2\pi\alpha$ and the drag comes only from vortex induction, so:

$$T = \frac{1}{4\pi}\rho c\int_0^{2\pi}(2\pi\alpha^2\frac{AR}{AR+2} - 4\pi^2\alpha^2\frac{AR}{\pi(AR+2)^2 e})U^2 d =$$

$$\left(\frac{AR}{AR+2} - \frac{2AR}{(AR+2)^2 e}\right)\cdot\frac{1}{2\pi}\int_0^{2\pi}\frac{1}{2}\rho c U^2(2\pi\alpha^2)d\theta = \left(\frac{AR}{AR+2} - \frac{2AR}{(AR+2)^2 e}\right)T_0 \qquad [6.20]$$

then:

$$\frac{T}{T_0} = \left(\frac{AR}{AR+2} - \frac{2AR}{(AR+2)^2 e}\right) \qquad [6.21]$$

The span efficiency factor, for coherence with the potential theory, is taken from Horner [23] that, for rectangular wings states:

$$e = \frac{1}{1+0.01\,AR} \qquad [6.22]$$

Thus the correction factor for the torque (and for the power) will be:

$$f = \left(\frac{AR}{AR+2} - \frac{2AR}{(AR+2)^2}(1+0.01\,AR)\right) \qquad [6.23]$$

The plot below confronts the proposed correction with the results of the literature example founded concerning only the tip losses effect for Darrieus turbines. The agreement is satisfactory.

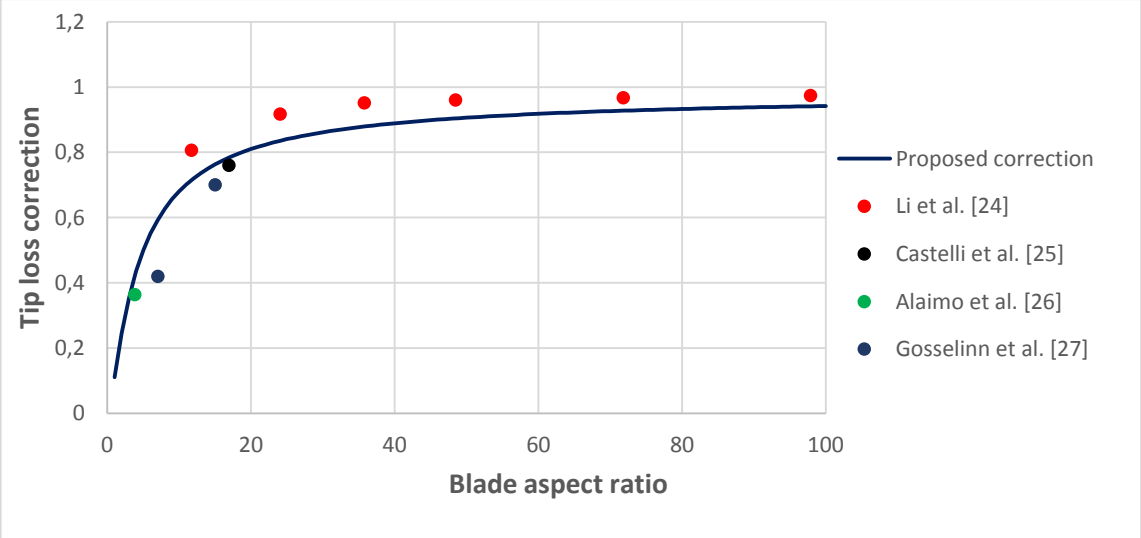

Graph 6.22 - Comparison between the correction from eq. 6.22 and some numerical results

6.5 Struts drag

The blades need for a certain number of arms linking them to the shaft. If they are supposed to have an aerodynamic section, the consequent drag can be rapidly estimated and there are also examples in literature [24]. In fact, being U_{tan} the tangential component of the absolute velocity in a polar coordinates system, the work made by a single arm per revolution is:

$$w = \int_0^{2\pi} \int_0^R \frac{1}{2} \rho c C_d (U_{tan} + \omega r)^2 \, r \, dr \, d\theta \qquad [6.24]$$

that can be easily seen as a surface integral of $\frac{1}{2} \rho c C_d (U_{tan} + \omega r)^2$ inside the rotor swept area. A simple algorithm has been implemented (see Appendix II) and the results are summarized in the chart below, imposing a NACA0012 with the same chord of the blades for the struts' profile.

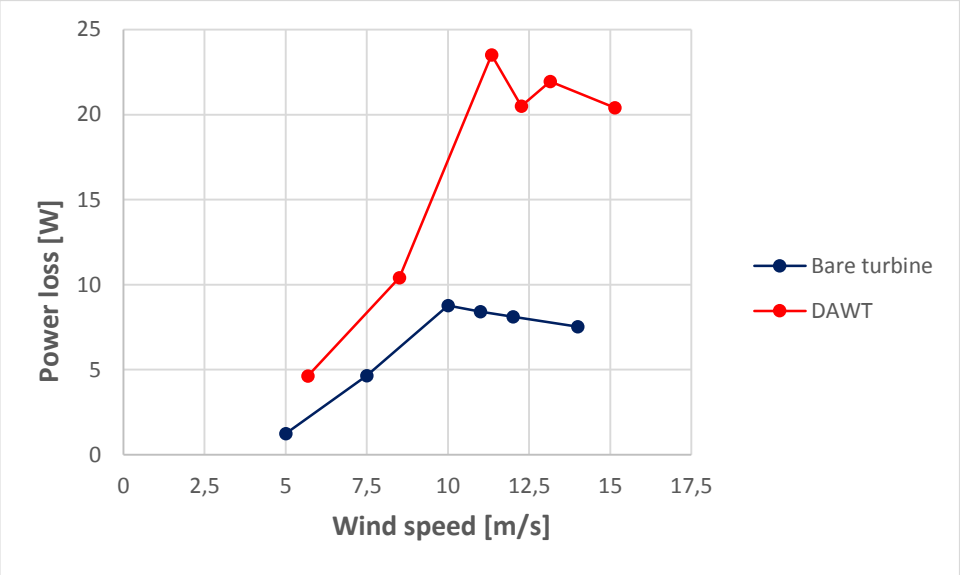

Graph 6.23 - Power loss due to a single arm

For the DAWT case, the results refer to an instantaneous flow field, because very small fluctuations (<1 W) of this values have been observed as a consequence of the shedding and have been neglected.

The power loss have to be multiplied by the number of arms that, as rule of thumb, has been taken as 3 times the turbine height in meters, with a lower threshold of 6, just like a visual confront with [6] suggests. A structural analysis, in facts, goes beyond the scope of this work.

6.6 Conversion losses

A base electrical scheme for a small VAWT is provided below from ref. [28].

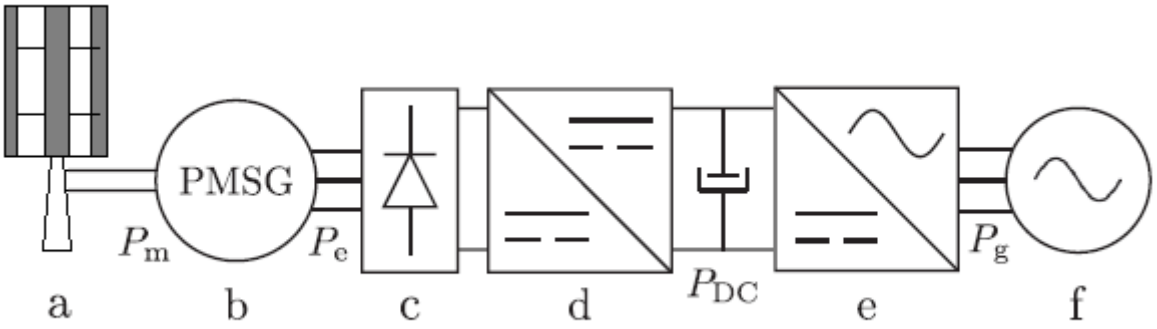

Figure 6.14 - Simplified layout of a small VAWT power system: **a**-VAWT, **b**-Permanent Magnet Generator , **c**-Diode rectifier, **d**-Boost dc/dc converter, **e**-Inverter, **f**-Grid or Utility

The turbine (**a**) drives the PMSG (**b**). Since the shaft speed is variable, the PMSG produces an AC with a variable frequency and amplitude, i.e., 'wild AC'. The wild AC is converted to a DC voltage proportional to the turbine's rotational speed by the diode rectifier (**c**). A boost DC/DC chopper (**d**) converts this variable DC voltage to a constant DC voltage while performing the MPPT. An inverter **(e**) then injects an AC current with a constant frequency into the grid(**f**).

The absence of a gearbox is claimed to ensure high mechanical efficiency at the nominal point [30]. Moreover, because of the lack of a detailed design of the bearings arrangement, for the sake of simplicity it has been considered constant and equal to 95%. This is roughly true for this kind of turbines, in fact, according to [28], the power loss due to friction on bearings can be roughly approximated by the product of radial force, friction coefficient, shaft radius and rotational speed, as follows:

$$P_f = \mu\, D\, \frac{d}{2}\omega \qquad [6.25]$$

but since in VAWT the overall trust force, for a give TSR, goes with $V_0{}^2$ just like the torque, it can be assumed:

$$P_f \propto T\, \omega \propto P \qquad [6.26]$$

The remaining energy losses come from:

- Imperfect MPPT
- Generator
- Inverter

The nominal value of modern Inverters and generators are around 95% [28, 29, 30]. It is very difficult to find reliable value of the efficiency of this kind of systems when it works in different regimes of rotational speed and power output. An interesting reference providing a simple experimental curve of performance has been found [2]. It is based on several experiments with a simulated turbine under variable speed operation.

With the adopted approximations, the system conversion efficiency is a linear function of capacity factor, as reported below.

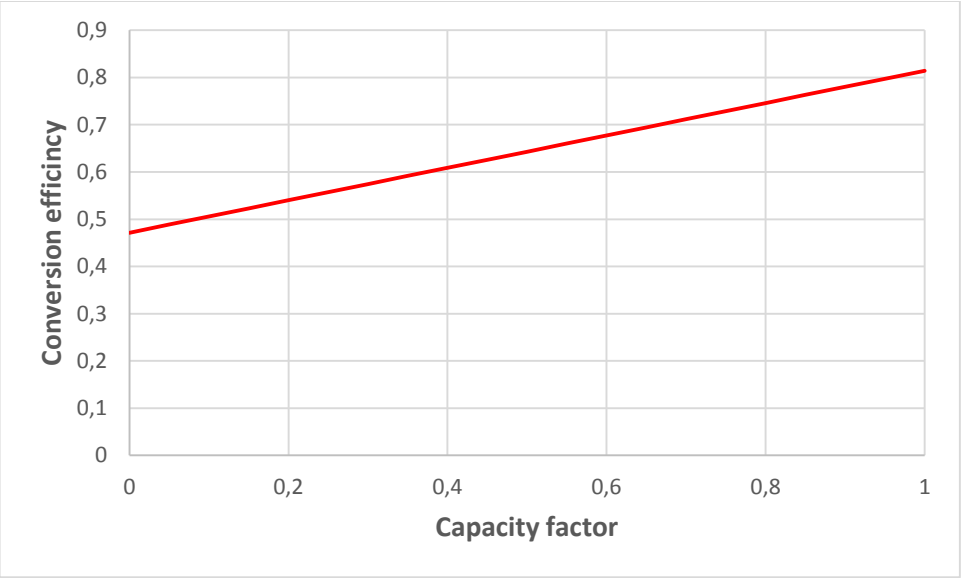

6.24 - System efficiency for partial-load operation

This simplified approach gives an unrealistic high value when the power approach zero. So, an appropriate cut-in speed has been fixed to avoid a physically inconsistent power production at very small wind speed. However, the errors due to the imperfect modeling of the slow wind conditions is no expected to be influent in the overall energy balance that have been performed, for the greater energy production takes place around the nominal speed.

VI References

[1] Burton T, Jenkins N, Sharpe D, Bossanyi E. *Wind Energy Handbook*, Second Edition.. © 2011 John Wiley & Sons, Ltd. Published 2011 by John Wiley & Sons, Ltd. ISBN: 978-0-470-69975-1

[2] Cuesta AB, Gomez-Gil F, Gomez-Gil FJ, Fraile JVM, Rodriguez JA, Calvo JR, Vara PV. *Feasibility of a Simple Small Wind Turbine with Variable-Speed Regulation Made of Commercial Components*, Energies 2013, 6, 3373-3391

[3] Li N, Patterson DJ, Hudgins JL, *Maximum Power Extraction from A Small Wind Turbine Using 4-phase Interleaved Boost Converter*, University of Nebraska-Lincoln, NE

[4] Sutherland HJ, Berg DE, Ashwill TD. *A Retrospective of VAWT Technology*, SANDIA REPORT, SAND2012-304, Unlimited Release, Printed January 2012

[5] Mason-Jonesa A, Morrisa CE, O'Dohertya T, Byrnea CB,. Pricketta PW, Grosvenora RI, Owenb I, Teddsb S, Pooleb RJ. *Non-dimensional scaling of tidal stream turbines*. Energy, Volume 44, Issue 1, August 2012, Pages 820-829

[6] *Power Performance Test Report for the Windspire Conducted by Windward Engineering*, LLC 10768 S. Covered Bridge Canyon Spanish Fork, UT 84660

[7] H. Glauert. *Wind tunnel interference on wings, bodies and airscrews*. A.R.C.-R. & M. 1566. September, 1933

[8] Herriot JC. *Blockage correction for three dimensional flow closed throat Wind tunnel with consideration of the effect of compressibility*. NACA R 995, 1950.

[9] Ramamurthy, A.S. and Ng, CP. *Effect of Blockage on Steady Force Coefficients*. Journal of Engineering Mechanics. Div., Proc. A.S.C.E., P9(1973) 755-772.

[10] Awbi, H.W. *The investigation of wind tunnel wall interference on bluff body models*. Ph.D Thesis, Trent Polytechnic, Nottingham, August 1974.

[11] Maskell EC. *A theory of the Blockage effect on Bluff Bodies and Stalled Wings in a closed Wind Tunnel*, ARC R&M 3400, Nov 1968.

[12] Ross I, Altman A. *Wind tunnel blockage corrections: Review and application to Savonius vertical-axis wind turbines*, J. Wind Eng. Ind. Aerodyn. 99 (2011) 523-538

[13] Sarlak H, Nishino T, Martinez-Tossas LA, Meneveau, Sørensen , JN *Assessment of blockage effects on the wake characteristics and power of wind turbines*, Renewable Energy 93 (2016) 340e352

[14] Newman, B. (1983). *Actuator-disc theory for vertical-axis wind turbines*. Journal of Wind Engineering and Industrial Aerodynamics, 15(3).

[15] Hutter U. *Optimum Wind-Energy Conversion Systems*. Ann. Rev. Fluid Mech., 9 (1977) pp. 399-419.

[16] De Vries O. *Fluid Dynamic Aspects of Wind Energy Conversion*, National Aerospace Laboratory NLR Anthony Fokkerweg 2 /1059 CM Amsterdam The Netherlands (1979)

[17] Forrest S, *Discussion Of Momentum Theory For Windmills*, Wind Energy Center Reports. Paper 20(1976).

[18] Glauert H. *The elements of aerofoil and airscrew theory*, second edition. Cambridge University Press, Cambridge, England, 1947.

[19] Hjort H, Sorsen H, *A Multi-Element Diffuser Augmented Wind Turbine*, Energies 7 (2014) , 3256-3281

[20] Lam HF, Peng HY. *Study of wake characteristics of a vertical axis wind turbine by two and three-dimensional computational fluid dynamics simulations*. Renewable Energy 90 (2016) 386e398

[21] Dixon K, Simao-Ferreira C, Hofemann C, Van Bussel G, Van Kuik G. *A 3D unsteady panel method for vertical axis wind*, DUWIND Delft University Wind Research Institute

[22] Antonelli M, Martorano L. *Elementi di Macchine*, ETS

[23] Horner SF. *Fluyd Dynamic Drag*, Dayton Ohio, Oterbein Press (1951) 7

[24] Li Y, Sanderc MC. *Three-dimensional effects and arm effects on modeling a vertical axis tidal current turbine*, Renewable Energy 35 (2010) 2325-2334

[25] Raciti Castelli M, Ardizzon G, Battisti L, Benini E, Pavesi G, *Modeling strategy and numerical validation for Darrieus vertical axis micro-wind turbine*, in: Proceedings of the ASME IMECE 2010, Vancouver, Canada, November 12-18,2010

[26] Alaimo A, Esposito A, Messineo A, Orlando C, Tumino D. *3D CFD Analysis of a Vertical Axis Wind Turbine*, Energies 2015, 8, 3013-3033

[27] Gosselin R, Dumas G, Boudreau M. *Parametric study of H-Darrieus vertical-axis turbines using URANS simulations*. Paper CFDSC-2013 #178, Session 13-6 - Rotating Machine I, 21st Annual Conference of the CFD Society of Canada, Sherbrooke, Canada, May 6-9, 2013.

[28] Jeroen DM, De Kooning JDM, Tine L, Vandoorn TL, Jan Van de Vyver JV, Bart Meersman, B Vandevelde L *Displacement of the maximum power point caused by losses in wind turbine systems*, Renewable Energy 85 (2016) 273e280

[29] *Low-speed permanent magnet generators*, The Switch Inc., Costumer's manual (2016)

[30] *www.allsmallwindturbines.it*, On-line

Part VII - Energy performance

In the last part of the work, both the bare and the new DAWT have been simulated in the operative conditions of the case study of the PRA project (par 1.1).

7.1 Wind resource estimation

Reliable wind speed measurements in the specific site were missing, but a physically consistent time series of wind speed and direction have been build (the direction were necessary for the PRA project because the original turbine arrangement was direction-sensitive). The available data were:

- the hourly sampled synoptic wind speed in Enna from CTI test reference year [1], having an unrealistic low average (1.4 m/s) for unknown reasons
- the direction frequencies and average intensity of the synoptic wind from ISTAT report [2]

It has been chosen to use the ISTAT data as main source and to use the CTI time series to evaluate significant statistical quantities. The values are here reported. The "lull" term refers to a speed below the 1 m/s threshold.

	Jan	Feb	Mar	Apr	May	Jun	Jul	Aug	Sep	Oct	Nov	Dec
N	12	7	12	6	13	8	4	12	12	13	6	8
NE	5	12	2	8	9	5	4	5	9	11	6	1
E		4	18	7	8	10	4	6	3	1	6	1
SE		1	3	3	4	4	4	2	2	3		1
S			3	2	5	8	4	7	3	8	9	5
SW		2	8	2	6	9	6	5	13	8	20	9
W	9	10	4	14	6	4	11	11	8	14	4	13
NW	38	28	16	19	6	11	24	12	8	7	18	28
Lull	31	28	31	33	37	31	30	33	34	30	27	29

Table 7.1 - Frequencies [%] of the wind direction in Enna (EN), Source: ISTAT [2]

	Jan	Feb	Mar	Apr	May	Jun	Jul	Aug	Sep	Oct	Nov	Dec
N	4.6	6.5	7.4	4.2	5	4.8	4.7	5.4	4.5	5.6	6.5	6.4
NE	5.3	7.8	10.5	8.3	9.8	4.5	4	3.3	3.3	5	4.9	5.6
E		14.1	11.7	9.6	7.8	3.3	4.6	7.1	5.8	4.6	9.5	7.7
SE		7.4	9.5	12.9	5.3	9.8	7.8	4.6	8.7	2.9		6.7
S			6	6.8	4.8	5.8	5.6	6	4.7	6.6	14.1	4.1
SW		12.5	7.7	7.2	6.4	5.5	5.1	8.2	5.7	5.3	7.7	7.2
W	5.3	7.4	4	6.6	5.4	6.1	6.5	5.5	4.7	7.1	8.2	7
NW	4.9	5.5	5.5	4.6	4.4	4.2	5.3	4.7	5.4	4.5	6.2	6.5
Lull	4.6	6.5	7.4	4.2	5	4.8	4.7	5.4	4.5	5.6	6.5	6.4

Table 7.2 - Wind speed [m/s] in Enna (EN), Source: ISTAT [2]

The algorithm that was adopted is based on a double random extraction of direction and speed according to the following statistical pdf:

1. the direction is extracted according to the given frequency for a specified month
2. the wind speed is extracted from a Weibull pdf having mean value corresponding to the previously calculated direction.

The Weibullian behavior of the wind speed frequency is established, but in the present work a further hypothesis was made, considering Weibullian distribution also for the single direction of each month. This really case-specific hypothesis lacks for a literature reference but seems the most reasonable as a pdf must be chosen for the extraction of the wind speed from a specific direction.

Three unknown parameter needed for an appropriate guess:

- the time span between a wind speed changes Δt_s
- the time span between direction changes Δt_d
- the Weibull function shape factor k

Δt_s has been estimated from the time autocorrelation function of the data provided by the CTI. In detail:

$$\Delta t_s = \int_0^\infty corr[V(t) - V(t-\tau)]d\tau \sim 5\ h \qquad [7.1]$$

Δt_d has been set equal to the synoptic peak associated to large scale meteorological scales (4 days) as observed by Van Der Hoven [3].

For a smart guess of the Weibull k factor, different sets of 100 year of wind history have been simulated with different shape factor. For each set the year the yearly averaged speed have been ranked and the 50^{th} rank (mid position) chosen as the most representative.

The qualitative confront of the so obtained new frequencies distribution and the original from CTI (with a properly scaled mean), suggested k ranging from 1.5 to 2, so 1.5 have been chosen in the end.

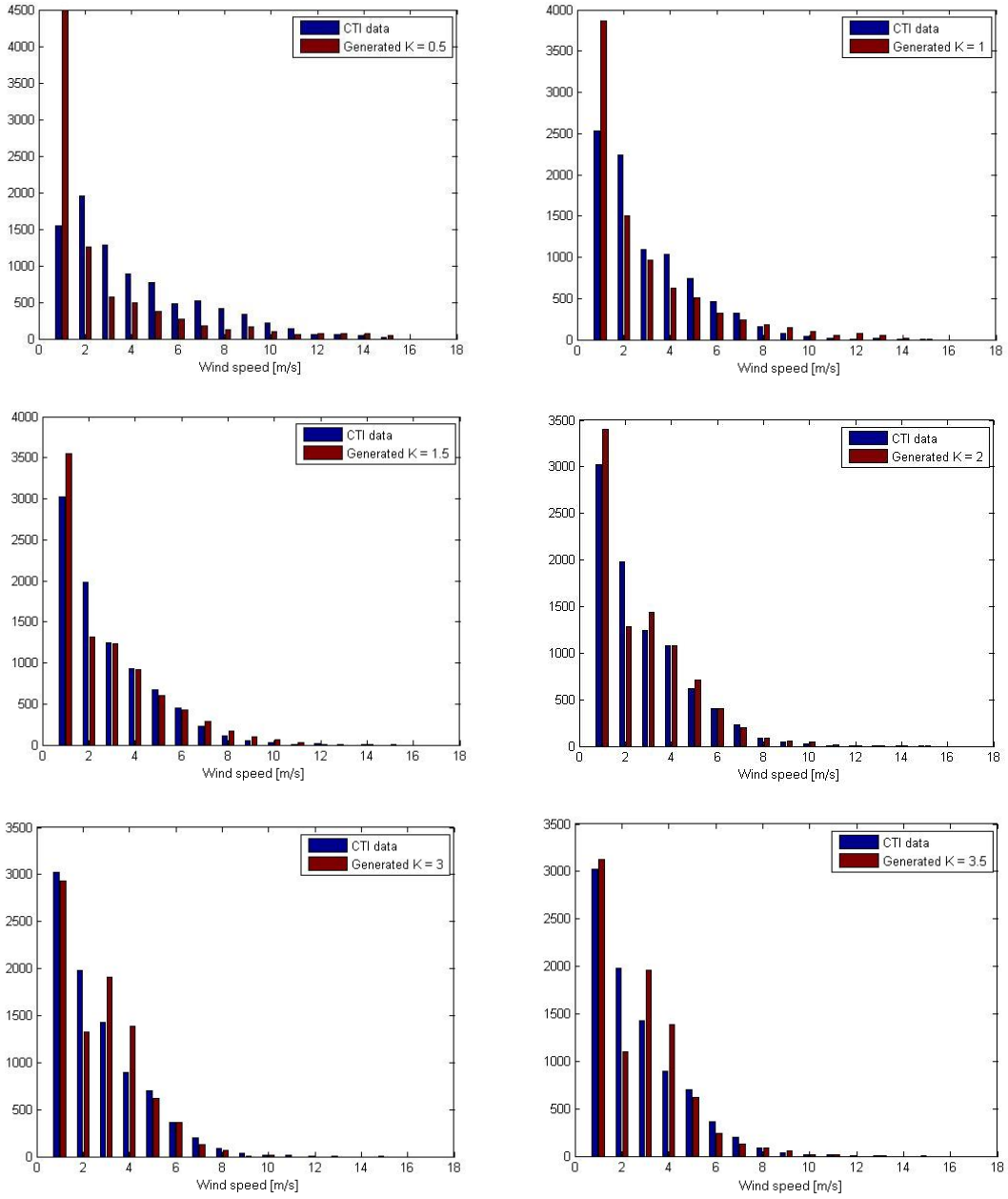

Graph 7.1 - Frequency distribution of wind speed from CTI [1] compared with generated data

7.2 Annual energy production

In the selected configuration the wind energy is produced by a Windspire 1.2 kW wind turbine. Its annual energy output is 1648 kWh, corresponding to 1093 equivalent hours (relatively to the peak power). Adopting the correction for 3D effects and conversion efficiency an equivalent turbine with the same energy production. This turbine is 4.5 m tall and its hub height is 9.25 m (wind shear have been considered, see further). The resulting fuel saving of the system overall with the new turbine differs from the original for less than 1%, so that the new machine can be considered equivalent to the original Windspire.

The power curves of the new turbine are plotted below and compared with the original Windspire experimental data [4]. The contribution to losses from different sources are also highlighted.

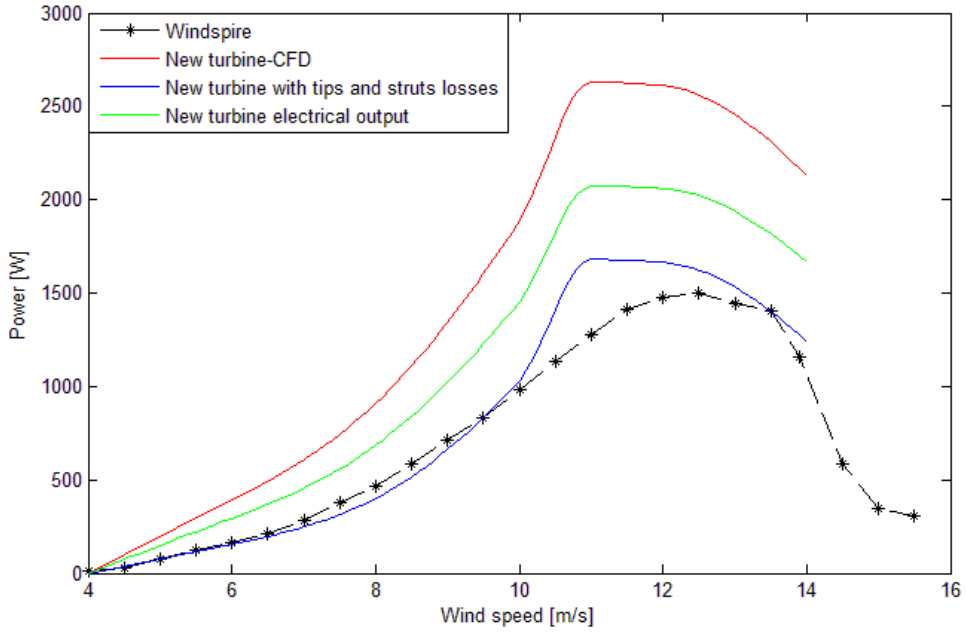

Graph 7.2 - Power curve of bare turbine equivalent to the Windspire rotor

The new created bare turbine have been adopted throughout the rest of this work for it represents a good basis for comparison with its diffuser-augmented version.

The DAWT production has been calculated with same wind time series for several designs differing by turbine height and hub height. To evaluate the effect of the wind gradient the following equation has been used [3]:

$$U(z) = U_{ref} \frac{\ln\left(\frac{z}{z_0}\right)}{\ln\left(\frac{z_{ref}}{z_0}\right)} \qquad [7.2]$$

where z_0 is the roughness height, taken as 0.1 m as [3] suggests for countryside with trees and hedges.

In the graph below, the results are compared with the bare turbine production.

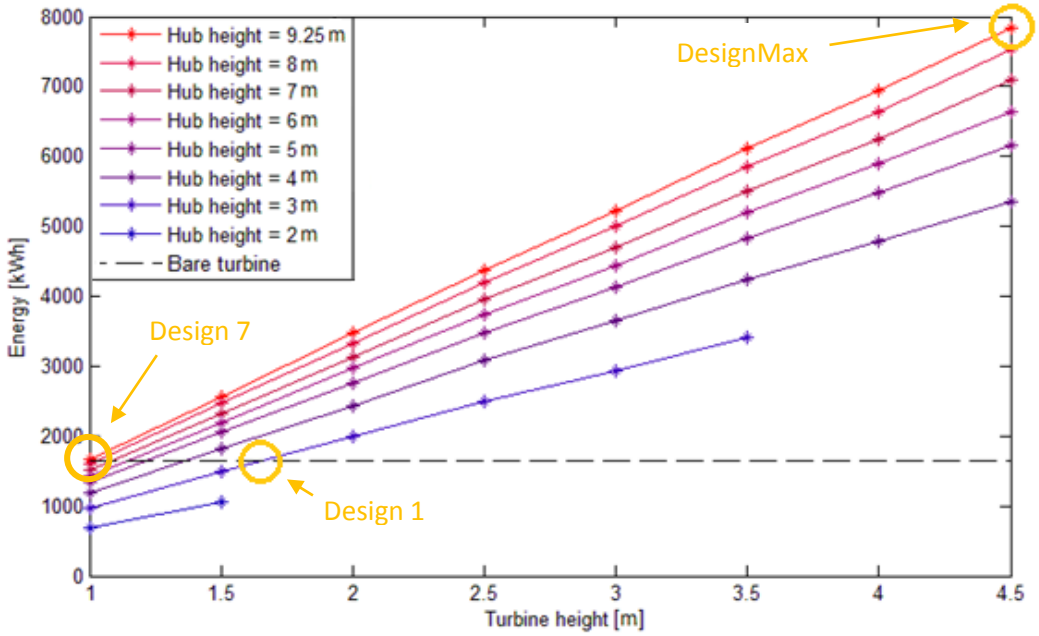

Graph 7.3 - Annual energy output from different design of DAWT

The straightforward result is that the energy output increases with hub and turbine height, becoming nearly 5 time higher when the same dimension of the bare turbine are adopted.

Thanks to this chart it has been possible to individuate 7 DAWT design matching the annual energy output of the bare turbine.

	Hub height [m]	Turbine height [m]	Frontal area [m^2]
Bare turbine	9.25	4.5	9
Design 1	3	1.66	16.6
Design 2	4	1.372	13.7
Design 3	5	1.22	12.2
Design 4	6	1.144	11.44
Design 5	7	1.085	10.85
Design 6	8	1.028	10.28
Design 7	9.25	0.99	9.9

Table 7.3 - Main geometric features of the new designs having the same energy production of the bare turbine

It is worthwhile to notice that the frontal area, even if it diminishes as the hub height increases (and this is reasonable, since higher winds are exploited) never becomes smaller than that of the bare turbine. This is an important result, since it proofs that the diffuser installation, even with a challenging and highly efficient design, does not permit to overcome the performance of a turbine with the same frontal area. So, the benefit of this technology should be searched elsewhere.

Three different designs have been chosen for in depth analysis:

- Deisgn1 of table 7.3, corresponding to the shorter turbine producing the same energy
- Design7 of table 7.3 that is the turbine placed at the same hub height of the bare one

- DesignMax, consisting in the DAWT with the same dimensions of the bare turbine

7.2.1 Design1

Since the power curve depends essentially on turbine height, this design has the highest peak power of the equivalent bare configuration .

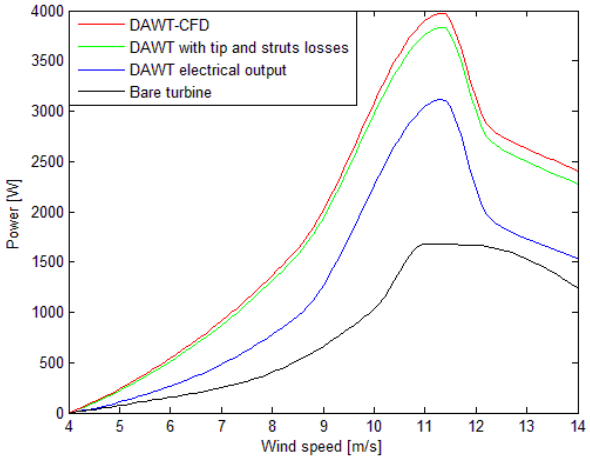

Graph 7.4 - Power curve for Design 1

The aerodynamic losses are very small since only six arms are mounted and the tip losses are neglected.

The power history shows how the production of the DAWT, as it could be expected, exhibits very high peaks and, since the overall energy is the same, this indicates a very irregular operation regime. This energy performance corresponds to 414 equivalent operating hour, thus the installed power is not cost-effectively exploited.

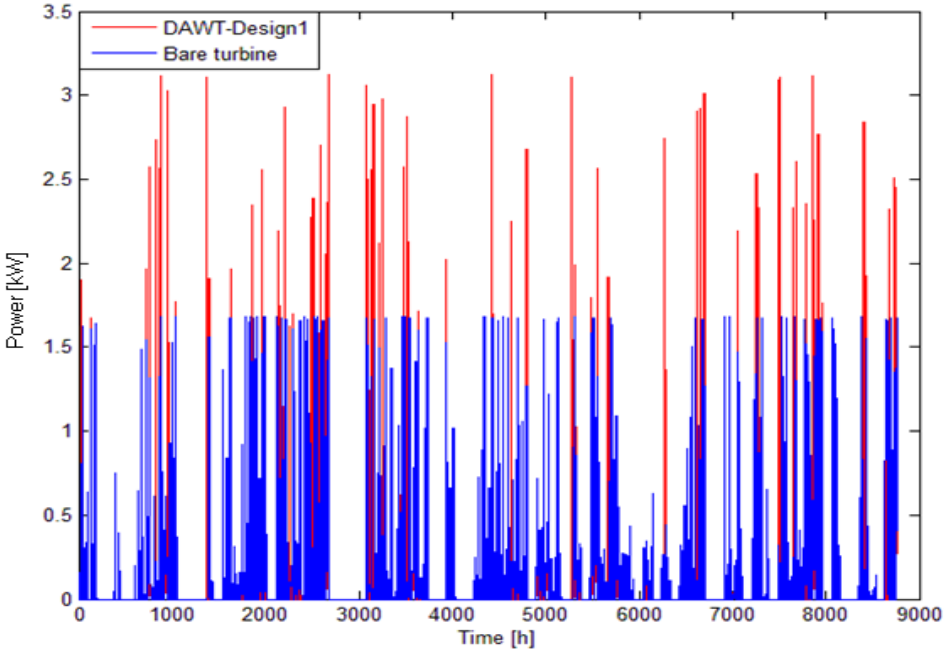

Graph 7.5 - Power production from bare turbine and DAWT with Design 1

It has been investigated weather this heavy fluctuation could have had negative influences in terms of overproduction due to the undersized electric storage, but small variation (5%) of the wasted energy was found (see table 7.4). This is because the turbine operates in a "highly PV-oriented" system, since 10 kW of photovoltaic power is installed, providing 17 MWh of energy per year. The storage, for it has been sized automatically sized by the optimizer algorithm according to overall power supply, has a 41 kWh capacity that is far sufficient to resist to power peak from the new wind turbine. The maximum energy input the electric storage can withstand in this system is 6 kW, 2 times the DAWT peak. The following figure compares the photovoltaic and the DAWT energy production.

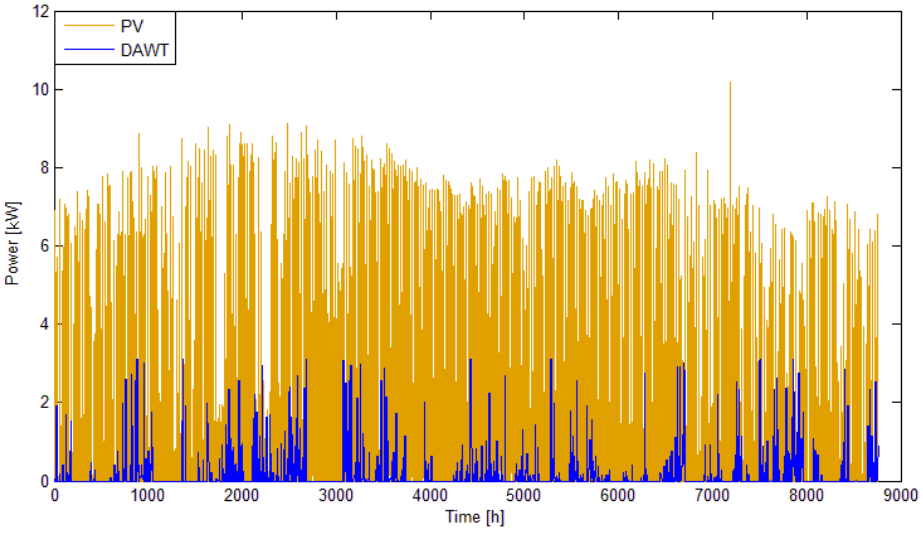

Graph 7.6 - Power production from DAWT with Design 1 and PV array

This PV supremacy subdues all the possible perturbations that a change in the wind power instantaneous production could have caused.

7.2.2 Design7

In this case the DAWT operates with the same wind of the bare turbine and, obviously, the power curves are similar.

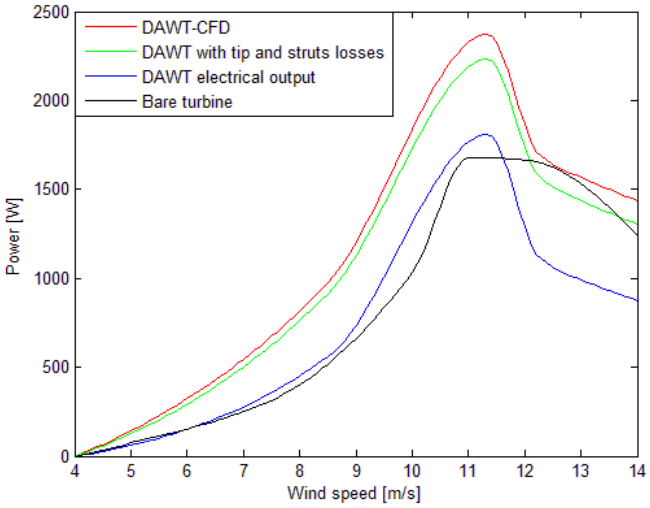

Graph 7.7 - Power curve for Design 7

Even the power production exhibit a similar pattern to the original case. No matter about the fact that this means almost null perturbation in the system as whole. The equivalent operating hours are less than in the bare turbine case, mainly because of the unfair shape of the power curve.

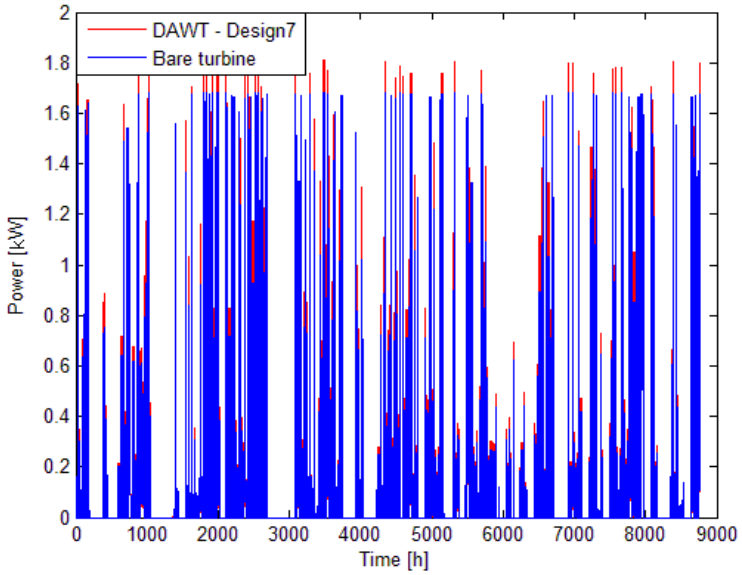

Graph 7.8 - Power production from bare turbine and DAWT with Design 1

7.2.3 DesignMax

The power curve and the energy production of the DAWT with the same height and position of the bare one are reported below, highlighting that a power production 5 time larger can be achieved installing the proposed diffuser.

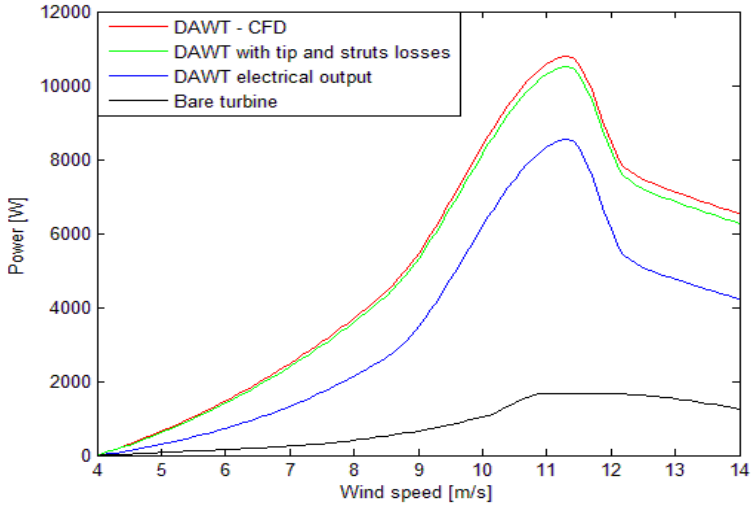

Graph 7.9 - Power curve for DesignMax

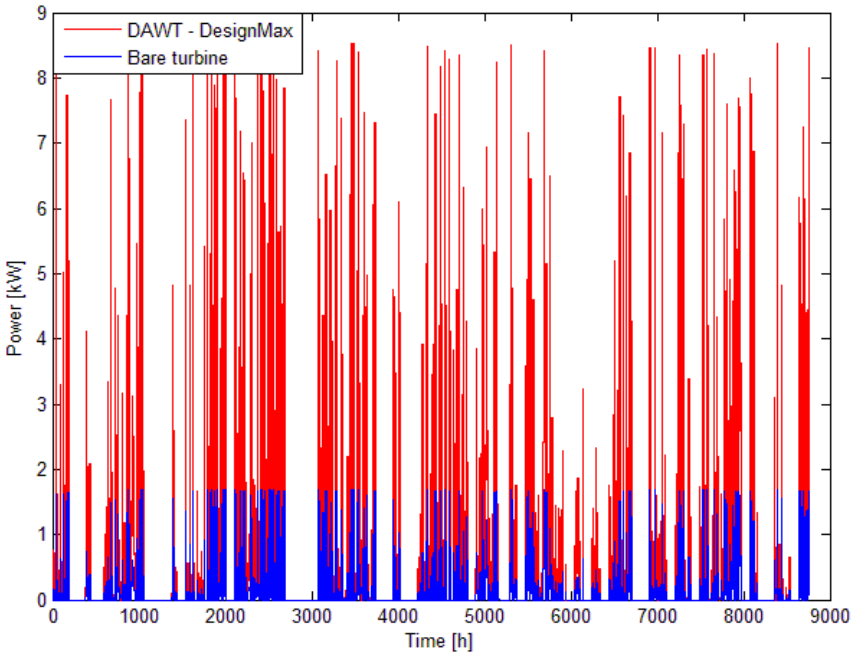

Graph 7.10 - Power production from bare turbine and DAWT with DesignMax

The turbine upgrading makes it more competitive against the solar panels, as the following plot shows.

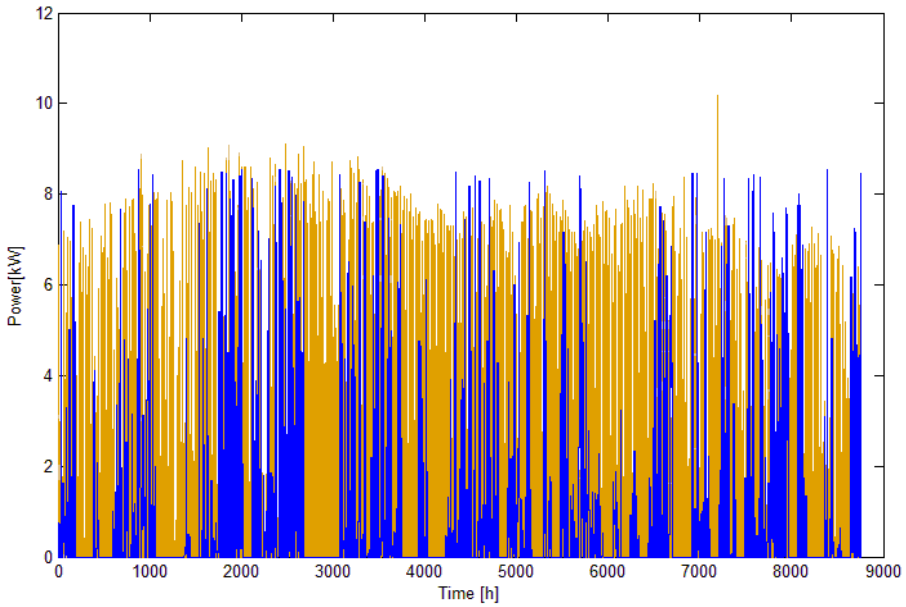

Graph 7.11 - Power production from DAWT with DesignMax and PV array

Concerning the storage capacity, the enhanced energy production from renewable source contributes in avoiding deep discharge (the average charge level passes from 56% to 64%) and this is positive for the batteries' health (see table 7.4). Nevertheless, the storage comes out to be undersized for the new configuration, as the almost tripled overproduction witnesses.

	Energy [kWh/y]	Eq. operating hours [h]	Fuel saved [kg/y]	Electric storage capacity depletion rate [1/y]	Electric storage mean charge level	Energy over production [kWh/y]
Bare turbine	1650	970	3575	14.7%	56%	3672
Design1	1656	414	3558	14.5%	56%	3827
Design7	1656	690	3576	14.7%	56%	3773
DesignMax	7830	710	3875	13.3%	64%	9230

Table 7.4 Energy performance of the system with different turbines

The following picture is a scaled down representation of the proposed designs (front view). The towers' designs do not correspond to any realistic installation but they are given only in order to make the picture more realistic.

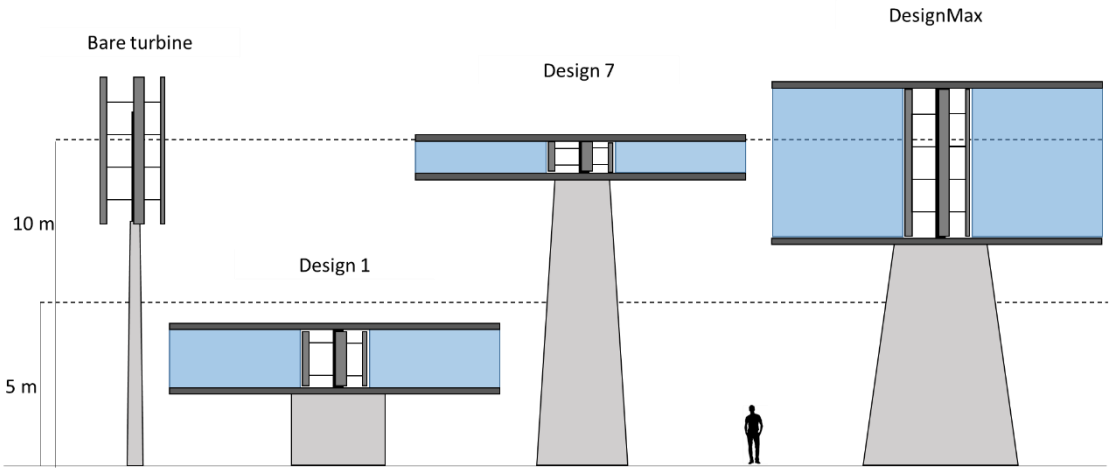

Figure 7.1 - Scaled down representation of the studied configuration

VII References

[1] *Test reference years*, Comitato Termotecnico Italiano Energia e Ambiente, www.cti2000.it, On_Line
[2] *Statistiche meteorologiche Anni 2000-2002*, ISTAT, Annuario, n. 29 - 2005
[3] Burton T, Jenkins N, Sharpe D, Bossanyi E. *Wind Energy Handbook*, Second Edition.. © 2011 John Wiley & Sons, Ltd. Published 2011 by John Wiley & Sons, Ltd. ISBN: 978-0-470-69975-1
[4] *Power Performance Test Report for the Windspire Conducted by Windward Engineering*, LLC 10768 S. Covered Bridge Canyon Spanish Fork, UT 84660

Part VIII - Conclusion

The optimal design of the DAWT obtained at the end of the optimization has a power five times higher than that of the original turbine. This remarkable performance enhancement goes beyond the expectancies. In this sense, the most influencing parameter was found out to be the diffuser angle and. In particular, the possibility of increasing the diffuser tilt far beyond the static angle of attack of the selected airfoil permitted the achievement of the over-mentioned result. The fact that an effect that in a first-order analysis would have been considered secondary became so fundamental is very interesting. More over, since the last designs in the optimization phase greatly differed form the original, unexpected effects, such as wake blockage and vortex shedding, took place.

This results were made possible by the hybrid CFD-BEM approach adopted, a model capable of performing a large amount of simulations of different geometries in a reasonable time. This model is not completely new, since other examples can founded in literature [1, 2, 3, 4], but the dynamic stall model proposed represent an innovation. However, the time-efficient calculation (up to 100 times faster) that these kind of models permit, are powerful instrument to investigate the influence of the different parameters of arbitrary geometries for cases in which the solution of the outer flow is more important than the accurate knowledge of the flow field near the turbine (e.g. DAWT, turbine placed in realistic environment, windmill farms). More generally, the separate modelling of simultaneous phenomena characterized by different time and length scales, can be regarded as an effective approach to complex realities.

Concerning the last part of the work, the integration of the proposed new design in a realistic hybrid power system, highlighted the limits of the adopted modelling. The aerodynamics-oriented approach adopted throughout the study, since it disregarded the structural, economical and more generally practical issues connected to the real installation of the machine, produced some results that appear unfeasible. In fact, besides the apparently encouraging power performance, the proposed diffuser caused some problems that could make it not much attractive. The high periodic loads induced by the shedding can cause fatigue and dangerous resonances in the whole structure. The power fluctuations can deteriorate the energy quality and stress the conversion system. The yaw control mechanism required by the DAWT can result complex and expensive. The equivalent operating hours are low, because of the uneven power curve shape. Moreover, none of the proposed designs energetically equivalent to the original turbine permitted the reduction of the frontal area, i.e. the overall conversion efficiency based on the actual area is lower than for conventional systems.

Nevertheless, an interesting benefit of the DAWT relies on the possibility of exploiting the wind resource with machines having a limited height. In contests where height constraints hold (e.g. urban environment, national parks) this technology could become attractive.

VIII References

[1] Torresi M, Fortunbato B, Camporeale S. Modello *CFD per il calcolo delle prestazioni e degli effetti di scia di turbine eoliche ad asse verticale*, La Termotecnica, Maggio 2013

[2] S. Antheaume, T. Maitre, J.-L. Achard, *Hydraulic Darrieus turbines efficiency for free fluid flow conditions versus power farms conditions*, Renew. Energy 33 (10) (2008) 2186e2198

[3] Dominguez F, Achard JL, Zanette J, Corre C. *Fast power output prediction for a single row of ducted cross-flow water turbines using a BEM-RANS approach*, Renewable Energy 89 (2016) 658e670

[4] Georgescu AM, Georgescu SC, Perte AM, Badea I, *Time efficient computing of the power coefficient for a ducted Achard turbine*, U.P.B. Sci. Bull., Series D, Vol. 74, Iss. 4, 2012

Appendix I - CFD solver equations

A.1.1 RANS

The RANS approach solves the time-averaged velocities and pressure fields for an incompressible flow. The time average operator is defined as follows:

$$\bar{f} = \frac{1}{\Delta t}\int_t^{t+\Delta t} f\, dt \qquad [A.1]$$

The fluctuating term for the generic scalar is:

$$f' = f - \bar{f} \qquad [A.2]$$

The time averaged N-S equations for an incompressible fluid with constant viscosity in 2D are:

$$\frac{\partial \bar{u}}{\partial x} + \frac{\partial \bar{v}}{\partial y} = 0 \qquad [A.3]$$

$$\rho\left(\frac{\partial \bar{u}}{\partial t} + \frac{\partial \bar{u}}{\partial x}\bar{u} + \frac{\partial \bar{u}}{\partial y}\bar{v}\right) = -\frac{\partial \bar{p}}{\partial x} + \mu\left(\frac{\partial^2 \bar{u}}{\partial x^2} + \frac{\partial^2 \bar{u}}{\partial y^2}\right) - \rho\left(\frac{\partial \overline{u'u'}}{\partial x} + \frac{\partial \overline{u'y'}}{\partial x}\right) \qquad [A.4]$$

$$\rho\left(\frac{\partial \bar{v}}{\partial t} + \frac{\partial \bar{u}}{\partial x}\bar{u} + \frac{\partial \bar{u}}{\partial y}\bar{v}\right) = -\frac{\partial \bar{p}}{\partial y} + \mu\left(\frac{\partial^2 \bar{v}}{\partial x^2} + \frac{\partial^2 \bar{v}}{\partial y^2}\right) + \rho\left(\frac{\partial \overline{v'v'}}{\partial x} + \frac{\partial \overline{u'y'}}{\partial x}\right) \qquad [A.5]$$

This approach allows the solutions of the average flow field but an appropriate modelling of the cross-correlation terms $\rho\overline{u_i{}'u_j{}'}$ is necessary.

A.1.2 $k-\omega$ *SST* Model[1]

Two additional scalar are introduced in order to have a robust estimation of the turbulent diffusivity:

- $k = \frac{1}{2}\left(\overline{u'^2} + \overline{v'^2}\right)$, the turbulent kinetic energy [m^2/s^2]
- ω, the specific dissipation rate [1/s]

The cross correlation terms are modeled via Boussinesq approximation [2], i.e.:

$$-\rho\overline{u'u'} = \mu_t\left(\frac{\partial \bar{u}}{\partial x} + \frac{\partial \bar{u}}{\partial x}\right) - \frac{2}{3}\rho k \qquad [A.6]$$

$$-\rho\overline{u'y'} = \mu_t\left(\frac{\partial \bar{u}}{\partial x} + \frac{\partial \bar{y}}{\partial x}\right) \qquad [A.7]$$

$$-\rho\overline{v'v'} = \mu_t\left(\frac{\partial \bar{v}}{\partial x} + \frac{\partial \bar{v}}{\partial x}\right) - \frac{2}{3}\rho k \qquad [A.8]$$

Where μ_t is the turbulent diffusivity, accounting for the enhanced mixing due to turbulent fluctuations. The following paragraphs show the most important equation of this model, but for the full set of equations and tuning constants please refer to [3].

A.1.2.1 *k* balance

$$\frac{\partial(\rho k)}{\partial t} + \frac{\partial(\rho k u_i)}{\partial x_i} = \frac{\partial}{\partial x_j}\left(\Gamma_k \frac{\partial k}{\partial x_j}\right) + \widetilde{G_k} - Y_k \quad [A.9]$$

Where:

- k is the turbulent kinetic energy
- Γ_k is the total diffusivity
- Y_k is the dissipative term due to turbulence
- $\widetilde{G_k}$ is the source term

A.1.2.1.1 Diffusivity modeling

$$\Gamma_k = \mu + \frac{\mu_t}{\sigma_k} \quad [A.10]$$

Where σ_k is the turbulent Prandtl number for the turbulent kinetic energy.

The turbulent viscosity μ_t is modeled as follows:

$$\mu_t = \frac{\rho k}{\omega} \frac{1}{\max[\frac{1}{\alpha^*}, \frac{SF_2}{0.31\omega}]} \quad [A.11]$$

Where S is the strain rate magnitude, defined as:

$$S = \sqrt{\frac{1}{2}\left(\frac{\partial u_i}{\partial x_j} + \frac{\partial u_j}{\partial x_i}\right)\left(\frac{\partial u_i}{\partial x_j} + \frac{\partial u_j}{\partial x_i}\right)} \quad [A.12]$$

And, moreover:

$$\sigma_k = \left(\frac{F_1}{1.176} + (1 - F_2)\right)^{-1} \quad [A.13]$$

$$\alpha^* = \frac{0.024 + Re_t/6}{1 + Re_t/6} \quad [A.14]$$

where the turbulent Reynolds number is:

$$Re_t = \frac{\rho k}{\mu \omega} \quad [A.15]$$

The F_1 and F_2 are the so-called blending functions that make possible a smooth transition between the k-ω and the k-epsilon models.

A.1.2.1.2 K production modeling

A production limiter to k production has been imposed, so that:

$$\widetilde{G_k} = \min(\mu_t S^2, 10\, \beta^* \rho k \omega) \quad [A.16]$$

Where $\beta^*$is a term depending from turbulent Reynolds and Mach numbers.

A.1.2.1.3 k dissipation modeling

A simplified form of the standard model formulation is here adopted:

$$Y_k = \rho\beta^* k\omega \qquad \text{[A.17]}$$

A.1.2.2 ω balance

$$\frac{\partial(\rho\omega)}{\partial t} + \frac{\partial(\rho\omega u_i)}{\partial x_i} = \frac{\partial}{\partial x_j}\left(\Gamma_k \frac{\partial\omega}{\partial x_j}\right) + \widetilde{G_\omega} - Y_\omega + D_\omega \qquad \text{[A.18]}$$

The only additional term with respect to the k equation is the cross diffusion source D_ω, and it has been to make this equation perfectly equivalent with the epsilon balance when the wall distance approaches infinity (i.e. in the freestream)

$$D_\omega = 2(1-F_1)\frac{\rho}{\sigma_{\omega,2}\omega}\frac{\partial k}{\partial x_j}\frac{\partial\omega}{\partial x_j} \qquad \text{[A.19]}$$

A.1.2.2.1 ω diffusivity modeling

In analogy with previous formulation, it is:

$$\Gamma_\omega = \mu + \frac{\mu_t}{\sigma_\omega} \qquad \text{[A.21]}$$

With the obvious following modification:

$$\sigma_\omega = \left(\frac{F_1}{\sigma_{\omega,1}} + \frac{(1-F_1)}{\sigma_{\omega,2}}\right)^{-1} \qquad \text{[A.22]}$$

A.1.2.2.2 Omega production modeling

A simple modified version of the k production term is adopted:

$$G_\omega = \frac{\alpha}{\nu_t} G_k \qquad \text{[A.23]}$$

Where α is a constant depending of the turbulent Reynolds and the blending function.

A.1.2.2.3 Omega production modeling

$$Y_k = \rho\beta\omega^2 \qquad \text{[A.24]}$$

Where β is a constant value changing only by virtue of the blending functions.

Appendix II - UDFs codes

A.2.1 AR source terms calculator

```
#include "udf.h"
int trovind (double angolo){
int inn=0;
        do{
inn++;
}while (inn*(360/40)<angolo);
return inn;
}
double trovvel(int settore, Thread *tt, int carac){
        cell_t cc;
        int conteggio;
        real z[ND_ND];
        double coseno2,thet2,ics2,yps2,somma;
        somma=0;
        conteggio=0;
        begin_c_loop(cc, tt)
        {
                C_CENTROID(z,cc,tt);
                ics2=z[0];
                yps2=z[1];
                coseno2=yps2/(sqrt(ics2*ics2+yps2*yps2));
                if (ics2<=0){
                        thet2=acos (coseno2)*180/3.14159;
                }
                if (ics2>0){
                        thet2=acos (coseno2)*180/3.14159;
                        thet2=180+(180-thet2);
                }

                if (fabs(trovind(thet2)-settore)<0.1){
                        if (carac==1) somma=somma+C_U(cc,tt);
                        if (carac==2) somma=somma+C_V(cc,tt);
                        conteggio++;
                }
        }
        end_c_loop(cc, tt)
        return somma/conteggio;
}
double clnaca(double alfa,double Re){
        double cl160[80];
        double cl360[80];
        double cl700[80];
        double cl2000[80];
        double clmin[80];
        double clmax[80];
        double remin,remax, clf, cl1, cl2;
        int i;
        int ind1,ind2;
        for (i=0;i<80;i=i+1){
                cl160[i]=0;
                cl360[i]=0;
                cl700[i]=0;
                cl2000[i]=0;
        }
```

```
cl160[0]=0;
cl160[6]=0.66;
cl160[7]=0.746;
cl160[8]=0.8274;
cl160[9]=0.8527;
cl160[10]=0.1325;
cl160[11]=0.1095;
cl160[12]=0.1533;
cl160[13]=0.203;
cl160[14]=0.2546;
cl160[15]=0.3082;
cl160[16]=0.362;
cl160[17]=0.42;
cl160[18]=0.4768;
cl160[19]=0.5322;
cl160[20]=0.587;
cl160[21]=0.641;
cl160[22]=0.6956;
cl160[23]=0.7497;
cl160[24]=0.8034;
cl160[25]=0.8512;
cl160[26]=0.9109;
cl160[27]=0.9646;
cl160[30]=0.915;
cl160[35]=1.02;
cl160[40]=1.075;
cl160[45]=1.085;
cl160[50]=1.04;
cl160[70]=0.65;

cl360[0]=0;
cl360[6]=0.66;
cl360[7]=0.77;
cl360[8]=0.8542;
cl360[9]=0.9352;
cl360[10]=0.9811;
cl360[11]=0.9132;
cl360[12]=0.4832;
cl360[13]=0.2759;
cl360[14]=0.2893;
cl360[15]=0.3306;
cl360[16]=0.3792;
cl360[17]=0.4455;
cl360[18]=0.5047;
cl360[19]=0.5591;
cl360[20]=0.612;
cl360[21]=0.6643;
cl360[22]=0.7179;
cl360[23]=0.7715;
cl360[24]=0.8246;
cl360[25]=0.878;
cl360[26]=0.9313;
cl360[27]=0.9846;
cl360[30]=0.915;
cl360[35]=1.02;
cl360[40]=1.075;
cl360[45]=1.08;
cl360[50]=1.04;
cl360[70]=0.65;

cl700[0]=0;
cl700[6]=0.66;
```

```
cl700[7]=0.77;
cl700[8]=0.88;
cl700[9]=0.9598;
cl700[10]=1.0343;
cl700[11]=1.0749;
cl700[12]=1.039;
cl700[13]=0.8737;
cl700[14]=0.6284;
cl700[15]=0.4907;
cl700[16]=0.4696;
cl700[17]=0.5195;
cl700[18]=0.5584;
cl700[19]=0.6032;
cl700[20]=0.6474;
cl700[21]=0.6949;
cl700[22]=0.7446;
cl700[23]=0.7948;
cl700[24]=0.8462;
cl700[25]=0.8984;
cl700[26]=0.9506;
cl700[27]=1.0029;
cl700[30]=0.915;
cl700[35]=1.02;
cl700[40]=1.075;
cl700[45]=1.085;
cl700[50]=1.04;
cl700[70]=0.65;

cl2000[0]=0;
cl2000[6]=0.66;
cl2000[7]=0.77;
cl2000[8]=0.88;
cl2000[9]=0.99;
cl2000[10]=1.0727;
cl2000[11]=1.1539;
cl2000[12]=1.2072;
cl2000[13]=1.2169;
cl2000[14]=1.1614;
cl2000[15]=1.0478;
cl2000[16]=0.9221;
cl2000[17]=0.7826;
cl2000[18]=0.7163;
cl2000[19]=0.7091;
cl2000[20]=0.7269;
cl2000[21]=0.7595;
cl2000[22]=0.7981;
cl2000[23]=0.8429;
cl2000[24]=0.8882;
cl2000[25]=0.9352;
cl2000[26]=0.9842;
cl2000[27]=1.0355;
cl2000[30]=0.915;
cl2000[35]=1.02;
cl2000[40]=1.07;
cl2000[45]=1.085;
cl2000[50]=1.04;
cl2000[70]=0.65;

if (Re<160000){
        for (i=0;i<80;i=i+1){
                        clmin[i]=cl160[i];
                        clmax[i]=cl160[i];
```

```
                remin=160;
                remax=160;
                }
        }
    if (Re>160000 && Re<360000){
        for (i=0;i<80;i=i+1){
                clmin[i]=cl160[i];
                clmax[i]=cl360[i];
                remin=160;
                remax=360;
                }
        }
    if (Re>360000 && Re<700000){
        for (i=0;i<80;i=i+1){
                clmin[i]=cl360[i];
                clmax[i]=cl700[i];
                remin=360;
                remax=700;
                }
        }
    if (Re>700000 && Re<2000000){
        for (i=0;i<80;i=i+1){
                clmin[i]=cl700[i];
                clmax[i]=cl2000[i];
                remin=700;
                remax=2000;
                }
        }
        if (Re>2000000){
        for (i=0;i<80;i=i+1){
                clmin[i]=cl2000[i];
                clmax[i]=cl2000[i];
                remin=2000;
                remax=2000;
                }
        }
        remin=remin*1000;
        remax=remax*1000;
        ind1= floor(alfa)+1;
        ind2=floor(alfa);
        if (clmin[ind1]== 0){
            do{
                ind1++;
            } while (clmin[ind1]==0);
        }

        if (ind2>0 && clmin[ind2]==0)
        {
            do{
                ind2--;
            } while (clmin[ind2]==0 && ind2>0);

        }
            cl1=clmin[ind2]+(clmin[ind1]-clmin[ind2])/(ind1-ind2)*(alfa-ind2);
            cl2=clmax[ind2]+(clmax[ind1]-clmax[ind2])/(ind1-ind2)*(alfa-ind2);

        clf=cl1+(cl2-cl1)/(remax-remin+1)*(Re-remin);
        return clf;
}
```

```
double coeffnaca(int inde,double Re1){
```

```
int i;
double vett160[8],vett360[8],vett700[8],vett2000[8],vettmin[8],vettmax[8],remin,remax,ve;

vett160[1]=0.0001;
vett160[2]=0.0002;
vett160[3]=0.0101;
vett160[4]=0.0545;
vett160[5]=-0.5048;
vett160[6]=0.023;
vett160[7]=-0.01562;

vett360[1]=0.00008;
vett360[2]=0.0003;
vett360[3]=0.0077;
vett360[4]=0.0542;
vett360[5]=-0.4215;
vett360[6]=0.0236;
vett360[7]=-0.1712;

vett700[1]=0.00007;
vett700[2]=0.0003;
vett700[3]=0.0064;
vett700[4]=0.0488;
vett700[5]=-0.3228;
vett700[6]=0.024;
vett700[7]=-0.1555;

vett2000[1]=0.00006;
vett2000[2]=0.00006;
vett2000[3]=0.0064;
vett2000[4]=0.0445;
vett2000[5]=-0.1306;
vett2000[6]=0.0246;
vett2000[7]=-0.1941;

if (Re1<160000){
        for (i=0;i<8;i=i+1){
                vettmin[i]=vett160[i];
                vettmax[i]=vett160[i];
                remin=160;
                remax=160;
        }
}
if (Re1>160000 && Re1<360000){
        for (i=0;i<8;i=i+1){
                vettmin[i]=vett160[i];
                vettmax[i]=vett360[i];
                remin=160;
                remax=360;
        }
}
if (Re1>360000 && Re1<700000){
        for (i=0;i<8;i=i+1){
                vettmin[i]=vett360[i];
                vettmax[i]=vett700[i];
                remin=360;
                remax=700;
        }
}
if (Re1>700000 && Re1<2000000){
for (i=0;i<8;i=i+1){
                vettmin[i]=vett700[i];
```

```
                        vettmax[i]=vett2000[i];
                        remin=700;
                        remax=2000;
                        }
        }
        if (Re1>2000000){
        for (i=0;i<8;i=i+1){
                        vettmin[i]=vett2000[i];
                        vettmax[i]=vett2000[i];
                        remin=2000;
                        remax=2000;
                        }
        }
        remin=remin*1000;
        remax=remax*1000;
        ve=vettmin[inde]+(vettmax[inde]-vettmin[inde])/(remax-remin+1)*(Re1-remin);
        return ve;
        }
```

```
DEFINE_EXECUTE_AT_END(execute_at_end)
{

        real x[ND_ND];
        real  source,coseno,ics,yps, thet,timvero,source2;
        cell_t ccc;
        Domain *dom;
        double        th,tim,alf,cx,cy,u,omega,tsr,r,wx,wy,w,dt,uinf,pi,rey,cor,tga,vett,l,d,rd,tn,t0,        oldalf,
        sgme,deralfa,rx,ry,valx,valy,valt,th2,newsource,newsourcey,sd,cl1,cld,s,tau,vpos,clqs,clmin,clmax,c
        l0d,omega1,cls,clnc,tt,ff,dert,omega03,omega3,omega4,anglev,clv,fff,clt,cdmin,cdmax,cdt,cdd,fact,
        vmin,vmax,umin,umax;
        double cl0[10000], calma[42],resy[42],torque[42];
        int ii, sgm,sgmold, sett, oldsett, indiceang, indice, cont, sn, oldindiceang,iii,levtrav,imin,imax;
        Thread *t;
        dom = Get_Domain(1);
        t= Lookup_Thread(dom,20);
        timvero =CURRENT_TIME;
        sgm=0;
        source=0;
        sn=0;
        sett=0;
        cont=0;
        oldsett=0;
        valx=0;
        valt=0;
        valy=0;
        pi=3.141592654;
        dt=0.0005;
        uinf=10;
        r=1;
        cor=0.2;
        tsr=4.5;
        omega=tsr*uinf/r;
        u=omega*r;
        indice=0;
        indiceang=-1;
        //if (fabs(CURRENT_TIME/0.02-floor((CURRENT_TIME+0.0001)/0.02))< 0.0001  ) {
                for (tim=pi/2/omega;tim<=4*pi/omega+pi/2/omega+0.001;tim=tim+dt){
                        indice++;
                        th=omega*tim;
                        oldindiceang=indiceang;
                        th2=th*180/pi-90;
```

```
if (th2<0) th2=th2+360;
if (th2>360) th2=th2-360;
indiceang=trovind(th2+4.5);
if (fabs(oldindiceang-indiceang)>0.1){
        imin=trovind(th2);
        imax=imin+1;
        if (trovind(th2)==trovind(th2+4.5)) {
                imin=imin-1;
                imax=imax-1;
        }
        if (imin<1)         imin=40;
        if( imax>40) imax=1;
        umin=trovvel(imin,t,1);
        umax=trovvel(imax,t,1);
        vmin=trovvel(imin,t,2);
        vmax=trovvel(imax,t,2);
}
fact=(th2-9*imin+4.5)/9;
if (imin==40&&th2<100) fact=(th2+4.5)/9;
cx=umin*(1-fact)+umax*fact;
cy=vmin*(1-fact)+vmax*fact;
wx=u*sin(th)+cx;
wy=-u*cos(th)+cy;
w=sqrt(wx*wx+wy*wy);
sgmold=sgm;
sgme=(wx*cos(th)+wy*sin(th));
if (sgme<0)  sgm=-1;
if (sgme>0)  sgm=1;
tga=(wx*cos(th)+wy*sin(th))/(-wx*sin(th)+wy*cos(th));
tga=sqrt(tga*tga);
oldalf=alf;
alf=atan(tga)*180/pi;
deralfa=(alf-oldalf)/dt;
deralfa=deralfa*pi/180;//in radianti la derivata!!!
rey=w*cor/(0.000018)*1.225;
if ( sgm*sgmold<=0){
        t0=tim;
        vpos=0;
        indice=1;
        sd=1;
        clv=0;
        levtrav=0;
        deralfa=alf/dt*pi/180;
}
clqs=clnaca(alf,rey);
clmin=coeffnaca(4,rey)*alf+coeffnaca(5,rey);
clmax=0.11*alf;
cl0[indice]=clmax;
cl0[0]=0;
if (alf>30)         clmin=clqs;
s=(clqs-clmin)/(clmax-clmin);
if (s>1) s=1;
if (s<0) s=0;
tau=cor/(2*w);
omega1=0.58/80*40/tau;
cls=clmin+(clmax-clmin)*s;
ff=0;
for (ii=1;ii<=indice;ii=ii+1)          {
        dert=(cl0[ii]-cl0[ii-1])/dt;
        ff=ff+dert*(1-0.5*exp((-omega1)*((indice-ii)*dt)))*dt;
}
cl0d=ff+cl0[0];
```

```
		clnc=pi*deralfa*tau;
		cl0d=cl0d+clnc;
		omega03=7*0.58/80/tau;
		omega3=omega03;
		if (vpos>0) omega3=omega03*7;
		if (vpos>=1 && alf>7) omega3=omega03;
		if (alf<7)		omega3=omega03*7;
		sd=sd+(s-sd)*omega3*dt;
		cld=clmin+(cl0d-clmin)*sd;
		omega4=150*0.58/80/tau;
		anglev=0.000009*rey+12.861*omega*tau-1.675+13.073;
		if (alf>anglev) levtrav=1;
		if (levtrav==1) vpos=vpos+w/3*dt/cor;
		if (vpos>1) vpos=1;
		if (vpos<1 && deralfa+fabs(deralfa)*levtrav*2>0){
			fff=omega4*(cl0d-cld-clv);
			if (fff>0) clv=clv+fff*dt;
		}
		else {
			clv=clv+omega4*(-clv)*dt;
			levtrav=0;
		}
		if (clv<0)		clv=0;
		clt=cld+clv;
		cdmin = coeffnaca(1,rey)* alf *alf + coeffnaca(2,rey) * alf + coeffnaca(3,rey);
		cdmax = coeffnaca(6,rey) * alf +coeffnaca(7,rey);
		if (cdmax < cdmin) cdmax = cdmin;
		if (alf > 30)  cdmin = clqs*tan(alf * 3.14159 / 180);
		cdd = cdmax + (cdmin - cdmax) * sd;
		cdt = cdd + clv * tan(alf * 3.14159 / 180);
		l=0.5*1.225*clt*w*w*cor;
		d=0.5*1.225*cdt*w*w*cor;
		tn=l*sin(alf/180*pi)-d*cos(alf/180*pi);
		rd=(l*cos(alf/180*pi)+d*sin(alf/180*pi))*sgm;
		rx=rd*cos(th)-tn*sin(th);
		ry=rd*sin(th)+tn*cos(th);
		oldsett=sett;
		sett = floor((th*180/pi-90)/9)+1;//40 divisioni
		if (oldsett!=sett && oldsett>0 && cont>0){
			sn++;
			calma[sn]=valx/cont/40*3;
			resy[sn]=valy/cont/40*3;
			torque[sn]=valt/cont;
			valy=0;
			valx=0;
			valt=0;
			cont=0;
		}
		if (th>2*pi+pi/2){
			cont++;
			valx=valx+rx;
			valy=valy+ry;
			valt=valt+tn;
		}
}
begin_c_loop(ccc, t)	{
		C_CENTROID(x,ccc,t);
		ics=x[0];
		yps=x[1];
		coseno=yps/(sqrt(ics*ics+yps*yps));
		if (ics<=0){
			thet=acos (coseno)*180/3.14159;
```

```
                        }
                        if (ics>0){
                                thet=acos (coseno)*180/3.14159;
                                thet=180+(180-thet);
                         }
                        indiceang=trovind(thet);
                        newsource=-calma[indiceang]/0.62804*40;
                        newsourcey=-resy[indiceang]/0.62804*40;
                        C_UDMI(ccc,t,0) =newsource;
                        C_UDMI(ccc,t,1) =newsourcey;
                        C_UDMI(ccc,t,2) =torque[indiceang]/(0.5*1.225*2*r*r*uinf*uinf);
                }
                end_c_loop(ccc, t)
}
DEFINE_SOURCE(x_momentum_source3,c,t,dS,eqn)
 {
        real sourcex;
        sourcex=0;
        if (CURRENT_TIME>0.02) sourcex=C_UDMI(c,t,0);
return sourcex;
}
DEFINE_SOURCE(y_momentum_source3,c,t,dS,eqn)
{
        real sourcey;
        sourcey=0;
        if (CURRENT_TIME>0.02) sourcey=C_UDMI(c,t,1);
return sourcey;
}
```

A.2.2 Struts drag

```
#include "udf.h"
DEFINE_ON_DEMAND (arms){
	real x[ND_ND], ics, yps, r, omega, thet, vtan, coseno, integ,vrad,re,cd,ll ;
	cell_t c;
	Domain *domain;
	Thread *t;
	domain = Get_Domain(1);
	integ=0;
	omega=39;
	thread_loop_c(t, domain){
	begin_c_loop(c, t)
	{
		C_CENTROID(x,c,t);
		ics=x[0];
		yps=x[1];
		r=sqrt(ics*ics+yps*yps);
		coseno=yps/(sqrt(ics*ics+yps*yps));
		if (ics<=0){
			thet=acos (coseno);
		}
		if (ics>0){
			thet=acos (coseno);
			thet=3.14159+(3.14159-thet);
		}
		if(ics*ics+yps*yps<1){
			vrad=-C_U(c,t)*sin(thet)+C_V(c,t)*cos(thet);
			vtan=C_U(c,t)*cos(thet)+C_V(c,t)*sin(thet);
			re=sqrt(vrad*vrad+vtan*vtan)*0.2*1.225/1.8*100000;

			cd=0.264*pow(re,-0.266);
	ll= vtan+omega*r;
			if (ll>0)
	integ=integ+C_VOLUME(c,t)*(0.5*1.225*0.2*cd)*(vtan+omega*r)*(vtan+omega*r);

		}
	}
	end_c_loop(c, c_thread)
	}
	integ=integ*omega/2/3.14159;
	printf("integ = %f", integ);
}
```

Appendix references

[1] Menter FR. *Two-Equation Eddy-Viscosity Turbulence Models for Engineering Applications*. AIAA Journal. 32(8). 1598-1605. August 1994
[2] Hinze JO. *Turbulence*. McGraw-Hill Publishing Co., New York. 1975
[3] *Fluent theory guide,* Ansys Inc. (2011)